

**Spatially-induced Momentum Transfer
over Water-worked Gravel Beds**

Volume 2

James Russell Cooper

A thesis presented for the degree of Doctor of Philosophy
The University of Sheffield
Department of Civil and Structural Engineering

September 2006

CHAPTER 5

THE SPATIAL VARIABILITY

IN TIME-AVERAGED

VERTICAL VELOCITY

5.1 Introduction

This is the second results chapter that examines the spatial variability in time-averaged flow fields. This chapter will investigate whether spatial variations exist in time-averaged vertical velocities over two water-worked gravel beds. It will be seen how this variability changes through the flow depth, and whether it remains significant in the regions of the flow where these variations are currently thought to be negligible. An examination will be made of whether the size is controlled by flow features that scale with flow depth, or by flow structures that are scaled by bed roughness. The chapter will also show how the degree of spatial variability changes with relative submergence, bed slope and between the two beds in order to understand what controls the size of this spatial variability. It will be seen whether expressions can be derived that describe the vertical variation in the degree of spatial variability, and whether it is related to the shape of the vertical profile of streamwise velocity profile. Furthermore, the chapter will examine the organisation of the spatial deviations over the beds and the relationship this has with bed surface topography and the water surface.

5.2 Distribution of Time-averaged Vertical Velocities over the Bed

To establish whether time-averaged streamwise velocities \bar{w} vary spatially over water-worked beds, the distributions of \bar{w} are firstly examined. This involves using the PIV measurements carried out in a vertical plane normal to the bed surface. The \bar{w} measurements from each of the nine lateral locations across the measurement area were combined to produce a matrix of \bar{w} measurements over and above the bed for a given experimental run. This assimilation resulted in a matrix of 549 \bar{w} values being produced over the bed for each vertical measurement position. Given this number, it was deemed appropriate to be able to use the vertical plane measurements to assess the

distribution of \bar{w} over the bed. The higher-order statistical moments of the distributions of \bar{w} are examined to quantify the spread and shape of their distributions. The standard deviation in \bar{w} over the bed, which is a measure of the degree of spatial variability in \bar{w} over the bed, will firstly be discussed. Then the skewness and kurtosis of the distributions will be examined, followed by how closely the distributions match a normal distribution.

Each of the experimental runs over the bimodal bed was designed so that the relative submergence and bed slope was the same as the runs over the unimodal bed. Therefore the values of the moments can be directly compared. This allows the distributions from all 22 experimental runs to be examined, producing a summary of the shape of the distributions over the two beds (Figure 5.1). It should provide an indication of the effect of the difference in bed surface topography between the beds on the way in which \bar{w} is distributed. It will also be possible to quantify what the differences are in the shapes of the distributions between experimental runs over a given bed. This sort of analysis enables the importance of the tails of the distributions, where the largest spatial variability is observed, to be determined.

5.2.1 Degree of Spatial Variability

The second-order moment of the distributions, its standard deviation $\sigma_{\bar{w}}$ can be used as a quantitative measure of the degree of spatial variation in \bar{w} at a given vertical height above the bed, and is given by

$$\sigma_{\bar{w}} = \sqrt{\frac{1}{N} \sum_{i=1}^N (\bar{w}_i - \langle \bar{w} \rangle)^2} \quad (5.1)$$

where N is the total number of measurements within the assimilated flow field. It is equivalent to $\sqrt{\langle \tilde{w}^2 \rangle}$, where \tilde{w} is the spatial deviation in \bar{w} , given by $\bar{w} - \langle \bar{w} \rangle$. Since \tilde{w} is a component of the form-induced stress, $\sigma_{\bar{w}}$ is an appropriate variable to parameterise in order to assess the significance of spatial variations for transferring fluid momentum. It is absolute, rather than relative, spatial deviations in the time-averaged flow field that produce form-induced stresses. This absolute measure is equivalent in spatial terms to the root mean square fluctuation in instantaneous vertical velocity.

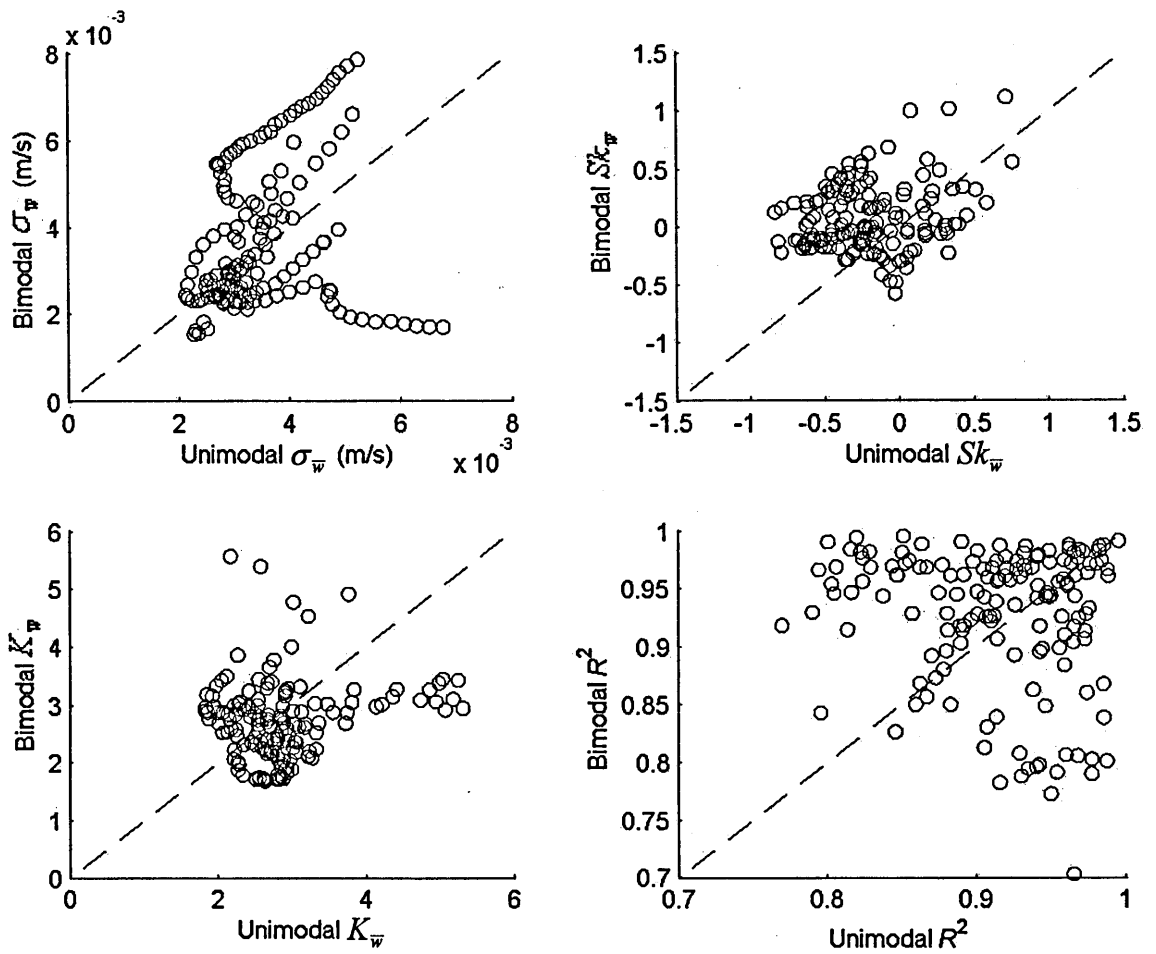


Figure 5.1. A comparison between the two beds of the shape of the distributions of \bar{w} for (a) $\sigma_{\bar{w}}$; (b) $Sk_{\bar{w}}$; (c) $K_{\bar{w}}$; and (d) R^2 of the regression between the probability density function of \bar{w} and the probability density function of a model normal distribution for those \bar{w} values, where $\sigma_{\bar{w}}$ is the degree of spatial variability in \bar{w} over the bed, \bar{w} is the time-averaged vertical velocity, $Sk_{\bar{w}}$ is the skewness of the distribution and $K_{\bar{w}}$ is the kurtosis of the distribution. The dashed line is a line of equality.

A comparison of $\sigma_{\bar{w}}$ between the two beds is shown in Figure 5.1a for all the measurements within the flow depth. It can be seen that the majority of the $\sigma_{\bar{w}}$ values are similar over each of the beds, with neither bed having $\sigma_{\bar{w}}$ values consistently higher than the other. There are, however, two lines of values within the plot which demonstrate that there can in some cases be large differences in $\sigma_{\bar{w}}$ between the two beds. Regardless of this, all the $\sigma_{\bar{w}}$ values are a magnitude lower than those for the

spatial variations in time-averaged streamwise velocities observed in Chapter 4. This suggests that if spatial variations in the time-averaged flow field induce form-induced stress, then the majority of this stress will be produced by the spatial variability in streamwise velocities. It needs to be established why a difference in $\sigma_{\bar{w}}$ occurs between the beds, along with why there is scatter in $\sigma_{\bar{w}}$ over each of the beds, albeit small in absolute terms. It could be, for example, due to differences in relative submergence, bed slope, $\langle \bar{u} \rangle$, u_* or the distance of the distribution from the bed surface. These differences will be the subject of the next section.

There are no values of $\sigma_{\bar{w}}$ reported in the literature, but Nikora *et al.* (2001) do present values of $\langle \tilde{w}^2 \rangle / u_*^2$ for two flows over a diamond array of spheres within a laboratory flume. If these values are converted to be equivalent to $\sigma_{\bar{w}}$, it gives values of $\sigma_{\bar{w}}$ from approximately 0.0025 to 0.012. The majority of the values in Figure 5.1a fall within this range for the measurements made at similar heights. Comparisons can also be made with its temporal equivalent, the root mean square deviations in instantaneous vertical velocities, and the absolute vertical turbulence intensity. This will allow the relative importance of the spatial variations to be discovered. The majority of studies into turbulence quote their measures for the degree of turbulence in terms of dimensionalised, rather than absolute values. However, for the studies that do, it reveals that these values are a magnitude higher than $\sigma_{\bar{w}}$ for measurements made at similar heights above gravel beds (Clifford, 1996; Buffin-Bélanger and Roy, 1998; Carling *et al.*, 2002). This again suggests that spatial variations in time-averaged vertical velocities are unlikely to contribute heavily to the transfer of momentum within the flow.

5.2.2 Skewness

The distributions of \bar{w} over the bed are further assessed by examining the skewness of the distributions, given by

$$Sk_{\bar{w}} = \frac{1}{N} \frac{\sum_{i=1}^N (\bar{w}_i - \langle \bar{w} \rangle)^3}{\sigma_{\bar{w}}^3} \quad (5.2)$$

In studies of turbulence, a positive skewness value for the distribution of instantaneous vertical velocities reflects the presence of infrequent, but high-speed (relative to \bar{w}) upward moving fluid, whilst a negative value indicates the occurrence of infrequent, but strong, downward motions. Skewness can therefore reveal the presence of infrequent fluid motions with a large deviation from the mean. It can also be used to assess whether upward or downward motions dominate temporally. A positive value can imply that weak downward motions are dominant, and a negative value that weak upward motions are most prevalent.

Transferring these ideas to the spatial domain enables similar interpretations for $Sk_{\bar{w}}$. A positive $Sk_{\bar{w}}$ value implies that the flow has localised areas of distinctly strong (relative to $\langle\bar{w}\rangle$) upward moving fluid, balanced by large areas of weak (just slightly lower-than-average), downward motions. Similarly a negative $Sk_{\bar{w}}$ value implies that the flow has localised areas of distinctly strong downward motions, balanced by large areas of weak upward motions.

It can be seen from Figure 5.1b that the distributions of \bar{w} are nearly equally positively and negatively skewed over each of the beds. The skewness in the distributions is weak, and is fairly similar over the two beds. Therefore it suggests that the spatial pattern of \bar{w} may have some similarity between the two beds.

There are no studies that have examined the skewness in the distributions of \bar{w} , so it is again useful to compare these values to their temporal equivalent, the skewness in the distributions of the instantaneous vertical velocities. There are however very few measurements made of this skewness. It has been found to vary from -0.5 to 0.75 within a gravel-bed river (Nikora and Goring, 2000) and between -0.6 and 0.2 over various fixed dune-shaped bedforms within a laboratory flume (McLean *et al.*, 1994). Bennett and Best (1996) discovered values of between -1.25 and 0.75 over fixed ripples, again in a laboratory flume. The distributions of \bar{w} demonstrate similar degrees of skewness and also show the same tendency to be both positively and negatively skewed for similar heights above the bed.

5.2.3 Kurtosis

The kurtosis of the distributions of \bar{w} is given by

$$K_{\bar{w}} = \frac{1}{N} \frac{\sum_{i=1}^N (\bar{w}_i - \langle \bar{w} \rangle)^4}{\sigma_{\bar{w}}^4} \quad (5.3)$$

The $K_{\bar{w}}$ values in Figure 5.1c show that the majority of the distributions of \bar{w} over the beds are either slightly platykurtic or have approximately the same kurtosis as a perfect normal distribution. The values are similar between the two beds, suggesting that the intensity of the velocities, relative to $\langle \bar{w} \rangle$, is also similar. There are also a number of distributions over each of the beds that are highly leptokurtic, of the order of 5 or 6. The statistical moments of the distributions of \bar{w} in Figure 5.1 do not vary greatly between the two beds, displaying less variation than was seen for the distributions of \bar{u} . It indicates that the different surface topographies of the beds caused larger changes in distributions of \bar{u} than in the distributions of \bar{w} .

There are no reported values of $K_{\bar{w}}$ within the literature, and there are only a small number of studies that have examined the kurtosis of the distributions of instantaneous vertical velocities. The only studies that present a suitable number of results from which to draw comparisons are those of McLean *et al.* (1994; 1996). Over various fixed dune-shaped bedforms, they found that the distributions of w were typically slightly leptokurtic (up to a value of around 4.8) or had approximately the same kurtosis as a normal distribution, which is comparable to many of the distributions in Figure 5.1c for the same heights above the bed.

5.2.4 Degree of Normality

The skewness and kurtosis values suggest that the majority of the distributions of \bar{w} do not display large departures from a perfect normal distribution. To test this more formally a linear regression between the theoretical probability associated with the ordered observation \bar{w}_i from a standard normal distribution and the observed probability for \bar{w}_i can be employed. The theoretical probability is given by

$$pr(Z \leq z_i) = \frac{i - 3/8}{N + 1/4} \quad (5.4)$$

where $Z \sim N(0, 1)$ and z_i is an observation taken from Z . The linear regression, through its R^2 value, produces an estimate of the percentage variability in \bar{w} explained by a perfect normal distribution. As was seen for the normal probability plot in Figure 4.4, the linear regression can have a high R^2 value even when the distribution is skewed, because the majority of the plot follows a straight line. The importance of the tails, which can heavily determine the normality of the distribution, can be hidden in such a regression. Therefore a distribution should only be considered to approximately follow a normal distribution when R^2 is very high, say above 0.99.

The R^2 values are shown in Figure 5.1d for the two beds. It can be seen that only a very small number of distributions of \bar{w} can be considered to be consistent with a normal distribution. There are a greater number of such distributions over the bimodal bed. The remaining distributions display significant departures from a normal distribution.

5.3 Vertical Distribution in the Degree of Spatial Variability

There were differences in $\sigma_{\bar{w}}$ between the distributions over each of the beds. A possible cause of this is the different vertical positions above the bed at which the measurements of \bar{w} were taken. To explore this, the vertical variation in $\sigma_{\bar{w}}$ in both absolute and non-dimensional forms is given in Figure 5.2. This includes values from 20 of the 22 experimental runs. Experimental runs 1U and 1B are not shown because they only contained measurements taken from a small number of heights above the bed, statistically too small to represent clearly the vertical profile of $\sigma_{\bar{w}}$. The vertical variation in $\sigma_{\bar{w}}$ in all of its forms is plotted against both z/d and z/D_{84} . This is to discover whether, respectively, spatial variability is controlled by flow features that scale with flow depth, or by flow structures that are scaled by bed roughness. As was pointed out in chapter 4, the spatial variability in the time-averaged flow field has been entirely associated with the effects of boundary on the flow (Gimenez-Curto and Corniero Lera, 1996). The assumption is that it “owes its existence to the presence of forms in the boundary”. It could be assumed therefore that the spatial variability in \bar{w} would be scaled by bed roughness. This needs to be tested, which will involve

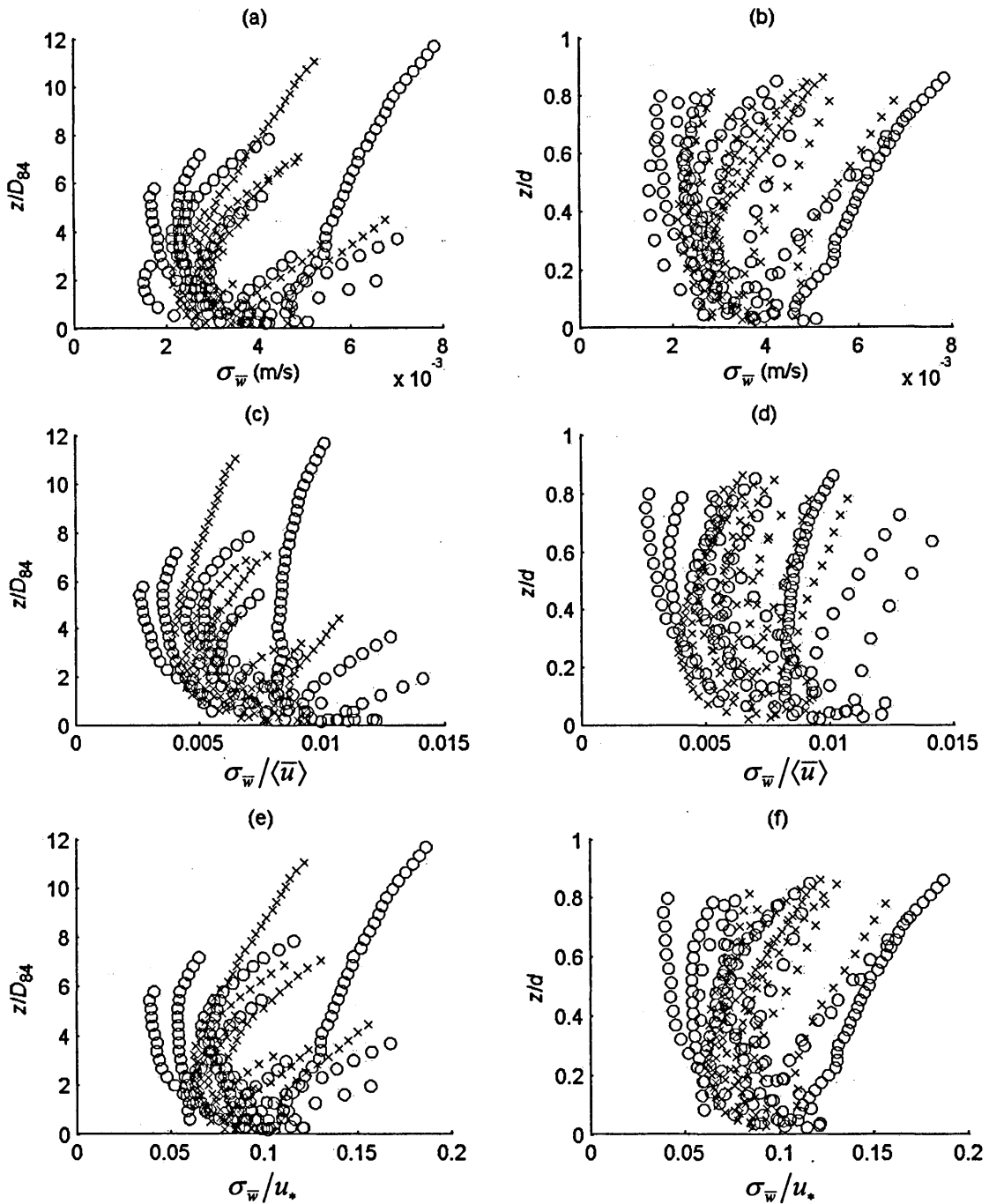


Figure 5.2. Vertical variability in the degree of spatial variability in \bar{w} over the bed, $\sigma_{\bar{w}}$ with (a) z/D_{84} ; (b) z/d , the vertical variability in $\sigma_{\bar{w}}/\langle\bar{u}\rangle$ with (c) z/D_{84} ; (d) z/d , and the vertical variability in $\sigma_{\bar{w}}/u_*$ with (e) z/D_{84} ; and (f) z/d , where \bar{w} is the time-averaged vertical velocity, z is the height above the maximum bed elevation and d is flow depth, D_{84} is the grain size at which 84 per cent of the bed material is finer, $\langle\bar{u}\rangle$ is the double-averaged streamwise velocity and u_* is the bed shear velocity.

examining whether $\sigma_{\bar{w}}$ is negligible above the form-induced layer, at a distance where the form of the bed is assumed to not induce spatial variability. The vertical variability in $\sigma_{\bar{w}}/\langle\bar{u}\rangle$ and $\sigma_{\bar{w}}/u_*$ is examined to discover whether the variability in $\sigma_{\bar{w}}$ values seen in Figure 5.1a can be scaled by the values of double-averaged streamwise velocity $\langle\bar{u}\rangle$ or bed shear velocity u_* .

The plots in Figure 5.2a and b reveal that the spatial variability in \bar{w} is not negligible above the form-induced layer, as previously assumed. It can have non-zero values, relative to that close to the bed surface, all the way up to the water surface. Surprisingly, in some cases these values can even be larger closer to the water surface than to the bed surface. This suggests either that the bed has a direct influence further up into the flow than many assume, or that the spatial variability is not entirely induced by the surface topography of the bed. This increase towards the water surface cannot be attributed to the presence of secondary currents within the flume because the width-depth ratios of the flows were much higher than four. Furthermore, vertical profiles of $\langle\bar{w}\rangle$ from the combined data of all nine vertical plane measurements in Chapter 3 (Figure 3.18) showed that $\langle\bar{w}\rangle$ is approximately zero throughout the flow depth for all experimental runs. It indicates that all the flows can sensibly be considered to be 2-D.

The difference in $\langle\bar{u}\rangle$ between the experimental runs appears to increase the spread of $\sigma_{\bar{w}}$ close to the bed, but to reduce it further up into the flow, at $z/D_{84} \approx 2$ and $z/d \approx 0.4$ (Figures 5.2c and d). Yet a large degree of spread still remains. The degree of spatial variability in the upper reaches of the flow is not as large, relative to that near to the bed surface, as was seen for $\sigma_{\bar{w}}$, scaled with $\langle\bar{u}\rangle$ causing a decrease in the gradient of the profiles.

There are no $\sigma_{\bar{w}}/\langle\bar{u}\rangle$ values within the literature with which to compare these values. A comparison to relative turbulence intensity for instantaneous vertical velocities, $\sigma_w/\langle\bar{u}\rangle$ for flows over gravel surfaces (e.g. Roy *et al.*, 1996; McLelland *et al.*, 1999; Nikora and Goring, 2000) shows that the degree of spatial variability is considerably less than the temporal variability. Typically it is a magnitude lower, but the higher values of $\sigma_{\bar{w}}/\langle\bar{u}\rangle$ can be around half of the lowest values of $\sigma_w/\langle\bar{u}\rangle$ found in the upper reaches of their flows. Therefore the spatial variations in \bar{w} are likely to induce considerably lower

degrees of momentum transfer between the fluid and the bed than those caused by turbulent fluctuations in w .

The difference in $\sigma_{\bar{w}}$ between experimental runs is at its smallest when non-dimensionalised by u_* (Figures 5.2e and f). It suggests that $\sigma_{\bar{w}}$ is better scaled by u_* and its vertical variation is less related to the vertical profile of $\langle \bar{u} \rangle$. The values of $\sigma_{\bar{w}}/u_*$ can therefore be used to assess whether $\sigma_{\bar{w}}$ is scaled by bed roughness or flow depth. Close to the bed, the difference in $\sigma_{\bar{w}}/u_*$ values between the experimental runs is nearly equal when plotted against z/d and z/D_{84} . However, higher up into the flow, $\sigma_{\bar{w}}$ appears to be better scaled by flow depth, as might be expected, especially given that high values of $\sigma_{\bar{w}}$ were found in the upper regions of the flow. Also the vertical profiles of $\sigma_{\bar{w}}/u_*$ are more consistent when plotted against z/d . Variability in $\sigma_{\bar{w}}/u_*$ does however remain between the experimental runs, and the likely cause of this needs to be further established.

The $\sigma_{\bar{w}}/u_*$ values in Figures 5.2e and f are again considerably lower than its temporal counterpart, the turbulence intensity for instantaneous vertical velocities, σ_w/u_* , measured for flows over gravel beds (e.g. Kironoto and Graf, 1994; Nikora and Goring, 2000, Papanicolaou and Hilldale, 2002; Campbell *et al.*, 2005). They are, on the whole, around a magnitude lower, with the higher values of $\sigma_{\bar{w}}/u_*$ again being typically half of σ_w/u_* found by these studies in the upper regions of the flow.

5.4 Parameterisation of the Degree of Spatial Variability

The variability in the shape of the vertical profiles of $\sigma_{\bar{w}}/u_*$ means that one equation cannot be derived to predict $\sigma_{\bar{w}}/u_*$ across the whole flow depth in these experimental runs. But all the profiles show that with increasing height above the bed surface $\sigma_{\bar{w}}/u_*$ has a tendency to decrease to a minimum value close to the bed, a turning point, and then to increase further into the flow. Therefore, for each individual experimental run, the profile can be separated into two segments; one segment close to the bed up to the z/d at which $\sigma_{\bar{w}}/u_*$ attains its minimum value, $(z/d)_{\min}$ and a second segment above this turning point. A function of the form

$$\frac{\sigma_{\bar{w}}}{u_*} = D_x \left(\frac{z}{d} \right)^{-0.129} \quad \text{for } 0 \leq z/d \leq (z/d)_{\min} \quad (5.5)$$

in which D_x and λ_x are empirical constants was found to produce a good prediction of $\sigma_{\bar{w}}/u_*$ for this lower segment, except for runs 3B, 4B and 7B (Table 5.1). All the other experimental runs had R^2 values greater than 0.90, with the average R^2 value being 0.96 across all the runs over the two beds. The second upper segment can be described by

$$\frac{\sigma_{\bar{w}}}{u_*} = D_y \exp(\lambda_y \frac{z}{d}) \quad \text{for } (z/d)_{\min} < z/d \leq 1 \quad (5.6)$$

in which D_y and λ_y are empirical constants. This also produced good agreement with the measured $\sigma_{\bar{w}}/u_*$ for all experimental runs. The average R^2 value was 0.99 and more than half of the runs had $R^2 > 0.99$ (Table 5.1). An example of the fitting of equations (5.5) and (5.6) to the measured values of $\sigma_{\bar{w}}/u_*$ is shown in Figure 5.3 for experimental run 6U over the unimodal bed. This method of fitting two equations to the vertical profile of $\sigma_{\bar{w}}/u_*$ was valid for all but two of the experimental runs, 9U and 12B (Table 5.1), where $(z/d)_{\min}$ occurred for the measurement height closest to the bed surface, for which equation (5.6) could be used to describe the profile for the whole flow depth.

There was variability in the values of the empirical constants in equations (5.5) and (5.6) between the experimental runs (Table 5.1); examining the least-squares fit that contained more than two measurement heights, D_x ranged from 0.036 to 0.085, λ_x from -0.26 to -0.04, D_y from 0.029 to 0.111 and λ_y from 0.35 to 1.6. The constants in neither of the equations were related to d/D_{84} , S , u_* , mean cross-sectional streamwise velocity, fluid Reynolds number or Froude number, so it is not possible to develop relations to estimate these values. This also applies to the values of $(z/d)_{\min}$ at the profile turning point. Therefore, it does not appear that a general expression can be developed for $\sigma_{\bar{w}}/u_*$.

Table 5.1. Summary of the parameters of $\sigma_{\bar{w}}/u_* = D_x(z/d)^{\lambda_x}$ and $\sigma_{\bar{w}}/u_* = D_y \exp(\lambda_y(z/d))$ to describe the variation in $\sigma_{\bar{w}}/u_*$ with z/d for the lower segment below the z/d at which $\sigma_{\bar{w}}/u_*$ attains its minimum value $(z/d)_{\min}$, and for the upper segment above $(z/d)_{\min}$, respectively, for each experimental run, where $(z/D_{84})_{\min}$ is the z/D_{84} at which $\sigma_{\bar{w}}/u_*$ attains its minimum value and, R_x^2 and R_y^2 is the proportion of variability in the data from a least-squares fit of the equations, respectively. * denotes that $(z/d)_{\min}$ occurred for the measurement position closest to the bed, so the variation in $\sigma_{\bar{w}}/u_*$ with z/d could be fully described by equation (5.6). # denotes that the fit was based on two measurement points.

Run	$(z/d)_{\min}$	$(z/D_{84})_{\min}$	D_x	λ_x	R_x^2	D_y	λ_y	R_y^2
2U	0.42	1.20	0.078	-0.09	0.98	0.065	0.58	1.00
3U	0.35	1.53	0.074	-0.08	0.99	0.057	0.83	0.99
4U	0.37	2.17	0.056	-0.13	0.98	0.047	0.73	1.00
5U	0.22	1.85	0.067	-0.09	0.99	0.057	0.94	0.98
6U	0.25	3.22	0.052	-0.13	0.96	0.046	1.13	1.00
7U	0.24	1.97	0.048	-0.18	0.99	0.045	1.03	0.96
8U	0.38	2.29	0.062	-0.11	0.99	0.053	0.66	0.97
9U	0.04	0.22	1.000*	0.69*	-*	0.097	0.59	0.97
10U	0.11	0.49	0.075#	-0.04#	-#	0.072	0.71	0.99
11U	0.30	0.85	0.062	-0.09	0.98	0.058	0.49	1.00
12U	0.37	0.85	0.085	-0.04	0.95	0.094#	0.00#	-#
2B	0.47	1.90	0.047	-0.26	0.98	0.038	0.80	1.00
3B	0.71	3.69	0.071	-0.15	0.84	0.071#	0.00#	-#
4B	0.54	3.69	0.061	-0.24	0.87	0.058	0.35	0.99
5B	0.48	4.37	0.063	-0.14	0.91	0.029	1.60	0.99
6B	0.05	0.66	0.092#	-0.06#	-#	0.108	0.62	0.99
7B	0.52	4.73	0.042	-0.25	0.88	0.033	0.86	0.96
8B	0.28	1.99	0.048	-0.20	0.98	0.045	0.98	0.98
9B	0.75	5.40	0.036	-0.25	0.95	0.041#	0.00#	-#
10B	0.12	0.59	0.085#	-0.05#	-#	0.082	1.00	1.00
11B	0.31	1.24	0.079	-0.07	0.95	0.070	0.63	0.99
12B	0.08	0.24	1.000*	0.89*	-*	0.085	0.98	1.00

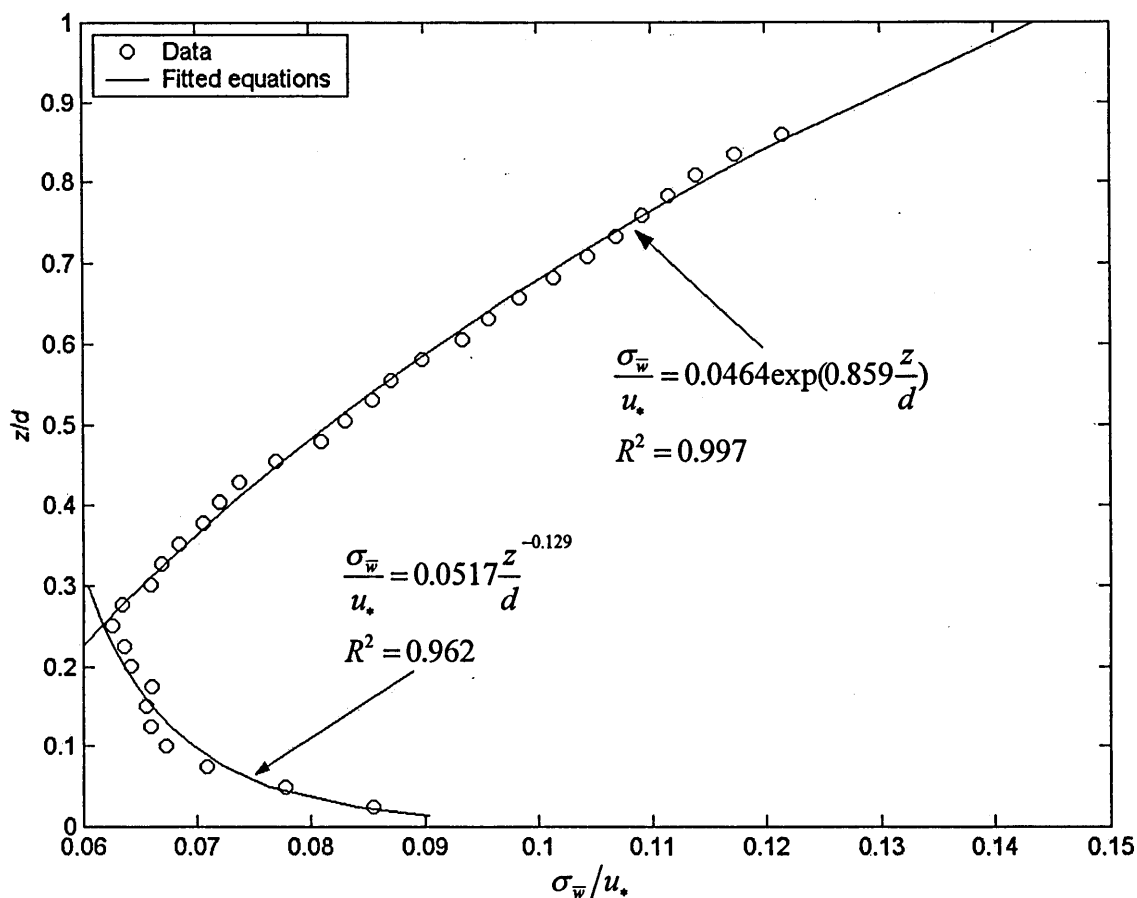


Figure 5.3. Vertical variability in $\sigma_{\bar{w}}/u_*$ with z/d for experimental run 6U over the unimodal bed with the equations 5 and 6 fitted to the lower and upper segments of the profiles, respectively, where $\sigma_{\bar{w}}$ is the degree of spatial variability in \bar{w} , \bar{w} is the time-averaged vertical velocity, u_* is the bed shear velocity, z is the height above the maximum bed elevation and d is flow depth.

At the turning point, $\sigma_{\bar{w}}$ is very small which suggests that at this height above the bed \bar{w} is almost zero everywhere within the flow, given that $\langle \bar{w} \rangle$ is zero at all heights with the flow depth. Yet above and below this, $\sigma_{\bar{w}}$ is larger and reveals that the flow is either predominately moving upward or downward in these flow regions. However, at the height of the turning point, these upwards and downward motions must almost cancel each other in order out to result in such a low value of $\sigma_{\bar{w}}$. It could suggest that the

lower segment of the vertical profile of $\sigma_{\bar{w}}$ point is controlled in some manner by the bed, and that the upper segment is controlled by some outer variable, or the water surface. Yet Table 5.1 shows that there is no noticeable difference in the parameters of equation (5.5), and it has been established that the parameters in equation (5.6) do not show any clear association with an outer variable. Therefore it does not appear that the vertical structuring of the spatial deviations in \bar{w} can be considered to be influenced in such a manner.

The height of the turning point above the bed does not coincide with the height of the form-induced sublayer. It therefore cannot be caused by the transition between the form-induced sublayer and the logarithmic layer. In Chapter 4 it was observed that the high-speed streaks in the spatial pattern of $\bar{u}/\langle\bar{u}\rangle$ were not present above $z/D_{84} = 1.57$, suggesting that they had disappeared somewhere between the lower measurement point above the bed at $z/D_{84} = 1.29$ and $z/D_{84} = 1.57$. Over the bimodal bed, this occurred between $z/D_{84} = 1.59$ and $z/D_{84} = 2.58$. The height of the turning points in Table 5.1 do not consistently correspond with the range of heights at which the high-speed streaks disappeared over either of the two beds, so the turning point does not appear to be located on the top of the high-speed streaks.

5.5 Variability in the Degree of Spatial Variability with Relative Submergence

A possible cause of the spread in $\sigma_{\bar{w}}/u_*$ values in Figures 5.2e and f is the difference in relative submergence between the experimental runs. To discover whether this is the case, the experimental runs carried out at a single bed slope but varying flow depths were examined (Tables 5.2 and 5.3). To allow a fair comparison between the runs for the whole of the flow depth the $\sigma_{\bar{w}}/u_*$ values from each of the runs are plotted against z/d in Figure 5.4. It is also important to examine the effect of relative submergence on $\sigma_{\bar{w}}$, because it is the absolute spatial variability in the time-averaged flow field that induces momentum transfer, therefore the variation in $\sigma_{\bar{w}}$ is also shown in Figure 5.4. Presenting the values in this way enables an examination of whether relative submergence influences the nature of the vertical variability in $\sigma_{\bar{w}}$ and $\sigma_{\bar{w}}/u_*$.

Table 5.2. Summary of the experimental conditions for the experimental runs carried out a single bed slope over the unimodal bed, where S is the bed slope, d is the flow depth, D_{84} is the grain size at which 84 per cent of the bed material is finer, \bar{U} is the average flow velocity (calculated from the ratio of flow discharge to the cross-sectional area of the flow), τ_0 is the bed shear stress and Fr is the Froude number (calculated from \bar{U}/\sqrt{gd} , where g is the force due to gravitational attraction).

Run	S	d (mm)	d/D_{84}	\bar{U} (m ² /s)	τ_0 (N/m ²)	Fr
1U	0.00285	18.1	2.6	0.18	0.47	0.42
2U	0.00285	28.6	4.1	0.27	0.72	0.51
3U	0.00285	39.5	5.6	0.32	0.95	0.52
4U	0.00285	48.4	6.9	0.36	1.13	0.52
5U	0.00285	62.8	9.0	0.45	1.40	0.57
6U	0.00285	90	12.9	0.62	1.85	0.66

Table 5.3. Summary of the experimental conditions for the experimental runs carried out a single bed slope over the bimodal bed, where S is the bed slope, d is the flow depth, D_{84} is the grain size at which 84 per cent of the bed material is finer, \bar{U} is the average flow velocity (calculated from the ratio of flow discharge to the cross-sectional area of the flow), τ_0 is the bed shear stress and Fr is the Froude number (calculated from \bar{U}/\sqrt{gd} , where g is the force due to gravitational attraction).

Run	S	d (mm)	d/D_{84}	\bar{U} (m ² /s)	τ_0 (N/m ²)	Fr
1B	0.00284	17.3	2.6	0.16	0.45	0.40
2B	0.00284	27.2	4.1	0.20	0.68	0.39
3B	0.00284	37.3	5.7	0.28	0.90	0.47
4B	0.00284	45.5	6.9	0.36	1.07	0.53
5B	0.00284	59.5	9.0	0.43	1.34	0.56
6B	0.00284	84.5	12.8	0.58	1.76	0.64

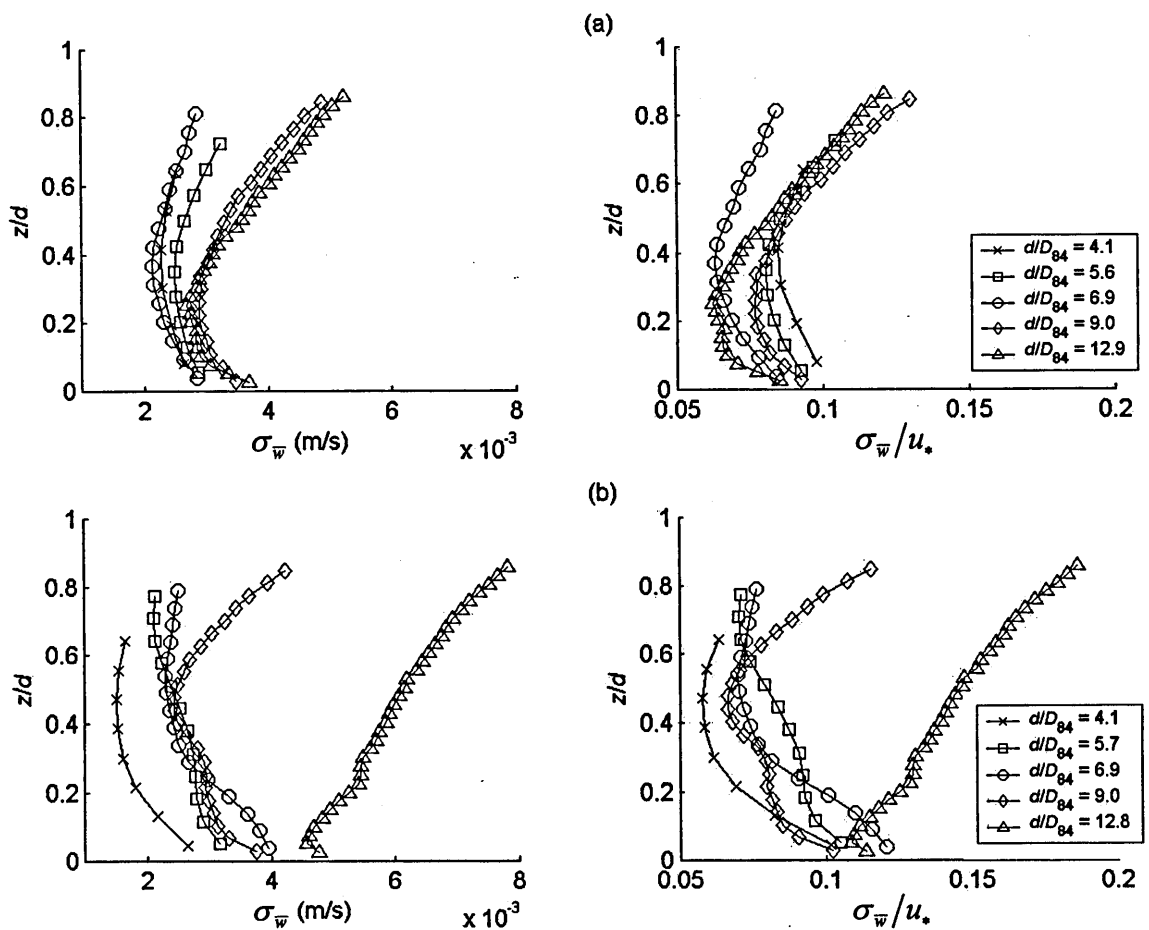


Figure 5.4. Vertical variability in the degree of spatial variability in \bar{w} over the bed, $\sigma_{\bar{w}}$ with z/d and $\sigma_{\bar{w}}/u_*$ with z/d for the experimental runs carried out at a single bed slope over (a) the unimodal bed; and (b) the bimodal bed, where \bar{w} is the time-averaged vertical velocity, z is the height above the maximum bed elevation, d is flow depth and D_{84} is the grain size at which 84 per cent of the bed material is finer.

5.5.1 Absolute Spatial Variability

For the unimodal bed, $\sigma_{\bar{w}}$ decreases with z/d in nearly the same manner for all the experimental runs (Figure 5.4a). It shows that $\sigma_{\bar{w}}$ decreases to a minimum value, the turning point, beyond which it increases into the upper regions of the flow. This causes in many cases for $\sigma_{\bar{w}}$ to be higher closer to the water surface than the bed surface. The position of this turning point displays some association with relative submergence, with it typically moving closer to the bed surface with increases in relative submergence. The degree of change in $\sigma_{\bar{w}}$ also increases with relative submergence. This is largely

because the rate of increase after the turning point is positively related to relative submergence. The difference in $\sigma_{\bar{w}}$ between the experimental runs is small, particularly within the lower fifth of the flow, above which the differences increase. The $\sigma_{\bar{w}}$ values at the same z/d are not consistently related to relative submergence, but the profiles do appear to be grouped into two, at the lower and higher relative submergences, with $\sigma_{\bar{w}}$ being typically higher at the higher submergences in the upper 75 % of the flow. Clifford (1996) found that the absolute vertical turbulence intensity σ_w was also higher at deeper flows over riffle-pool sequences in a gravel-bed river.

Over the bimodal bed, there also appears to be grouping of the profiles according to relative submergence, at the low, mid and high relative submergences. It means that there is greater variability in $\sigma_{\bar{w}}$ between the experimental runs. Again, however, there is no consistent relationship between $\sigma_{\bar{w}}$ at the same z/d and relative submergence. The shape of the vertical profiles is more variable between the experimental runs, but they do display some similarity to those over the unimodal bed. The $\sigma_{\bar{w}}$ values again decrease up to a turning point, beyond which they increase towards the water surface. The turning point appears higher up into the flow than over the unimodal bed. It does not consistently move closer to the bed surface with relative submergence, but is typically lower at the higher submergences. In addition, $\sigma_{\bar{w}}$ displays greater vertical change with increasing relative submergence. It results in $\sigma_{\bar{w}}$ being higher nearer the water surface than the bed surface for the two experimental runs performed at the highest submergences.

5.5.2 Relative Spatial Variability

The $\sigma_{\bar{w}}/u_*$ values over the unimodal bed show a similar change with z/d (Figure 5.4), as seen for $\sigma_{\bar{w}}$. This is almost a mirror image of the vertical variation in vertical turbulence intensity, σ_w/u_* found by Campbell *et al.* (2005) over a fixed, artificial gravel bed, with the turning points occurring at very similar z/d values. The profiles of $\sigma_{\bar{w}}/u_*$ display similar degrees of vertical change, unlike that seen for $\sigma_{\bar{w}}$. There is no longer any grouping of the profiles, with differences between the experimental runs being particularly small in the upper half of the flow as the profiles converge. There is

no consistent relationship between $\sigma_{\bar{w}}/u_*$ and relative submergence at the same z/d , although there is slight tendency for the values to be lower at the higher relative submergences.

Over the bimodal bed, the profiles of $\sigma_{\bar{w}}/u_*$ again display more variability between the experimental runs, although the shape of the profiles are very similar, as for $\sigma_{\bar{w}}$. The degree of vertical change in $\sigma_{\bar{w}}/u_*$ increases with relative submergence, although the $\sigma_{\bar{w}}/u_*$ values at the same z/d have no such association. The $\sigma_{\bar{w}}/u_*$ values are more variable between the experimental runs than seen for $\sigma_{\bar{w}}$, but there is no grouping of the profiles according to relative submergence. There is a better collapse of the data than when $\sigma_{\bar{w}}$ was plotted against z/d , although the collapse is better over the unimodal bed.

5.6 Variability in the Degree of Spatial Variability with Bed Slope

The experimental runs performed at the same relative submergence are now analysed in order to discover whether bed slope has an effect on the degree of spatial variability in \bar{w} (Figures 5.5 and 5.6). For each bed, there are four relative submergences at which different experimental runs have the same submergence (Tables 5.4 and 5.5). These runs were created through a combination of flow discharges and bed slopes.

5.6.1 Absolute Spatial Variability

Over the unimodal bed, it can be seen that $\sigma_{\bar{w}}$ again decreases up to a turning point, above which it increases towards the water surface (Figure 5.5). The $\sigma_{\bar{w}}$ values at the same z/d consistently increase with bed slope, for all but the experimental runs performed at a relative submergence of 9.0. The difference in $\sigma_{\bar{w}}$ between the experimental runs also typically decreases when the difference in bed slopes between the runs is lower. Indeed, when the difference in slope is at its lowest (Figure 5.5d), the $\sigma_{\bar{w}}$ are nearly identical for the whole of the flow depth. Bed slope does not appear to greatly influence, however, the degree of change in $\sigma_{\bar{w}}$ with z/d , nor the relative height of the inflection point in the profile, with all profiles at the same relative

submergence displaying near identical profiles and rates of vertical decrease. However, there is an increase in this vertical reduction in $\sigma_{\bar{w}}$ and a decrease in the relative height of the turning point with relative submergence between the four plots, as was seen in Figure 5.4.

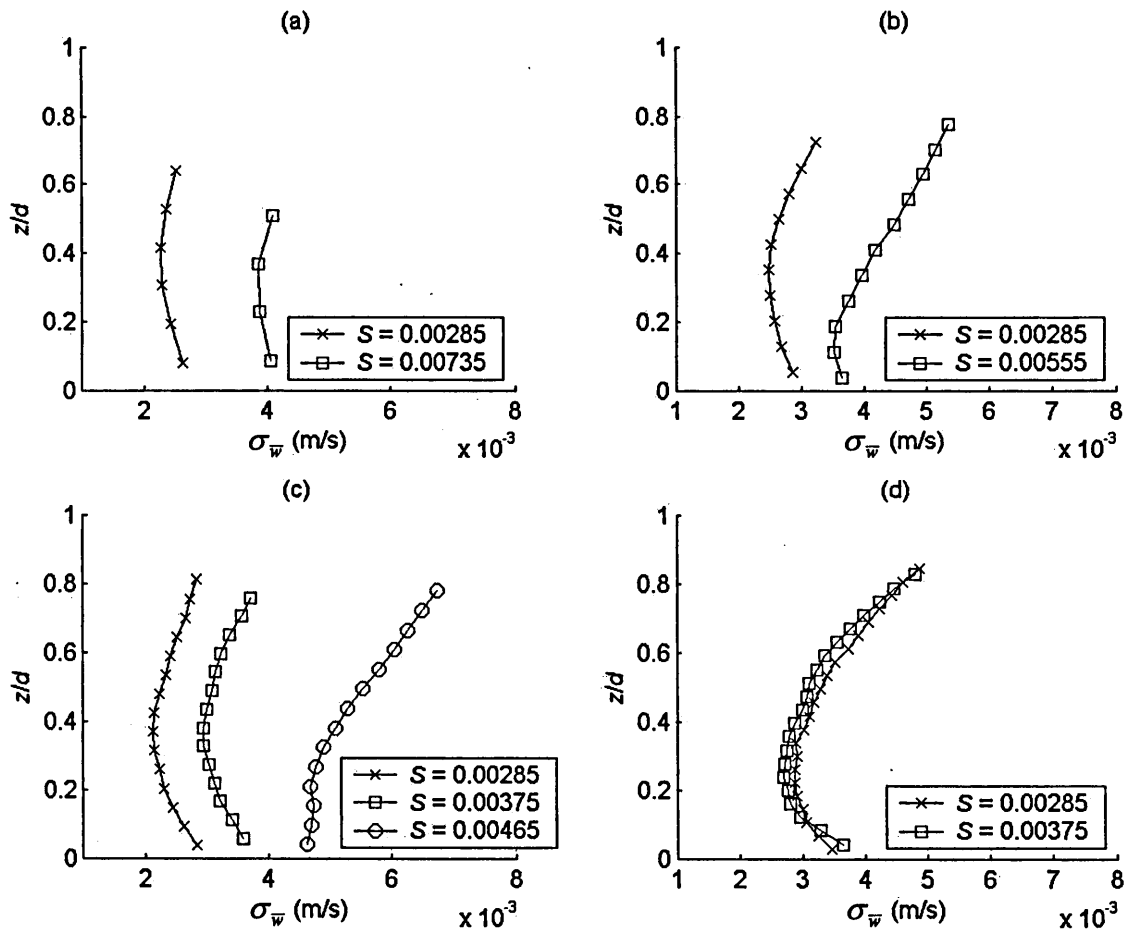


Figure 5.5. Vertical variability in the degree of spatial variability in \bar{w} , $\sigma_{\bar{w}}$ over the unimodal bed with z/d for the experimental runs carried out at the same relative submergences (a) $d/D_{84} = 4.1$; (b) $d/D_{84} = 5.6$; (c) $d/D_{84} = 6.9$; and (d) $d/D_{84} = 9.0$, where \bar{w} is the time-averaged vertical velocity, z is the height above the maximum bed elevation, d is flow depth, D_{84} is the grain size at which 84 per cent of the bed material is finer and S is bed slope.

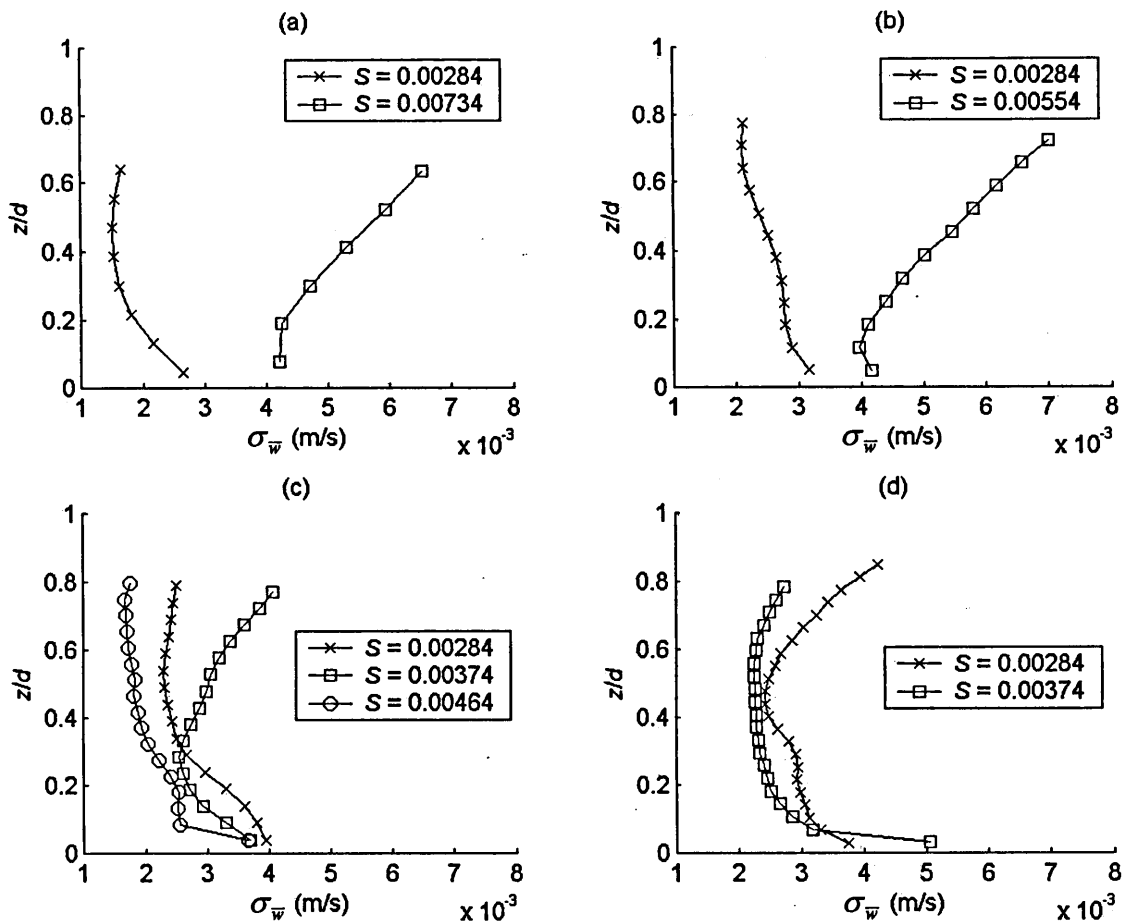


Figure 5.6. Vertical variability in the degree of spatial variability in \bar{w} , $\sigma_{\bar{w}}$ over the bimodal bed with z/d for the experimental runs carried out at the same relative submergences (a) $d/D_{84} = 4.1$; (b) $d/D_{84} = 5.7$; (c) $d/D_{84} = 6.9$; and (d) $d/D_{84} = 9.0$, where \bar{w} is the time-averaged vertical velocity, z is the height above the maximum bed elevation, d is flow depth, D_{84} is the grain size at which 84 per cent of the bed material is finer and S is bed slope.

The vertical profiles of $\sigma_{\bar{w}}$ are once again more variable in shape between the experimental runs over the bimodal bed (Figure 5.6). However, the shapes of the profiles become more consistent when the difference in slopes is small, such that the profiles are again quite similar at a relative submergence of 9.0. The difference in $\sigma_{\bar{w}}$ between the experimental runs tends to be greater in the upper half of the flow, but is also lower when the difference in bed slope is small. The degree of vertical change in $\sigma_{\bar{w}}$ also appears to be influenced by bed slope, with it being lower at the shallower

slopes. The $\sigma_{\bar{w}}$ values at the same z/d do not, however, display a consistent relationship with bed slope, although when the difference in bed slope is large, $\sigma_{\bar{w}}$ is higher at the steeper slopes (Figures 5.6a and b).

Table 5.4. Summary of the experimental conditions for the experimental runs carried out at the same relative submergences over the unimodal bed, where S is the bed slope, d is the flow depth, D_{84} is the grain size at which 84 per cent of the bed material is finer, \bar{U} is the average flow velocity (calculated from the ratio of flow discharge to the cross-sectional area of the flow), τ_0 is the bed shear stress and Fr is the Froude number (calculated from \bar{U}/\sqrt{gd} , where g is the force due to gravitational attraction).

Run	S	d (mm)	d/D_{84}	\bar{U} (m ² /s)	τ_0 (N/m ²)	Fr
2U	0.00285	28.6	4.1	0.27	0.72	0.51
12U	0.00735	29.5	4.2	0.44	1.90	0.83
3U	0.00285	39.5	5.6	0.32	0.95	0.52
10U	0.00555	39.9	5.7	0.49	1.87	0.78
4U	0.00285	48.4	6.9	0.36	1.13	0.52
8U	0.00375	48.2	6.9	0.47	1.77	0.69
9U	0.00465	49.2	7.0	0.50	1.87	0.72
5U	0.00285	62.8	9.0	0.45	1.40	0.57
7U	0.00375	63.5	9.1	0.51	1.86	0.65

5.6.2 Relative Spatial Variability

The $\sigma_{\bar{w}}/u_*$ values over the unimodal bed once again show the same vertical profiles as seen earlier (Figure 5.7). The experimental runs at the same relative submergences display the same profile shape and degree of vertical change. This is not influenced by bed slope. Instead the vertical change and the degree of curvature increase with relative submergence between the four plots. Also the position of the turning point moves further down into the flow with increases in relative submergence. The difference in $\sigma_{\bar{w}}/u_*$ values at the same relative submergence is small for the majority of the

experimental runs, even when the difference in bed slope is large. It means that $\sigma_{\bar{w}}/u_*$ at the same z/d does not have any strong association with bed slope.

Over the bimodal bed, the difference in $\sigma_{\bar{w}}/u_*$ is much larger, and the shape of the profiles is more variable (Figure 5.8). However, the profiles do become more consistent in shape when the difference in bed slope is small, such as at a relative submergence of 9.0 (Figure 5.8d). The difference in $\sigma_{\bar{w}}/u_*$ between the experimental runs is also lower when the difference in bed slope is small. But for all four of the relative submergences, the difference is quite small close to the bed surface, which then tends to increase with z/d . The degree of vertical change in $\sigma_{\bar{w}}/u_*$ is not consistently influenced by bed slope, and nor are the $\sigma_{\bar{w}}/u_*$ values at the same z/d .

Table 5.5. Summary of the experimental conditions for the experimental runs carried out at the same relative submergences over the bimodal bed, where S is the bed slope, d is the flow depth, D_{84} is the grain size at which 84 per cent of the bed material is finer, \bar{U} is the average flow velocity (calculated from the ratio of flow discharge to the cross-sectional area of the flow), τ_0 is the bed shear stress and Fr is the Froude number (calculated from \bar{U}/\sqrt{gd} , where g is the force due to gravitational attraction).

Run	S	d (mm)	d/D_{84}	\bar{U} (m ² /s)	τ_0 (N/m ²)	Fr
2B	0.00284	27.2	4.1	0.20	0.68	0.39
12B	0.00734	26.8	4.1	0.27	1.74	0.52
3B	0.00284	37.3	5.7	0.28	0.90	0.47
10B	0.00554	37.1	5.6	0.39	1.75	0.65
4B	0.00284	45.5	6.9	0.36	1.07	0.53
8B	0.00374	46.6	7.1	0.40	1.71	0.60
9B	0.00464	47.2	7.2	0.47	1.80	0.69
5B	0.00284	59.5	9.0	0.43	1.34	0.56
7B	0.00374	59.4	9.0	0.47	1.76	0.62

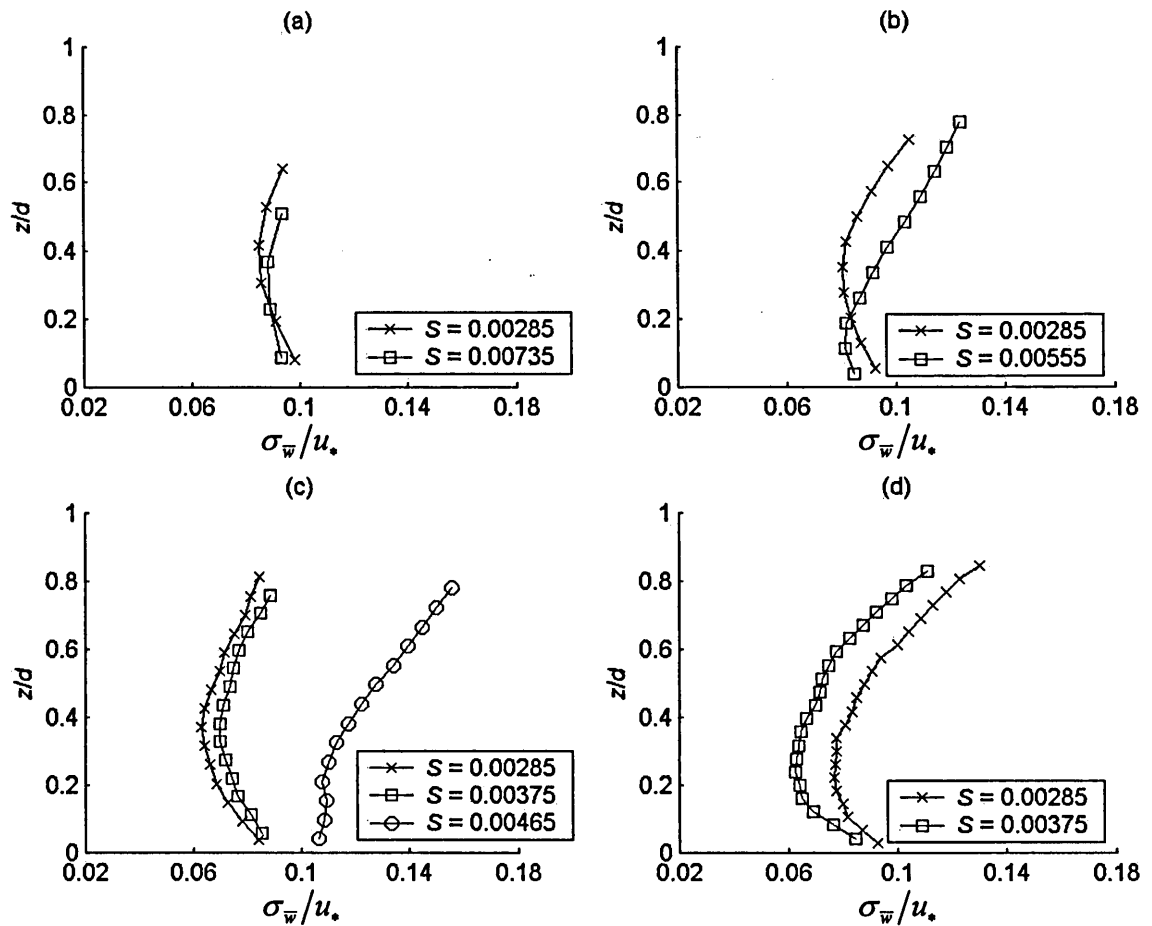


Figure 5.7. Vertical variability in $\sigma_{\bar{w}}/u_*$ over the unimodal bed with z/d for the experimental runs carried out at the same relative submergences (a) $d/D_{84} = 4.1$; (b) $d/D_{84} = 5.6$; (c) $d/D_{84} = 6.9$; and (d) $d/D_{84} = 9.0$, where $\sigma_{\bar{w}}$ is the degree of spatial variability in \bar{w} , \bar{w} is the time-averaged vertical velocity, u_* is the bed shear velocity, z is the height above the maximum bed elevation, d is flow depth, D_{84} is the grain size at which 84 per cent of the bed material is finer and S is bed slope.

5.7 Variability in the Degree of Spatial Variability Under Conditions of Constant Bed Shear Stress

The experimental runs that were carried out at the same mean bed shear stress (Tables 5.6 and 5.7) are now assessed for each bed. These experimental runs involved a combination of bed slopes and flow depths, and therefore encompass the effects of both relative submergence and bed slope. It means that an assessment can be made of which of these two variables has the primary influence on the degree of spatial variability in

\bar{w} by examining which of the effects of the variables, established from above, are evident. Under these conditions of constant mean bed shear stress the implication is that the average rate of momentum transfer at the bed is approximately the same for each of the experimental runs. Therefore, if the degree of spatial variability in \bar{w} changes under these conditions, it implies that the distribution of \bar{w} over the bed is different. It suggests that the momentum transfer mechanisms might be different between the experimental runs even when the average rate of transfer is the same. The variable that is the primary cause of these changes can then be inferred.

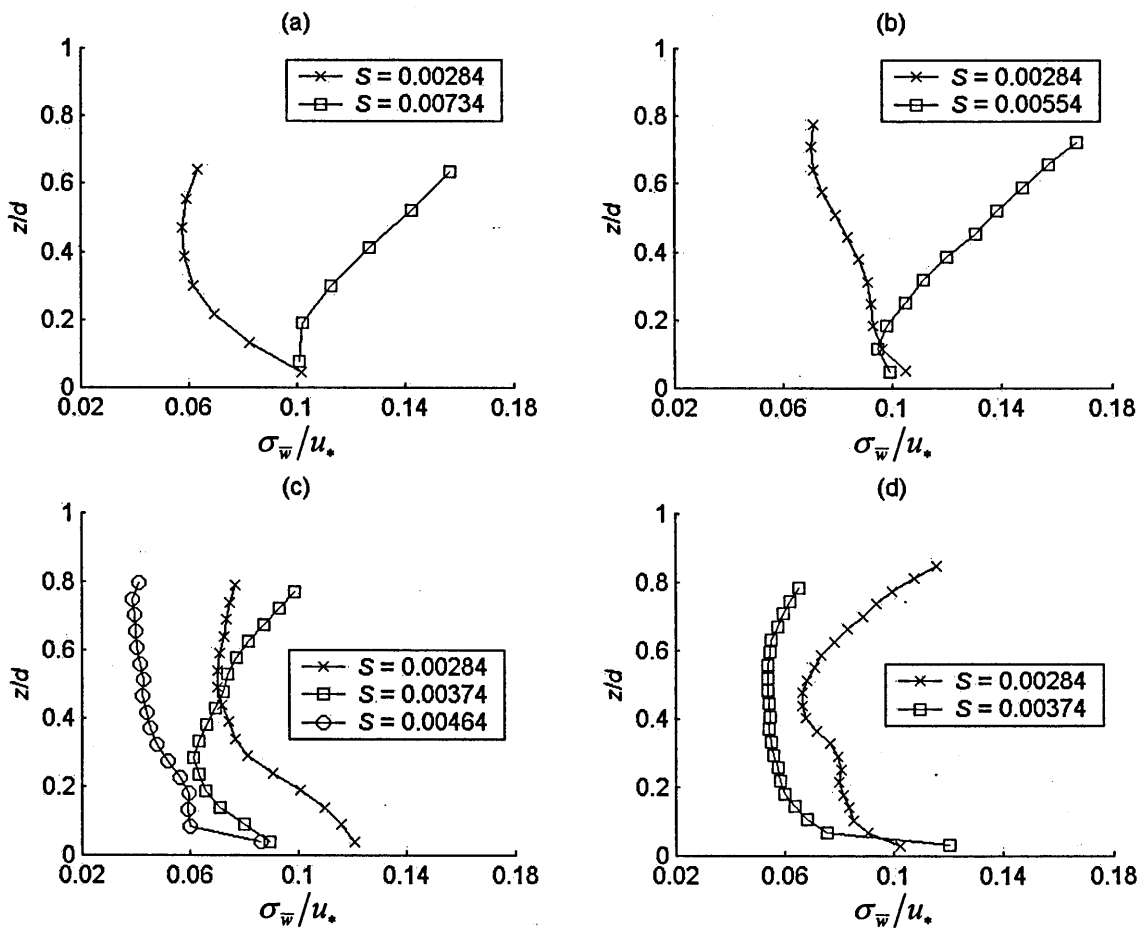


Figure 5.8. Vertical variability in $\sigma_{\bar{w}}/u_*$ over the bimodal bed with z/d for the experimental runs carried out at the same relative submergences (a) $d/D_{84} = 4.1$; (b) $d/D_{84} = 5.7$; (c) $d/D_{84} = 6.9$; and (d) $d/D_{84} = 9.0$, where $\sigma_{\bar{w}}$ is the degree of spatial variability in \bar{w} , \bar{w} is the time-averaged vertical velocity, u_* is the bed shear velocity, z is the height above the maximum bed elevation, d is flow depth, D_{84} is the grain size at which 84 per cent of the bed material is finer and S is bed slope.

5.7.1 Absolute Spatial Variability

The vertical variations in $\sigma_{\bar{w}}$ under these conditions of constant mean bed shear stress are examined in Figure 5.9 for both beds. The nature of this variation will not be described, because these plots contain the experimental runs that have been previously examined. Over the unimodal bed, it can be seen that the variation in $\sigma_{\bar{w}}$ values between experimental runs is actually greater than seen at a single bed slope despite u_* being approximately the same for each run. There is no grouping of the profiles according to relative submergence that was observed at a single bed slope, and the $\sigma_{\bar{w}}$ values at the same z/d display no relationship with relative submergence, and therefore bed slope. It is likely that the positive relationship observed with relative submergence at a single bed slope was counteracted by the same association with bed slope discovered for the experimental runs performed at the same relative submergence. The degree of change in $\sigma_{\bar{w}}$ with z/d in Figure 5.9 and the positions of the turning points are also not consistently related to relative submergence and bed slope. However, they were associated with relative submergence at a single bed slope, suggesting that the disassociation with bed slope seen for the experimental runs performed at the same relative submergences may have caused this result.

Over the bimodal bed, the variability in $\sigma_{\bar{w}}$ between the experimental runs is much greater, although it is small close to the bed, beyond which it generally increases with z/d (Figure 5.9). This variability is not consistently related to relative submergence and bed slope, so again it appears that the positive relationship seen earlier with bed slope has been contrasted by the disassociation with bed slope discovered for the experiments performed at the same relative submergences. The degree of vertical change in $\sigma_{\bar{w}}$ is also not associated with relative submergence and bed slope in Figure 5.9. This is likely to be because of the positive relationships that were observed earlier with relative submergence and bed slope, which oppose each other under these conditions of constant mean bed shear stress.

Table 5.6. Summary of the experimental conditions for the experimental runs carried out at the same mean bed shear stress over the unimodal bed, where S is the bed slope, d is the flow depth, D_{84} is the grain size at which 84 per cent of the bed material is finer, \bar{U} is the average flow velocity (calculated from the ratio of flow discharge to the cross-sectional area of the flow), τ_0 is the bed shear stress and Fr is the Froude number (calculated from \bar{U}/\sqrt{gd} , where g is the force due to gravitational attraction).

Run	S	d (mm)	d/D_{84}	\bar{U} (m ² /s)	τ_0 (N/m ²)	Fr
6U	0.00285	90.0	12.9	0.62	1.85	0.66
8U	0.00375	63.5	9.1	0.51	1.86	0.65
9U	0.00465	49.2	7.0	0.50	1.87	0.72
10U	0.00555	39.9	5.7	0.49	1.87	0.78
11U	0.00645	33.5	4.8	0.413	1.87	0.72
12U	0.00735	29.5	4.2	0.44	1.90	0.83

Table 5.7. Summary of the experimental conditions for the experimental runs carried out at the same mean bed shear stress over the bimodal bed, where S is the bed slope, d is the flow depth, D_{84} is the grain size at which 84 per cent of the bed material is finer, \bar{U} is the average flow velocity (calculated from the ratio of flow discharge to the cross-sectional area of the flow), τ_0 is the bed shear stress and Fr is the Froude number (calculated from \bar{U}/\sqrt{gd} , where g is the force due to gravitational attraction).

Run	S	d (mm)	d/D_{84}	\bar{U} (m ² /s)	τ_0 (N/m ²)	Fr
6B	0.00284	84.5	12.8	0.58	1.76	0.64
8B	0.00374	59.4	9.0	0.47	1.76	0.62
9B	0.00464	47.2	7.2	0.47	1.80	0.69
10B	0.00554	37.1	5.6	0.39	1.75	0.65
11B	0.00644	31.7	4.8	0.35	1.77	0.62
12B	0.00734	26.8	4.1	0.27	1.74	0.52

5.7.2 Relative Spatial Variability

The same conclusions can be also be drawn from the vertical profiles of $\sigma_{\bar{w}}/u_*$ (Figure 5.9), as for the vertical profiles of $\sigma_{\bar{w}}$. This is because u_* is approximately the same for the experimental runs over each of the beds.

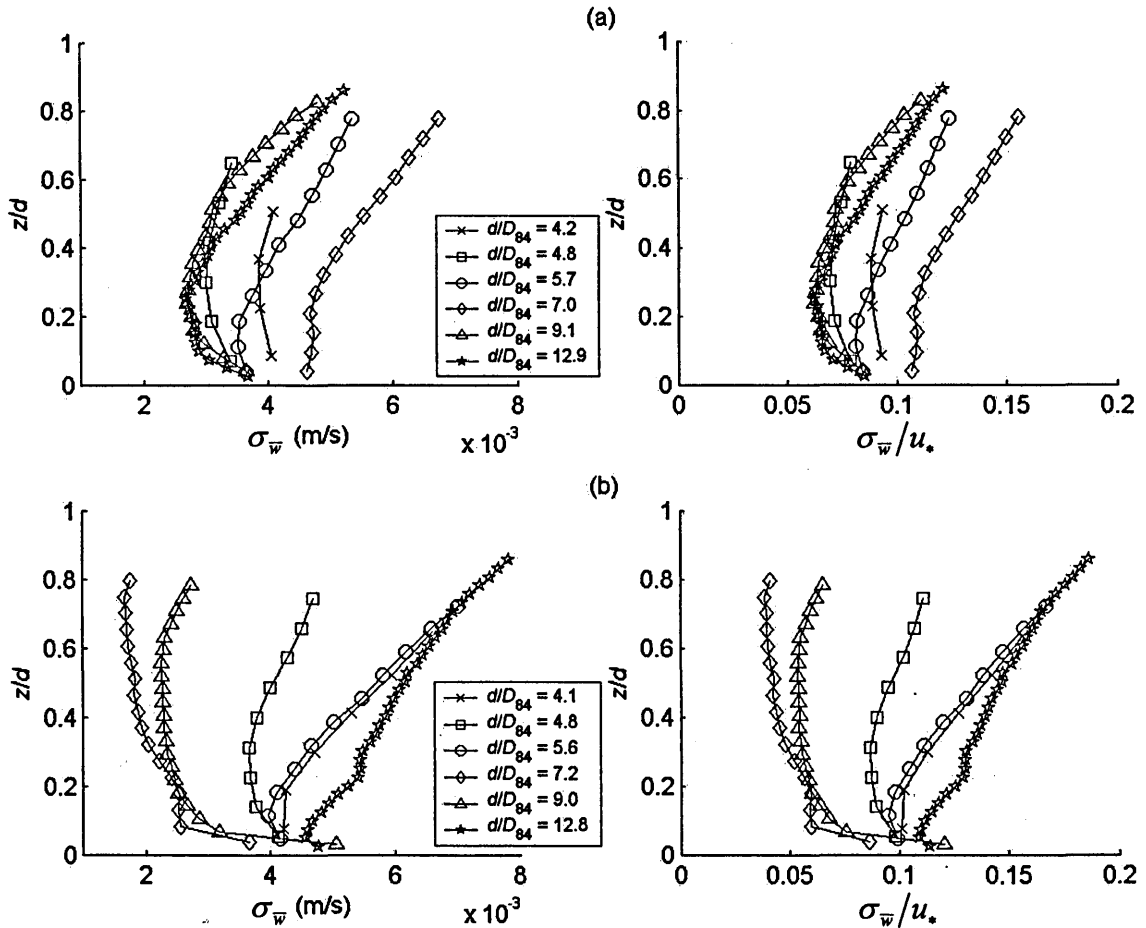


Figure 5.9. Vertical variability in the degree of spatial variability in \bar{w} over the bed, $\sigma_{\bar{w}}$ with z/d and $\sigma_{\bar{w}}/u_*$ with z/d for the experimental runs carried out at the same mean bed shear stress over (a) the unimodal bed; and (b) the bimodal bed, where \bar{w} is the time-averaged vertical velocity, z is the height above the maximum bed elevation, d is flow depth, u_* is the bed shear velocity and D_{84} is the grain size at which 84 per cent of the bed material is finer.

The variability in $\sigma_{\bar{w}}$ between the experimental runs over the two beds shows that $\sigma_{\bar{w}}$ is not fully scaled by u_* . Instead, at the same mean bed shear stress, different degrees of spatial variability in \bar{w} are observed over both beds, particularly over the bimodal bed. This was also discovered for the spatial variability in \bar{u} in Chapter 4. It suggests that, if the magnitude of the spatial variations is sufficient to produce form-induced stresses within the flow, the momentum transfer mechanisms might be different even when the average rate of transfer at the bed is the same.

5.8 Does Relative Submergence or Bed Slope have the Greater Influence on the Degree of Spatial Variability?

Although the experimental runs performed at the same mean bed shear stress provide an indication as to whether relative submergence or bed slope has the primary influence on the degree of spatial variability in \bar{w} , a more rigorous approach is required. This can be achieved by carrying out a multiple linear regression between the predictor variables, relative submergence and bed slope, and the response variable $\sigma_{\bar{w}}$,

$$\sigma_{\bar{w}} = \alpha + \beta_1 \frac{d}{D_{84}} + \beta_2 S \quad (5.7)$$

This provides a simple model for estimating $\sigma_{\bar{w}}$ at a given z/d , and for calculating the percentage of the variation in $\sigma_{\bar{w}}$ between experimental runs that is explained by differences in relative submergence and bed slope, given by R^2 . A bivariate linear regression was also carried out between $\sigma_{\bar{w}}$ and relative submergence, and between $\sigma_{\bar{w}}$ and bed slope. These values were taken from each of the 11 experimental runs over the two beds, but for measurement heights high into the flow a lower number of experimental runs were involved in the regression. A regression was not carried out unless seven or more runs were available for regression. The R^2 values from these regressions are compared to establish the relative strength of the relationships of the two variables with $\sigma_{\bar{w}}$, and by what degree each variable contributed to the strength of the associations in equation (5.7). It was found that a simple linear regression between $\sigma_{\bar{w}}$ and relative submergence, and between $\sigma_{\bar{w}}$ and bed slope produced higher R^2 values

than through any multiplicative transform of the variables (not shown). This multiple and linear regression approach was then repeated for $\sigma_{\bar{w}}/u_*$.

5.8.1 Absolute Spatial Variability

In Figure 5.10 the R^2 values resulting from these bivariate and multiple regressions for $\sigma_{\bar{w}}$ are shown. It can be seen that over the unimodal bed, there is no strong association between $\sigma_{\bar{w}}$ and relative submergence throughout the whole of the flow depth. This also applies over the bimodal bed for all but two vertical positions within the flow, where the correlation is quite strong. Bed slope also does not appear to have a strong relationship with $\sigma_{\bar{w}}$ over either bed. It has a stronger association, however, than relative submergence, although it still remains weak throughout the flow. The R^2 values for bed slope are typically higher over the unimodal bed, which corresponds with the results found for the experimental runs carried out at the same relative submergences. The vertical variation in these values largely influences the variation in the R^2 values from the multiple regression. However, over the bimodal bed, it is a combination of the vertical variation in the R^2 values of both relative submergence and bed slope. The multiple regression model does not produce accurate estimations of $\sigma_{\bar{w}}$ over either of the beds, and does not perform better in any particular region of the flow.

The vertical variation in the β values from equation (5.7) with z/d is also shown in Figure 5.10 for each of the two beds. It shows that the influence of bed slope is very similar between the two beds and consistently increases with z/d . A very similar pattern is also seen for the influence of relative submergence (Figure 5.11), although in this case, the influence is greater over the bimodal bed.

The p -values for β_1 and β_2 are shown in Figure 5.12 for each of the beds. Over the unimodal bed it can be seen that the association between relative submergence and $\sigma_{\bar{w}}$ is not statistically significant at the 5 % level in any part of the flow depth, although its significance does increase with z/d . The effect of bed slope is consistently greater on $\sigma_{\bar{w}}$ than relative submergence over this bed, but only on five occasions is it a statistically significant influence. This association displays no clear trend of variation

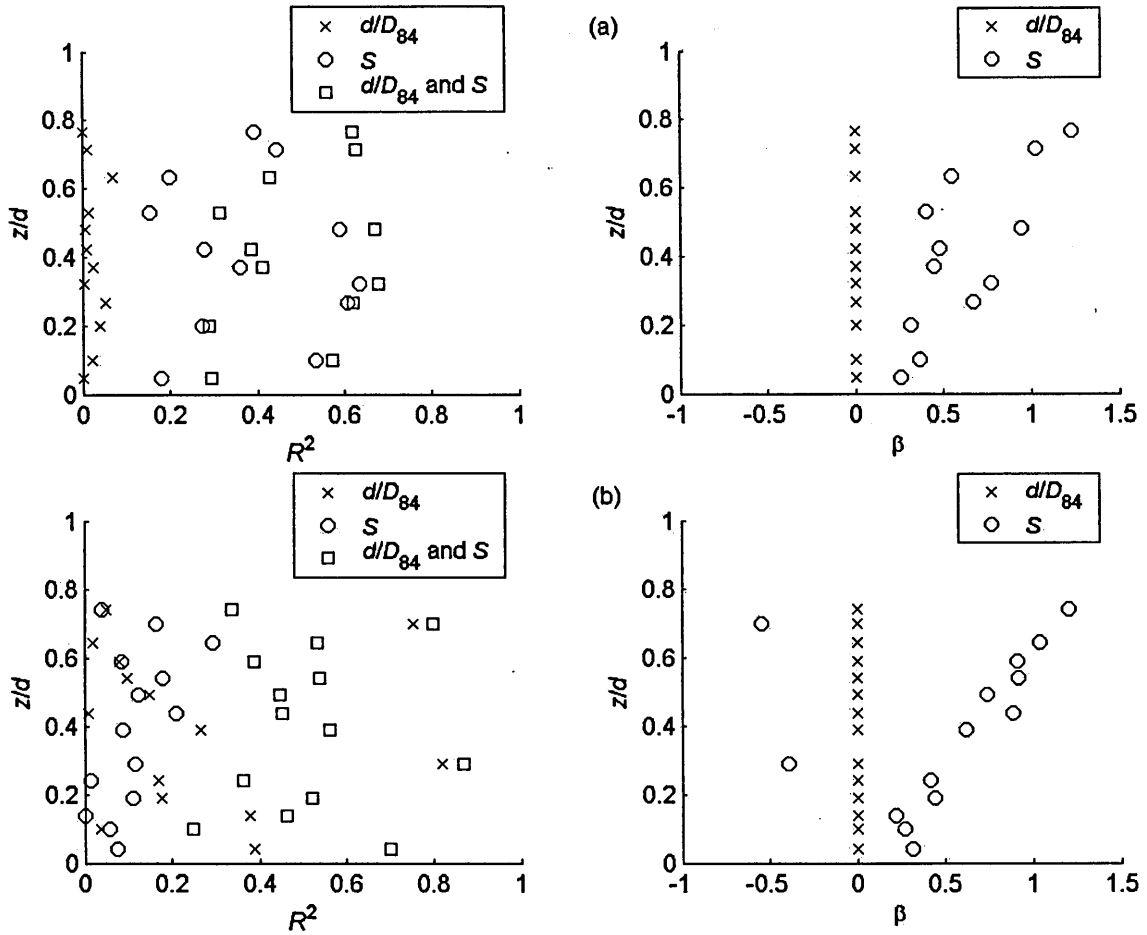


Figure 5.10. Vertical variability in the R^2 of the linear regression between relative submergence d/D_{84} and the degree of spatial variability in \bar{w} over the bed, $\sigma_{\bar{w}}$, in R^2 of the linear regression between bed slope S and $\sigma_{\bar{w}}$, and in the R^2 of the multiple linear regression between predictor variables, relative submergence and bed slope, and response variable $\sigma_{\bar{w}}$, with z/d . Also shown is the vertical variability in the multiplying coefficients of these regressions β with z/d . This is carried out for (a) the unimodal bed; and (b) the bimodal bed, where \bar{w} is the time-averaged vertical velocity, z is the height above the maximum bed elevation, d is flow depth and D_{84} is the grain size at which 84 per cent of the bed material is finer.

with z/d , as is also seen over the bimodal bed. The p -values for bed slope are higher over the bimodal bed, indicating that bed slope has less of an influence on $\sigma_{\bar{w}}$ than over the unimodal bed. However, the reverse is the case for relative submergence, resulting in relative submergence having a greater influence than bed slope on $\sigma_{\bar{w}}$ over the bimodal bed. The results from Figures 5.10 and 5.12 indicate that, for both beds, neither relative submergence nor bed slope has a particularly strong or significant influence on $\sigma_{\bar{w}}$.

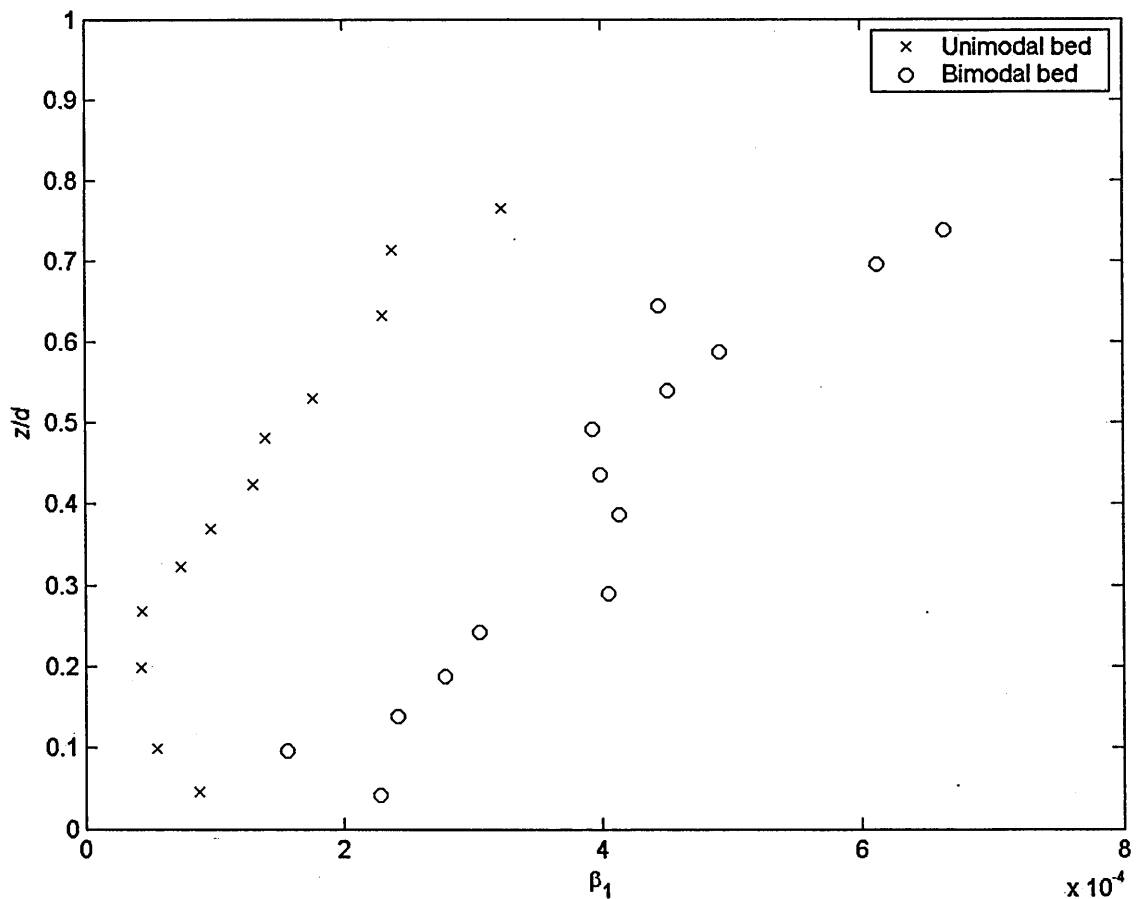


Figure 5.11. Vertical variability in the multiplying coefficient for relative submergence β_1 for the multiple linear regression between predictor variables, relative submergence and bed slope, and response variable, degree of spatial variability in \bar{w} over the bed, $\sigma_{\bar{w}}$ with z/d , where \bar{w} is the time-averaged vertical velocity, z is the height above the maximum bed elevation, d is flow depth and D_{84} is the grain size at which 84 per cent of the bed material is finer. This is performed for each of the two beds.

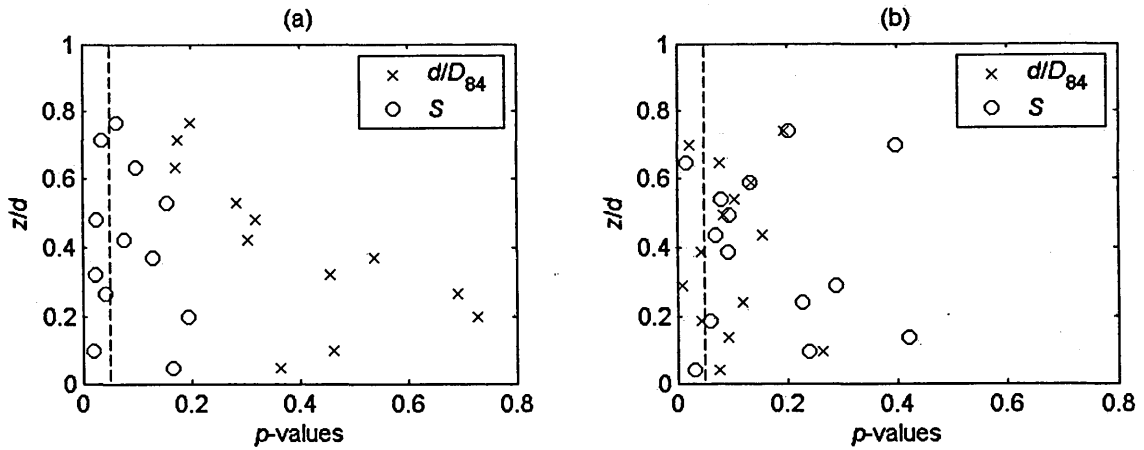


Figure 5.12. Vertical variability in the p -values of the multiplying coefficients for relative submergence d/D_{84} and bed slope S for the multiple linear regression between predictor variables, relative submergence and bed slope, and response variable, degree of spatial variability in \bar{w} over the bed, $\sigma_{\bar{w}}$ with z/d for (a) the unimodal bed; and (b) the bimodal bed, where \bar{w} is the time-averaged vertical velocity, z is the height above the maximum bed elevation, d is flow depth and D_{84} is the grain size at which 84 per cent of the bed material is finer. The dashed line indicates the 0.05 significance level.

5.8.2 Relative Spatial Variability

The vertical variability in the R^2 values for the bivariate and multiple regression for $\sigma_{\bar{w}}/u_*$ is shown in Figure 5.13. They indicate that neither relative submergence nor bed slope has a strong association with $\sigma_{\bar{w}}/u_*$. The strength of this association is quite similar for both variables, unlike that seen for $\sigma_{\bar{w}}$. Again, the multiple regression model performs poorly.

The vertical variation in β for the multiple regression for $\sigma_{\bar{w}}/u_*$ is similar to that observed for $\sigma_{\bar{w}}$, except that bed slope can cause both increases and decreases in $\sigma_{\bar{w}}/u_*$. Bed slope has a fairly similar influence over each of the beds, and it again increases with z/d . The increase also occurs for relative submergence (Figure 5.14).

The p -values from this linear regression indicate that, in general, neither relative submergence nor bed slope has a statistically significant influence on $\sigma_{\bar{w}}/u_*$ at the 5 %

level over either of the beds (Figure 5.15). Only on two occasions over the bimodal bed, does either variable have a significant influence. The significance of their influence does increase, however, with z/d over this bed. Over both of the beds, neither of the variables has a consistently greater influence on $\sigma_{\bar{w}}/u_*$, unlike seen for $\sigma_{\bar{w}}$.

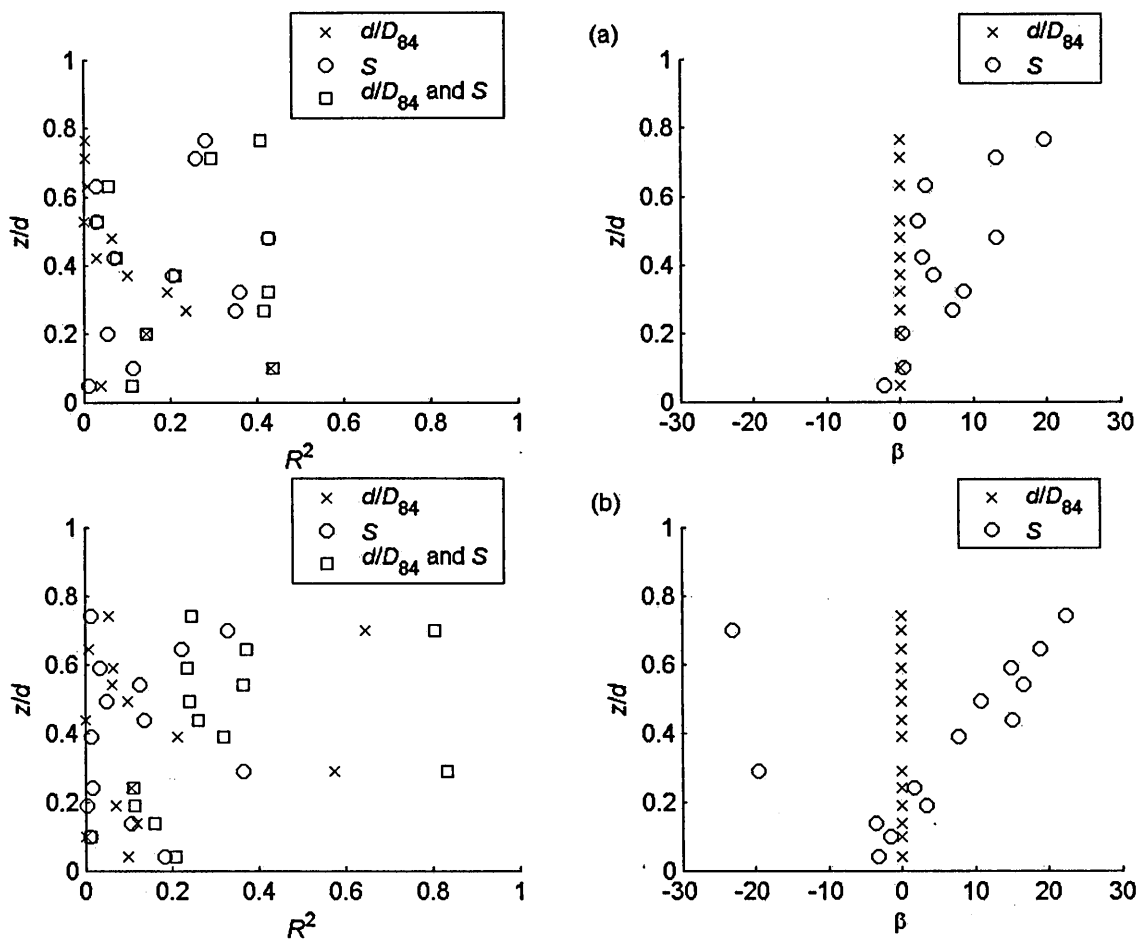


Figure 5.13. Vertical variability in the R^2 of the linear regression between relative submergence d/D_{84} and $\sigma_{\bar{w}}/u_*$, in R^2 of the linear regression between bed slope S and $\sigma_{\bar{w}}/u_*$, and in the R^2 of the multiple linear regression between predictor variables, relative submergence and bed slope, and response variable $\sigma_{\bar{w}}/u_*$ with z/d . Also shown is the vertical variability in the multiplying coefficients of these regressions β_1 with z/d . This is for carried out for (a) the unimodal bed; and (b) the bimodal bed, where $\sigma_{\bar{w}}$ is the degree of spatial variability in \bar{w} , \bar{w} is the time-averaged vertical velocity, u_* is the bed shear velocity, z is the height above the maximum bed elevation, d is flow depth and D_{84} is the grain size at which 84 per cent of the bed material is finer.

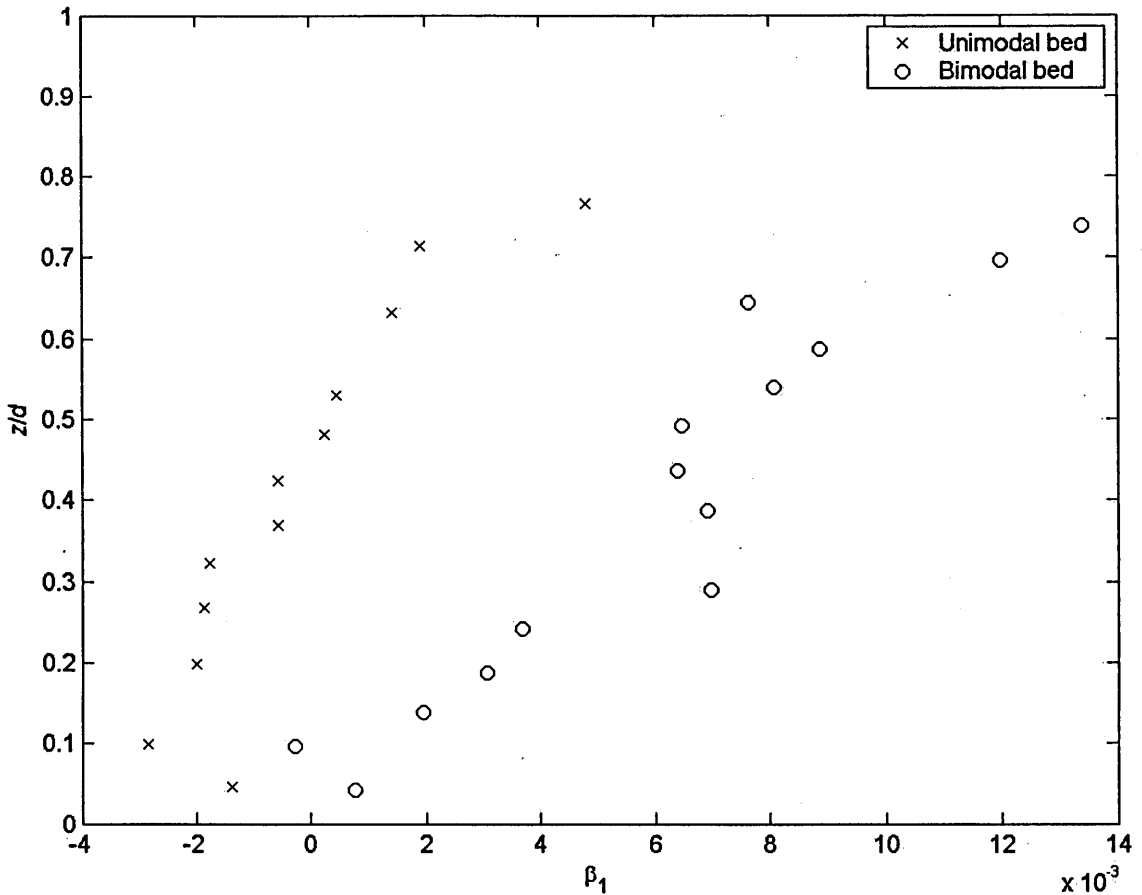


Figure 5.14. Vertical variability in the multiplying coefficient for relative submergence β_1 for the multiple linear regression between predictor variables, relative submergence and bed slope, and response variable $\sigma_{\bar{w}}/u_*$ with z/d , where $\sigma_{\bar{w}}$ is the degree of spatial variability in \bar{w} , \bar{w} is the time-averaged vertical velocity, u_* is the bed shear velocity, z is the height above the maximum bed elevation, d is flow depth and D_{84} is the grain size at which 84 per cent of the bed material is finer. This is performed for each of the two beds.

In Chapter 4 it was discovered that the influence of relative submergence on $\sigma_{\bar{u}}$ and $\sigma_{\bar{u}}/\langle\bar{u}\rangle$ also increased with z/d . It was concluded that it is highly probable that bed roughness (and the vertical extent of its influence, scaled by z/d) is most likely to determine the degree of effect of relative submergence on $\sigma_{\bar{u}}$ and $\sigma_{\bar{u}}/\langle\bar{u}\rangle$, and where its effects become apparent. In the case of $\sigma_{\bar{w}}$ and $\sigma_{\bar{w}}/u_*$, although the values of β_1

and β_2 increase with z/d , the low R^2 and p -values indicate that a similar conclusion can not be drawn for the effects of relative submergence and bed slope.

5.9 The Pattern of Spatial Deviations over the Bed

The focus so far has been on a spatially integrated measure of the degree to which \bar{w} changes over the bed, $\sigma_{\bar{w}}$. Attention now turns to the pattern or structure of the spatial deviations in \bar{w} over the bed. The vertical profiles of $\sigma_{\bar{w}}$ and $\sigma_{\bar{w}}/u_*$ have shown that spatial variability can exist in the upper regions of the flow where the effect of bed roughness is thought to be negligible, and that flow depth rather than bed roughness may be a better scaling of this variability in this part of the flow above the turning point. An examination of the spatial pattern and the bed surface topography of the beds should further elucidate the relationship between the bed and \bar{w} , this time focussing on the grain-scale deviations.

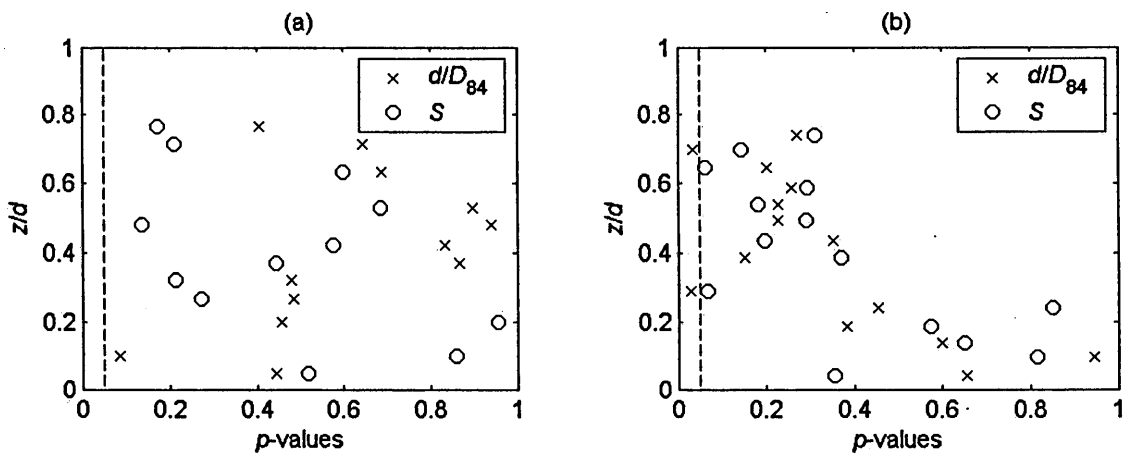


Figure 5.15. Vertical variability in the p -values of the multiplying coefficients for relative submergence d/D_{84} and bed slope S for the multiple linear regression between predictor variables, relative submergence and bed slope, and response variable $\sigma_{\bar{w}}/u_*$ with z/d for (a) the unimodal bed; and (b) the bimodal bed, where $\sigma_{\bar{w}}$ is the degree of spatial variability in \bar{w} , \bar{w} is the time-averaged vertical velocity, u_* is the bed shear velocity, z is the height above the maximum bed elevation, d is flow depth and D_{84} is the grain size at which 84 per cent of the bed material is finer. The dashed line indicates the 0.05 significance level.

Vertical plane PIV measurements were carried out at nine lateral positions for each of the experimental runs. The spatial deviation in \bar{w} at position x, z (adopting the right-handed coordinate system) within one of the vertical planes $\tilde{w}_{x,z}$ is given by $\bar{w}_{x,z} - \langle \bar{w} \rangle_z$. The $\langle \bar{w} \rangle_z$ value is the average of the $\bar{w}_{x,z}$ values taken from all nine lateral locations over the bed. It is the $\tilde{w}_{x,z}$ values that contribute to the form-induced stress.

Contour plots are produced of \tilde{w}/u_* to enable comparisons to be made between each of the experimental runs, and so that the relative size of the variability could be easily assessed. These plots allow a visual examination of the size of the spatial variations in \bar{w} between different positions over and above the bed. Also given the definition of \tilde{w} , if any spatially coherent or persistent pattern exists it should reveal that this pattern is also persistent over time. Contour plots have been produced for each of the nine lateral positions over the bed that should provide some indication of the lateral variability in the spatial pattern, which will be the subject of a later section.

Bed surface elevation profiles are shown for each of the nine lateral positions in Figures 5.16 and 5.17 for the unimodal and bimodal beds, respectively. A lateral position of 0 mm denotes the centreline of the flume and the increasing values in the streamwise position are in the direction of the flow. These are provided so that it can be seen how the spatial patterns in \tilde{w}/u_* relate to that of the bed surface, and this will be returned to in more detail in a later section.

5.9.1 Variability with Relative Submergence

To discover whether relative submergence influences the distribution of the spatial variation in \bar{w} over the two beds, contour plots of \tilde{w}/u_* are produced for the experimental runs carried out at a single bed slope but varying flow depths (Tables 5.2 and 5.3). The streamwise positions within the plots in Figures 5.18 and 5.19 relate to the streamwise positions in the bed elevation profiles in Figures 5.16 and 5.17. Each row of contour plots relates to a lateral position over the bed.

It is immediately apparent that there is a degree of spatial organisation in \tilde{w}/u_* , and that this pattern changes with relative submergence (Figure 5.18). At the lowest relative submergence of 4.1 (Figure 5.18a), for many of the lateral locations over the bed there

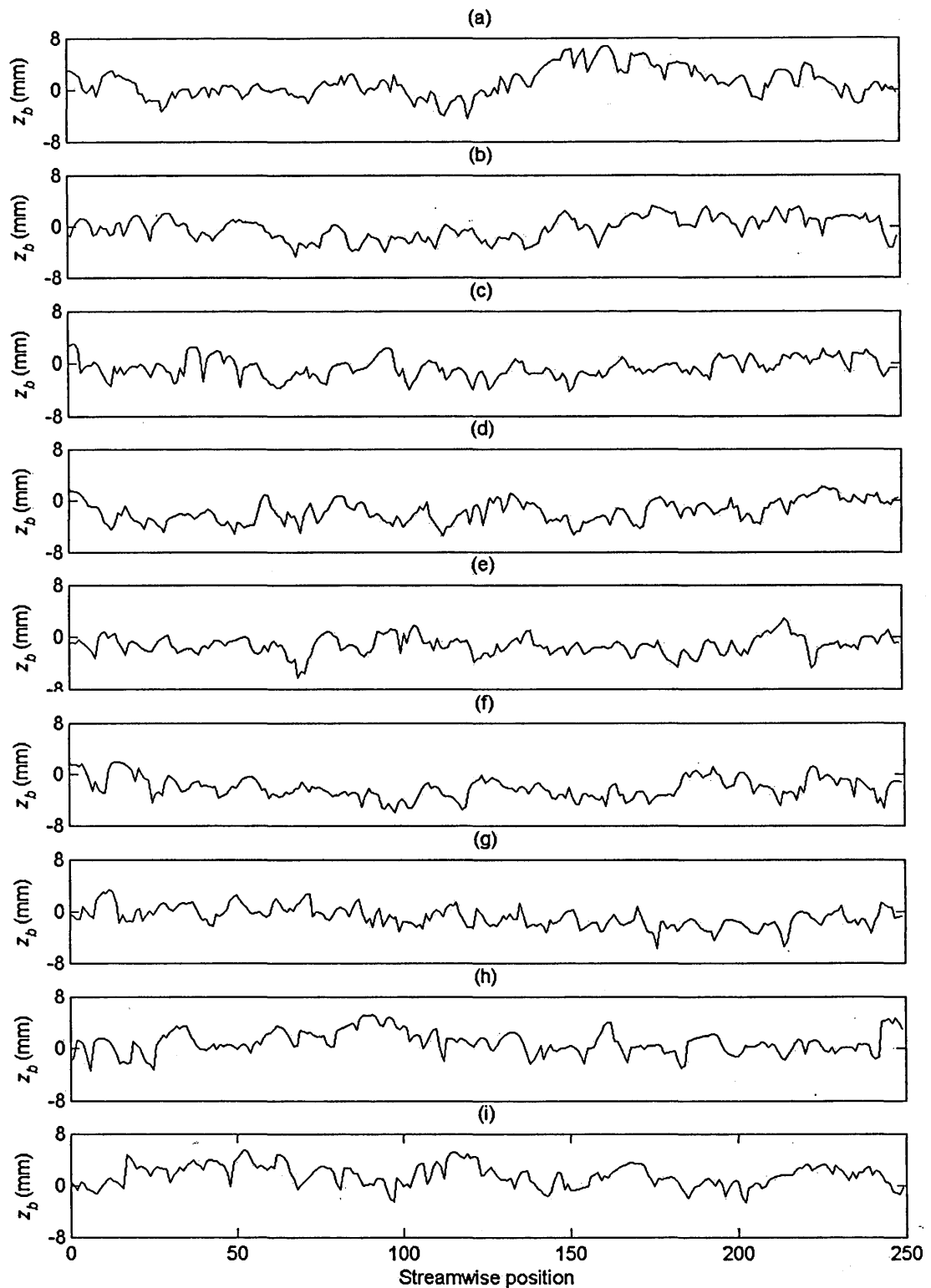


Figure 5.16. The streamwise change in bed surface elevation z_b of the unimodal bed at lateral positions of (a) -87 mm; (b) -65 mm; (c) -43 mm; (d) -21 mm; (e) 0 mm; (f) 23 mm; (g); 45 mm; (h) 67 mm; and (i) 89 mm produced by a laser bed scanner. A lateral position of 0 mm denotes the centreline of the flume and the increasing values in the streamwise position are in the direction of the flow.

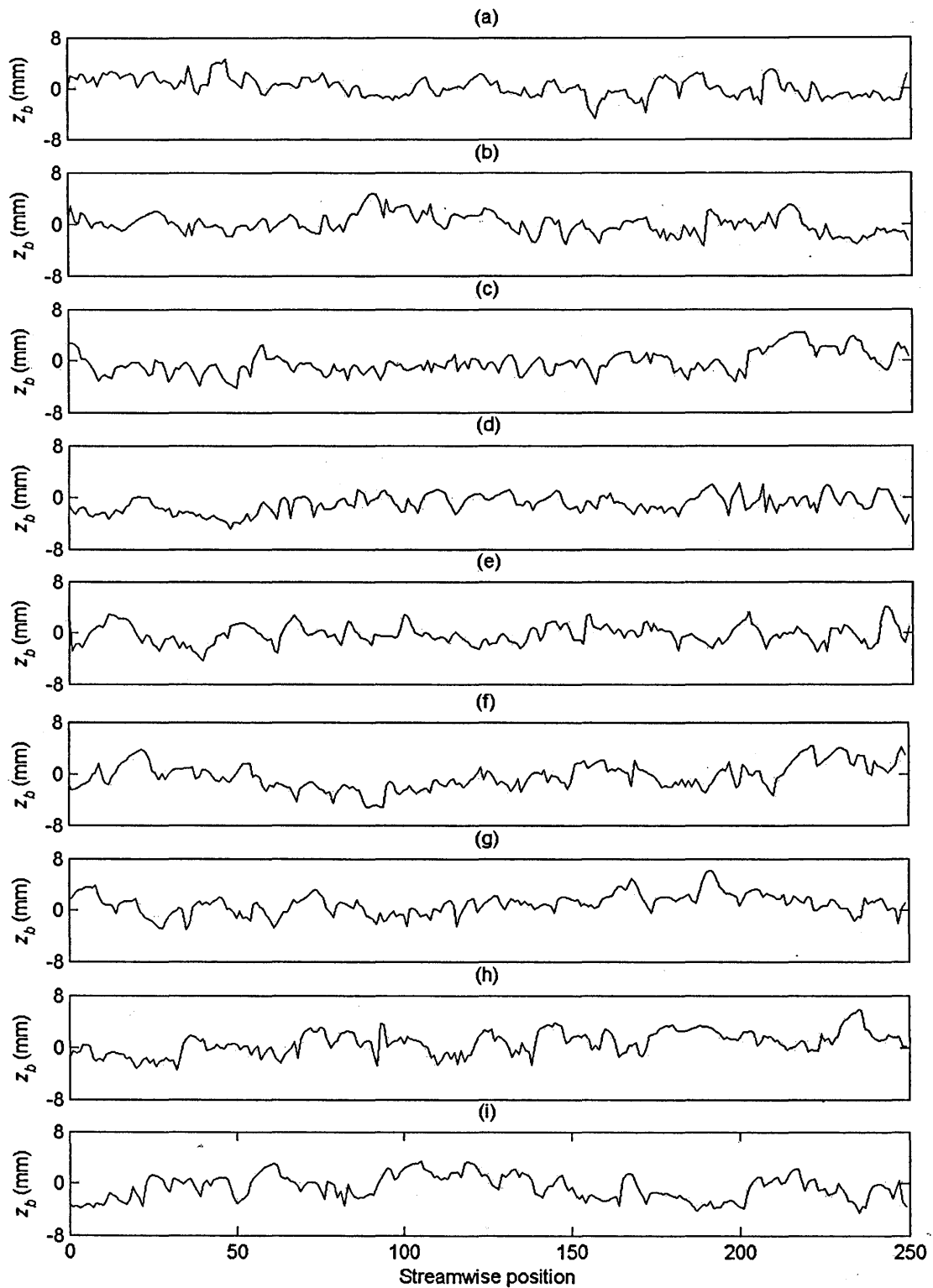


Figure 5.17. The streamwise change in bed surface elevation z_b of the bimodal bed at lateral positions of (a) -87 mm; (b) -65 mm; (c) -43 mm; (d) -21 mm; (e) 0 mm; (f) 23 mm; (g); 45 mm; (h) 67 mm; and (i) 89 mm produced by a laser bed scanner. A lateral position of 0 mm denotes the centreline of the flume and the increasing values in the streamwise position are in the direction of the flow.

are distinct vertical zones of positive and negative \tilde{w}/u_* values. Given that it was seen in chapter 3 (Figure 3.18) that $\langle \bar{w} \rangle$ was approximately zero for the whole depth of the flow, it means that the bed is covered by vertical zones of upward and downward moving fluid. All but one of these zones extends fully from the bed surface towards the water surface. For the majority of the lateral locations, these upward and downward moving vertical zones form an alternating pattern. With an increase in relative submergence to $d/D_{84} = 5.6$, at each of the lateral locations, the spatial pattern present at $d/D_{84} = 4.1$ is still present, but has been slightly modified (Figure 5.18b). This modification is largely through a decrease in the number of these vertical zones. This decrease appears to be associated with an increase in their streamwise length, such that at some locations just one zone of either upward or downward moving fluid dominates over the measurement section. Again, all but one of these zones fully extends from the bed surface to the outer region of the flow. At a relative submergence of 6.9, there is further reduction in the number of zones and an increase in their streamwise length (Figure 5.18c). These zones have also decreased in their vertical extent, with many not extending from the bed surface to the outer region of the flow. Indeed there are small zones that are restricted to close to the bed surface. The locations of these zones correlates well with the appearance of the vertical zones at the lower two submergences, which suggests that they are the same flow feature. An increase in relative submergence therefore appears to have caused a decrease in the vertical propagation of the zones into the flow. This also occurs at a relative submergence of 9.0, whereby there is a further increase in the number of small areas of upward moving fluid near the bed surface (Figure 5.18d). The streamwise length of zones has also continued to rise, but this mainly occurs for the upward moving regions of flow. These regions have also become noticeably more intense, relative to $\langle \bar{w} \rangle$. At a relative submergence of 12.9, the thin vertical zones of upward and downward moving fluid have all but disappeared, with many plots being covered by larger regions of either positive or negative \tilde{w}/u_* values (Figure 5.18e). The spatial patterns at this submergence at a given lateral position bear little resemblance to those at the lowest submergence, despite the bed surface being the same. But it does appear that the small areas of upward and downward moving fluid at $d/D_{84} = 12.9$, are a constituent component of the vertical zones of fluid at the lower submergences. An increase in relative submergence across the five experimental runs has caused a progressive decrease in the spatial organisation of the flow, which was also seen for the pattern of spatial deviations in \bar{u} in chapter 4.

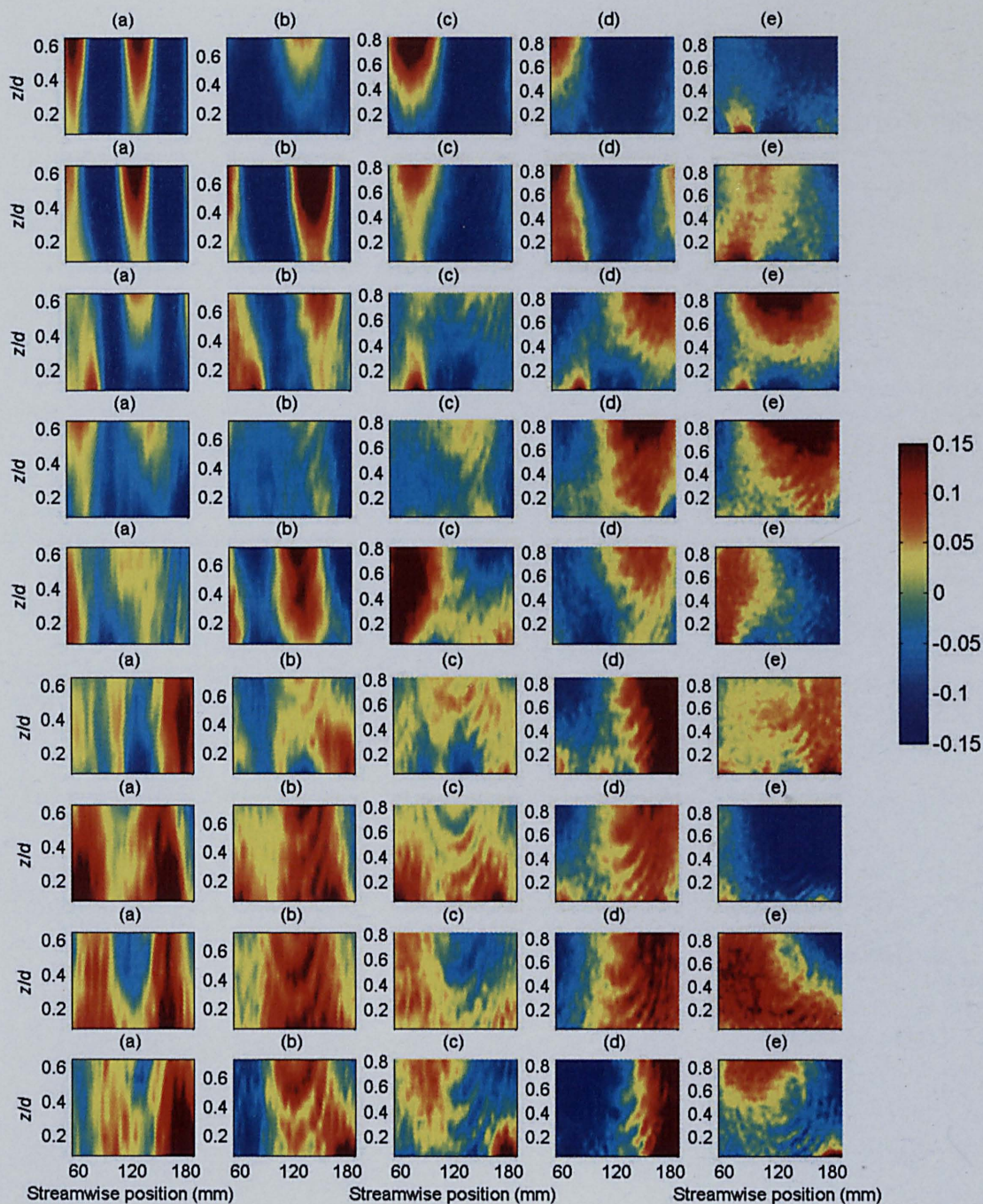


Figure 5.18. The spatial distribution of \tilde{w}/u_* over the unimodal bed for the experimental runs performed at a single bed slope with (a) $d/D_{84} = 4.1$; (b) $d/D_{84} = 5.6$; (c) $d/D_{84} = 6.9$; (d) $d/D_{84} = 9.0$; and (e) $d/D_{84} = 12.9$, where \tilde{w} is the spatial deviation in time-averaged vertical velocity, u_* is the bed shear velocity, d is flow depth and D_{84} is the grain size at which 84 per cent of the bed material is finer. Each row of contour plots relates to a lateral position over the bed; from the top to the bottom row are lateral positions of -87 mm, -65 mm, -43 mm, -21 mm, 0 mm, 23 mm, 45 mm, 67 mm, 89 mm. Note that the vertical axes do not have the same scale.

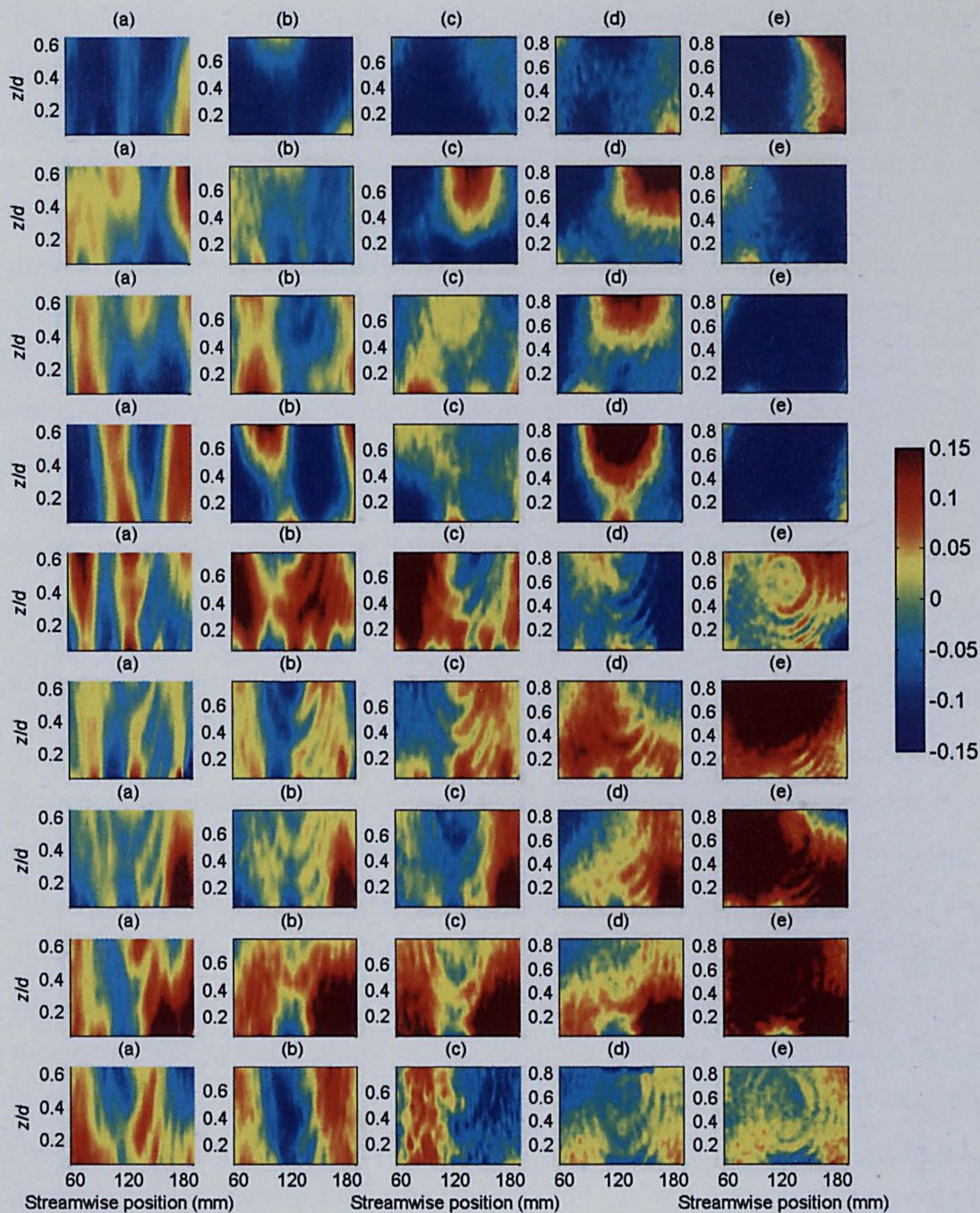


Figure 5.19. The spatial distribution of \tilde{w}/u_* over the bimodal bed for the experimental runs performed at a single bed slope with (a) $d/D_{84} = 4.1$; (b) $d/D_{84} = 5.7$; (c) $d/D_{84} = 6.9$; (d) $d/D_{84} = 9.0$; and (e) $d/D_{84} = 12.8$, where \tilde{w} is the spatial deviation in time-averaged vertical velocity, u_* is the bed shear velocity, d is flow depth and D_{84} is the grain size at which 84 per cent of the bed material is finer. Each row of contour plots relates to a lateral position over the bed; from the top to the bottom row are lateral positions of -87 mm, -65 mm, -43 mm, -21 mm, 0 mm, 23 mm, 45 mm, 67 mm, 89 mm. Note that the vertical axes do not have the same scale.

The change in the spatial patterns of \tilde{w}/u_* with relative submergence over the bimodal bed is shown in Figure 5.19. It is striking that at the lowest relative submergence a similar spatial pattern of vertical zones of upward and downward moving fluid, with many alternating in the streamwise direction, is also seen (Figure 5.19a). The zones are however, narrower and less distinct than seen over the unimodal bed. The vertical zones of downward moving fluid are, in particular, less consistent through the whole flow depth. However, the spatial pattern changes in a similar manner with relative submergence. An increase in relative submergence to 5.7 results in an increase in the streamwise length of many of the vertical zones, and in some cases, a reduction in the number of these zones (Figure 5.19b). Yet some of the vertical zones at the lowest submergence do again appear at this submergence, but often either in the form of a small area concentrated at the bed surface and or through the amalgamation of two of these zones. At a relative submergence of 6.9, a similar change occurs. For three of the lateral locations, the vertical zones no longer appear, with the zones again being organised into smaller features of upward and downward moving fluid close to the bed (Figure 5.19c). A further increase in relative submergence to 9.0 produces the same changes in the spatial patterns (Figure 5.19d). The zones become more intense, relative to $\langle \bar{w} \rangle$, and this is the first submergence at which the spatial pattern is noticeably different to that seen at the lowest submergence. However, the small, discrete patches of upward or downward moving fluid close to the bed, which correspond in spatial location to the vertical zones at the lowest submergence, are still present. At a relative submergence of 12.8, the spatial pattern has become further disassociated with that at lower submergences, with none of the lateral locations displaying any vertical zones of fluid (Figure 5.19e). Indeed, the majority of the locations are dominated by either one area of intense upward or downward moving fluid. Despite this, there still remain very small features close to the bed which appear to be a constituent component of many of the vertical zones of fluid at the lower submergences.

The contour plots for the two beds show that the spatial pattern of \tilde{w}/u_* can have greater similarity at similar relative submergences between two beds of different surface topographies, than the spatial pattern between low and high submergences over the same topography. The spatial pattern of vertical zones of upward and downward moving fluid over the two beds is in accordance to the conclusions drawn from the skewness values of the distributions of \bar{w} . The skewness values suggested that the flows over neither of the beds was consistently covered by either large areas of weak

(just slightly lower-than-average) downward motions or large areas of weak upward motions. Instead, both large areas could be present over the two beds, as has been seen in the contour plots of \tilde{w}/u_* . The spatial patterns demonstrate why the distributions of \bar{w} were both positively and negatively skewed.

5.9.2 Variability with Bed Slope

The experimental runs performed at the same relative submergence (Tables 5.4 and 5.5) are now analysed in order to discover whether bed slope influences the distribution of the spatial variation in \bar{w} over the two beds. The contour plots of \tilde{w}/u_* for those experimental runs performed over the unimodal bed are shown in Figures 5.20 to 5.21. It can be seen that vertical zones of upward and downward moving fluid also appear for these experimental runs, often in an alternating pattern.

At a relative submergence of 4.1, an increase in bed slope appears to result in a reduction in the number of these zones, through an associated increase in their streamwise length (Figures 5.20a and b). This is the same change that was seen with increasing relative submergence. But the strength of the zones, relative to $\langle \bar{w} \rangle$, displays little variability with bed slope. For the majority of the lateral locations, there is little correspondence in the locations of the vertical zones between the two bed slopes. This suggests that the zones, rather than being modified by an increase in bed slope, are shifted to different locations over the bed. Yet there is greater spatial correspondence at a relative submergence of 5.6 (Figures 5.20c and d). There is, however, no consistent change in the spatial pattern of \tilde{w}/u_* with bed slope for all lateral locations. At a relative submergence of 6.9, an increase in bed slope from $S = 0.00285$ to $S = 0.00375$ (Figures 5.21a and b), in general, causes a greater distinction in the alternating pattern of upward and downward moving fluid, and an increase in the strength of the zones, relative to $\langle \bar{w} \rangle$. This largely results in the number of vertical zones that fully extend over the whole flow depth to increase with bed slope. However, from $S = 0.00375$ to $S = 0.00465$ the opposite occurs, whereby the streamwise length of the zones increases and in some cases can result in nearly all of the measurement section being occupied by just one zone of upward moving fluid. It shows that there is no consistent change in the spatial pattern of \tilde{w}/u_* with bed slope. This is also the case at a relative submergence of 9.0 (Figures 5.21d and e). Yet in general for all the experimental runs an increase in bed

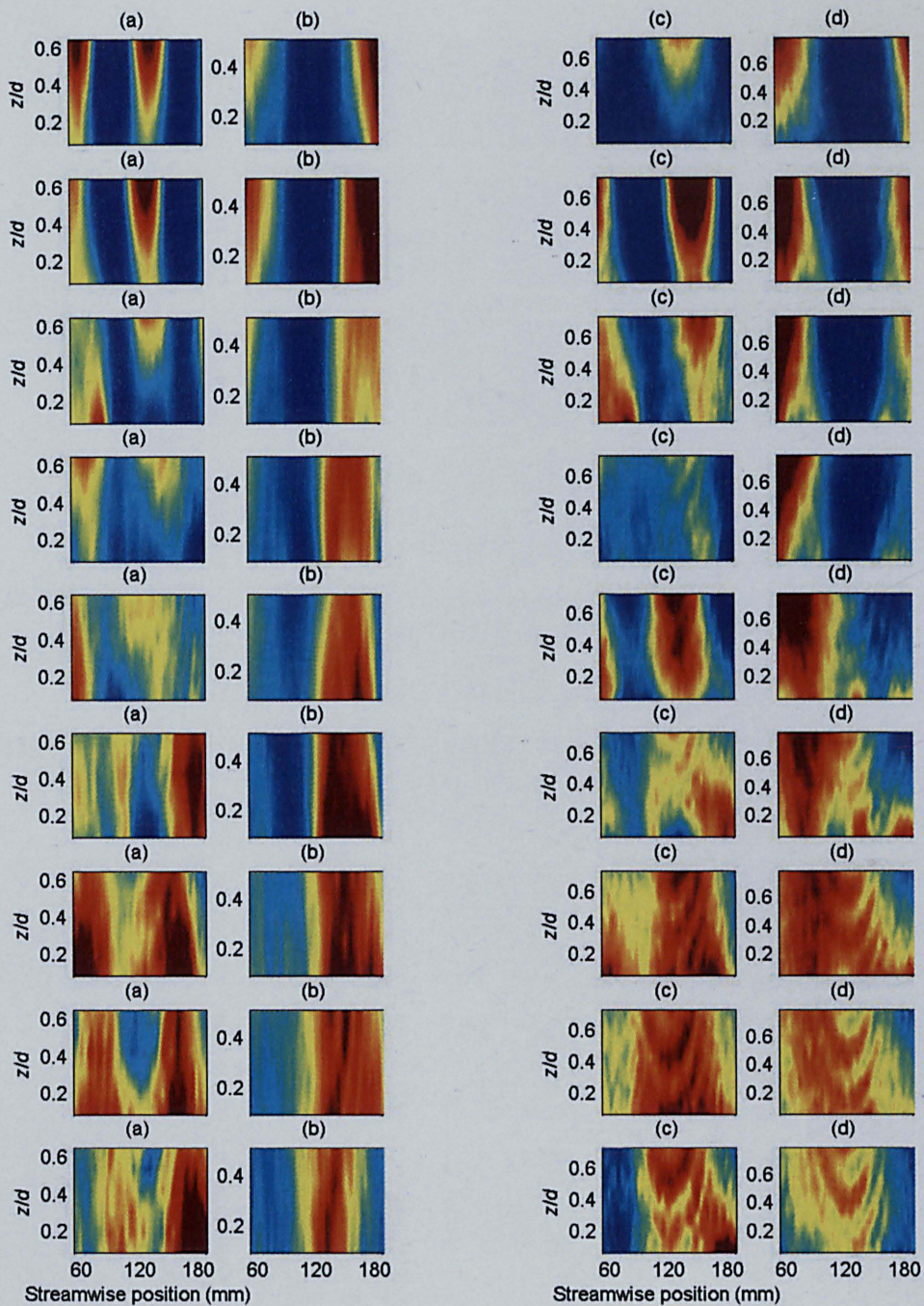


Figure 5.20. The spatial distribution of \tilde{w}/u_* over the unimodal bed for the experimental runs performed at $d/D_{84} = 4.1$ with (a) $S = 0.00285$; and (b) $S = 0.00735$, and at $d/D_{84} = 5.6$ with (c) $S = 0.00285$; and (d) $S = 0.00555$, where \tilde{w} is the spatial deviation in time-averaged vertical velocity, u_* is the bed shear velocity, d is flow depth and D_{84} is the grain size at which 84 per cent of the bed material is finer. From the top to the bottom row are lateral positions of -87 mm, -65 mm, -43 mm, -21 mm, 0 mm, 23 mm, 45 mm, 67 mm, 89 mm. Note that the vertical axes do not have the same scale. Colour scale is the same as for Figure 5.18.

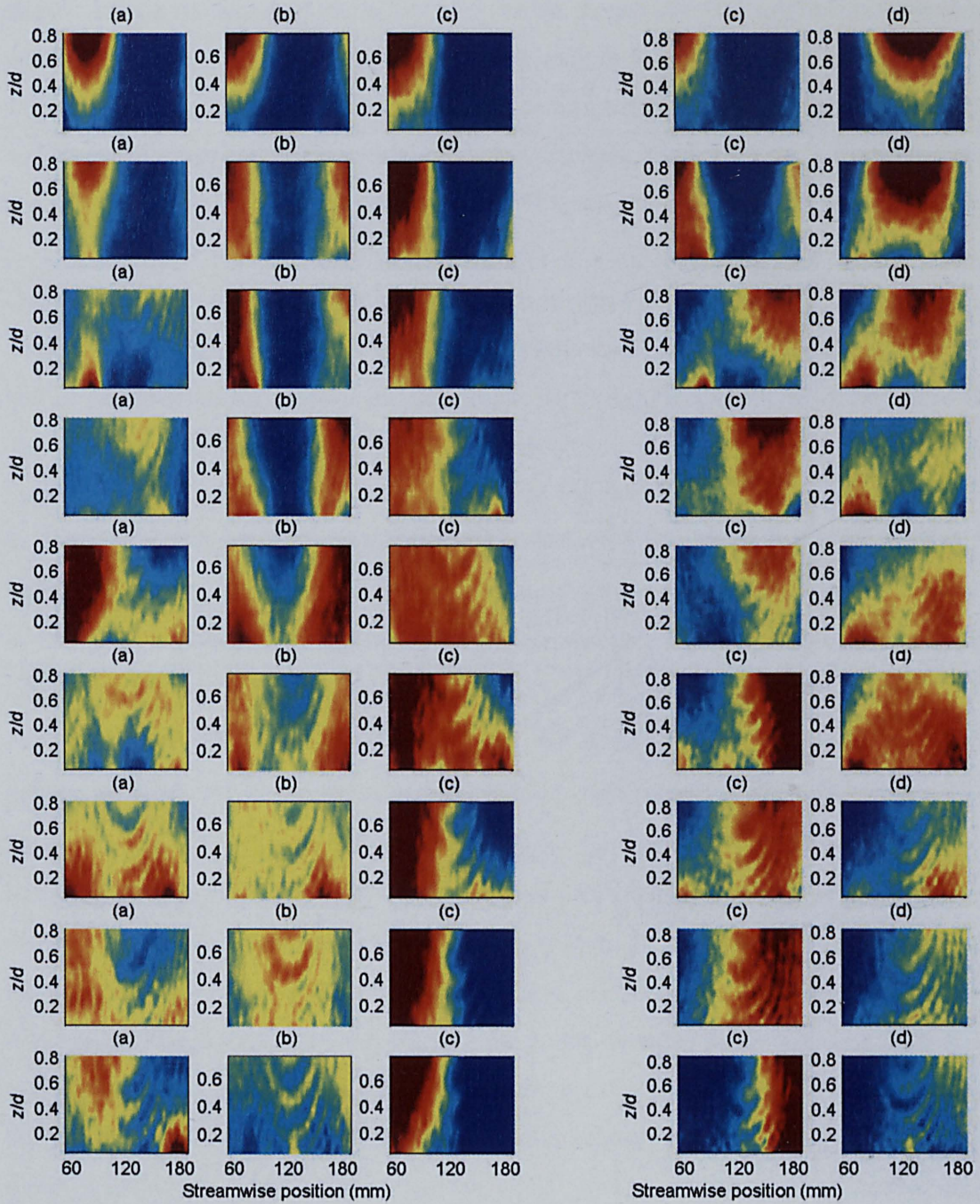


Figure 5.21. The spatial distribution of \tilde{w}/u_* over the unimodal bed for the experimental runs performed at $d/D_{84} = 6.9$ with (a) $S = 0.00285$; (b) $S = 0.00375$; and (c) $S = 0.00465$, and at $d/D_{84} = 9.0$ with (d) $S = 0.00285$; and (e) $S = 0.00375$, where \tilde{w} is the spatial deviation in time-averaged vertical velocity, u_* is the bed shear velocity, d is flow depth and D_{84} is the grain size at which 84 per cent of the bed material is finer. From the top to the bottom row are lateral positions of -87 mm, -65 mm, -43 mm, -21 mm, 0 mm, 23 mm, 45 mm, 67 mm, 89 mm. Note that the vertical axes do not have the same scale. Colour scale is the same as for Figure 5.18.

slope causes a reduction in the number of vertical zones of either upward or downward moving fluid over the bed and for the streamwise length of these zones to increase. The degree of correspondence in the streamwise location of the zones between the different bed slopes also appears to be greater when the difference in bed slope between the plots is small.

Over the bimodal bed, a similar spatial pattern is again observed for the majority of the contour plots (Figures 5.22 and 5.23). At a relative submergence of 4.1 an increase in bed slope results in the number of zones reducing to just two, a similar reduction to that seen with bed slope and with relative submergence at a single bed slope over the unimodal bed. There is a change in the area of the flow being occupied by downward moving fluid at the shallower slope to being occupied by upward moving fluid at the higher bed slope, or vice versa. There are therefore far fewer of the same zones that appear at both slopes. This was also seen with a change in bed slope at the same relative submergence over the unimodal bed. The strength of the zones, relative to $\langle \bar{w} \rangle$, at a relative submergence of 4.1 increase with bed slope. These changes in the spatial pattern of \tilde{w}/u_* are also seen at a relative submergence of 5.6 (Figures 5.22c and d). However, there is no consistent change slope that was seen at the lower relative submergence in the number of vertical zones and their length across all the lateral locations with bed. The only general trend is that an increase in bed slope causes the vertical zones to become less distinct. At this relative submergence, there is more correspondence in the spatial locations of the zones between the two slopes. This might be related to the smaller difference in bed slope, as seen over the unimodal bed. An inconsistent pattern of change is also seen at a relative submergence of 6.9 (Figures 5.23a, b and c). At a relative submergence of 9.0, there is a tendency for the alternating pattern of upward and downward moving fluid to become clearer, through an increase in the number of zones over the bed (Figures 5.23c and d). The spatial locations of the zones again appear to have greater correspondence when the difference in bed slope is smaller. The results across Figures 5.22 and 5.23 shows that there is once again no consistent change in the spatial pattern of \tilde{w}/u_* with bed slope. However, there is a general trend for an increase in bed slope to cause a reduction in the number of vertical zones of either upward or downward moving fluid over the bed and for the streamwise length of the zones to increase, as seen over the unimodal bed.

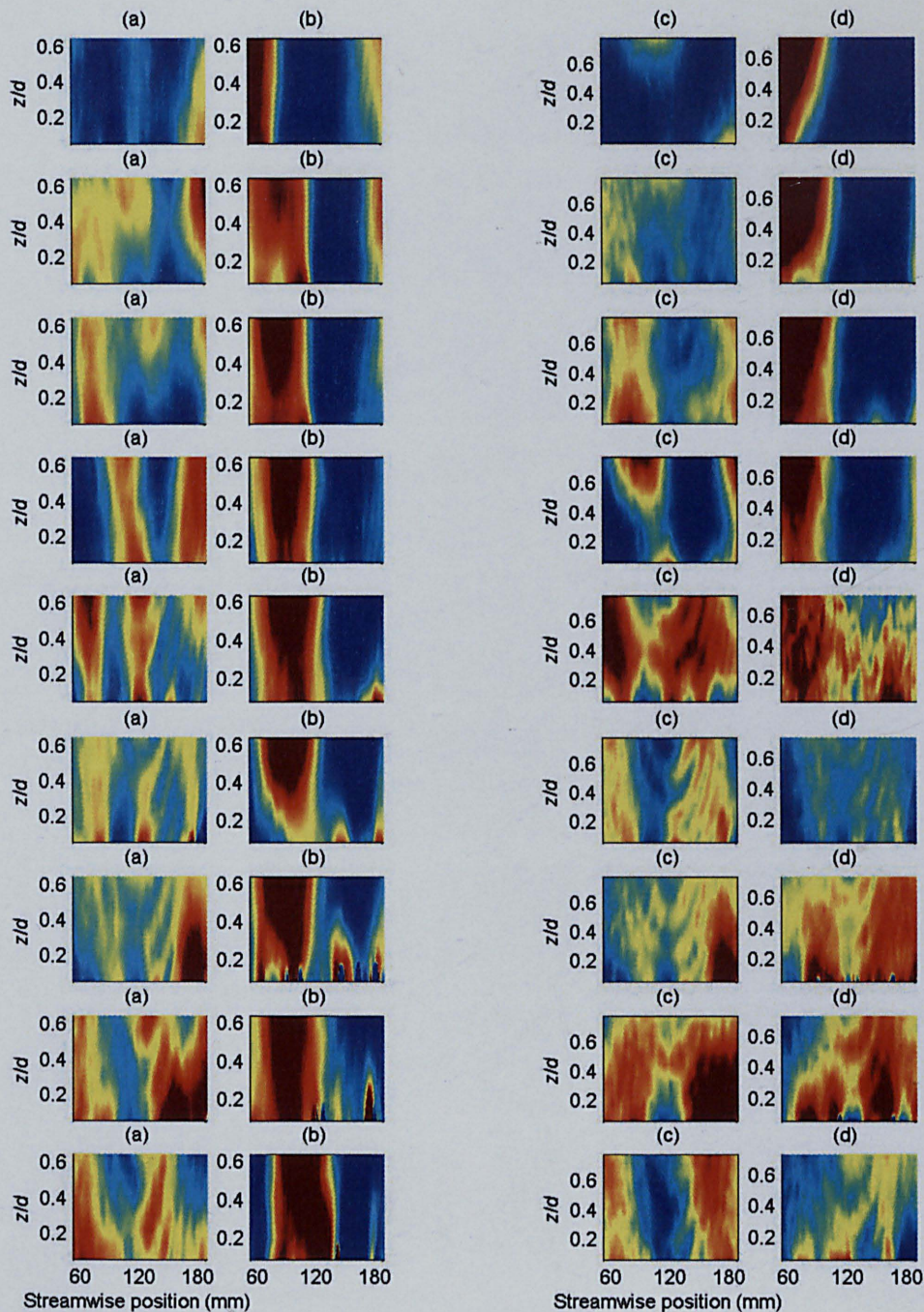


Figure 5.22. The spatial distribution of \tilde{w}/u_* over the bimodal bed for the experimental runs performed at $d/D_{84} = 4.1$ with (a) $S = 0.00284$; and (b) $S = 0.00734$, and at $d/D_{84} = 5.7$ with (c) $S = 0.00284$; and (d) $S = 0.00554$, where \tilde{w} is the spatial deviation in time-averaged vertical velocity, u_* is the bed shear velocity, d is flow depth and D_{84} is the grain size at which 84 per cent of the bed material is finer. From the top to the bottom row are lateral positions of -87 mm, -65 mm, -43 mm, -21 mm, 0 mm, 23 mm, 45 mm, 67 mm, 89 mm. Note that the vertical axes do not have the same scale. Colour scale is the same as for Figure 5.18.

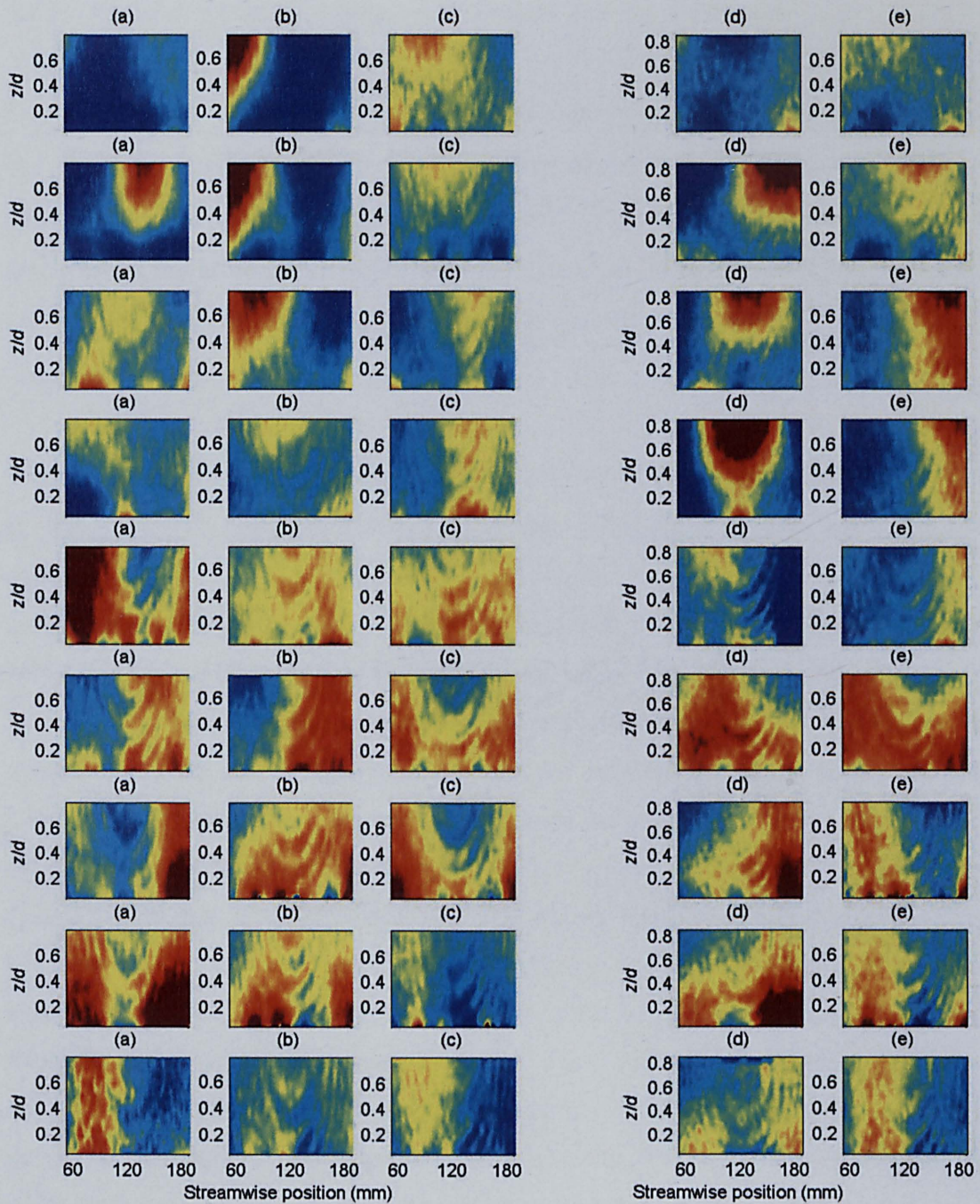


Figure 5.23. The spatial distribution of \tilde{w}/u_* over the bimodal bed for the experimental runs performed at $d/D_{84} = 6.9$ with (a) $S = 0.00284$; (b) $S = 0.00374$; and (c) $S = 0.00464$, and at $d/D_{84} = 9.0$ with (d) $S = 0.00284$; and (e) $S = 0.00374$, where \tilde{w} is the spatial deviation in time-averaged vertical velocity, u_* is the bed shear velocity, d is flow depth and D_{84} is the grain size at which 84 per cent of the bed material is finer. From the top to the bottom row are lateral positions of -87 mm, -65 mm, -43 mm, -21 mm, 0 mm, 23 mm, 45 mm, 67 mm, 89 mm. Note that the vertical axes do not have the same scale. Colour scale is the same as for Figure 5.18.

5.9.3 Variability Under Conditions of Constant Bed Shear Stress

Contour plots of \tilde{w}/u_* for the experimental runs that were carried out at the same mean bed shear stress (Tables 5.6 and 5.7) are now assessed for each bed. If the spatial patterns of \tilde{w}/u_* are different over the bed, it suggests that the momentum transfer mechanisms might be different between the experimental runs even when the average rate of transfer at the bed is the same. It will demonstrate whether u_* scales the spatial distribution of \tilde{w} .

It can be seen that over the unimodal bed there is indeed variability in the spatial pattern of \tilde{w}/u_* between the experimental runs (Figure 5.24). This variability appears to be again related to increases in relative submergence, but these effects are more subtle than those seen at a single bed slope. There is a tendency for the streamwise length of the zones to increase from the low to mid submergences, and therefore from high to mid bed slopes. At the highest submergences and shallowest slopes, the zones are less numerous, and the areas of upward and downward moving fluid restricted to close to the bed surface. In addition, there are lower degrees of persistence in the vertical zones through the flow depth and lower overall degrees of spatial organisation. This kind of spatial pattern was also only associated with higher relative submergences at a single bed slope. The vertical variation in the length of the zones increases with relative submergence, such that at the lower submergence the zones have almost the same length throughout the whole flow depth, but at the higher submergences, the length demonstrates much greater variation with height. The small areas of upward or downward moving fluid restricted to close to the bed surface at the higher submergence, again appear to have some spatial correlation with the vertical zones of fluid at the lower submergences, but less so than at a single bed slope. It was seen for the experimental runs performed at the same relative submergences that this is likely to be due to changes in bed slope. Therefore the appearance of the small areas close to the bed cannot wholly be associated with a decrease in the vertical propagation of the vertical zones of upward and downward moving fluid at the lower submergences.

Over the bimodal bed, the spatial pattern of \tilde{w}/u_* is not well scaled by u_* (Figure 5.25). The changes in the spatial pattern with relative submergence and bed slope are not as consistent as seen over the unimodal bed. However, there is still the tendency for

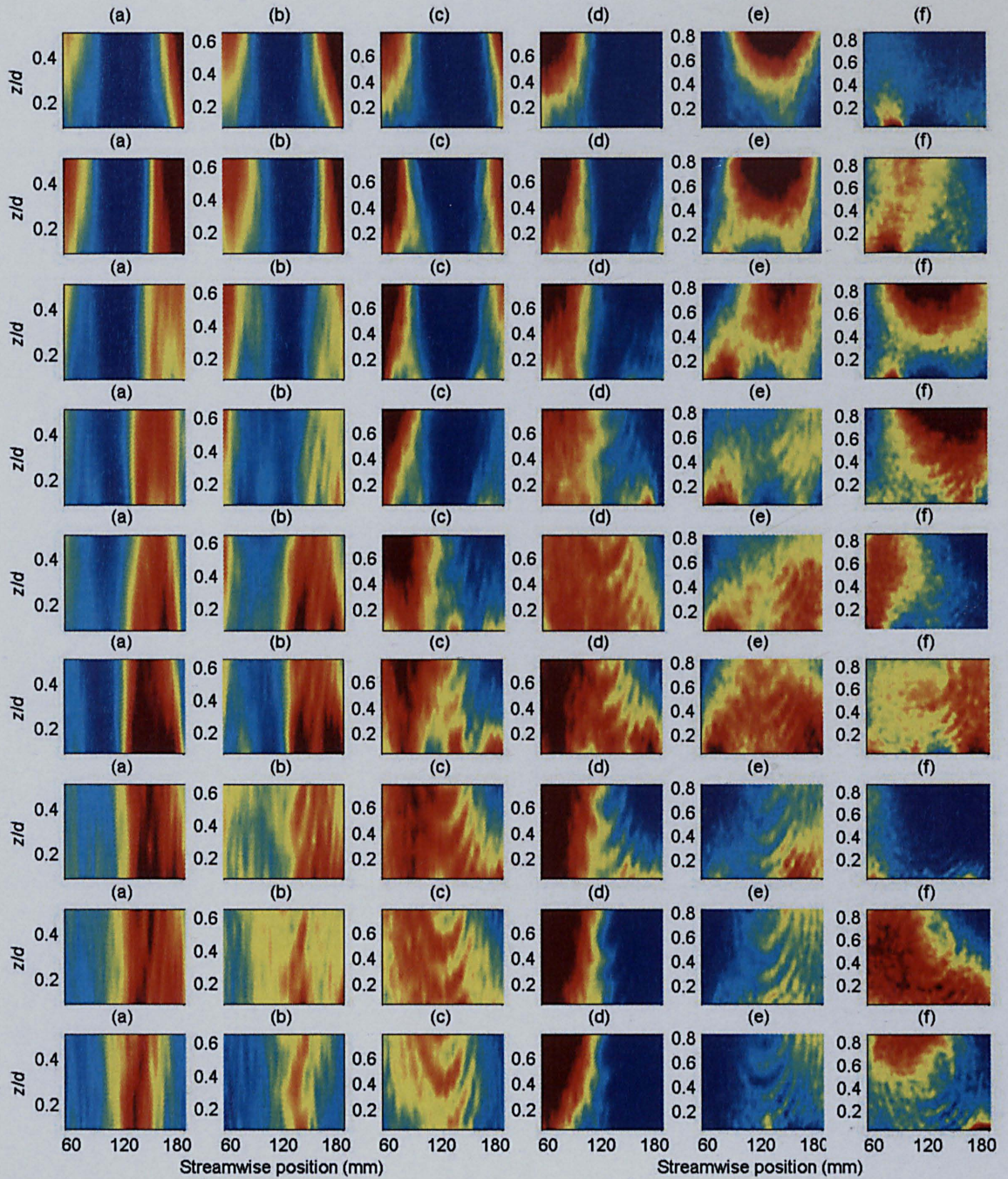


Figure 5.24. The spatial distribution of \tilde{w}/u_* over the unimodal bed for the experimental runs carried out at the same mean bed shear stress with (a) $d/D_{84} = 4.2$; (b) $d/D_{84} = 4.8$; (c) $d/D_{84} = 5.7$; (d) $d/D_{84} = 7.0$; (e) $d/D_{84} = 9.1$; and (f) $d/D_{84} = 12.9$, where \tilde{w} is the spatial deviation in time-averaged vertical velocity, u_* is the bed shear velocity, d is flow depth and D_{84} is the grain size at which 84 per cent of the bed material is finer. From the top to the bottom row are lateral positions of -87 mm, -65 mm, -43 mm, -21 mm, 0 mm, 23 mm, 45 mm, 67 mm, 89 mm. Note that the vertical axes do not have the same scale. Colour scale is the same as for Figure 5.18.

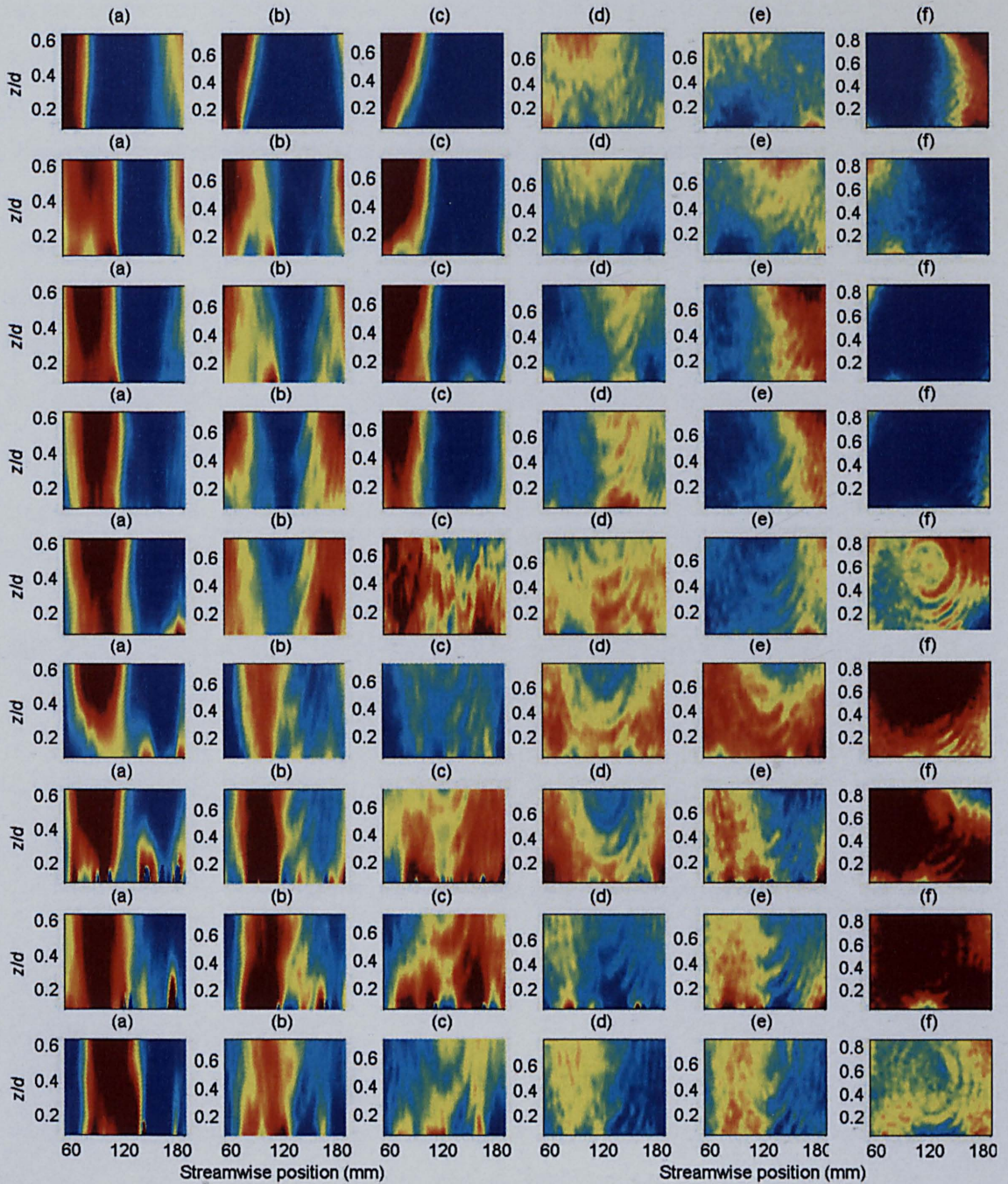


Figure 5.25. The spatial distribution of \tilde{w}/u_* over the bimodal bed for the experimental runs carried out at the same mean bed shear stress with (a) $d/D_{84} = 4.1$; (b) $d/D_{84} = 4.8$; (c) $d/D_{84} = 5.6$; (d) $d/D_{84} = 7.2$; (e) $d/D_{84} = 9.0$; and (f) $d/D_{84} = 12.8$, where \tilde{w} is the spatial deviation in time-averaged vertical velocity, u_* is the bed shear velocity, d is flow depth and D_{84} is the grain size at which 84 per cent of the bed material is finer. From the top to the bottom row are lateral positions of -87 mm, -65 mm, -43 mm, -21 mm, 0 mm, 23 mm, 45 mm, 67 mm, 89 mm. Note that the vertical axes do not have the same scale. Colour scale is the same as for Figure 5.18.

the spatial pattern to become less dominated by vertical zones of upward and downward moving fluid with increases in relative submergence, and therefore decreases in bed slope. It means that at the lower submergence, and higher bed slopes, the flow is dominated by alternating vertical zones but at the highest submergence and shallowest bed slope, the flow at nearly all lateral locations is entirely occupied by just upward or downward moving fluid. There is again a lower degree of correspondence in the spatial locations of the upward and downward moving zones of fluid between the experimental runs than seen at a single bed slope. The poor scaling of the spatial pattern of \tilde{w}/u_* by u_* corresponds with the poor scaling of the vertical profiles of $\sigma_{\tilde{w}}$ over the bimodal bed that were observed earlier.

5.10 Lateral Variability in the Pattern of Spatial Deviations over the Bed

The contour plots of \tilde{w}/u_* have shown that there is a variation in the distribution of spatial deviations in \bar{w} with lateral location over the bed. To determine this lateral variability it is necessary to re-examine the plots shown earlier. It will then also be possible to obtain an indication of how the lateral variability in the bed surface topography has an influence on the spatial pattern, and whether a given section of the bed induces the same spatial pattern. The contour plots presented above will be returned to.

5.10.1 Unimodal Bed

The experimental runs performed at a single bed slope are firstly described. The contour plots of \tilde{w}/u_* in Figure 5.18a at a relative submergence of 4.1 show that there is a similar alternating pattern of upward and downward moving fluid across all nine lateral locations. From a lateral position of -87 mm towards the centreline of the flume this pattern becomes less distinct, but still demonstrates a good degree of similarity across these lateral positions (Figure 5.18a). This is despite the bed surface topography being different between the five lateral locations (Figure 5.16). Then at a lateral position of 23 mm a new pattern is evident, whereby all but one of the vertical zones of upward and downward moving fluid are positioned at different streamwise positions over the bed. A similar spatial pattern then persists for the remaining lateral locations. This pattern is slightly modified towards the highest lateral location through the zones of upward

moving fluid becoming greater in length. It is arguable that certain facets of the spatial pattern observed at the lower lateral positions are also evident at these high positions, especially in the form of the upward moving regions. Therefore there appears to be a slight and progressive change in the spatial pattern of \tilde{w}/u_* across the bed.

A similar grouping of the spatial patterns into two can also be seen for the contour plots at a relative submergence of 5.6 (Figure 5.18b). One pattern persists from a lateral position of -87 mm to the centreline of the flume, and another at the higher lateral locations. This observation is based on the change in the streamwise positions of the zones between the different lateral locations over the bed. There is no progressive change in the pattern with lateral location however, as was seen at a relative submergence of 4.1. At the high lateral locations it could again be argued that certain facets of the spatial pattern observed at the lower lateral positions is also evident, especially in the form of the upward moving regions. Indeed the large upward moving vertical zones at the higher lateral positions have a similar spatial location to those at the lower positions. The clear difference between the upper and lower plots is the lack of appearance, in all but one of the plots, of vertical zones of downward moving fluid in the lower plots.

At a relative submergence of 6.9, there appears to be a progressive change in the spatial pattern (Figure 5.18c). The pattern at a lateral position of -87 mm becomes less and less distinct up until a lateral position of -21 mm. Beyond this a new pattern forms and this becomes progressively more organised into vertical zones towards the highest lateral position over the bed. A very similar progression can also be seen at a relative submergence of 9.0, with the change in pattern occurring at a slightly lower lateral position of -45 mm (Figure 5.18d). At the highest submergence, although there is some similarity in the spatial patterns between several of the adjacent lateral positions, there is no clear change or grouping of the patterns with lateral position over the bed (Figure 5.18e). There is greater lateral variability in the spatial pattern of \tilde{w}/u_* at this submergence than at any other.

For the other experimental runs that are displayed in Figures 5.20, 5.21 and 5.24 this broad range of lateral changes in the spatial patterns can also be seen. However, there are also some runs where the spatial pattern displays very little lateral variability, such as in Figures 5.24a and d.

5.10.2 Bimodal Bed

By returning to the contour plots of \tilde{w}/u_* for the experimental runs at single bed slope over the bimodal bed (Figure 5.19) it can be seen that a progressive change in the spatial pattern of \tilde{w}/u_* is also noticeable for the experimental runs performed at the two lowest submergence (Figures 5.19a and b), with the exception of the plots at a lateral position of -87 mm. This is particularly clear at a relative submergence of 4.1 (Figure 5.19a). Some evidence of such a change is also present at a relative submergence of 6.9, but it only occurs across a number of the lateral positions (Figure 5.19c). It results in there being three different dominant patterns over the bed, with a progression occurring within each of these patterns, but not from one pattern to another. At a relative submergence of 9.0, the spatial patterns can be once again grouped into two, in which there is a progressive change within each (Figure 5.19d). One pattern becomes progressively more developed from a lateral position of -87 to -21 mm. At the centreline of the flume, there is a transition between the pattern in the upper plots and a different pattern that appears in the lower plots. A very similar grouping and lateral change is also seen at the highest relative submergence (Figure 5.19e). The transition in the two patterns also occurs at the centreline of the flume. However, at the highest lateral position, the contour plot demonstrates a different pattern to the adjacent plots and does not follow the general progression in the pattern in the lower half of the plots.

Once again these lateral changes in the spatial patterns shown in Figure 5.19 are also displayed for other experimental runs in Figures 5.22, 5.23 and 5.25. There are a few examples of where the spatial pattern displays little lateral variability, for instance, in Figures 5.25a and b.

It would appear that the spatial pattern in \tilde{w}/u_* is not closely associated with its lateral position over either of the beds. Indeed, the spatial pattern can appear just as consistent across the nine different lateral locations for a given experimental run as it can across the experimental runs at a given lateral position. Given that relative submergence, rather than bed slope, was found to have a more consistent influence on the spatial patterns, this suggests that relative submergence may have just as large an effect on the spatial pattern of \tilde{w}/u_* as bed surface topography. However, the variability in the spatial pattern across the bed also indicates that bed surface topography must have some

influence. Only a small number of particular features of the spatial pattern appeared in all the experimental runs at a given lateral position, suggesting that bed surface topography may have a more localised influence on \tilde{w}/u_* , whilst relative submergence has a greater influence across the flow field as a whole. This is logical given that the effect of relative submergence must be spread over the whole flow depth, it cannot produce localised changes in the spatial pattern because it is a spatially-integrated flow property. Bed elevation is a point measurement and is therefore likely to have only an isolated, localised influence on a small area of the fluid. This might be seen, for instance, in the form of small regions of upward and downward fluid close to the bed surface. The similarity in the spatial patterns of \tilde{w}/u_* between adjacent lateral positions suggests one of two things. Either the influence of the bed on the flow spans a greater lateral width than is commonly assumed, or some inherent feature or instability of the flow is causing this similarity in the spatial patterns across the bed, and this instability is modified by the effects of relative submergence. The bed surface elevation profiles (Figure 5.16 and 5.17) demonstrate that there is no bed structure that persists across a number of lateral positions, so the latter appears most likely.

The effect of relative submergence was further seen by the fact that the experimental runs that were performed at adjacent relative submergence had a greater similarity in spatial pattern, than those with large differences in relative submergence. In addition, its effects were seen in how the areas of fluid that appeared in all of the experimental runs at a given lateral position were in the form of vertical zones at the lower relative submergences but in the form of small areas close to the bed for the higher submergences. It was suggested in Chapter 4 that bed roughness influences the effect of relative submergence on the spatial deviations in \bar{u} . If this is also the case for \bar{w} , it could explain why some of these areas of fluid were always present close to the bed. However, in the upper regions of the flow, where the influence of the bed on the flow is small and the influence of relative submergence might be greater, there is more variability in the spatial pattern between the experimental runs.

5.11 Vertical Scaling of the Pattern of Spatial Deviations over the Bed

The contour plots of \tilde{w}/u_* over both of the beds have shown that its spatial pattern can change quite markedly at the same z/d . The areas of upward and downward moving

fluid reached the outer regions of the flow at low submergences but were concentrated close to the bed at the higher submergences. In addition, the influence of relative submergence was less apparent close to the bed. It is therefore likely that the spatial patterns will have a greater similarity at the same z/D_{84} , than at the same z/d . Thus, contour plots have been produced of \tilde{w}/u_* as a function of z/D_{84} , and this has been carried out for each lateral position.

It was decided that only the experimental runs performed at a single bed slope (Tables 5.2 and 5.3) will be explored. This is reasonable given the spatial pattern in these experimental runs are representative of the range of spatial patterns observed for the all the experimental runs. Over the unimodal bed, it can be seen in Figure 5.26 that the small areas of upward and downward motions that occurred close to the bed when plotted against z/d at the higher relative submergences do largely correspond with the vertical zones of fluid at the lower submergences. It means that there is less variability in the spatial patterns of \tilde{w}/u_* at a given lateral position than when \tilde{w}/u_* was plotted against z/d . Nonetheless, there are still regions of upward and downward fluid at the lower submergences that do not appear at the higher submergences.

The contour plots of \tilde{w}/u_* in Figure 5.27 over the bimodal bed again show that the patterns are not as variable as seen at the same z/d . The small areas of upward and downward motions at the bed at the higher submergences again correspond with some of the vertical zones at the lower submergences, but less so than seen over the unimodal bed. Although, the plots at the higher submergences still demonstrate considerable variability in spatial pattern to those at the lower submergences.

Since these plots are produced from measurements at the same z/D_{84} , it demonstrates that bed roughness produces a better scaling of the spatial pattern than flow depth, but it cannot fully account for the variability in the spatial pattern between the plots. There is more spatial persistence in some of the regions of upward and downward fluid than at the same z/d , but there is always the occurrence of additional regions that do not appear in experimental runs, with relative submergence influencing the degree of spatial persistence in these regions. In addition, the plots at the higher submergences still demonstrate considerable variability in spatial pattern to those at the lower

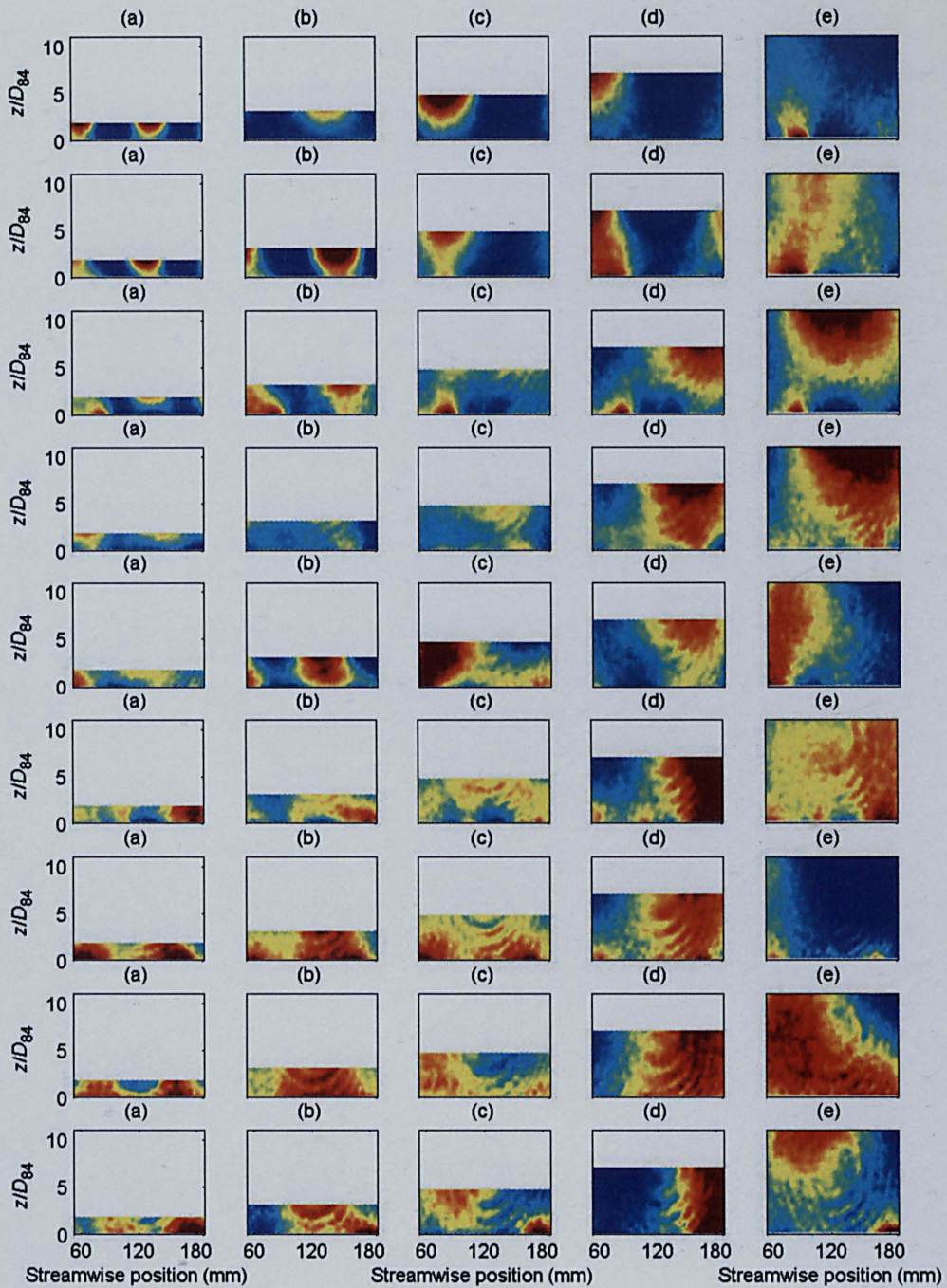


Figure 5.26. The spatial distribution of \tilde{w}/u_* over the unimodal bed for the experimental runs performed at a single bed slope with (a) $d/D_{84} = 4.1$; (b) $d/D_{84} = 5.6$; (c) $d/D_{84} = 6.9$; (d) $d/D_{84} = 9.0$; and (e) $d/D_{84} = 12.9$, where \tilde{w} is the spatial deviation in time-averaged vertical velocity, u_* is the bed shear velocity, d is flow depth and D_{84} is the grain size at which 84 per cent of the bed material is finer. From the top to the bottom row are lateral positions of -87 mm, -65 mm, -43 mm, -21 mm, 0 mm, 23 mm, 45 mm, 67 mm, 89 mm. Note that the vertical axes do not have the same scale. Colour scale is the same as for Figure 5.18.

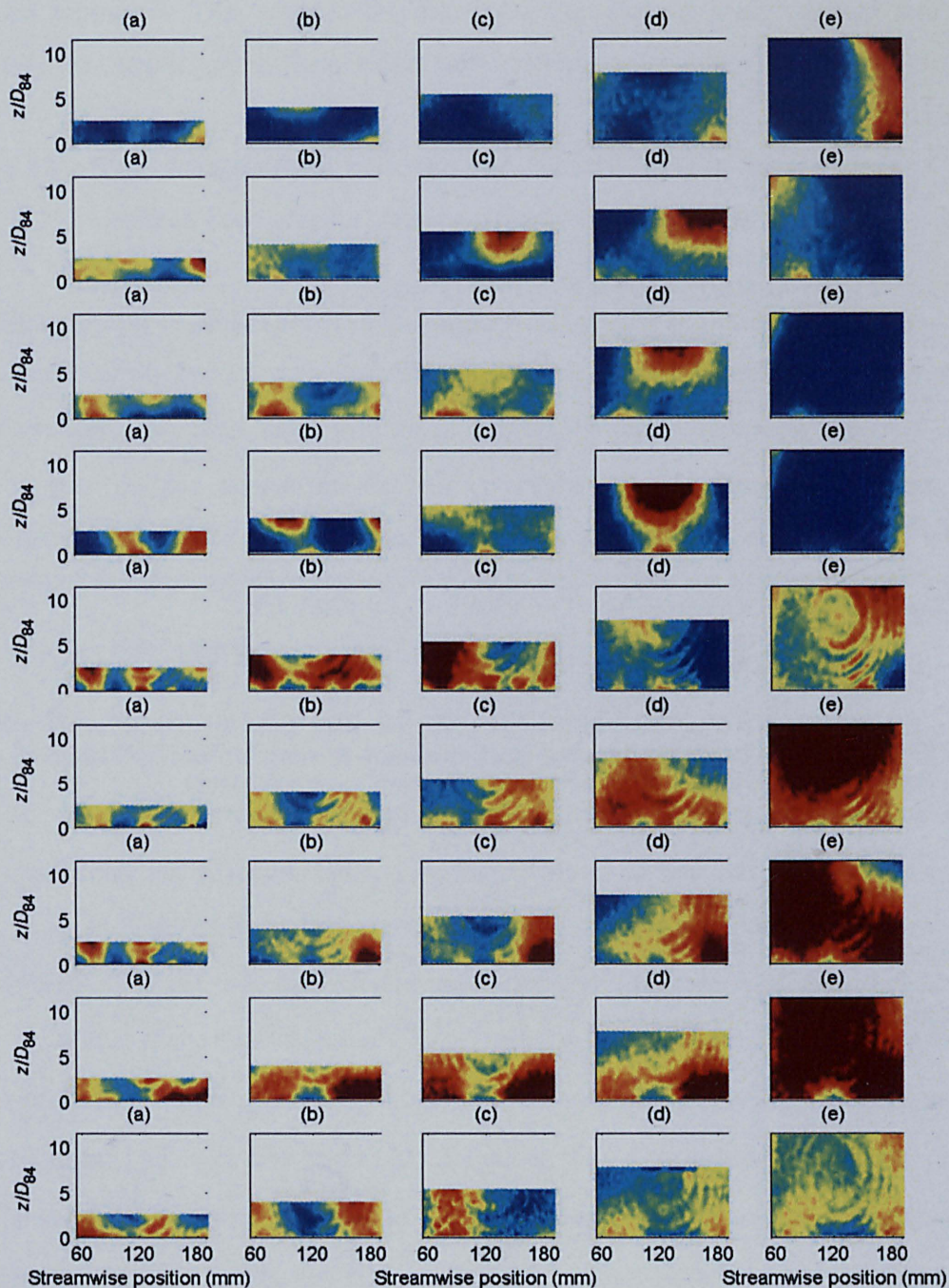


Figure 5.27. The spatial distribution of \tilde{w}/u_* over the bimodal bed for the experimental runs performed at a single bed slope with (a) $d/D_{84} = 4.1$; (b) $d/D_{84} = 5.7$; (c) $d/D_{84} = 6.9$; (d) $d/D_{84} = 9.0$; and (e) $d/D_{84} = 12.8$, where \tilde{w} is the spatial deviation in time-averaged vertical velocity, u_* is the bed shear velocity, d is flow depth and D_{84} is the grain size at which 84 per cent of the bed material is finer. From the top to the bottom row are lateral positions of -87 mm, -65 mm, -43 mm, -21 mm, 0 mm, 23 mm, 45 mm, 67 mm, 89 mm. Note that the vertical axes do not have the same scale. Colour scale is the same as for Figure 5.18.

submergences. This suggests that flow structures that are scaled by both bed roughness and flow depth must influence the spatial pattern.

5.12 The Relationship between the Pattern of Spatial Deviations and Bed Surface Topography

The manner in which some of the regions of upward and downward fluid change their location from one lateral position to another suggests that there may be some correlation between \tilde{w}/u_* and local aspects of the bed surface topography. Given that all the regions do not appear at all relative submergences, there may be an important relationship between bed surface topography and relative submergence, whereby the effects of the bed on \tilde{w}/u_* is suppressed at higher submergences. It will be seen whether this is the case.

To discover whether there is an association between the spatial pattern of \tilde{w}/u_* and the bed surface topography, a cross-correlation between \tilde{w}/u_* and bed surface elevation is performed for different streamwise lags. This is carried out for the measurements of \tilde{w}/u_* and bed surface elevation that have the same lateral positions over the bed. This clearly does not take into account any lateral or streamwise correlation in bed surface elevations that could influence \tilde{w}/u_* , or any lateral correlation between bed surface elevation and \tilde{w}/u_* . In other words it does not account for the effect of any spatially coherent bed structure that could influence \tilde{w}/u_* . A cross-correlogram was used to quantify the spatial covariance between pairs of \tilde{w}/u_* and bed surface elevation measurements. A series of streamwise lag l_x between \tilde{w}/u_* and bed surface elevation z_b were applied to take into account the streamwise propagation of the flow relative to the bed. Using a cross-correlogram in this way means that the cross-covariance C between \tilde{w}/u_* and z_b is given by

$$C(l_x) = \frac{1}{N_C} \sum_{x=2.265}^{N_C} \frac{\tilde{w}}{u_*}(x) \cdot z_b(x - l_x) - m_{\tilde{w}/u_*} \cdot m_{z_b} \quad (5.7)$$

where

$$m_{\tilde{w}/u_*} = \frac{1}{N_C} \sum_{x=2.265}^{N_C} \frac{\tilde{w}}{u_*}(x) \quad (5.8)$$

$$m_{z_b} = \frac{1}{N_C} \sum_{x=2.265}^{N_C} z_b(x-l_x) \quad (5.9)$$

and N_C is the number of cross-correlated measurements and x is the streamwise position within the measurement section. A cross-correlogram was used to calculate the correlation coefficient η to provide a measure of spatial cross-correlation (Legleiter *et al.*, in press):

$$\eta(l_x) = \frac{C(l_x)}{\sqrt{\sigma_{\tilde{w}/u_*}^2 \cdot \sigma_{z_b \Delta x}^2}} \in [-1, +1] \quad (5.10)$$

where

$$\sigma_{\tilde{w}/u_*}^2 = \frac{1}{N_C(l_x)} \sum_{x=2.265}^{N_C} \left[\frac{\tilde{w}}{u_*}(x) - m_{\tilde{w}/u_*} \right]^2 \quad (5.11)$$

and

$$\sigma_{z_b l_x}^2 = \frac{1}{N_C} \sum_{x=2.265}^{N_C} [z_b(x-l_x) - m_{z_b}]^2 \quad (5.12)$$

A maximum lag of 100 mm was chosen to account fully for the propagation possible for the range of $\langle \bar{u} \rangle$ values. This resulted in less than the whole matrix of \tilde{w}/u_* values being available for the correlation, given the streamwise length of the DEM's.

The η values are shown in Figure 5.28 for the unimodal bed at all nine of the lateral positions over the bed at $z/D_{84} = 0.23$, the closest measurement position to the bed surface, and therefore the position at which the correlation should be strongest. This again is only performed for the experimental runs performed at single bed slope. They show that there is a relatively good association between \tilde{w}/u_* and z_b , but only at a

small number of the lateral positions is the correlation good. At different lateral locations, and for different experimental runs, the nature of the correlation can be different. For example, at a lateral location of -65 mm, reasonably high positive and negative values of η are found at the streamwise lag at which the peak η values occur. Yet at four other lateral locations all the experimental runs display a remarkable similarity in their change in η values with the streamwise lag. It is therefore clear that the direction of the association is not the same over the whole bed. It is likely that this is dependent both on the nature of the streamwise changes in z_b , and on the nature of the streamwise changes in \tilde{w}/u_* .

By examining the η values at $z/D_{84} = 1.85$, the measurement height closest to the water surface at a relative submergence of 4.1, it can be seen in Figure 5.29 that there is no great reduction in the strength of the association, despite being higher above the bed surface. It suggests that the correlation can be just as strong at the bed surface as at the water surface at this submergence. This is likely to be due to the vertical nature of the patterns of \tilde{w}/u_* over the bed. Yet it is important to note that the nature of the change in η with l_x at a given lateral location over the bed is now more variable. It would suggest that the spatial patterns in \tilde{w}/u_* are also more variable between the runs at this height. Very similar results are also seen at $z/D_{84} = 3.15$ (Figure 5.30), the closest measurement height to the water surface at a relative submergence of 5.6. This also continues to occur at the measurement positions closest to the water surface for all the other higher relative submergences (not shown).

Over the bimodal bed, very similar results are seen at $z/D_{84} = 0.26$ as those over the unimodal bed at a similar height (Figure 5.31). Increases in height to the measurements position closest to the water surface at a relative submergence of 4.1 (Figure 5.32) and 5.7 (Figure 5.33), and indeed for all other relative submergences (not shown), causes a very similar variation in the η values.

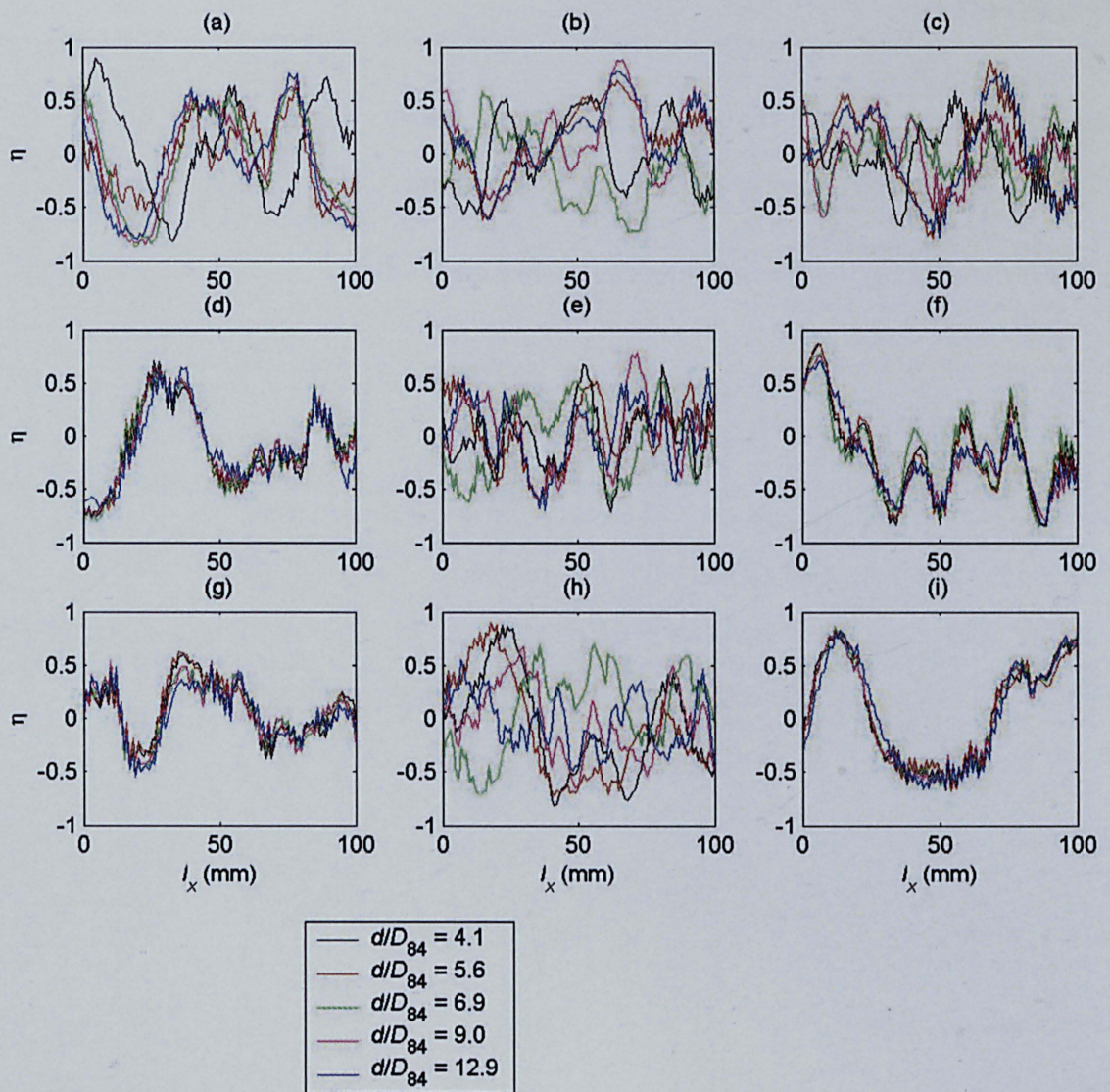


Figure 5.28. The coefficient of cross-correlation η between \tilde{w}/u_* and bed surface elevation at $z/D_{84} = 0.23$ for the experimental runs carried out at a single bed slope over the unimodal bed at lateral positions of (a) -87 mm; (b) -65 mm; (c) -43 mm; (d) -21 mm; (e) 0 mm; (f) 23 mm; (g); 45 mm; (h) 67 mm; and (i) 89 mm, where \tilde{w} is the spatial deviation in time-averaged vertical velocity, u_* is the bed shear velocity, z is the height above the maximum bed elevation, D_{84} is the grain size at which 84 per cent of the bed material is finer, l_x is the streamwise lag between bed surface elevation and \tilde{w}/u_* , and d is flow depth.

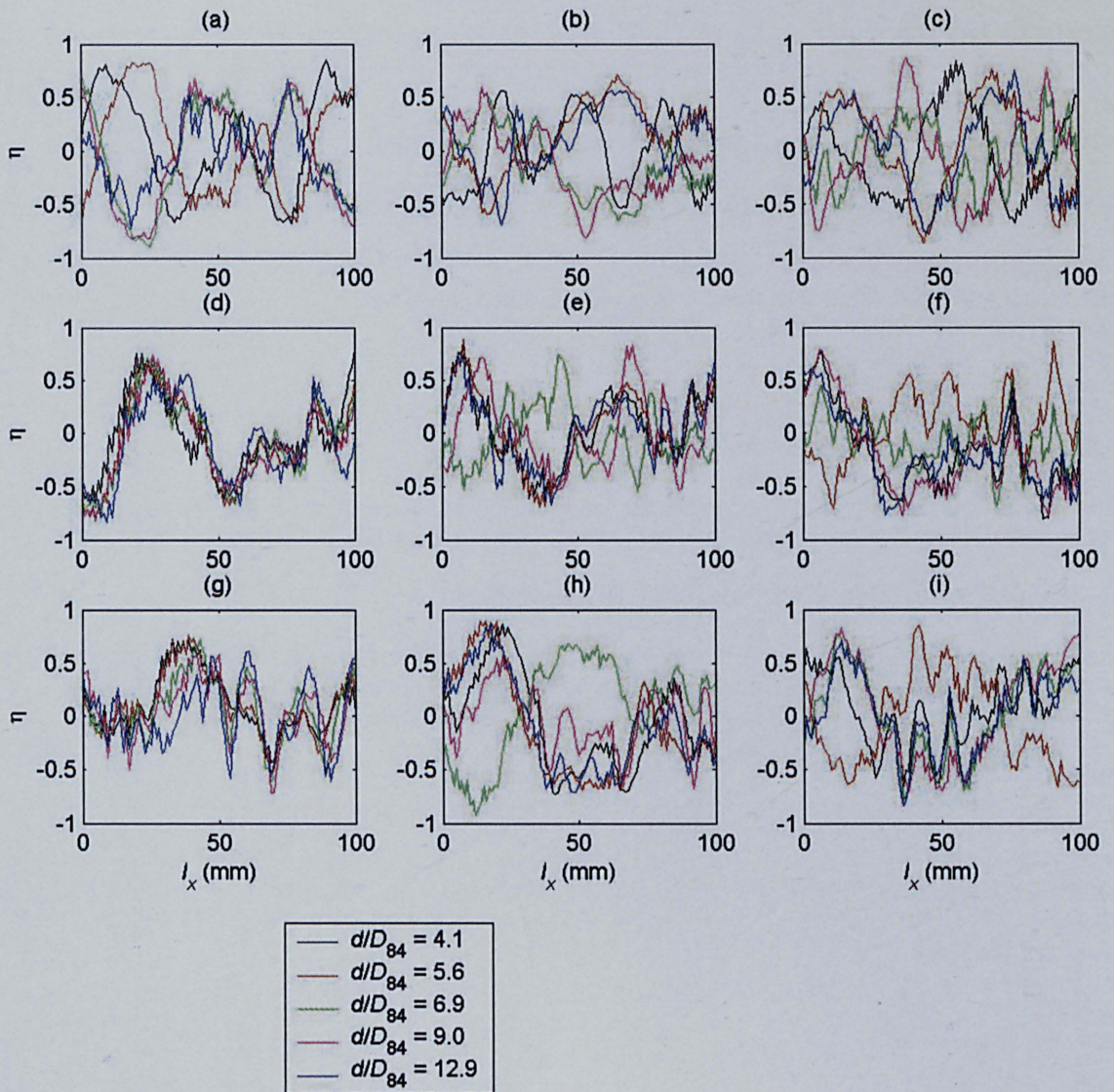


Figure 5.29. The coefficient of cross-correlation η between \tilde{w}/u_* and bed surface elevation at $z/D_{84} = 1.85$ for the experimental runs carried out at a single bed slope over the unimodal bed at lateral positions of (a) -87 mm; (b) -65 mm; (c) -43 mm; (d) -21 mm; (e) 0 mm; (f) 23 mm; (g); 45 mm; (h) 67 mm; and (i) 89 mm, where \tilde{w} is the spatial deviation in time-averaged vertical velocity, u_* is the bed shear velocity, z is the height above the maximum bed elevation, D_{84} is the grain size at which 84 per cent of the bed material is finer, l_x is the streamwise lag between bed surface elevation and \tilde{w}/u_* , and d is flow depth.

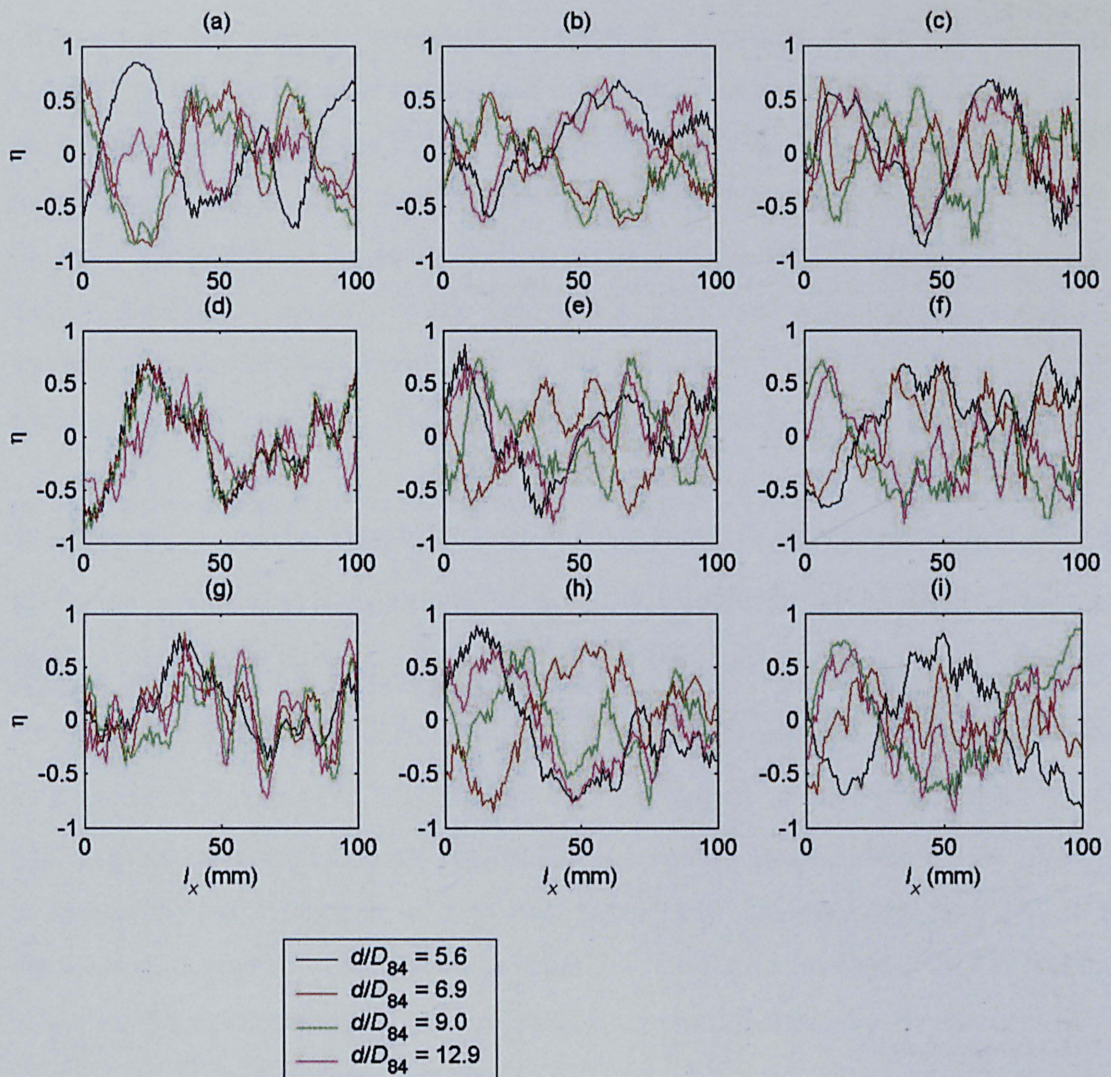


Figure 5.30. The coefficient of cross-correlation η between \tilde{w}/u_* and bed surface elevation at $z/D_{84} = 3.15$ for the experimental runs carried out at a single bed slope over the unimodal bed at lateral positions of (a) -87 mm; (b) -65 mm; (c) -43 mm; (d) -21 mm; (e) 0 mm; (f) 23 mm; (g); 45 mm; (h) 67 mm; and (i) 89 mm, where \tilde{w} is the spatial deviation in time-averaged vertical velocity, u_* is the bed shear velocity, z is the height above the maximum bed elevation, D_{84} is the grain size at which 84 per cent of the bed material is finer, l_x is the streamwise lag between bed surface elevation and \tilde{w}/u_* , and d is flow depth.

The results over both beds therefore show that a reasonable correlation between \tilde{w}/u_* and z_b persists from the bed surface to the water surface. This suggests that either the influence of bed surface topography persists to a greater height than previously assumed, or that the zones of upward and downward moving fluid that are generated at the bed can propagate all the way to the water surface, without being heavily disturbed in their length and position through the water surface. These scenarios might occur at the lower submergences but are unlikely to occur at the higher submergences. Therefore another possible explanation is that there was an additional production mechanism for the spatial pattern, which would account for why only a reasonable correlation was found between \tilde{w}/u_* and z_b . This will form part of the next section.

The periodicity in the change in η with l_x is intriguing. The expected variation would be for the η values to increase initially to a peak value and then to decrease to nearly zero as l_x increased, as seen for the association between $\bar{u}/\langle\bar{u}\rangle$ and z_b in Chapter 4. The peaks within the plots occur at nearly the same l_x , whether it is a peak of positive or negative η values. This lag position does not appear to be influenced by relative submergence and therefore the degree of streamwise propagation of the flow. In addition, relative submergence does not consistently influence the strength of the association, or whether it is positive or negative. There are a number of lateral positions at which the cyclical pattern is very similar, as was revealed by the plots of \tilde{w}/u_* against z/D_{84} . This suggests that at these locations there was a similarity in the spatial pattern of \tilde{w}/u_* at this absolute height between the different experimental runs. Stronger correlations do not appear to be concentrated between any adjacent lateral positions, suggesting that there are no large-scale bed features which span a large lateral width which may influence \tilde{w}/u_* .

Legleiter *et al.* (in press) examined the association between the \bar{w}/u_* and bed roughness d/k_s , where k_s is the equivalent sand roughness height. This was based on ADV measurements carried out within North Fork Cache La Poudre River, Colorado, a cobble-bedded river. This was performed over a riffle at three different discharges. They discovered that the correlation was weaker than the results described above. Yet they also discovered that its strength was not consistently related to relative submergence.

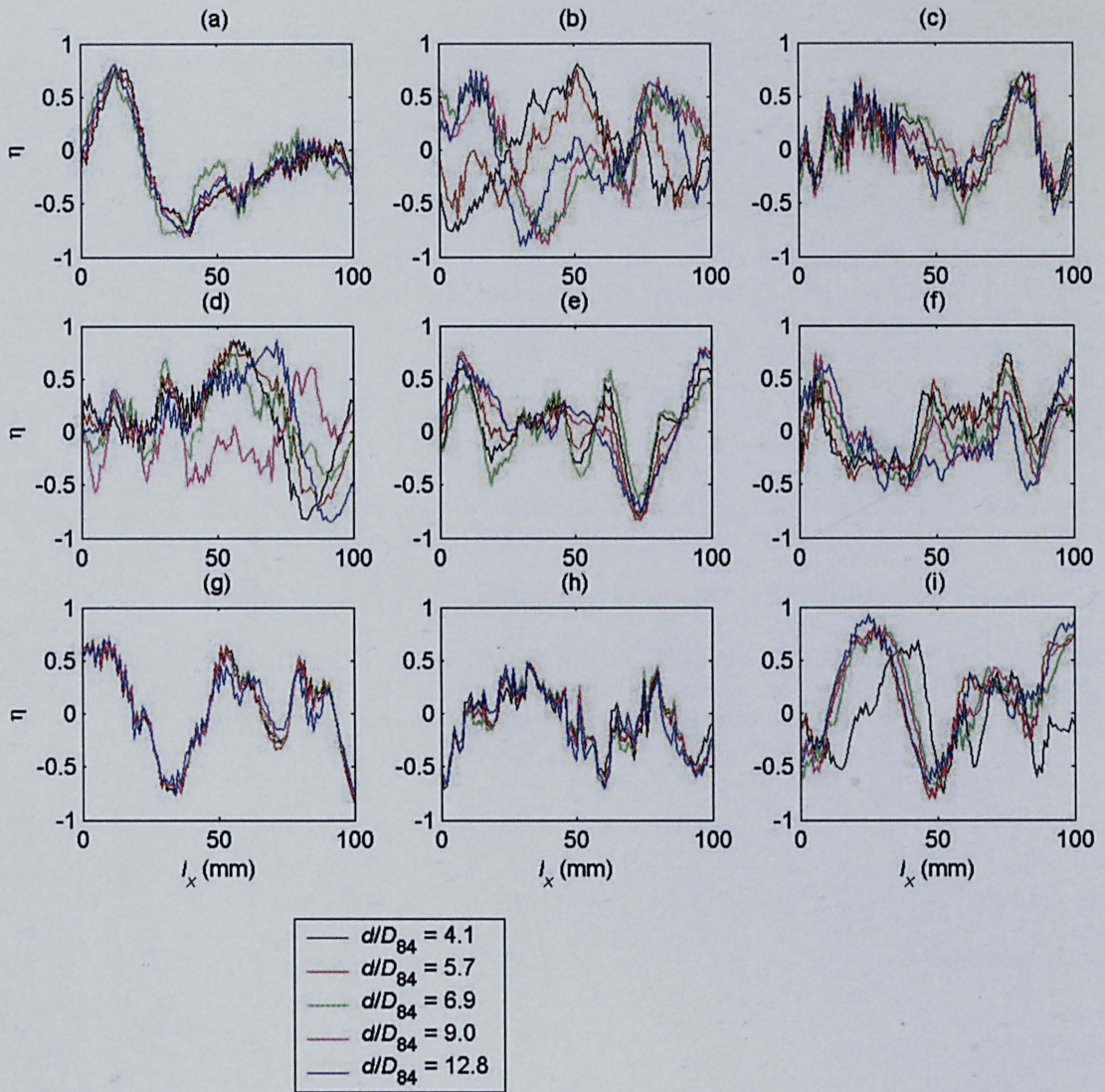


Figure 5.31. The coefficient of cross-correlation η between \tilde{w}/u_* and bed surface elevation at $z/D_{84} = 0.26$ for the experimental runs carried out at a single bed slope over the bimodal bed at lateral positions of (a) -87 mm; (b) -65 mm; (c) -43 mm; (d) -21 mm; (e) 0 mm; (f) 23 mm; (g); 45 mm; (h) 67 mm; and (i) 89 mm, where \tilde{w} is the spatial deviation in time-averaged vertical velocity, u_* is the bed shear velocity, z is the height above the maximum bed elevation, D_{84} is the grain size at which 84 per cent of the bed material is finer, l_x is the streamwise lag between bed surface elevation and \tilde{w}/u_* , and d is flow depth.

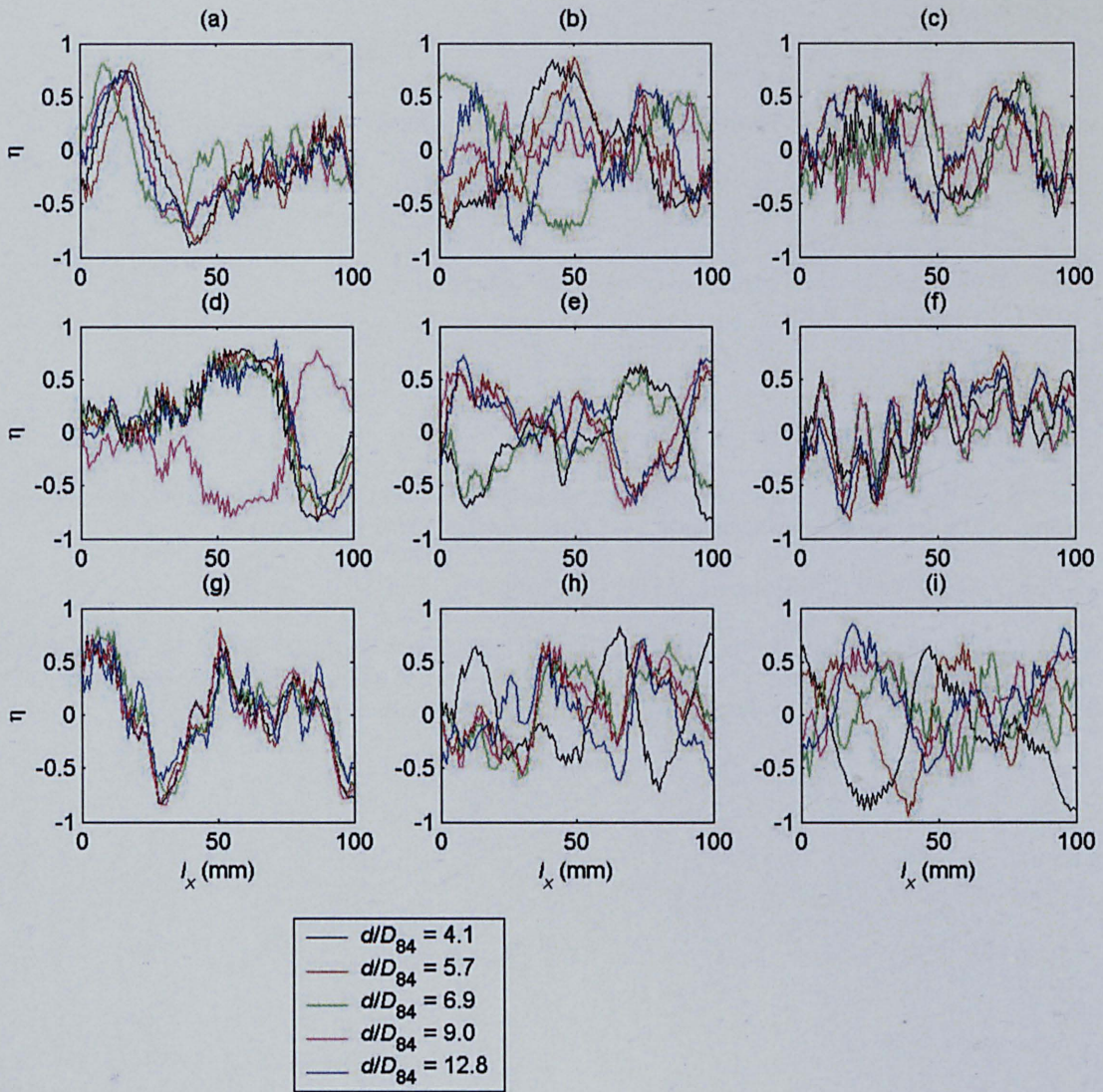


Figure 5.32. The coefficient of cross-correlation η between \tilde{w}/u_* and bed surface elevation at $z/D_{84} = 2.66$ for the experimental runs carried out at a single bed slope over the bimodal bed at lateral positions of (a) -87 mm; (b) -65 mm; (c) -43 mm; (d) -21 mm; (e) 0 mm; (f) 23 mm; (g); 45 mm; (h) 67 mm; and (i) 89 mm, where \tilde{w} is the spatial deviation in time-averaged vertical velocity, u_* is the bed shear velocity, z is the height above the maximum bed elevation, D_{84} is the grain size at which 84 per cent of the bed material is finer, l_x is the streamwise lag between bed surface elevation and \tilde{w}/u_* , and d is flow depth.

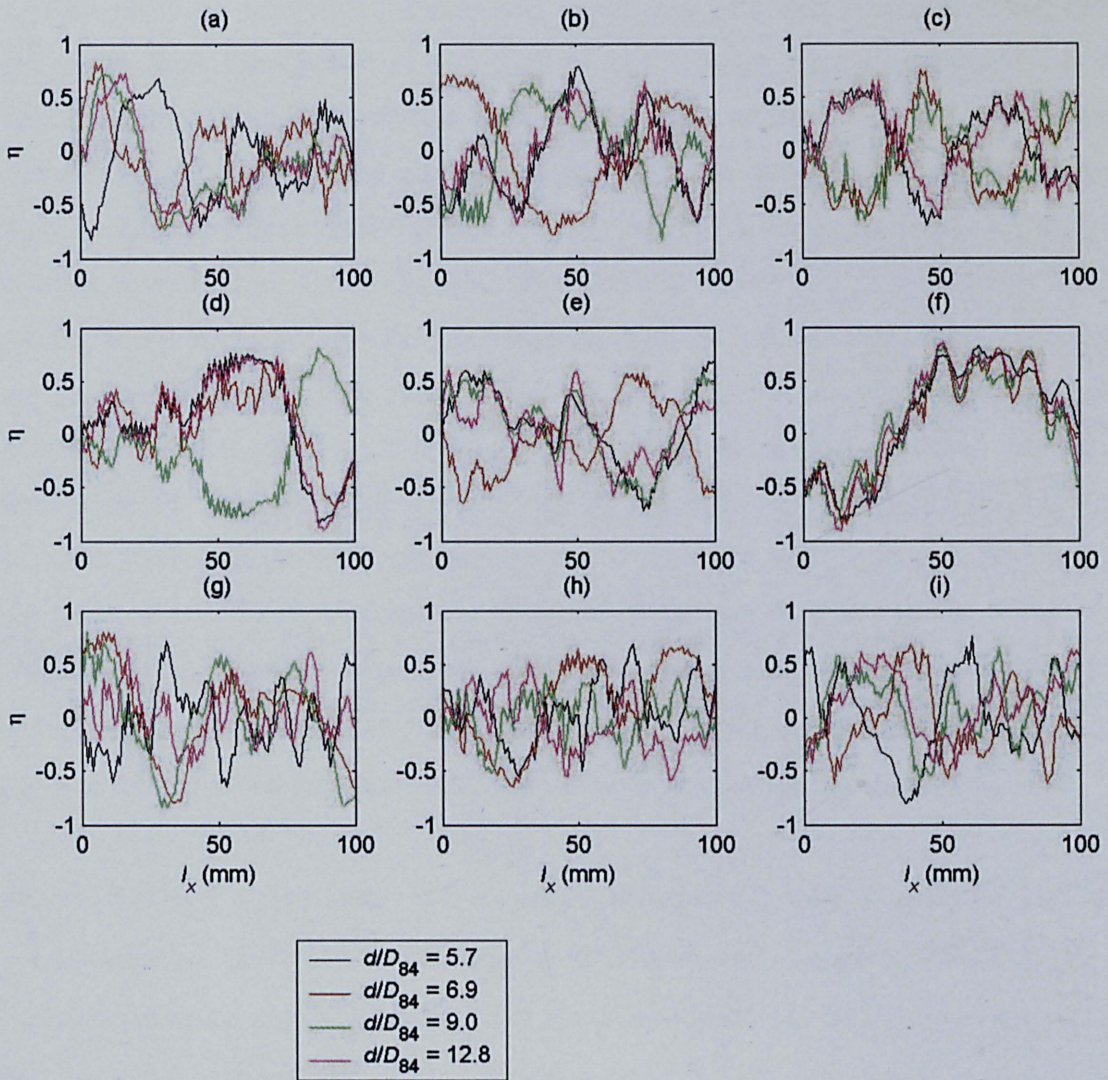


Figure 5.33. The coefficient of cross-correlation η between \tilde{w}/u_* and bed surface elevation at $z/D_{84} = 4.03$ for the experimental runs carried out at a single bed slope over the bimodal bed at lateral positions of (a) -87 mm; (b) -65 mm; (c) -43 mm; (d) -21 mm; (e) 0 mm; (f) 23 mm; (g); 45 mm; (h) 67 mm; and (i) 89 mm, where \tilde{w} is the spatial deviation in time-averaged vertical velocity, u_* is the bed shear velocity, z is the height above the maximum bed elevation, D_{84} is the grain size at which 84 per cent of the bed material is finer, l_x is the streamwise lag between bed surface elevation and \tilde{w}/u_* , and d is flow depth.

However, because of the low spatial resolution of velocity measurements within the reach and the low number of bed roughness measurements on which to relate these measurements of velocity to, their conclusions may not well supported. Only five streamwise lags were possible, with each having a metre separation between them. Therefore, the effects of bed roughness on the flow could only be very coarsely determined. Furthermore, the correlation was based on averaging \bar{w} measurements taken within a vertical profile at one location to give a single value of \bar{w} for that location over the bed. Often this was based on only one or two measurements in the profile, and it is unclear, at each location, how many \bar{w} values were averaged and the measurement height of these averaged values. The measurement height would heavily influence the averaged value. This may become clearer in the final published version of their study. Furthermore, measurements were not possible very close to the bed because of errors arising in the ADV measurements and problems with accurately positioning the probe. It is difficult to assess the effect of relative submergence on the strength of the association between \bar{w}/u_* and d/k_s from only three discharges, and they acknowledge that at the mid discharge the flow patterns could not be well-defined because several of the measurements were discarded due to poor quality.

Legleiter *et al.* (in press) state that an erratic change in η with l_x indicates that the spatial structure in \bar{w} is not well-developed. This erratic change was observed over both the unimodal and bimodal beds, but the contour plots of \tilde{w}/u_* showed the spatial structure of \bar{w} was well-developed. They also report, which appears to be contradictory to their previous statement, this kind of change indicates a very localised interaction between \bar{w} and individual clasts. This is unlikely to be the case here given the streamwise length of the zones of upward and downward moving fluid. Instead, the periodicity in the change in η with l_x must be either a consequence of some systematic relationship between \tilde{w}/u_* and z_b , or a consequence of particular anomalous values (\tilde{w}/u_* or z_b) that drop into and out of the correlated sample. In this latter sense, a scatter plot between \tilde{w}/u_* and z_b can be dominated by a random cloud of points, but a single outlier in either the top or bottom right of the plot can give a high η value. An examination of the scatter plots for the streamwise lags at which the peak η value occurred revealed that this is not the case, and therefore that the periodicity must be explained by a systematic relationship between \tilde{w}/u_* and z_b . There is no noticeable

periodicity in the bed surface elevation profiles (Figure 5.16 and 5.17) so it might be that the alternating nature of the zones of upward and downward moving fluid can account for some of the periodicity in the change in η with l_x . Despite this, the η values still demonstrate that there is no strong and simple relationship between \tilde{w}/u_* and z_b . However, it is important to note that a low η value does not necessarily mean that there is no correlation at all. The results do not rule out any subtle or more complicated association between \tilde{w}/u_* and z_b , such as a high non-linear correlation, or a relationship between \tilde{w}/u_* and any spatially coherent bed features.

The conclusion that \tilde{w}/u_* and z_b are only reasonably well associated is not surprising given that the DEMs (Figure 3.9) and the structure function plots (Figures 3.15 and 3.16) indicated that the beds were organised in a different manner, yet there is a degree of similarity in the patterns of spatial deviations between the two beds. It may be that this kind of organisation of the time-averaged flow field is an inherent feature or instability of turbulent flows over water-worked gravel beds, as was found for $\bar{u}/\langle\bar{u}\rangle$ in Chapter 4. Given that the spatial pattern is modified by relative submergence, which is known to modify the flow, this further suggests it is an inherent feature of the flow.

This spatial pattern displays a similarity to the spatial structure observed for turbulent, instantaneous flow fields. Over recent years, many studies have reported on the existence of vortically-based, large-scale flow structures over water-worked gravel surfaces. The generally accepted model for these structures has at its foundation the presence of cyclic and alternating patterns of large regions of faster and slower moving wedges of fluid, which occupy a large portion of the flow depth and extend into the outer layer of the flow (Kirkbride and Ferguson, 1995; Ferguson *et al.*, 1996; Buffin-Bélanger *et al.*, 2000; Schvidchenko and Pender, 2001; Roy *et al.*, 2004). They are also known to be a persistent and dominant feature of flows over smooth and other rough boundaries, both in water (Favre *et al.*, 1957; Pratury and Brodkey, 1978; Nakagawa and Nezu 1981, Tamburrino and Gulliver, 1999; Liu *et al.*, 2001) and in air (e.g. Blackwelder and Kovasznay, 1972; Falco, 1977; Brown and Thomas, 1977). This spatial structure of alternating high-speed and low-speed regions consists of quasi-cyclic ‘bursting’ events, in which there is an upwelling of high-speed fluid away from the bed (an ejection), followed by an inrush of slow moving fluid toward the bed surface (a sweep). This alternating pattern of upward and downward moving fluid is

very similar to the patterns observed in the distribution of the spatial deviations in \bar{w} over the bed. Further information on large-scale flow structures and the mechanism of their formation can be found in Shvidchenko and Pender (2001) and Roy *et al.* (2004).

A further similarity is the way in which the turbulent structures and the pattern in the spatial deviations are influenced by flow depth. Studies have found that large-scale flow structures over both smooth and rough boundaries typically have a streamwise length of 2-5 d , and a lateral width of 0.5-2 d (Nakagawa and Nezu, 1981; Komori *et al.*, 1989; Yalin, 1992; Shvidchenko and Pender, 2001; Roy *et al.*, 2004). This results in the upward and downward regions increasing in streamwise length with increases in flow depth. This was also seen in the spatial pattern of \tilde{w}/u_* . Roy *et al.* (2004) reviewed previous studies on large-scale flow structures and reported that the astonishing feature of large-scale flow structures is the similarity in their scaling with flow depth, irrespective of wall roughness condition. The vertical nature of the spatial patterns in the spatial deviations in \bar{w} were better scaled at the same z/D_{84} rather than at the same z/d , but there were still large differences in the spatial pattern between the lower and higher relative submergences, in particular in the streamwise lengths of the zones of upwards and downward moving fluid. It would appear, therefore, that the spatial patterns, as well as being scaled by bed roughness, were scaled by flow depth like large-scale flow structures.

The fact that large-scale flow structures have been found over boundaries of various roughness and bed configurations has led many to believe that these structures can be viewed as a self organising mechanism and universal feature of turbulent, open-channel flows. Shvidchenko and Pender (2001) found that large-scale flow structures caused the development of gravel bedforms, rather than it being induced by these bed features. The bed surface topographies of the unimodal and bimodal bed were different and yet produced a similar pattern for the spatial deviations in \bar{w} over the bed, and were largely disassociated with the bed surface elevations, which is inline with this thought.

This does not necessarily suggest that what has been observed in the pattern of the spatial deviations in \bar{w} is a result of these turbulent features. For large-scale flow structures to appear in the time-averaged flow field they must be both temporally and spatially persistent. In other words they must occur in the same location and to be large

enough in magnitude and to occur frequently enough to still appear after time averaging. For example, if the regions of upwelling and downwelling within the large-scale structures are of a similar departure from \bar{w} , then they must occur at the same location for more than 50 % of the time. Previous studies do not provide any extensive information on whether this would be possible, but it does appear to be unlikely. It has been stated that bursting motions occur randomly in space and time (e.g. Nychas *et al.*, 1973; Smith, 1996; Nikora and Smart, 1997), so it is likely that large-scale flow structures also occur randomly in space and time, as suggested by Nezu and Nakagawa (1993). Furthermore, large-scale flow structures have a relatively low frequency of occurrence, from 0.04 to 0.15 Hz (which is strongly variable) over a given area of the bed (Buffin-Bélanger *et al.*, 2000; Roy *et al.*, 2004) and only last up to a maximum of three seconds (Buffin-Bélanger *et al.*, 2000; Schvidchenko and Pender, 2001; Roy *et al.*, 2004). Assuming that the regions of upwellings and downwellings have a similar departure from $\langle \bar{w} \rangle$, for large-scale structures to occur within a flow field which was averaged over a time period of five and a half minutes, it would mean that at a maximum duration of three seconds the frequency of occurrence would have to be greater than 0.33 Hz. Or at a maximum frequency of 0.15 Hz, the structures would have to last for greater than 1111.1 seconds. Therefore, large-scale flow structures are highly unlikely to have caused the alternating zones of upward and downward moving fluid in the time-averaged flow field. Instead, it is likely that what has been observed is a different class of flow features: spatially coherent time-averaged flow structures. This class of structure was also discovered in Chapter 4 for the distribution of \bar{u} over the bed. In addition, large, outer region structures which span the majority of the turbulent boundary layer and dominate the flow when viewed on a time-averaged basis have been reported over smooth boundaries (e.g. Kovaszny *et al.*, 1970; Falco, 1977; Smith *et al.*, 1991). Furthermore, time-averaged vortical structures have also been discovered over regularly spaced roughness elements in both air (Kanda *et al.*, 2004; Lien and Yee, 2004; Coceal *et al.*, submitted) and water (Campbell, pers. comm.; Clunie, pers. comm.).

5.13 Possible Interaction Between the Pattern of Spatial Deviations and the Water Surface

One possible reason for the occurrence of this structure is the appearance of secondary currents within the flume. However, it was outlined earlier that all experimental runs

were carried out at high width/depth ratios (greater than 4) and the vertical profiles of $\langle \bar{w} \rangle$ in Chapter 3 showed that $\langle \bar{w} \rangle$ was sensibly zero throughout the flow depth. This was also the case for the vertical profiles of $\langle \bar{w} \rangle$ for each of the nine lateral locations over the bed. Furthermore, if they were caused by secondary currents, the expectation would be that the alternating zones of upward and downward fluid would be stronger at the higher submergences, because of the lower width to depth ratios. Yet the opposite was observed.

The vertical profiles of both $\sigma_{\bar{w}}$ and $\sigma_{\bar{w}}/u_*$ showed that the spatial variability in \bar{w} increased in the upper regions of the flow towards the water surface, and that in some cases it could be higher in these regions than close to the bed. This suggested that either the bed has a direct influence further up into the flow than many assume, or that the spatial variability is not entirely induced by the surface topography of the bed. The former is only likely to occur at the lower submergences and the cross-correlation between \tilde{w}/u_* and bed surface elevation showed that the latter is likely to be true. The only other boundary that can have a shearing effect on the flow, and therefore might be associated with the spatial variability in \bar{w} , is the boundary between air and water at the water surface.

Many believe that macro-turbulent structures, such as kolk-boil vortexes (e.g. Coleman, 1969; Jackson, 1976; Müller and Gyr, 1986; Nezu and Nakagawa, 1993; Babakaiff and Hickin, 1996), and large-scale flow structures (Nezu and Nakagawa, 1993; Roy *et al.*, 2004) express themselves on the water surface, often in the form of boils (circular regions of local upwelling) on the water surface. Some researchers have suggested that the generation of these surface features is due to flow separation in the lee of obstacles, such as dunes (Dyer, 1986; Müller and Gyr, 1986; Nezu and Nakagawa, 1993). However others suggest that boil generation occurs with the absence of flow separation, over beds with few or no bedforms (Jackson, 1976; Allen, 1986; Roy *et al.*, 2004), suggesting these are general features of wall shearing flows with a free surface.

For example, Kumar *et al.* (1998) have examined in detail the characteristics of the water surface over a smooth flume floor. Visualisation of the water surface indicated that persistent structures occur on the water surface and that they could be classified as upwellings, downdrafts and spiral eddies. Upwellings appeared as patches of fluid with

flow moving into the upwelling from one side and flow moving away at the opposite side, which caused the inception of rotational motion in opposite directions at the edges of the upwelling. These were termed 'splat-like' structures by Kumar *et al.* (1998) but have also been termed 'surface renewal eddies' by others (Komori *et al.*, 1989; Komori *et al.*, 1982; Rashidi *et al.*, 1991). Upwellings were shown to be related to turbulent bursts originating at the channel floor which reached the water surface, propagated with the surface for some time and then moved downward in the flow. This has also been shown by Rashidi and Banerjee (1988) and Komori *et al.* (1989), whereby they discovered that between 76 to 90 % of bursting events reach the water surface. This downward movement of a burst following the formation of the upwelling caused a downdraft of the flow and therefore a downwelling on the water surface. Spiral eddies were observed by Kumar *et al.* (1998) to be generated at the edges of the upwellings, from the development of rotational motion associated with the upwelling. In general, an upwelling was observed to generate one or more pair(s) of spiral eddies in the time it stayed at the water surface. The eddies were therefore considered to form from the upwellings and the turbulent bursting. The eddies often merged if they were rotating in the same direction, and formed pairs if they rotated in opposing directions, although these were few in number. Kumar *et al.* (1998) also measured the free-surface flow field using PIV. They examined the spatial distribution of the gradient in instantaneous vertical velocity (dw/dy), where y is the lateral dimension, and how this related to synchronised visualisation of upwellings and downwellings on the water surface. They discovered that upwellings were characterised by positive dw/dy , and downwellings with negative dw/dy . Also by visualising the flow in a vertical plane they demonstrated that bursting motions caused upwellings on the water surface, and these upwellings consequently formed spiral eddies and downwellings. It appears, therefore, that there is an important association between the turbulent flow structures and the features on the water surface. Although the patterns in the spatial deviations of \bar{w} are not turbulent structures, the time-averaged patterns may be related in some way to the water surface.

Figure 5.34 shows images of water surfaces for experimental runs 2U and 6U over the unimodal bed. These are representative of the range of the water surfaces that were seen over the two beds. The flow direction is towards the reader. At the lower relative submergence the photograph shows that superimposed on to a relatively 'flat' water surface are many small, circular upwellings that are elongated in the lateral direction. In the wake of these features are often downwellings in the water surface (Figure 5.34a).

These upwellings and downwellings occurred over the whole width and length of the flume, and resemble the features described by Kumar *et al.* (1998). At the higher relative submergence, the water surface is much rougher in appearance and is dominated by a smaller number of much larger, laterally elongated upwellings (Figure 5.34b). It is interesting that they are laterally orientated rather than elongated in the streamwise direction due to the streamwise direction of the flow. It is thought that this occurs because the water surface causes a reduction in the vertical component of the turbulent kinetic energy and its energy is redistributed laterally (Komori *et al.*, 1982; Brumley and Jirka, 1987; Rashidi and Banerjee, 1988). In the wake of these upwellings, are again areas of downwellings. These features resemble standing wave type features observed by Tinkler (1997). Superimposed on these waves are smaller ripples. The waves showed no visual association with the surface topography of the bed. It is likely that these changes in the water surface with relative submergence could be associated with an increase in the Froude number of the flow with relative submergence.

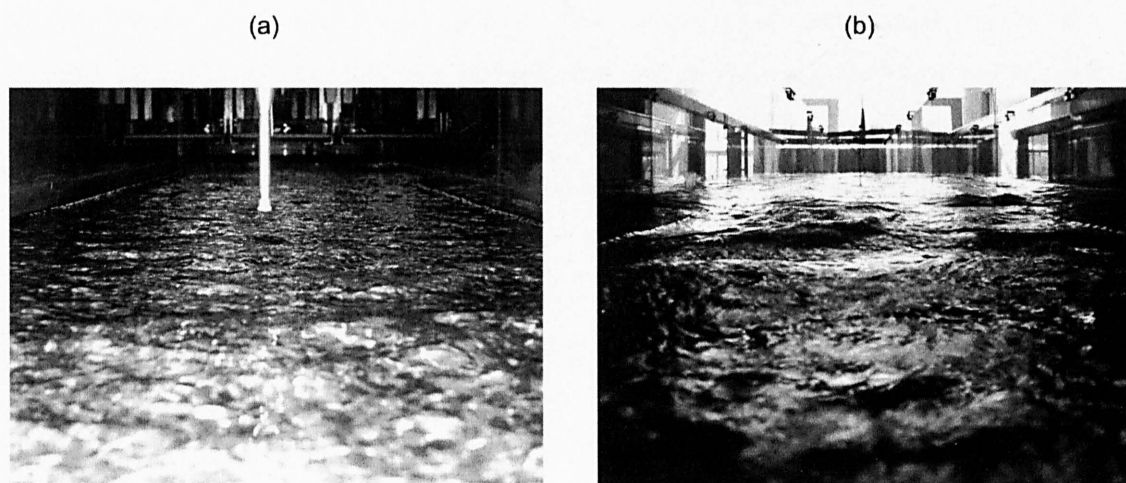


Figure 5.34. Still images of the water surface for experimental runs (a) 2U and (b) 6U over the unimodal bed. As a guide for scale, the separation between the glass walls of the flume is 0.5 m.

The water surfaces at all relative submergences were found to be well defined by these areas of upwellings and downwellings, with the wave pattern only occurring at the higher of the submergences. These water surface features appeared to be temporally persistent features and to occupy the same part of the water surface for the majority of

time. As relative submergence was reduced, the regions of upwellings and downwellings became smaller (their wavelength reduced) but their spatial frequency over the bed increased both in the streamwise and lateral direction, meaning that the surface was no longer just characterised by a small number of large upwellings or downwellings across the bed, but by many smaller undulations.

It is doubtful that the upwellings are boils, at least in their classical form. However, there are parallels between these features and boils in the manner in which they are scaled by flow depth. A number of studies have found that the mean diameter of boils is positively related to flow depth and that mean boil period is inversely related to flow depth (Jackson, 1976; Kostaschuck and Church, 1993; Babakaiff and Hickin, 1996). Furthermore, boils have also been found to have a good deal of spatial persistence (Nezu and Nakagawa, 1993).

Kumar *et al.* (1998) also discovered a very similar dependence for the water surface structure on flow depth. By examining three different flow depths, they discovered that at the lowest depth the water surface was covered by many small vortices and upwellings within a relatively flat surface, and that an increase in flow depth caused a gradual change towards a condition at the highest flow depth in which the surface was covered with noticeably larger vortices. The number of upwellings on the water surface was discovered to decrease with an increase in flow depth at a given Reynolds number. This therefore resulted in the number of spiral eddies also being higher for flows of small depths. This was discovered to be related to the number of new upwellings also decreasing with an increase in flow depth for a given Reynolds number. They also reported that the vortex size increased with increasing depth for a fixed Reynolds number. These results are all in correspondence with the visual observations made here over the two water-worked gravel beds.

More striking is the similarity in the streamwise pattern of the water surface and that of the spatial deviations in \bar{w} . There is an alternating pattern of upwellings and downwellings which could match the alternating pattern of vertical zones of upward and downward moving fluid. It is conceivable that upwellings could be caused by the movement of fluid towards the water surface and downwellings by fluid moving away from the water surface, especially given the evidence presented by Kumar *et al.* (1998). Since the zones of upward and downward moving fluid appear within the time-averaged

flow field, this would mean that the upwellings and downwellings would have to occur in the same location for the majority of the time, which visual observations confirmed could occur. The change in the water surface with relative submergence also corresponds well with the changes in the pattern of the spatial deviations in \bar{w} . The number of upwellings and vertical zones of upward moving fluid decrease with relative submergence, and their streamwise length increases with relative submergence. This also appears to occur for the downwellings and vertical zones of downward motions.

5.14 Spectral Analysis of the Dynamics of Turbulent Water Surfaces

The changes in the water surface with relative submergence need to be tested more formally, to see whether these changes do match those in the pattern of the spatial deviations in \bar{w} . This will also be carried out for the experimental runs performed at the same relative submergences and the same mean bed shear stress to see whether the correspondence between the water surface and the pattern of spatial deviations in \bar{w} also prevails under these conditions.

As part of a supplementary series of tests, an Armfield H40 conductivity wave-probe was used to measure the temporal changes in water surface elevation over the bimodal bed. This probe was constructed from two 1.5 mm diameter stainless steel wires which were aligned in parallel and separated by a distance of 12.5 mm. The wires were 300 mm in length and were partly submerged within the water column. The electrical conductivity between the two wires was measured, and this was linearly proportional to their depth of immersion, enabling the water surface elevation at a point over the bed to be determined. This method was free of meniscus and ‘wetting’ effects. The probe was positioned on the centreline of the flume within the centre of the PIV measurement area. The readings were recorded with an acquisition unit with a buffer capacity of 4000 recordings. There are no studies that provide information on the likely range of water elevation frequencies so recordings were performed at 100 Hz to ensure that a suitable range was captured. Given the buffer capacity, recordings could only be made for 40 seconds. This was carried out four times for each of the 11 experimental runs over the bimodal bed.

To examine the differences in the dynamics of the water surface between the experimental runs, the power spectral densities were calculated. For a signal of

frequency f the power spectral density of the signal $P_{z_w}(f)$ is mathematically related to its correlation sequence R_{z_w} by the discrete-time Fourier transform. It gives the power per unit frequency carried by a wave. In terms of normalised frequency f/f_s , where f_s is the sampling frequency, $P_{z_w}(f)$ is given by

$$P_{z_w}(f) = \frac{1}{f_s} \sum_{m=-\infty}^{\infty} R_{z_w}(l_t) e^{-2\pi i f m / f_s} \quad (5.13)$$

where $R_{z_w}(l_t) = \overline{z_w(t) \cdot z_w(t + l_t)}$ and l_t is a time lag. The one-sided Welch method was used for calculating $P_{z_w}(f)$. This method consists of dividing the time series data into overlapping segments, computing a periodogram (power spectrum) for each segment, and then averaging the power spectral density estimates from the periodogram over the frequency components of each segment. The time series was divided into eight segments of equal length with 50 % overlap. The use of 8 periodograms decreases the variance of $P_{z_w}(f)$ relative to using a single periodogram of the entire time series to compute $P_{z_w}(f)$. A Hanning window was used to compute the periodogram of each segment. The overlap between segments introduces redundant information, and this effect was diminished by the use of a non-rectangular window, which reduced the importance or weight given to the end samples of the segments (the samples that overlap). However, the combined use of short data records and nonrectangular windows results in reduced resolution for $P_{z_w}(f)$. There is a balance between variance reduction and resolution. The $P_{z_w}(f)$ values from each of the four samples were averaged to give $\overline{P_s}(f)$.

5.14.1 Variability with Relative Submergence

The power spectra of the water surface elevations for the five experimental runs carried out a single bed slope are shown in Figure 5.35. They show that the majority of the energy in the water surface is carried by low frequency, large-scale features on the water surface. The spectra do not display any significant peaks, so it appears that the voltage signals were not affected by electronic noise. There is a decrease in $\overline{P_s}$ with frequency, showing that the amount of energy that is carried decreases with the size of

the water surface features. The nature of this change in \bar{P}_s is very similar for all five experimental runs. From a frequency of 0.7 to nearly 1.4 Hz there is constant gradient of linear decrease for all the runs. This gradient then increases, and again is linear and constant up to 4 or 5 Hz. At higher frequencies, there is a further constant and higher gradient decrease up to just over 8 Hz. At higher frequencies there are then sharper fluctuations in \bar{P}_s . Energy is only carried by frequencies up to 20 Hz showing that a sampling frequency of 100 Hz was sufficient.

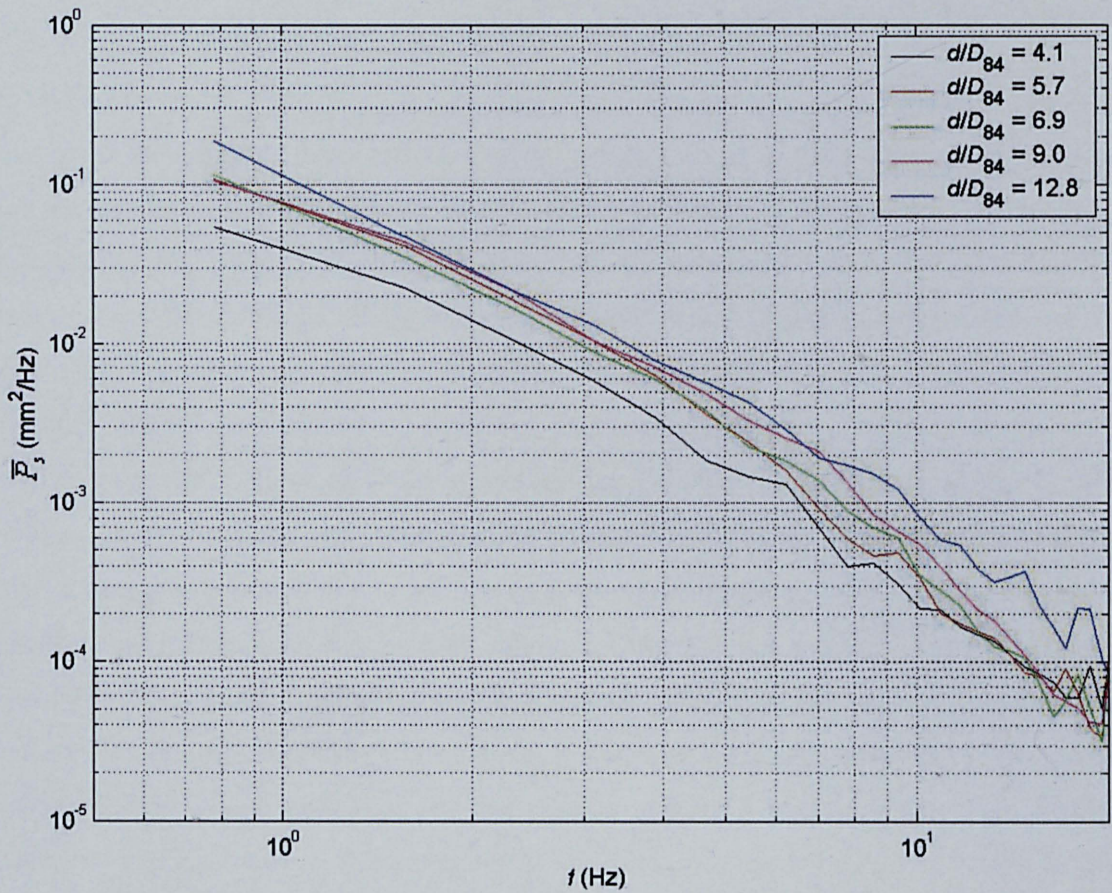


Figure 5.35. Power spectrum of the water surface elevations, shown in terms of the variation in power spectral density \bar{P}_s with the temporal frequency of variation f for the experimental runs carried out at a single bed slope over the bimodal bed, where d is flow depth and D_{84} is the grain size at which 84 per cent of the bed material is finer.

The change in the gradient of the decrease in \bar{P}_s with frequency and the sharp fluctuations at high frequencies resembles the power spectra of turbulent fluctuations in

velocity. It shows that there is an energy cascade related to the water surface variations. It suggests that the large-scale features of the water surface carry much of the energy within the water surface. If these features break down, its energy is transferred to smaller water surface features in a cascade of energy. If the large-scale features coalesce, the energy transfers to the larger-scale features. Energy is transferred from the mean water surface by means of strong interactions among large-scale features. Therefore coherent features contain most of the energy. This implies that coherent water surface features may be present, as suggested earlier, and therefore could be associated with the alternating vertical zones of upward and downward moving fluid.

The different gradients in \bar{P}_s suggest that there is a subdivision in the water surface spectra. For velocity spectra, a three-range model is considered to be present, which is related to the regions where different rates of decay occur in the spectra. It consists of (1) the production range; (2) the inertial subrange (there is no energy production or dissipation; the turbulence energy flows from larger scales to smaller ones until it reaches the viscous range where dissipation occurs); and (3) the viscous range, where spectra decay much faster than in the inertial subrange. Recently, it has been suggested that this should be replaced by a model that consists of four ranges of scales with different spectral behaviour (Nikora and Goring, 2000): (1) The range of the largest eddies, where turbulent energy production occurs; (2) the range of intermediate eddies, where energy production and cascade energy transfer coexist; (3) the range of relatively small eddies, known as the inertial subrange; and (4) the viscous range where the spectra decay rapidly. Visually the water surface spectra appear to have a four-range subdivision but this needs to be confirmed. If a similar subdivision occurs for the power spectra for the water surface as for the velocity spectra it could indicate that there is some association between the water surface features and the turbulent structure within the flow.

This was examined by carrying out a linear least-squares fit to the variation in $\log(\bar{P}_s)$ with $\log(f)$ of the form

$$\log(\bar{P}_s) = a \log(f) + b \quad (5.14)$$

for progressively higher values of $\log(f)$ until a break in gradient was identified at which the fit was ceased. This break of gradient was defined as occurring at $\log(f_i)$ when $|a_i - a_{i-1}| > |0.01a_{i-1}|$. The values of a_1 and b_1 from equation (5.14) for spectral range (1) were derived for the fit up to $\log(f_{i-1})$. The upper frequency of the range was assumed to occur midway between $\log(f_i)$ and $\log(f_{i-1})$. A linear least-squares fit to the variation in $\log(\bar{P}_s)$ with $\log(f)$ of the form of equation (5.14) was then used for progressively higher values of $\log(f)$ which included and were higher than $\log(f_i)$, until a break of gradient was again identified. Values of a_2 and b_2 could then be produced for spectral range (2). This was repeated again up until the value of $\log(f)$ at which an erratic change in $\log(\bar{P}_s)$ with $\log(f)$ occurred. Above this $\log(f)$ no attempt was made to identify breaks of gradient because of this erratic change, and a linear fit was performed. Analysing the spectra in such a manner identifies the number of ranges in the scaling of water surface elevation spectra. Given that $\langle \bar{u} \rangle$ is known for close to the water surface, the length scales can be assigned to each spectral range.

It was discovered that for each experimental run the water surface spectra indeed have four ranges of scaling. It would therefore appear that the water surface may have some association with the turbulent flow structure beneath. An example of a four-range subdivision of the spectra is seen in Figure 5.36. Figures 5.37a and b show how the upper length scale and the range of length scales, of each of the four spectral ranges changes with relative submergence, respectively. There is a clear increase in both the upper limit and the range of the four ranges with relative submergence. This corresponds with the increase in mean velocity (Table 5.3), and is inline with the increase in streamwise length of the zones of upward and downward moving fluid that was observed within the spatial pattern of \tilde{w}/u_* with relative submergence (Figure 5.19).

It can be seen in Figure 5.35 that there is a clear reduction in the total spectral energy contained within the water surface with a decrease in relative submergence. This is related to lower water surface velocities. There are subtle differences in the gradients of \bar{P}_s in these log-log plots between the experimental runs, and it is these rates of decrease in \bar{P}_s that influence the degree of energy cascade. The change in these gradients with relative submergence can be seen by examining the variation in a in

equation (5.14) for each of the four spectral ranges (Figure 5.37c). It shows that spectral range (2) approximately follows the Kolmogorov $-5/3$ power law, which is known to hold for velocity spectra in this same spectral range. Kumar *et al.* (1998) have also shown that the Kolmogorov $-5/3$ power law holds for water surface velocity spectra. Range (1) in Figure 5.37c has an exponent close to -1 , which has also been found to occur in the first spectral range for velocity fluctuations (Nezu and Nakagawa, 1993; Nikora and Goring, 2000). At ranges (3) and (4) several of the experimental runs have spectra that have a slope of approximately -3 . This was also found by Kumar *et al.* (1998) for higher frequencies of water surface velocities and for internal velocity spectra by Kraichnan (1967) and Batchelor (1969). This suggests that the water surface features are likely to have some association with the turbulent properties of the flow. If this is assumed to be the case it would reveal that range (2) in the water surface spectra is equivalent to the inertial subrange for velocity spectra. Kumar *et al.* (1998) suggest that upwellings may be associated with the transition between the $-5/3$ and -3 spectral ranges. Therefore for the wave surface spectra, the upwellings may be approximately associated with the transition from spectral range (2) to range (3). The length scale of this transition, which is equal to the upper length scale of range (2), is shown to consistently increase with relative submergence in Figure 5.37a, suggesting that the size of the upwellings also increase with relative submergence. This corresponds with the results of Kumar *et al.* (1998).

The results in Figure 5.37c also show that for each of the ranges the rate of decrease in \bar{P}_s with f in general increases with relative submergence. It means that an increase in relative submergence causes a greater degree of energy cascade from the low frequency, large-scale features to the high frequency, small-scale features. Assuming that the energy carried by a given frequency is proportional to the frequency of its occurrence in the time series, it implies that small water surface features are relatively more prevalent at lower submergences and, large-scale features are relatively more prevalent at the higher submergences. This is in accordance with the visual observations of the water surface and the results of Kumar *et al.* (1998). These changes suggest that if there is a relationship between the water surface and the patterns in the spatial deviations in \bar{w} then there would be a larger number of small vertical zones of upward and downward moving fluid at the low submergences, but fewer, large zones at the higher submergences. This was indeed observed for the spatial patterns of \tilde{w}/u_* in Figure 5.19.

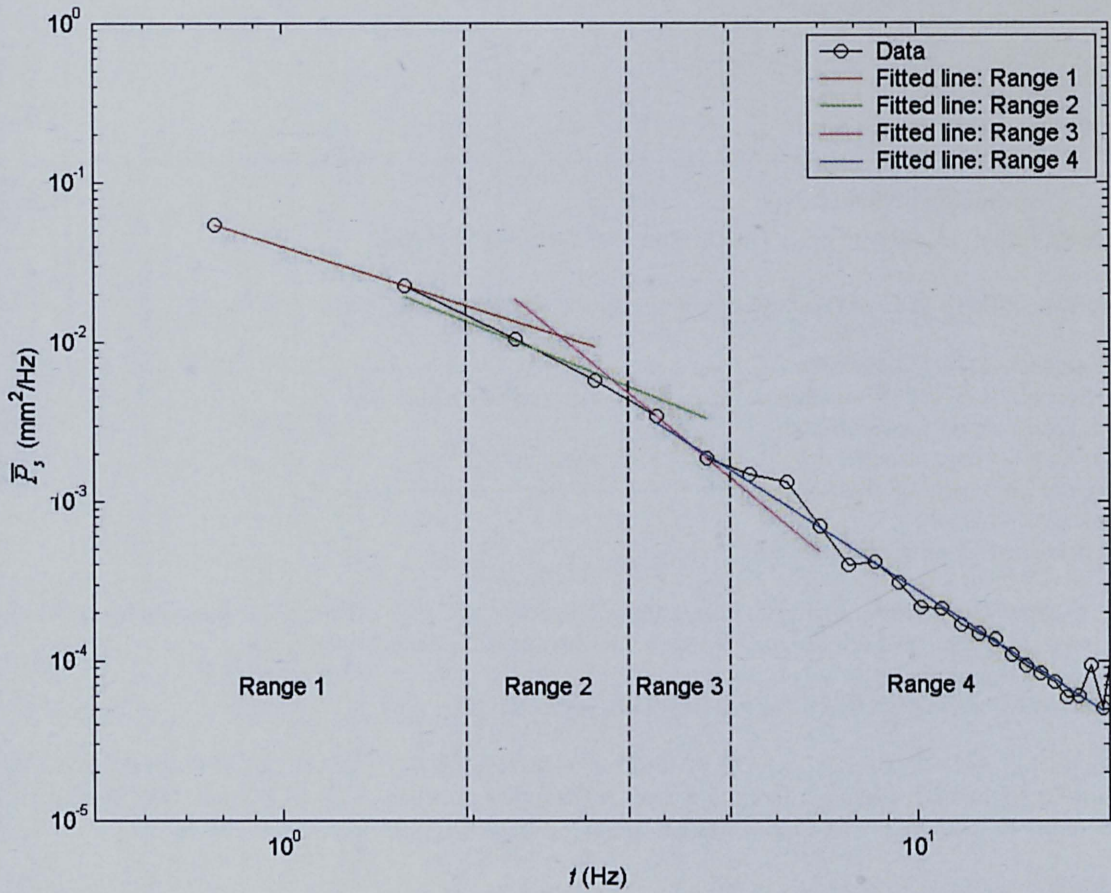


Figure 5.36. Subdivision of the power spectrum of water surface elevations into four spectral ranges according to breaks in the gradients of linear least-square fits to the variation in power spectral density \bar{P}_s with the temporal frequency of variation f for experimental run 2B. The length of the fitted lines for each range has been extended to more clearly display the changes in gradient.

The difference in \bar{P}_s between the experimental runs is, on the whole, largest at the higher frequencies, with many experimental runs having similar values at frequencies between around 0.7 to 4 Hz, for all but the run carried out the lowest relative submergence. This is further confirmed by the gradient of decrease in \bar{P}_s displaying greater variation between the runs at spectral ranges (3) and (4) (Figure 5.37c). It suggests that the largest difference in the water surfaces is related to the coverage of small-scale features.

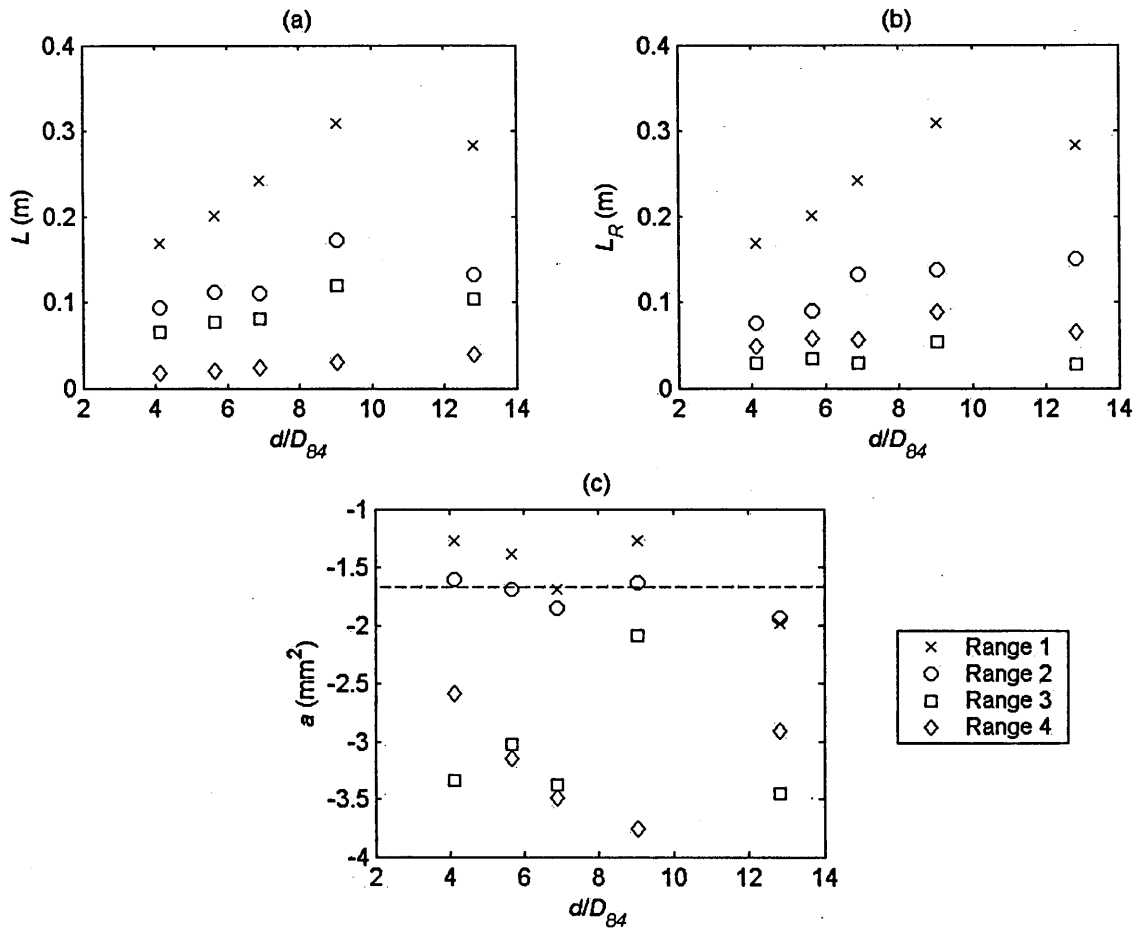


Figure 5.37. The change in (a) the upper length scale L ; (b) the range of length scales L_R ; and (c) the gradient of the linear least-squares fit a of each of the four spectral ranges for the power spectrum of water surface elevations with relative submergence for the experimental runs carried out at a single bed slope over the bimodal bed, where x is the spectral range, d is flow depth and D_{84} is the grain size at which 84 per cent of the bed material is finer. The dashed line indicates where $a = -5/3 \text{ mm}^2$.

5.14.2 Variability with Bed Slope

The change in the power spectra with bed slope for the experimental runs performed at the same relative submergences are shown in Figure 5.38. There is a similar pattern to the change in \bar{P}_s with frequency that was seen at a single bed slope, with it again being consistent across the experimental runs. The spectra show that the total spectral energy is clearly lower at the shallower slopes, related to the slightly lower mean velocities at

these slopes. It means that the difference in spectral energy decreases with a reduction in the difference in bed slope between runs.

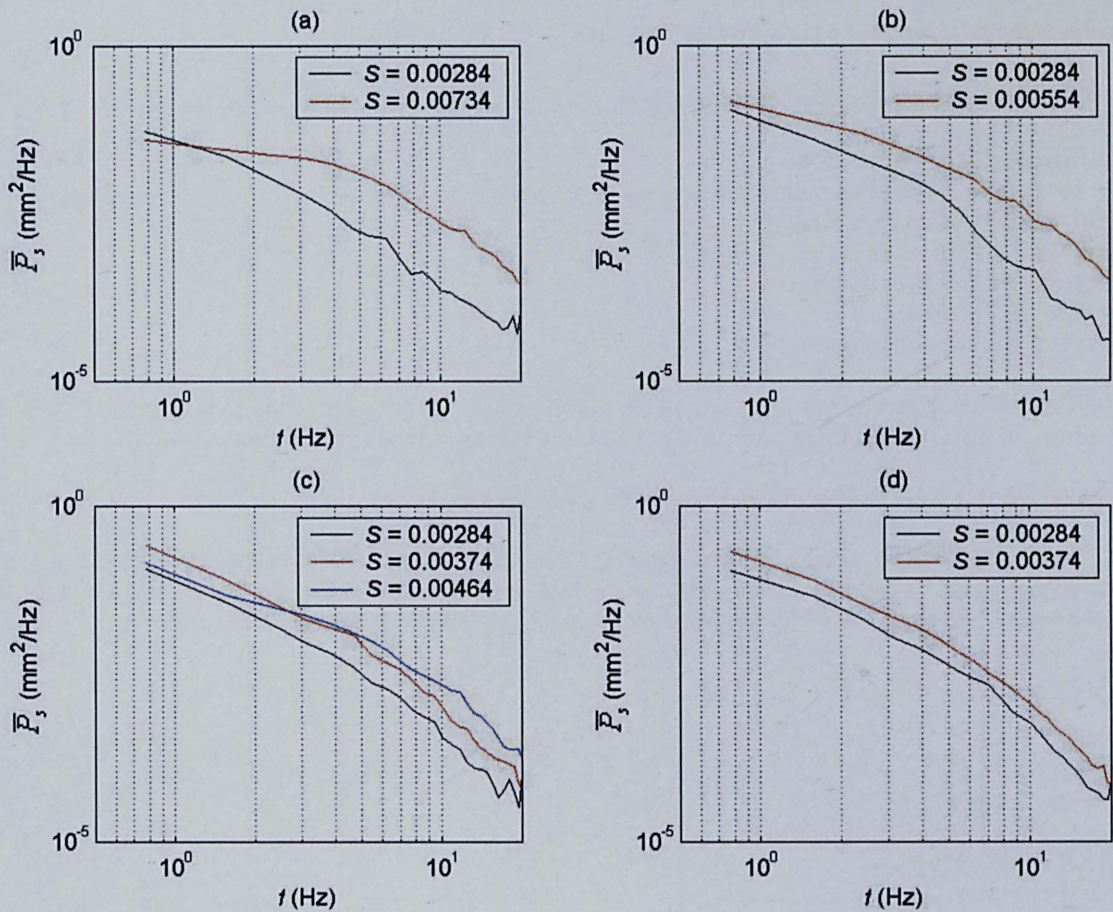


Figure 5.38. Power spectrum of the water surface elevations, shown in terms of the variation in power spectral density \bar{P}_s with the temporal frequency of variation f for the experimental runs carried out at the same relative submergences over the bimodal bed (a) $d/D_{84} = 4.1$; (b) $d/D_{84} = 5.7$; (c) $d/D_{84} = 6.9$; and (d) $d/D_{84} = 9.0$, where d is flow depth and D_{84} is the grain size at which 84 per cent of the bed material is finer.

The water surface elevation spectra are once again subdivided into four spectral ranges. Figures 5.39 and 5.40 show the upper length scale, and the range of length scales, of each of the four spectral ranges, and how this changes with bed slope, respectively. An increase in bed slope causes both to increase, which once again corresponds with an increase in mean velocity with bed slope at a given relative submergence (Table 5.5). This demonstrates that the size of the upwellings increase with bed slope. This increase

in length scales again corresponds with the general trend for the zones of upward and downward moving fluid to become longer with an increase in bed slope (Figures 5.22 and 5.23).

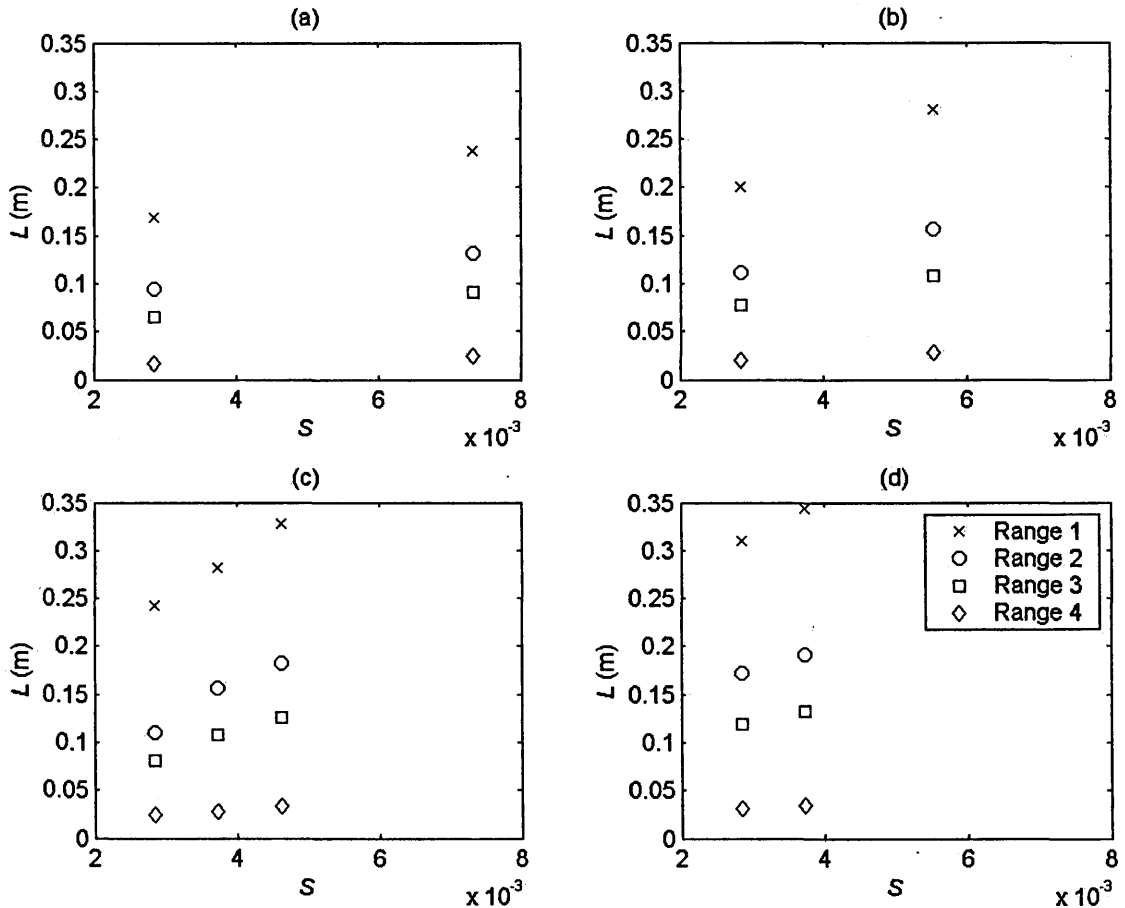


Figure 5.39. The change in the upper length scale L of each of the four spectral ranges for the power spectrum of water surface elevations with bed slope S for the experimental runs carried out at the same relative submergences over the bimodal bed (a) $d/D_{84} = 4.1$; (b) $d/D_{84} = 5.7$; (c) $d/D_{84} = 6.9$; and (d) $d/D_{84} = 9.0$, where d is flow depth and D_{84} is the grain size at which 84 per cent of the bed material is finer.

The exponents of the fitted lines to the change in \bar{P}_s with frequency for the four spectral ranges are shown in Figure 5.41. There are much clearer differences in the gradient of the decrease in \bar{P}_s with increasing frequency, when the difference in bed slope is large. The rate of decrease in \bar{P}_s is typically higher at the lower bed slopes across all four

spectral ranges, indicating that there is a greater degree of cascading of spectral energy at these slopes. It means that relatively more of the energy is carried by low frequency, large-scale features and relatively less energy is carried by high frequency, small-scale features at steeper slopes in comparison to shallower slopes.

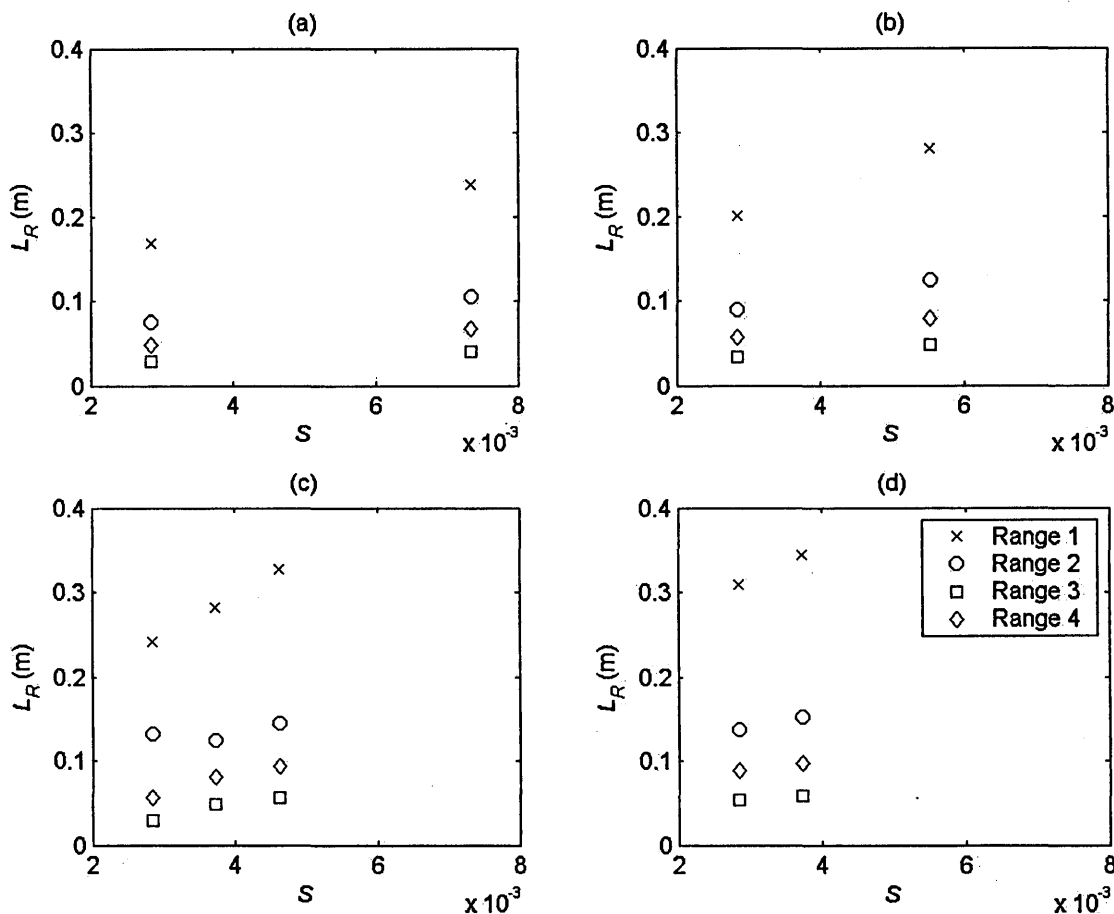


Figure 5.40. The change in the range of length scales L_R for each of the four spectral ranges of the power spectrum of water surface elevations with bed slope S for the experimental runs carried out at the same relative submergences over the bimodal bed (a) $d/D_{84} = 4.1$; (b) $d/D_{84} = 5.7$; (c) $d/D_{84} = 6.9$; and (d) $d/D_{84} = 9.0$, where x is the spectral range, d is flow depth and D_{84} is the grain size at which 84 per cent of the bed material is finer.

These changes suggest that, if there is a relationship between the water surface and the patterns in the spatial deviations in \bar{w} , there would be a larger number of small vertical zones of upward and downward moving fluid at the low bed slopes, but fewer, large

zones at the steeper slopes. Although the change in the spatial patterns of \tilde{w}/u_* in Figures 5.22 and 5.23 were far from consistent, there was general trend towards such a change. This further implies that there is some association between the water surface and the patterns in the spatial deviations in \bar{w} . The difference in \bar{P}_s between the experimental runs is again, on the whole, largest at the higher frequencies.

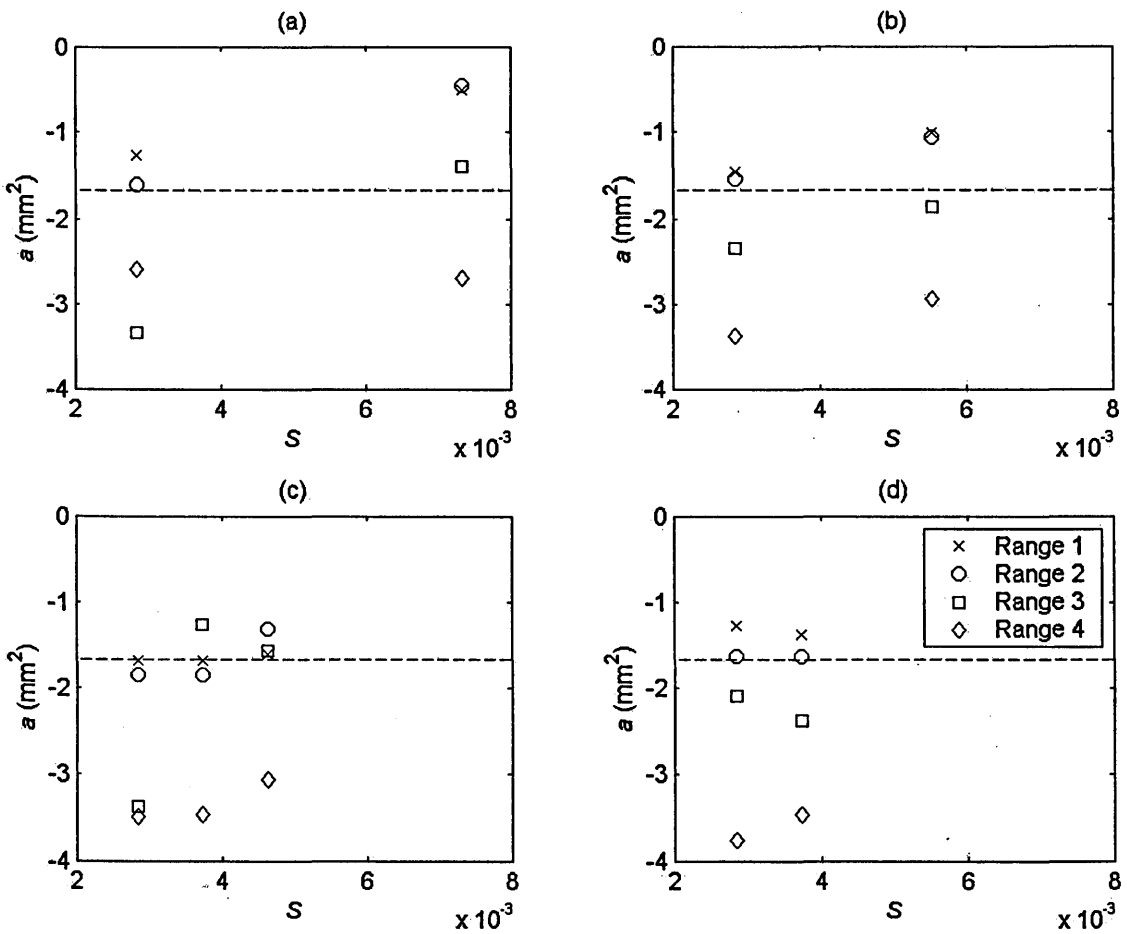


Figure 5.41. The change in the gradient of the linear least-squares fit a of each of the four spectral ranges for the power spectrum of water surface elevations with bed slope S for the experimental runs carried out at the same relative submergences over the bimodal bed (a) $d/D_{84} = 4.1$; (b) $d/D_{84} = 5.7$; (c) $d/D_{84} = 6.9$; and (d) $d/D_{84} = 9.0$, where x is the spectral range, d is flow depth and D_{84} is the grain size at which 84 per cent of the bed material is finer. The dashed line indicates where $a = -5/3$ mm^2 .

5.14.3 Variability Under Conditions of Constant Bed Shear Stress

The power spectra of the water surface elevations for the experimental runs carried at the same mean bed shear stress are shown in Figure 5.42. It can be seen that there is greater variability in the pattern of change in \bar{P}_s with frequency, than has been seen before. It suggests that u_* does not produce a good scaling of the power spectra.

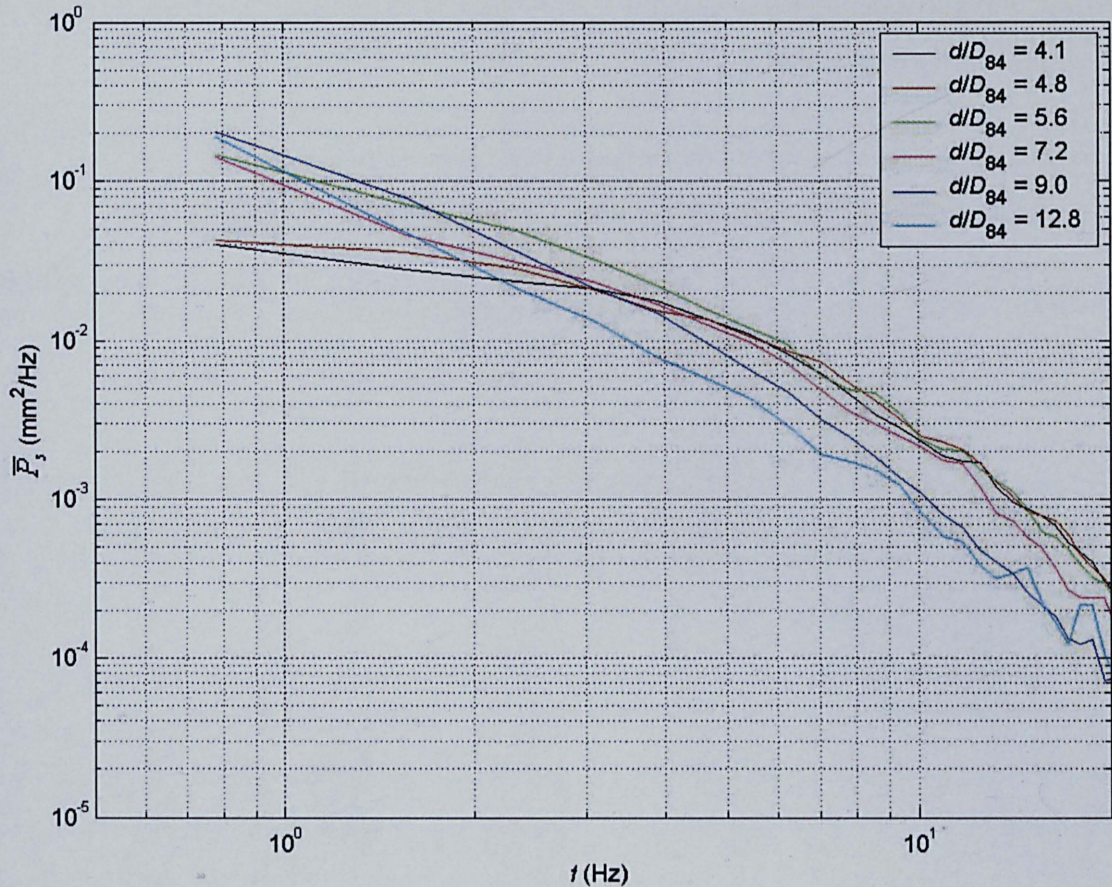


Figure 5.42. Power spectrum of the water surface elevations, shown in terms of the variation in power spectral density \bar{P}_s with the temporal frequency of variation f for the experimental runs carried out at the same mean bed shear stress over the bimodal bed, d is flow depth and D_{84} is the grain size at which 84 per cent of the bed material is finer.

The upper length scales, and the range of length scales, of each of the four ranges is shown in Figures 5.43a and b, respectively. There is once again a clear increase in both with relative submergence, and therefore a decrease in bed slope. This is again related to

changes in mean velocity (Table 5.7). Of particular relevance is that the upper length scale of spectral range (2), which is at the transition from spectral range (2) to range (3), increases with relative submergence, suggesting that the size of the upwellings also increase with relative submergence. This corresponds with the results of Kumar *et al.* (1998) and the results found at a single bed slope.

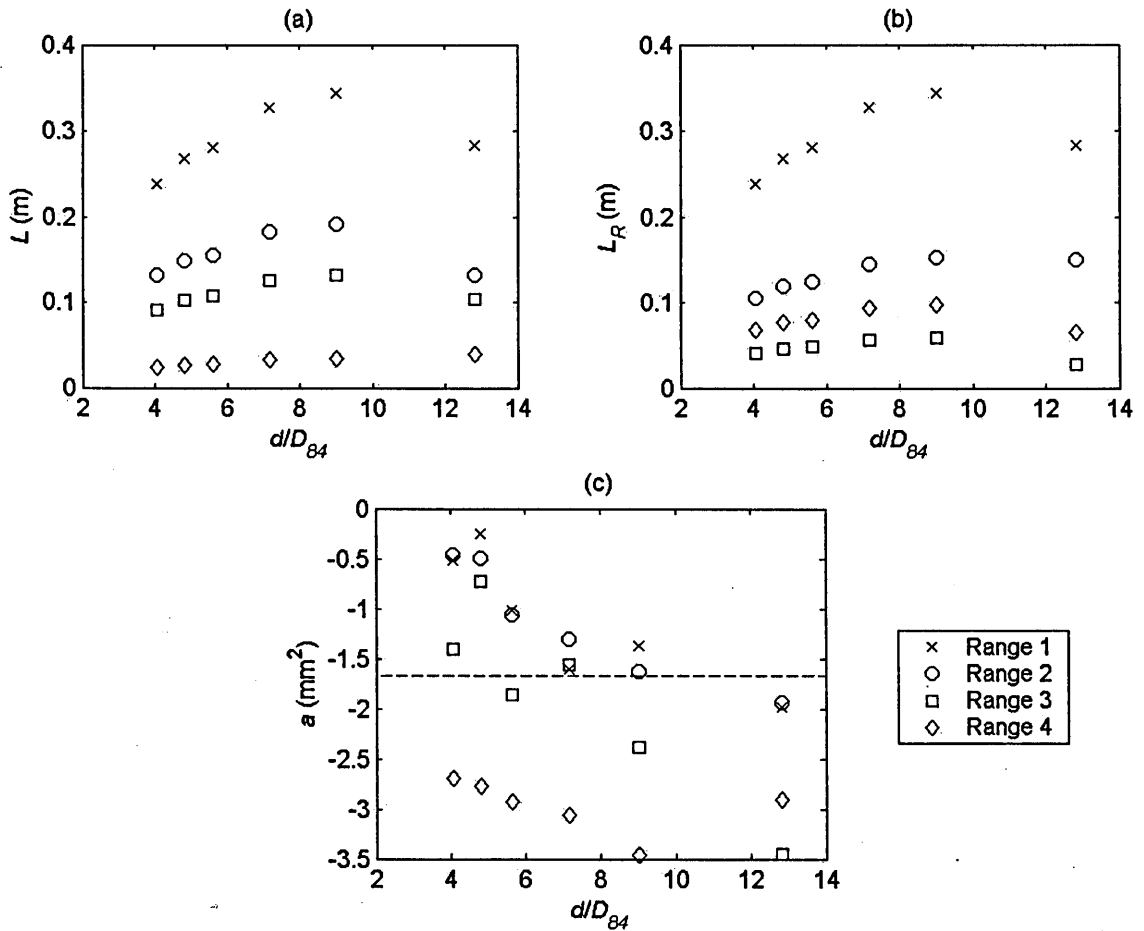


Figure 5.43. The change in (a) the upper length scale L ; (b) the range of length scales L_R ; and (c) the gradient of the linear least-squares fit a of each of the four spectral ranges for the power spectrum of water surface elevations with relative submergence for the experimental runs carried out at the same mean bed shear stress over the bimodal bed, where x is the spectral range, d is flow depth and D_{84} is the grain size at which 84 per cent of the bed material is finer. The dashed line indicates where $a = -5/3 \text{ mm}^2$.

There is also a general increase in the fitted gradients of \overline{P}_s for each of the four ranges with increasing relative submergence and decreasing bed slope (Figure 5.43c). This relationship with relative submergence and bed slope is the same as that seen at a single bed slope and for the experimental runs performed at the same relative submergences. A decrease in relative submergence and an increase in bed slope progressively cause relatively more of the energy to be carried by low frequency, large-scale features and relatively less energy to be carried by high frequency, small-scale features. There is a greater degree of cascading of energy at the higher relative submergences and shallower slopes. It implies that small-scale water surface features are relatively more prevalent at higher submergences and shallower slopes and, large-scale features are relatively more prevalent at the lower submergences and steeper slopes. This again corresponds with the changes in the spatial patterns of \tilde{w}/u_* in Figure 5.25, in which the flow was covered by larger vertical zones of upward and downward moving fluid at the lower submergences and steeper slopes. Clearly the dynamics of the water surface can be different even when the degree of shearing on the flow is the same.

It has been shown that the changes in the dynamics of the water surface with relative submergence and bed slope within the three experimental phases correspond with the changes observed in the spatial pattern of deviations in \overline{w} within the flow. Furthermore, the power spectra of the water surface elevations displayed a four range subdivision, and had similar gradients of decrease with increasing frequency, as that discovered for velocity spectra. Also Kumar *et al.* (1998) have shown that the $-5/3$ and -3 power laws hold for water surface velocities. This suggests that the water surface features are likely to have some association with the turbulent properties of the flow. If this is the case, the correlation should persist throughout a time interval, and therefore the time-averaged characteristics of the water surface could also be correlated with the time-averaged flow field. This could imply that there is an association between the regions of upward and downward moving fluid and the upwellings and downwellings on the water surface.

5.14.4 Scaling

The results have shown that relative submergence, bed slope and u_* do not scale the variation in the power spectra of the water surface elevations between the experimental

runs. The variation in the upper length scale of the four spectral ranges with the Reynolds number of the flow Re , the Froude number of the flow Fr and the double-averaged streamwise velocity at the height closest to the water surface $\langle \bar{u} \rangle_s$, is shown in Figure 5.44. This includes the upper length scales from all 11 experimental runs. It reveals that the length scale of all four spectral ranges increase linearly with these three variables, most consistently so with $\langle \bar{u} \rangle_s$. This is also seen for the variation in the range of length scales (Figure 5.45). The fitted gradients of \bar{P}_s also increase with Fr and $\langle \bar{u} \rangle_s$, but there is no clear change in the gradients of spectral ranges (1) and (3) with Re (Figure 5.46). This suggests that changes in the water surface are most closely associated with changes in Fr and $\langle \bar{u} \rangle_s$. The total spectral energy is generally greater at the higher Froude numbers and higher values of $\langle \bar{u} \rangle_s$, more clearly so with Froude number (Figure 5.47). The changes in the water surface with relative submergence and bed slope largely reflect the changes with Fr and $\langle \bar{u} \rangle_s$.

5.15 Potential Significance of Changes in the Water Surface

It is unclear whether the flow causes the formation of the water surface features or whether the water surface modifies the flow. The study by Kumar *et al.* (1998) showed that bursting events may cause the water surface dynamics, but this was carried out over a smooth bed. The interdependency between the water surface and the flow variables is poorly understood over rough boundaries, and the interaction is unlikely to be as simple. For example at low relative submergences, it will be difficult to isolate the effects of bed surface topography, the effects of the Froude number and the effects of bursting events on the water surface. Large grains on the bed could cause locally higher elevations in the water surface and the Froude number could influence the more temporally prominent organisation in the water surface, or the ‘average’ water surface, and this effect will be modified by the mean velocity of the flow. Overlain on this ‘average’ surface could be local and episodic water surface features that are caused by turbulent bursting. Despite this lack of understanding it is still worthwhile considering how changes in the water surface may influence flow properties over water-worked gravel beds.

It is likely to have a large influence on the vertical velocity profile within the outer region of the flow, and the thickness of this region. It should change the degree of

departure of the profile from a logarithmic profile, and this may change spatially with the spatial variability in the water surface. These effects are likely to be dependent on the Froude number and of the flow and the mean velocity.

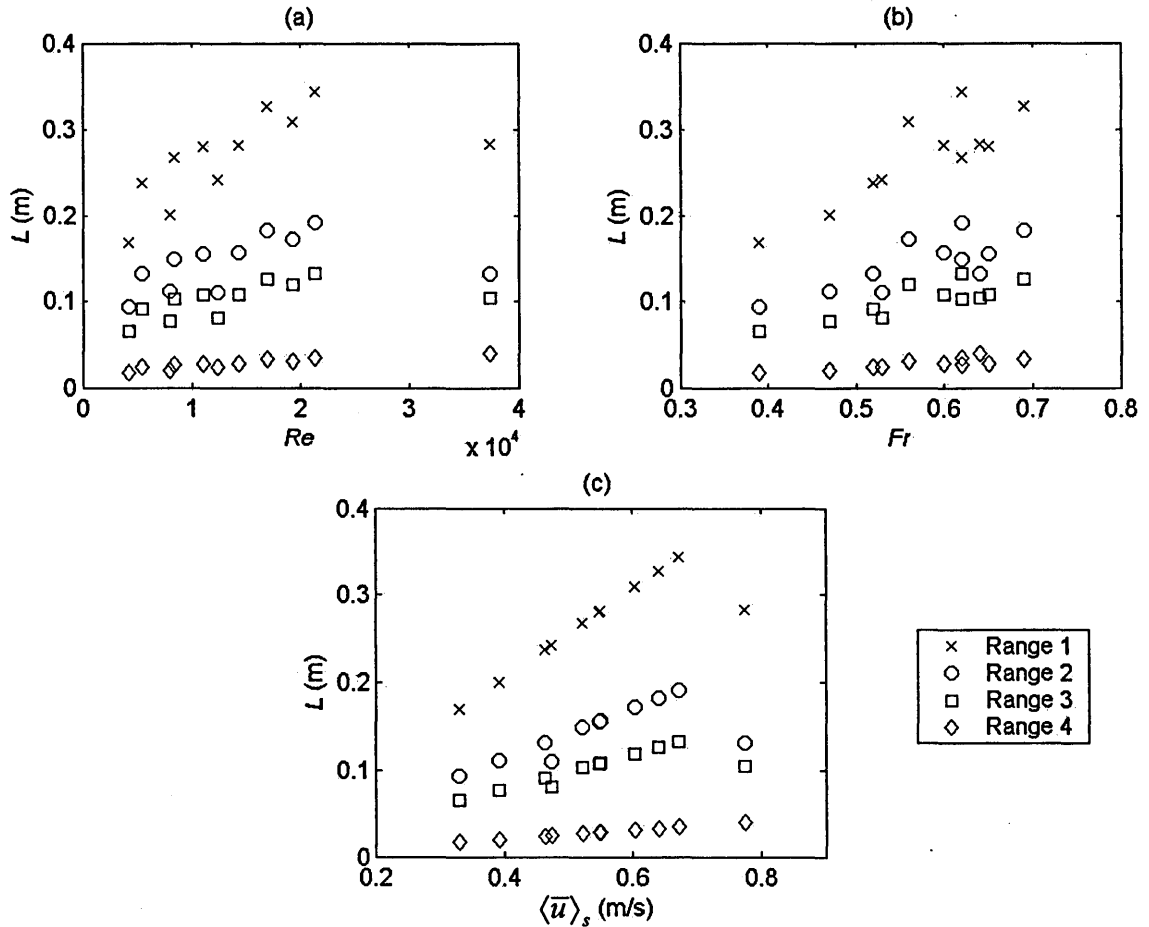


Figure 5.44. The change in the upper length scale L of the four spectral ranges for the power spectrum of water surface elevations for 11 of the experimental runs carried out over the bimodal bed with (a) the Reynolds number of the flow Re ; (b) the Froude number of the flow Fr ; and (c) the double-averaged streamwise velocity at the height closest to the water surface $\langle \bar{u} \rangle_s$.

The water surface suppresses the vertical movement of eddies (Nezu and Nakagawa, 1993), and therefore surface waves can have some effect on turbulent structure. The turbulent dissipation rate within the outer region is larger than the generation rate, so turbulent energy is supplied from the near-bed region to the outer region by turbulent diffusion through bursting. If the velocities are changing within the outer region due to

water surface effects, then presumably the degree of turbulent dissipation, and therefore diffusion will also demonstrate temporal and spatial variability. As such, turbulence generation close to the bed will display similar variability. This is based on the presumption that the water surface influences the internal flow structure, but the relationship may be reversed.

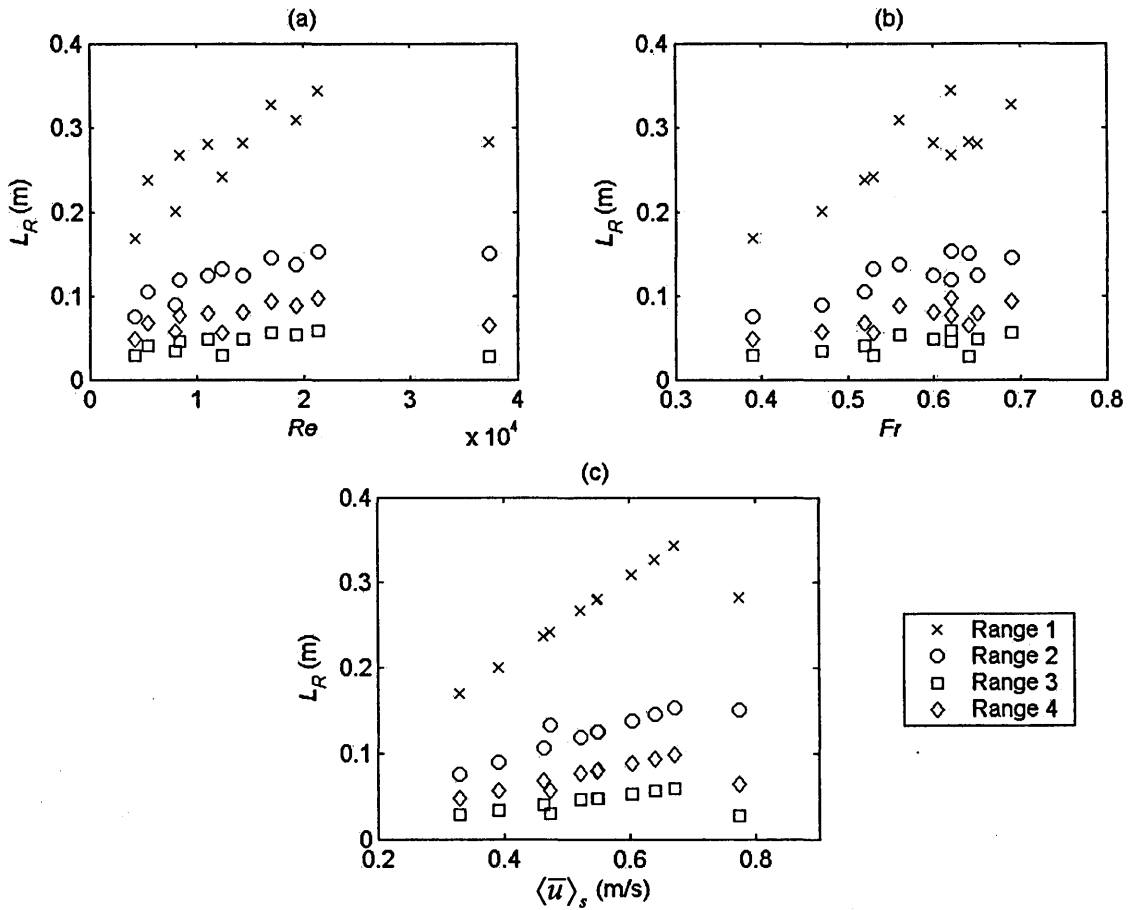


Figure 5.45. The change in the range of length scales L_R of the four spectral ranges for the power spectrum of water surface elevations for 11 of the experimental runs carried out over the bimodal bed with (a) the Reynolds number of the flow Re ; (b) the Froude number of the flow Fr ; and (c) the double-averaged streamwise velocity at the height closest to the water surface $\langle \bar{u} \rangle_s$.

The results under conditions of constant mean bed shear stress have shown that the dynamics of the water surface are different even when the average rate of momentum transfer at the bed is the same. Turbulent properties, such as turbulence intensity, have

been shown by previous studies to be scaled by u_* , therefore the water surface results suggest that the manner of the interdependency between the turbulent flow structure and the water surface may also change when the rate of momentum transfer at the bed is the same.

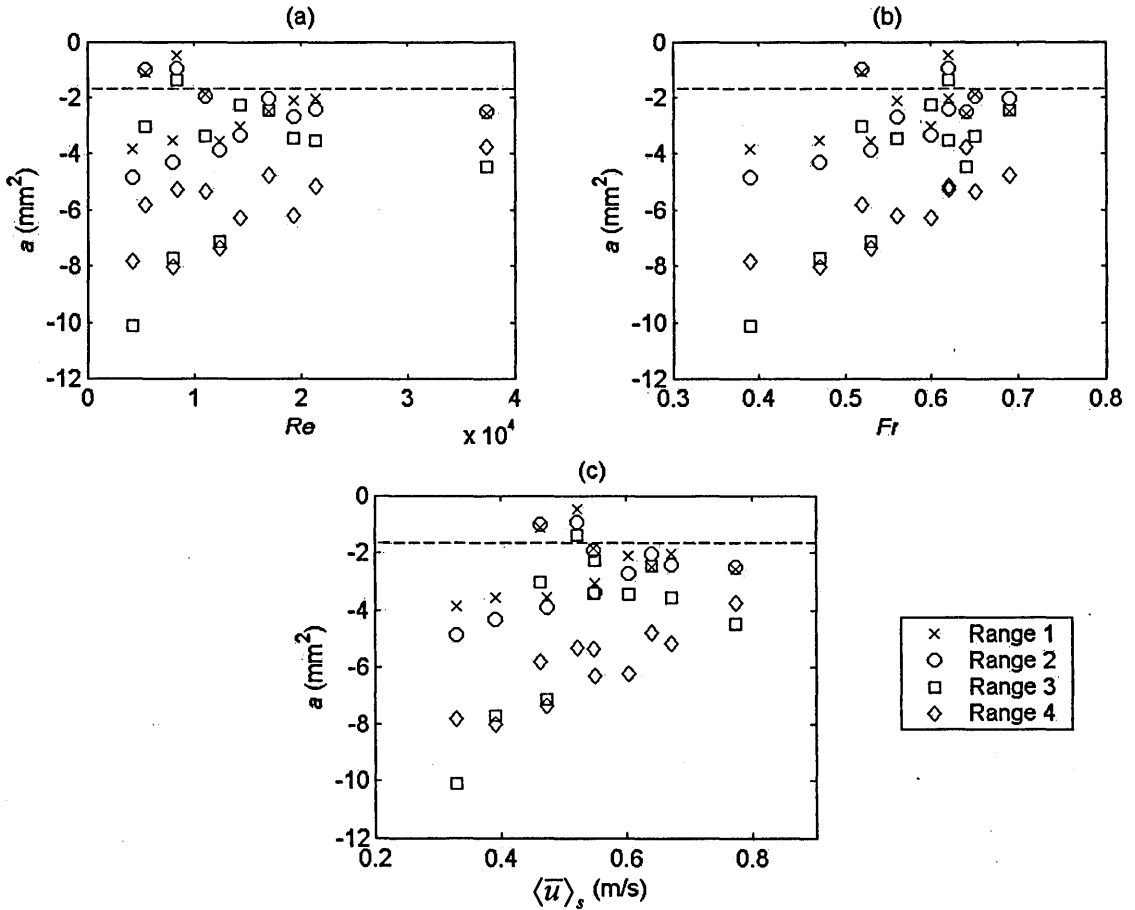


Figure 5.46. The change in the gradient of the linear least-squares fit a of the four spectral ranges for the power spectrum of water surface elevations for 11 of the experimental runs carried out over the bimodal bed with (a) the Reynolds number of the flow Re ; (b) the Froude number of the flow Fr ; and (c) the double-averaged streamwise velocity at the height closest to the water surface $\langle \bar{u} \rangle_s$. The dashed line indicates where $a = -5/3 \text{ mm}^2$.

Previous studies have found that vertical turbulence intensities are greater at higher Froude numbers, and that they are also higher, relative to the bed, in the outer region (Smutek, 1969; Komori *et al.*, 1982; Nezu and Nakagawa, 1993). It has been suggested

that the degree of increase in the intensities is dependent on whether the surface tension is large enough to prevent the production of significant surface waves, which suppress the vertical movement of eddies, and therefore damps the vertical fluctuations (Nezu and Nakagawa, 1993). The change in the power spectra with Froude number in Figure 5.46, which suggested that large surface waves are more apparent at high Froude numbers, appears to indicate that this thought is correct. Presumably the degree of increase in vertical turbulent intensity will be spatially variable because of the spatial nature of the water surface.

The power spectra results show that a flat or symmetric water surface cannot be assumed for numerical simulations of turbulent flows over rough boundaries. Therefore, more detailed investigations of the turbulent nature of the water surface, and its interaction with the flow is required.

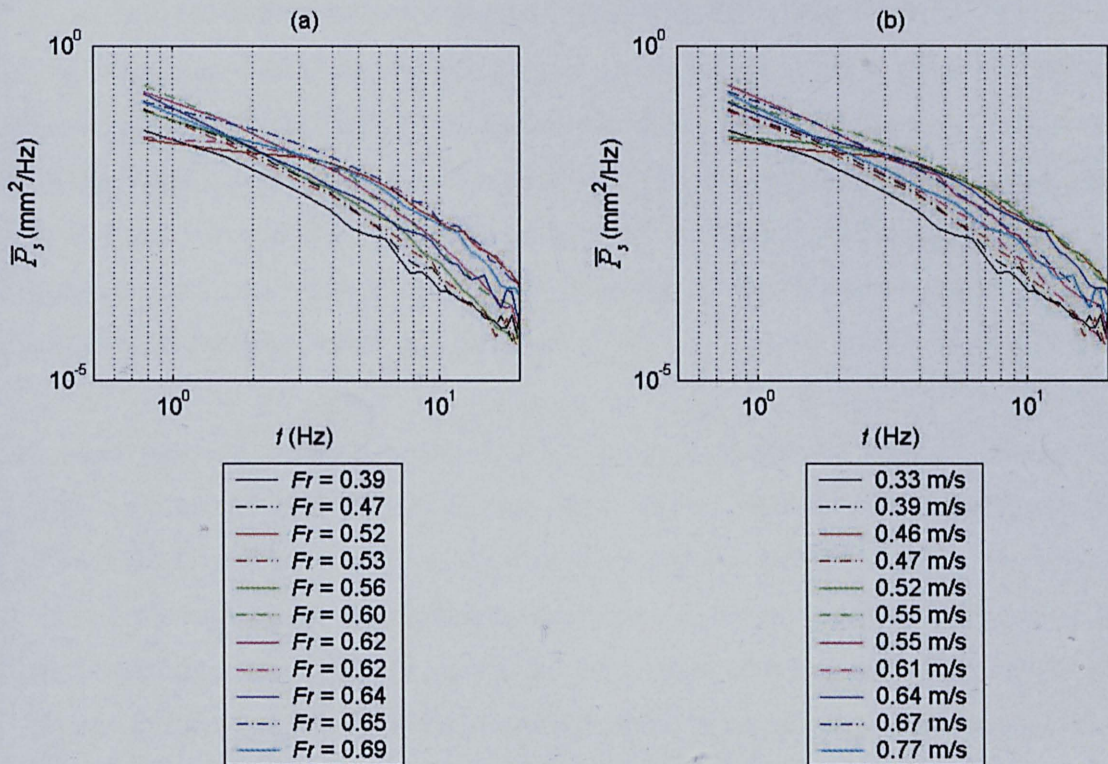


Figure 5.47. Power spectrum of the water surface elevations, shown in terms of the variation in power spectral density \bar{P}_s with the temporal frequency of variation f for 11 of the experimental runs carried out over the bimodal bed, in relation to (a) the Froude number of the flow Fr ; and (b) the double-averaged streamwise velocity at the height closest to the water surface.

5.16 Summary

This chapter has investigated whether time-averaged vertical velocities are spatially variable over two water-worked gravel beds. The degree of spatial variability was examined by calculating the standard deviation in these values over the beds. It was discovered that the degree of spatial variability was a magnitude lower than was observed for the time-averaged streamwise velocities. This suggested that form-induced stress is likely to be predominantly produced by spatial variations in time-averaged streamwise velocities rather than those in vertical velocities. Furthermore, the degree of spatial variability in time-averaged vertical velocities was a magnitude lower than the temporal variations in instantaneous vertical velocities. This indicated that spatial variations are likely to induce lower degrees of momentum transfer within the flow than turbulence.

The degree of spatial variability was of a similar size over both beds, despite the differences in the bed surface topography. Spatial variability was found to increase in the upper regions of the flow, and in some cases to be higher closer to the water surface than the bed surface, indicating that spatial variability does not disappear within the logarithmic and outer layer as previously thought. This suggested that spatial variability was not entirely induced by bed surface topography. Its vertical profile for an individual experimental run was well approximated by a power relationship close to the bed, and an exponential function further into the flow.

Bed shear velocity, rather than the double-averaged streamwise velocity, scaled the degree of spatial variability. This indicated that it was not related to the vertical velocity profile of the flow. The vertical variation in the degree of spatial variability was scaled by flow depth rather than bed roughness. Furthermore, it was shown that the degree of spatial variability was typically greater at the higher submergences than the lower submergences, such that it could be as much as three times larger. These changes were equally large for the experimental runs carried out at the same mean bed shear stress. This showed that differences in relative submergence could result in a change in how much momentum is carried by turbulent and spatial fluctuations in the flow, even when the mean bed shear stress is the same.

The patterns of the spatial deviations showed a considerable degree of organisation over the two beds. They were structured into alternating vertical zones of upward and downward moving fluid that could extend from the bed surface up into the outer region of the flow. These flow features were remarkably consistent over the two beds, and represented spatially coherent time-averaged flow structures. This spatial organisation was found to be heavily dependent on relative submergence, but to have less of an association with the bed surface topography beneath. It suggested that these flow structures might be an inherent feature of turbulent flows over water-worked gravel beds.

An increase in relative submergence caused a progressive decrease in the number of vertical zones of upward and downward moving fluid over the bed, and an increase in their streamwise length. This spatial structure varied across the bed, and only showed small degrees of persistence across the different experimental runs at the same lateral position over the bed. Indeed, the patterns could be just as variable at the same lateral position with relative submergence as they could be across the bed. This further demonstrated the important influence that relative submergence has on the spatial patterns in the time-averaged flow. But flow depth did not scale the vertical variability in the spatial pattern. Instead, bed roughness appeared to control more heavily the spatial pattern observed across the different experimental runs, demonstrating that spatial patterns must be controlled by flow structures that scale with both bed roughness and flow depth. This demonstrated that relative submergence could potentially have as important an influence on momentum transfer over water-worked gravel beds as bed surface topography.

Spectral analysis of the temporal dynamics of water surface elevations showed that the changes in the dynamics of the water surface with relative submergence and bed slope correspond with the changes in the pattern of spatial deviations within the flow. Furthermore, the power spectra of the water surface elevations displayed a four range subdivision, which has also been reported for velocity spectra. This implied that there could be an association between the regions of upward and downward moving fluid within the flow and the upwellings and downwellings on the water surface. The results also showed that a flat or symmetric water surface cannot be assumed for numerical simulations of turbulent flows over rough boundaries.

CHAPTER 6

FORM-INDUCED STRESS OVER WATER-WORKED GRAVEL BEDS

6.1 Introduction

This chapter will investigate the significance of the spatial patterns in time-averaged flow described in Chapters 4 and 5 for transferring fluid momentum in flows over water-worked gravel beds. This will be achieved by examining the fluid stress that arises from the correlations between point-to-point spatial deviations in time-averaged velocity, termed the form-induced stress, and how this contributes to the total fluid stress above two water-worked gravel beds. It will be seen how these contributions change through the flow depth, and whether they remain significant above the form-induced sublayer where these stresses are thought to be negligible. It will also be shown how the significance of the form-induced stresses to momentum transfer change with relative submergence, bed slope and between beds with different surface topographies in order to understand what controls these stresses. Furthermore, it will be examined whether form-induced stresses display significant spatial variability over the beds. The significance of the stresses at different spatial scales is explored, and the characteristic spatial scale at which the form-induced stresses operate over will also be investigated. It is determined what size of averaging area is required to derive representative form-induced stress values, and how this relates to properties of the fluid and the bed. This is used to assess critically whether it is likely that previous studies examining form-induced stresses over gravel beds have produced representative values. From all of these results, it will be discussed whether accurate predictions of mean bed shear stress can be made by solely accounting for Reynolds stresses over water-worked gravel beds.

6.2 Deriving Form-induced Stress

In order to assess the significance of the patterns of spatial variability in the time-averaged flow field described in Chapters 4 and 5, the fluid stresses (momentum fluxes) associated with these spatial flow patterns are investigated. The time-averaged Navier-

Stokes equations, Reynolds equations, make no explicit consideration of the influence of spatial variability in the time-averaged flow field on momentum transfer when attempting to estimate shear stress

$$\frac{\partial \bar{u}_i}{\partial t} + \bar{u}_j \frac{\partial \bar{u}_i}{\partial x_j} = g_i - \frac{1}{\rho} \frac{\partial \bar{p}}{\partial x_i} - \frac{\partial \overline{u'_i u'_j}}{\partial x_j} + \nu \frac{\partial^2 \bar{u}_i}{\partial x_j^2} \quad (6.1)$$

$$\frac{\partial \bar{u}_i}{\partial x_i} = 0 \quad (6.2)$$

where the equations are obtained in Cartesian-tensor notation, where the straight overbar denotes the time-average of the flow variables, u' is the temporal fluctuation in velocity (given by $u' = u - \bar{u}$, where u is the instantaneous velocity), p is fluid pressure, t is time, x is distance, ρ is fluid density, g is gravitational acceleration and ν is kinematic viscosity. This influence can only be taken into account explicitly by supplementing the time-averaging of the Navier-Stokes equation with spatial area (or volume) averaging in the plane parallel to the averaged bed surface. This produces new continuity and momentum equations which are averaged both in time and space.

Studies into atmospheric boundary layers considered spatial-area averaging the flow over a horizontal plane intersecting the vegetation canopy (Wilson and Shaw, 1977; Raupach and Shaw, 1982). Finnigan (1982) extended these concepts to enable the flow to be averaged over any volume within the canopy, and derived volume-averaged equations. Both approaches become equivalent when the averaging volume is considered as an extensive, infinitesimally thin horizontal slab. The averaging procedure for spatial area averaging at level z is defined as (Gimenez-Curto and Corniero Lera, 1996; Nikora *et al.*, 2001)

$$\langle F \rangle(x, y, z, t) = \frac{1}{A_f} \int_{A_f} \int F(x', y', z, t) dx' dy' \quad (6.3)$$

where F is the flow variable defined in the fluid to be spatially averaged over the fluid domain A_f . This fluid domain is assumed to be planar and parallel to the averaged bed surface, and to be the area occupied by the fluid on the x, y -plane at level z within the

total area A_0 . The total area includes the domains occupied by both fluid and the intervening solid surfaces. This definition is combined with a decomposition of time-averaged variables into spatially-averaged (denoted by angle brackets) and spatially fluctuating (denoted by a wavy overbar) components (Gray, 1975) that is analogous to the Reynolds decomposition for instantaneous variables $F = \bar{F} - F'$:

$$\bar{F} = \langle \bar{F} \rangle - \tilde{F} \quad (6.4)$$

The spatial fluctuations arise from the difference between the double-averaged $\langle \bar{F} \rangle$ and time-averaged \bar{F} values ($\tilde{F} = \bar{F} - \langle \bar{F} \rangle$, $\langle \tilde{F} \rangle = 0$), similar to the conventional Reynolds decomposition of $F' = F - \bar{F}$, $\bar{F}' = 0$.

By applying equation (6.3) and the decomposition used in equation (6.4) to equation (6.1), it is possible to obtain double-averaged (in time and then in space) momentum and mass conservation equations for the flow both above and below the maximum bed elevation z_c . In the flow region above the maximum bed elevation $z > z_c$, where $A_0 = A_f$

$$\frac{\partial \langle \bar{u}_i \rangle}{\partial t} + \langle \bar{u}_j \rangle \frac{\partial \langle \bar{u}_i \rangle}{\partial x_j} = g_i - \frac{1}{\rho} \frac{\partial \langle \bar{p} \rangle}{\partial x_i} - \frac{\partial \langle \overline{u'_i u'_j} \rangle}{\partial x_j} - \frac{\partial \langle \tilde{u}_i \tilde{u}_j \rangle}{\partial x_j} + \nu \frac{\partial^2 \langle \bar{u}_i \rangle}{\partial x_j^2} \quad (6.5)$$

$$\frac{\partial \langle \bar{u}_i \rangle}{\partial x_i} = 0 \quad (6.6)$$

and in the flow region below the maximum bed elevation $z < z_c$, where the averaging region is multiply connected because of the intersection by roughness elements

$$\begin{aligned} \frac{\partial \langle \bar{u}_i \rangle}{\partial t} + \langle \bar{u}_j \rangle \frac{\partial \langle \bar{u}_i \rangle}{\partial x_j} = g_i - \frac{1}{\rho} \frac{\partial \langle \bar{p} \rangle}{\partial x_i} - \frac{1}{\phi} \frac{\partial \phi \langle \overline{u'_i u'_j} \rangle}{\partial x_j} - \frac{1}{\phi} \frac{\partial \phi \langle \tilde{u}_i \tilde{u}_j \rangle}{\partial x_j} \\ + \frac{\nu}{\phi} \frac{\partial^2 \phi \langle \bar{u}_i \rangle}{\partial x_j^2} - \frac{2\nu}{\phi} \frac{\partial \langle \bar{u}_i \rangle}{\partial x_j} \frac{\partial \phi}{\partial x_j} - \frac{\nu \langle \bar{u}_i \rangle}{\phi} \frac{\partial^2 \phi}{\partial x_j^2} + \nu \left\langle \frac{\partial^2 \tilde{u}_i}{\partial x_j^2} \right\rangle - \frac{1}{\rho} \left\langle \frac{\partial \bar{p}}{\partial x_i} \right\rangle \end{aligned} \quad (6.7)$$

$$\frac{\partial \phi \langle \bar{u}_i \rangle}{\partial x_i} = 0 \quad (6.8)$$

where ϕ is the normalised value of A_f , $\phi = A_f/A_0$. This has been termed the roughness geometry function (Nikora *et al.*, 2001) because it accounts for the geometry of the bed by deriving the proportion of the bed within A_0 , which means that $\phi = f(x, y, z)$. Detailed mathematical analysis and full derivations of equations (6.5) and (6.7) for incompressible turbulent fluid flow are given in detail in Gimenez-Curto and Corniero Lera (1996). Equations (6.5) and (6.7) relate to the time-averaged Reynolds equations, in the same manner in which the Reynolds equations relate to the Navier-Stokes equations for instantaneous flow variables. Velocities and pressures, as well as their moments, in these double-averaged equations represent spatially-averaged flow parameters.

The spatial averaging of the Reynolds equations has introduced some additional terms in equations (6.5) and (6.7) to those in equation (6.1). These new terms are form-induced stress $\langle \tilde{u}_i \tilde{u}_j \rangle$, form drag $(1/\rho) \langle \partial \tilde{p} / \partial x_i \rangle$ and viscous drag $\nu \langle \partial^2 \tilde{u}_i / \partial x_j^2 \rangle$. The latter two terms only appear in equation (6.7) for the flow below the maximum bed elevation. This equation also demonstrates a dependence on the parameter ϕ , and therefore on the roughness geometry. This parameter is important if the density and cross-sections of the roughness elements change spatially, but disappear if they are spatially homogeneous. It means that the spatially-averaged flow parameters can be related to the roughness parameters by averaging in the same spatial domain.

Of most importance to this chapter is the appearance of the form-induced stress term $\langle \tilde{u}_i \tilde{u}_j \rangle$ in equations (6.5) and (6.7). This appears as a result of spatial averaging of the Reynolds equations in the same way as the Reynolds stress $\overline{u'_i u'_j}$ appears as a result of time-averaging of the Navier-Stokes equations. This means that $\langle \tilde{u}_i \tilde{u}_j \rangle$ arise due to the spatial heterogeneity in the time-averaged flow. More specifically, form-induced stresses represent the contribution to momentum transfer from correlations between point-to-point variations in the time-averaged flow. This term represents the opportunity to assess whether the spatial flow patterns described in Chapters 4 and 5 can induce momentum exchange between the fluid and the bed. The term form-induced stress was

coined by Gimenez-Curto and Corniero Lera (1996), because they felt it was the “force due to the mean momentum flux for boundary disturbances” and that it “owes its existence to the presence of forms in the boundary”. It is the name preferred for studies of hydraulic flows in open-channels (Nikora *et al.*, 2001; Maddux *et al.*, 2003; Campbell *et al.*, 2005; Nikora *et al.*, in press b).

In this chapter consideration is given to the simplest case of 2-D, steady, uniform flow above the maximum bed elevation, in which the flow is in spatial equilibrium and has a free surface which is parallel to the average bed slope. Such a flow possesses the following properties (from Nikora *et al.* (2001)):

1. No long-term trends in flow properties, such that all variations can be considered to have only been caused by turbulence. This was ensured by measuring for five and half minutes to produce steady, time-averaged flow values (this was confirmed to be correct for all measurements). In this manner the averaging time is sufficiently long to ensure that many cycles of the rapid turbulent fluctuations in a flow property are captured, but sufficiently short that the external large-scale variations in the flow property are not present. No long-term trends in flow properties was also ensured by carrying out measurements for flows when the bed was not mobile so that the bed surface topography was not changing with time, which could cause such long-term trends or changes in flow discharge.
2. The vertical change in spatially-averaged flow properties is significantly stronger than those in the lateral directions.
3. $\langle \bar{v} \rangle$ and $\langle \bar{w} \rangle$ are equal to zero throughout the flow depth and there is no correlation between u and v and between v and w .
4. The water surface is parallel to the averaged bed slope so that the energy and bed slope is the same. This was achieved by adjusting the sharp-edged adjustable weir.
5. The bed roughness (i.e. the field of bed elevations) is statistically homogeneous in the x, y -plane. In other words, the bed surface is random, the spatial autocorrelation is stationary and isotopic, and a probability density function of bed elevations can describe a bed uniquely. Therefore, the roughness geometry function ϕ depends only on the vertical coordinate z , i.e. $\phi = \phi(z)$. This assumption does not hold for water-worked beds. Marion *et al.* (2003) showed that it is possible to have beds with very different topographies but with the same probability density function. Water-worked beds have a 3-D structure so the roughness geometry function is actually

equivalent to $\phi = \phi(x, y, z)$. But given that the flow above the maximum bed elevation is only considered here, where the momentum equation (6.5) is not a function of ϕ , this assumption is not a concern.

The right-handed coordinate system is adopted throughout the chapter. For the laboratory flume, the x -axis is orientated along the main flow parallel to the averaged bed (streamwise direction, u -velocity component), the y -axis is oriented to the left side of the flume looking downstream (lateral direction, v -velocity component), and the z -axis is orientated towards the water surface (vertical distance from an arbitrary origin, w -velocity component). The tensor notation used earlier, with the Einstein convention, means that x_i ($i = 1, 2, 3$) corresponds to the directions x , y , and z ; and u_i ($i = 1, 2, 3$) corresponds to the velocity components u , v , and w .

For high Reynolds number 2-D flows (which apply to the flows considered in this chapter) equation (6.5) can be reduced to

$$gS - \frac{\partial \langle \overline{u'w'} \rangle}{\partial z} - \frac{\partial \langle \widetilde{uw} \rangle}{\partial z} = 0 \quad (6.9)$$

$$g \cos \alpha + \frac{1}{\rho} \frac{\partial \langle \overline{p} \rangle}{\partial y} + \frac{\partial \langle \overline{v'w'} \rangle}{\partial y} + \frac{\partial \langle \widetilde{vw} \rangle}{\partial y} = 0 \quad (6.10)$$

where S is the slope of the averaged bed surface, such that $S \approx \sin \alpha$, which can be considered to be equal to the streamwise slope of the water surface, because of the uniform flows created in the flume. Equation (6.9) represents the double-averaged momentum equation in the streamwise domain and equation (6.10) in the vertical domain. Given that the flow is assumed to be 2-D the equations in the transverse domain disappear. The viscous drag term, $\nu \langle \partial^2 \widetilde{u}_i / \partial x_j^2 \rangle$ is also neglected given the high Reynolds numbers of the flows.

The interest is in the form-induced stress term in equation (6.9). By integrating equation (6.9) from z to the water surface z_{ws} the following relationship for the total stress distribution τ can be derived for the flow above the maximum bed elevation

$$\frac{\tau(z)}{\rho} = gS[z - z_{ws}] = [-\langle \overline{u'w'} \rangle(z) - \langle \widetilde{u}\widetilde{w} \rangle(z)] \quad (6.11)$$

It follows that the gravity force $gS[z - z_{ws}]$ is balanced by the turbulent shear stress and the form-induced shear stress. Nikora *et al.* (2001) subdivided this flow region above the maximum bed elevation into two further layers. The outer and logarithmic layer, where $\langle \widetilde{u}\widetilde{w} \rangle(z) = 0$

$$\frac{\tau(z)}{\rho} = gS[z - z_{ws}] = -\langle \overline{u'w'} \rangle(z) = -\overline{u'w'}(z) \quad (6.12)$$

and the form-induced sublayer

$$\frac{\tau(z)}{\rho} = gS[z - z_{ws}] = [-\langle \overline{u'w'} \rangle(z) - \langle \widetilde{u}\widetilde{w} \rangle(z)] \quad (6.13)$$

The explicit statement made through these equations by Nikora *et al.* is that form-induced stresses are not significant, and spatial averaging of the Reynolds stress is not required, above the form-induced sublayer (presumably so called because this is where the form-induced stresses and the spatial variability caused by the form of the bed are to be found). It implies that in the outer and logarithmic layers of the flow the total stress must be comprised entirely of the Reynolds stress. The implication is that it is assumed that a linear fit to the Reynolds stress (from one point measurement, rather than from spatially-averaged measurements) in these regions can be used to predict the total boundary shear stress. This assumption needs to be examined.

6.3 Quantifying Form-induced Stress

In order to assess the form-induced stresses, it can be seen from equation (6.11) that the spatial deviations in \overline{u} and \overline{w} need to be examined. This can be achieved by utilising the streamwise and vertical velocity measurements obtained using the vertical plane PIV measurements. The time-averaged flow field data from each of the nine lateral locations over the bed for a given experimental run were assimilated. Each vertical plane measurement at a given level above the bed contained 61 vectors, so the assimilation produced a matrix of 549 vectors at each measurement level above the bed.

Spatial averaging was performed over a thin streamwise slab of time-averaged fluid at a constant height above the bed in order to preserve the characteristic spatial variability in the flow in the vertical direction. The double-averaged velocities $\langle \bar{u} \rangle$ and $\langle \bar{w} \rangle$ could then be derived and used to calculate the spatial deviations \tilde{u} and \tilde{w} , respectively at each of the 549 positions at each vertical level within the flow field. Using all nine vertical plane measurements to derive $\langle \bar{u} \rangle$ and $\langle \bar{w} \rangle$ means that these double-averaged quantities were obtained at nine different lateral locations over the bed. The height of the averaging slab was determined by the separation distance between vertical measurement heights, which was 2.265 mm. This was also the streamwise separation distance between measurement points at a given height above the maximum bed elevation. This means that the streamwise length over which \bar{u} and \bar{w} were taken from within each vertical plane measurement for the data assimilation was equal to 138.165 mm ($= 61 \times 2.265$). This means that $\langle \bar{u} \rangle$ and $\langle \bar{w} \rangle$ were derived by spatially-averaging over an area of 2816.5 mm^2 ($= [138.165 \times 9] \times 2.265$).

The product of the spatial deviations $\tilde{u}\tilde{w}$ was calculated for each of the measurement positions for the different heights above the bed. The mean of these values was then taken at each position above the bed to give $\langle \tilde{u}\tilde{w} \rangle(z)$, the form-induced stress over the bed at height z . Averaging in this manner also resulted in $\tilde{u}\tilde{w}$ being spatially-averaged over an area of 2816.5 mm^2 . This is not equivalent to volume averaging because of the separation distance between each of the nine lateral locations. However, given that the light sheet had a thickness of $\sim 3 \text{ mm}$, it effectively means that volume averaging was performed across each vertical plane measurement.

To discover the relative size of momentum fluxes created by these spatial deviations, the ratio of the form-induced stress relative to the total fluid stress was assessed. This was given by the proportion of the total fluid stress contributed by the form-induced stresses FS_f , expressed at a given height above the maximum bed elevation z , as the ratio to the square of the bed shear velocity

$$FS_f = \frac{-\langle \tilde{u}\tilde{w} \rangle}{u_*^2 (1 - z/d)} \quad (6.14)$$

in which u_* is the bed shear velocity given by $u_* = (\tau_0/\rho)^{0.5}$, where τ_0 is the bed shear stress, which is defined in equation (3.5) in Chapter 3, and d is flow depth. The FS_f values can therefore be considered to be the fractional contributions of form-induced stress to the total fluid stress.

6.4 Vertical Distribution of Form-induced Stress

The variation in FS_f with height above both the beds is shown in Figure 6.1, which provides a clear indication of the size of the fractional contributions made by form-induced stresses to the total fluid stress. This is shown in terms of its variation with absolute height, z/d and z/D_{84} . This is in order to establish whether the variability in FS_f between experimental runs and the two beds can be accounted for by differences in flow depths, or by the difference in D_{84} of the beds, used as an approximation to the difference in roughness between the two beds.

It can be seen that the form-induced stresses can make both positive and negative contributions to the total fluid stress. A positive contribution indicates that the form-induced stress is acting downstream, and a negative contribution, that it is acting in the upstream direction. Over the unimodal bed, form-induced stress can make a positive contribution of up to around 5 % to the total fluid stress, whilst also making a negative contribution of up to 7.5 %. There appears to be a near equal distribution of positive and negative contributions over this bed. However, over the bimodal bed the contributions are predominately positive, up to around 12 %, with the negative contributions only being up to nearly 5 %. The contributions, made in either direction, are not large over either bed, but cannot be ignored as many previous studies have supposed. If the assumption is made that the Reynolds stress is equal to $1 - FS_f$, the variability in the sign and magnitude of FS_f shows that the size of the contributions made by Reynolds stresses may also display variability between the experimental runs and the two beds.

The FS_f values are highest closest to the maximum bed elevation of the beds, but the contributions from the form-induced stresses can, on some occasions, be comparable in size to these values at up to around half way up into the flow depth. This indicates that the form-induced stresses are significant, relative to those close to the bed, outside the

form-induced sublayer. This suggests that Nikora *et al.*'s (2001) assumption that the total fluid stress is purely carried by the Reynolds stress in the logarithmic layer is inappropriate given the results presented here. Indeed some of FS_f values in Figure 6.1 would also suggest that the same might apply for the outer region of the flow for some of the experimental runs. Equation (6.11) appears to provide a better explanation of the stress distributions for the entire flow depth over the two beds, than the subdivision suggested by Nikora *et al.* (2001). Therefore measurements of Reynolds stresses alone, whether spatially-averaged or not, cannot be used to determine the total fluid stress over these water-worked gravel beds. Clearly, for flows above the maximum bed elevation, shear stress cannot be predicted accurately by an assumed linear distribution of Reynolds stress with depth.

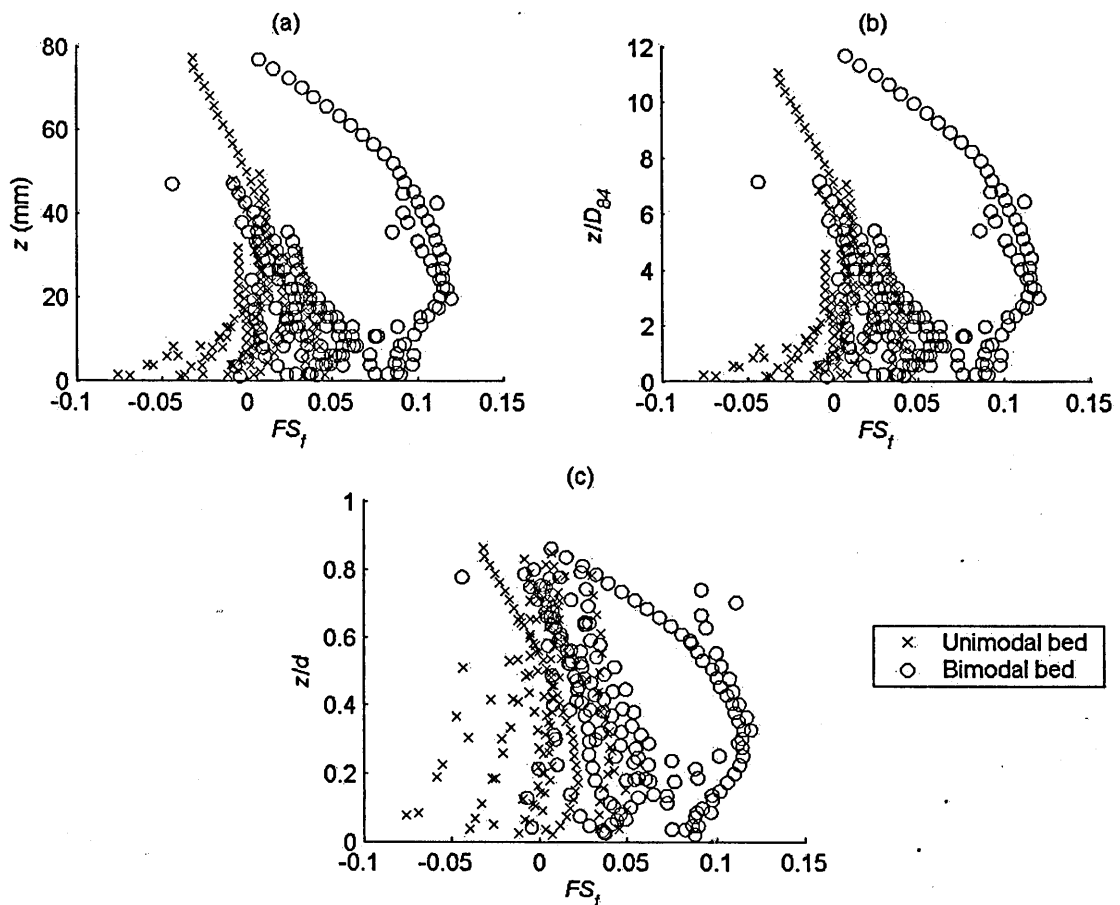


Figure 6.1. Vertical variability in the fractional contributions made by the form-induced stresses to the total fluid stress FS_f with (a) height above the maximum bed elevation z ; (b); z/D_{84} and (c) z/d , where d is flow depth and D_{84} is the grain size at which 84 per cent of the bed material is finer.

This type of vertical distribution in FS_f has also been found for various other types of bed roughness. Nikora *et al.* (in press b) brought together results from several studies that have examined the significance of form-induced stresses. These stresses have been found to make contributions of up to around 10 % and 8 % for up to half of the flow depth for various fixed 2-D dune shaped bedforms and 2-D transverse ribs in a laboratory flume, respectively. This was also discovered by Pokrajac *et al.* (2003), again for a 2-D transverse rib configuration. Both positive and negative contributions were observed over all these fixed bedforms. In all these cases, the largest contributions for the flow above the boundaries were found to be at or just above the maximum bed elevation, as displayed in Figure 6.1. This was also discovered for three experimental runs of varying flow depths over a static armoured gravel bed, also given in Nikora *et al.* (in press b). The contributions, however, were purely positive above the maximum bed elevation over this bed. Yet the size of these contributions is very similar to those presented in Figure 6.1. The contributions over the fixed bedforms are, however, typically larger by a few percent just above the maximum bed elevation, but are very similar for the remaining upper sections of the flow.

Campbell *et al.* (2005) examined the significance of form-induced stresses for flows above an artificially created and fixed gravel bed. They examined how this significance changed with the addition of bedload using different feed rates and feed grain sizes. They too found that the contributions were largest just above the maximum bed elevation, and could be both negative and positive. They, however, only found the contributions to remain significant for the lower 10 – 20 % of the flow. Yet the size of the contributions within this region for the flows that contained bedload are very similar to those in Figure 6.1. It is only for the clear water flows, where the contributions were found to be up to 30 %, that they are much larger, typically double in size. Their form-induced stresses were derived from one vertical plane over the bed, which provided a spatial averaging area that they said “was chosen to be representative of the fixed sediment bed topography throughout the flume”. However, their analysis reveals that one isolated particle on the bed created the majority of this stress. Yet this particle was purely an artefact of the screeding process, and the image of the bed they provide reveals that this is an artificial feature because of its degree of protrusion into the flow. This was shown to account greatly for spatial variability in the time-averaged flow field. Given this, and that one vertical plane measurement was used, and that measurements were taken over a very small area of 67 × 61 mm, it is doubtful that their measurements

have produced representative values of form-induced stress over the whole bed. Further to this, they suggest that the addition of bedload diminished the effect of the isolated particle on the flow through the deposition of the load on the surrounding areas of the bed. This reduced its relative protrusion into the flow, and it was for the flows with bedload that similar contributions levels to those in Figure 6.1 were seen. This shows that once the effects of this particle were limited the results were more representative of what has been presented in Figure 6.1.

Form-induced stress contributions were examined by Maddux *et al.* (2003) for fixed, artificial 2-D dune shapes at two different flow depths. They also found the contributions to be highest above the maximum bed elevation, and to remain significant up to a third of the way into the flow for the shallowest flow and to just above the maximum bed elevation for the deeper flow. These contributions in the later case were typically higher than those displayed in Figure 6.1, but for the lower flow depth, the values are very similar, including the values up to the water surface. Therefore, Maddux *et al.* also found the form-induced stresses to still be present above the form-induced sublayer, and for equation (6.11) to be a better description of the stress distribution in the logarithmic layer.

Several studies have examined the contributions made by form-induced stresses for aerodynamic flows within vegetation canopies. For experiments within a wind-tunnel using model canopies, the contributions have been found to be negligible above the canopy (Mulhearn, 1978; Raupach *et al.*, 1980; Raupach *et al.*, 1986; Böhm *et al.*, 2000; Poggi *et al.*, 2004). The same results have been found for flows over surfaces covered with staggered arrays of cubes to simulate urban-like roughness using wind-tunnels (Cheng and Castro, 2002), CFD using Reynolds-averaged Navier-Stokes equations (Lien and Yee, 2004) and direct numerical simulation (DNS) using the double-averaged Navier-Stokes equations (Coceal *et al.*, submitted). However, LES by Kanda *et al.* (2004) and the DNS results of Lien and Yee (2004) have revealed that form-induced stress contributions can be up to 20 % above cubes within a square arrangement, with the maximum values attained at the maximum bed elevation, in contrast to that over staggered arrays. Also, Poggi *et al.* (2004) has found that for model canopies consisting of tall, steel cylinders arranged in a regular pattern within a hydraulic flume, the contributions can be up to 5 % close to the water surface. A short measurement period also appears to affect the interpretation of the contributions made by the form-induced

stress. Coceal *et al.* (submitted) found that although the contributions are negligible over a long sampling period, a short period results in contributions being as high as 5 % for a significant distance above the maximum bed elevation. The major flaw with all of the wind-tunnel studies is the low number of measurements made across the arrays, usually only between 10 and 25 measurements, and very often biased to a particular region of the array. It is doubtful that this fully characterised the spatial variability within the flow field and may not be an accurate representation of the form-induced stress. Nonetheless, the studies over square arrays of cubes and the recent results by Poggi *et al.* (2004) for a model canopy have revealed very similar results to those seen in Figure 6.1.

The results in Figure 6.1 also show that there appears to be substantial differences in the contributions made by the form-induced stresses between experimental runs over a given bed, and also between the two beds. This variability is clearly higher closer to the bed. It was concluded from Chapter 4 that the degree of spatial variability in \bar{u} and \bar{w} (given by $\sigma_{\bar{u}}$ and $\sigma_{\bar{w}}$, respectively) showed a general increase with relative submergence and it is possible that this association could account for this variability between experimental runs. However, this measure of spatial variability accounted for the spatial deviation over the whole flow field rather than from point-to-point deviations. Form-induced stresses are created by correlations between point-to-point variations in the time-averaged flow, rather than correlations between $\sigma_{\bar{u}}$ and $\sigma_{\bar{w}}$. Therefore, it is unclear whether the positive association of $\sigma_{\bar{u}}$ and $\sigma_{\bar{w}}$ with relative submergence can account for this difference in FS_f between experimental runs for a given bed. It is therefore important to examine whether relative submergence or bed slope has the greater influence on FS_f .

The variability in FS_f between the experimental runs over a given bed, and between the beds appears to be at its least when FS_f is plotted against z/d rather than absolute height above the maximum bed elevation or z/D_{84} . It therefore suggests that FS_f values should be compared at the same z/d in order to establish whether relative submergence or bed slope has the greatest influence, and what kind of effect the difference in bed surface topographies between the two beds has on their sign and magnitude.

It has been decided to examine the FS_f values at one position closest to the maximum bed elevation. This is for several reasons. Firstly, this is the position at which the variability between experimental runs is at its greatest, and therefore the position at which the effect of relative submergence, bed slope, and bed surface topography is also likely to be at its greatest. Secondly, the contributions made by form-induced stresses for the flow regions above the maximum bed elevation have been found both here and by others (Maddux *et al.*, 2003; Pokrajac *et al.*, 2003; Campbell *et al.*, 2005; Nikora *et al.*, in press b) to be at their highest at or just above the maximum bed elevation. Thirdly, this is the area of the flow at which all previous studies have made measurements of form-induced stress, allowing more comparisons to be made. Finally, this is also the position at which the variation in form-induced stresses, and therefore in Reynolds stress, is likely to have the most effect on sediment mobility.

Over the unimodal bed, the closest position to the maximum bed elevation at which all experimental runs have near identical values of (within $\pm 5\%$) z/d , is $z/d = 0.074$. For the bimodal bed this value is $z/d = 0.060$, meaning that the results from the two beds can be compared directly. The measurement positions closest to the maximum bed elevation for runs 1U and 1B (Tables 6.1 and 6.2) were not within the $\pm 5\%$ limits of the examined z/d values so they were not used.

6.5 Variability in Form-Induced Stress with Relative Submergence

In order to discover the influence of relative submergence on FS_f , the experimental runs at a single bed slope but varying flow depths were examined (Tables 6.1 and 6.2). The change in FS_f with relative submergence is shown for both the unimodal and bimodal bed in Figure 6.2. It can be seen immediately that there are clear differences in the direction of contribution made by the form-induced stress between the two beds. Over the unimodal bed, it is predominately negative contributions, indicating that the spatial contribution is in the opposite direction to the total fluid shear stress. Whereas over the bimodal bed, with the exception of one experimental run at the lowest relative submergence, the contributions are positive and are in the downstream direction. Given equation (6.11), by inference it indicates that the contributions made by the Reynolds stress are higher over the unimodal bed.

Table 6.1. Summary of the experimental conditions for the experimental runs carried out a single bed slope over the unimodal bed, where S is the bed slope, d is the flow depth, D_{84} is the grain size at which 84 per cent of the bed material is finer, \bar{U} is the average flow velocity (calculated from the ratio of flow discharge to the cross-sectional area of the flow), τ_0 is the bed shear stress and Fr is the Froude number (calculated from \bar{U}/\sqrt{gd} , where g is the force due to gravitational attraction).

Run	S	d (mm)	d/D_{84}	\bar{U} (m ² /s)	τ_0 (N/m ²)	Fr
1U	0.00285	18.1	2.6	0.18	0.47	0.42
2U	0.00285	28.6	4.1	0.27	0.72	0.51
3U	0.00285	39.5	5.6	0.32	0.95	0.52
4U	0.00285	48.4	6.9	0.36	1.13	0.52
5U	0.00285	62.8	9.0	0.45	1.40	0.57
6U	0.00285	90	12.9	0.62	1.85	0.66

Table 6.2. Summary of the experimental conditions for the experimental runs carried out a single bed slope over the bimodal bed, where S is the bed slope, d is the flow depth, D_{84} is the grain size at which 84 per cent of the bed material is finer, \bar{U} is the average flow velocity (calculated from the ratio of flow discharge to the cross-sectional area of the flow), τ_0 is the bed shear stress and Fr is the Froude number (calculated from \bar{U}/\sqrt{gd} , where g is the force due to gravitational attraction).

Run	S	d (mm)	d/D_{84}	\bar{U} (m ² /s)	τ_0 (N/m ²)	Fr
1B	0.00284	17.3	2.6	0.16	0.45	0.40
2B	0.00284	27.2	4.1	0.20	0.68	0.39
3B	0.00284	37.3	5.7	0.28	0.90	0.47
4B	0.00284	45.5	6.9	0.36	1.07	0.53
5B	0.00284	59.5	9.0	0.43	1.34	0.56
6B	0.00284	84.5	12.8	0.58	1.76	0.64

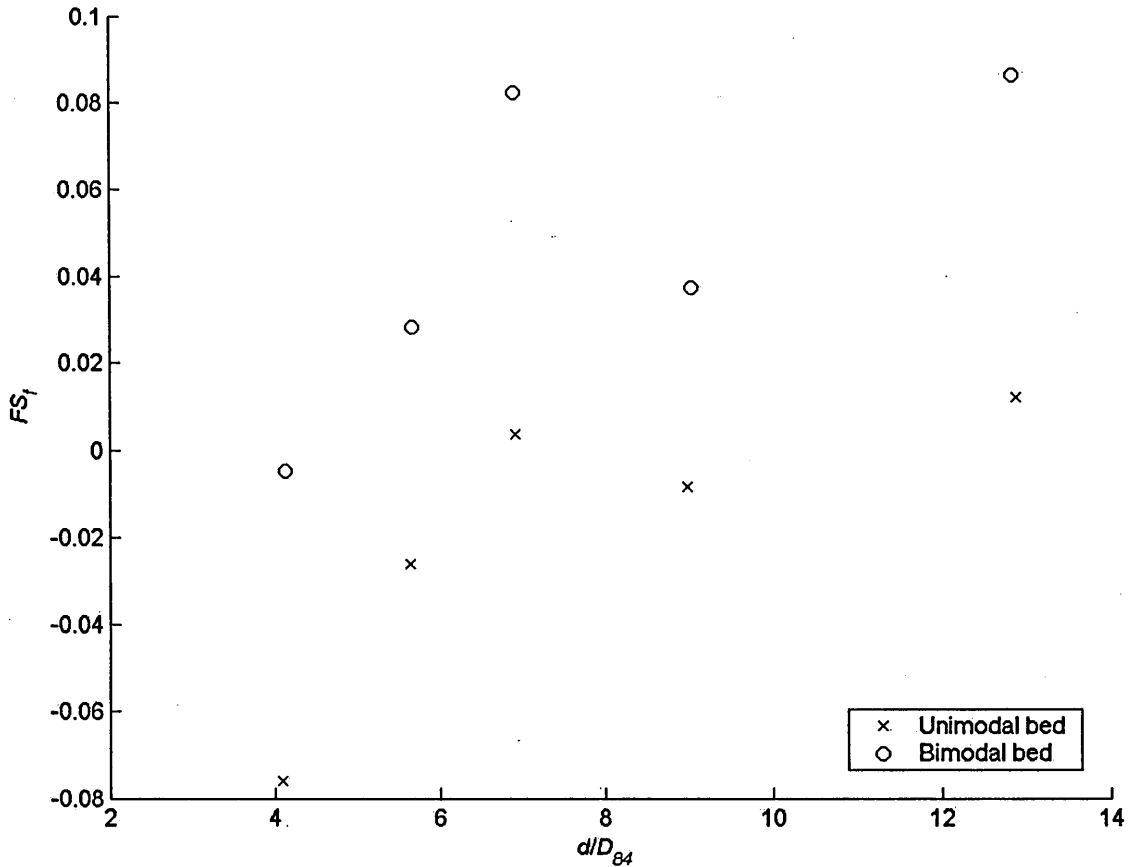


Figure 6.2. Variation in the fractional contributions made by the form-induced stresses to the total fluid stress FS_f with relative submergence d/D_{84} for the experimental runs carried out at a single bed slope over each of the beds, where d is flow depth and D_{84} is the grain size at which 84 per cent of the bed material is finer.

The contributions made by the form-induced stresses are small. Over the unimodal bed, the largest positive contribution is around 1 %, and the largest negative contribution is larger but still only nearly 8 %. Over the bimodal bed the range is from around a negative contribution of 0.5 % to up to a positive contribution of nearly 9 %. Clearly, the range of FS_f values for each bed is similar. It was seen in Chapter 4 that $\sigma_{\bar{u}}$ was consistently higher over the bimodal bed, albeit with $\sigma_{\bar{w}}$ being similar between the two beds. It would suggest therefore that the difference in spatial variability in \bar{u} , reflected through $\sigma_{\bar{u}}$, does not correspond with the difference in FS_f between the two beds.

There is a significant positive relationship between FS_f and relative submergence for both beds, and this corresponds with the general increase in $\sigma_{\bar{u}}$ and $\sigma_{\bar{w}}$ that was also

found with relative submergence in Chapters 4 and 5. It means that at the lowest submergences, the contributions made by the form-induced stresses are negative, but at the higher submergences, the contributions are positive. In other words, with an increase in relative submergence, it implies that there is a change from Reynolds stresses being greater than the total resultant fluid stress at the lower submergences to being lower than the total resultant fluid stress at the highest submergences. It would therefore suggest that an increase in relative submergence can result in a change in the amount of momentum carried by turbulent and spatial fluctuations in the flow. This suggests that the accuracy of using a linear extrapolation of Reynolds stress to the bed to predict mean bed shear stress could be a function of relative submergence. It means that a true and fair comparison with previous studies can only be made by comparing the values presented here to those values reported by others that were carried out at similar relative submergences. No other studies that have used different flow depths when studying the significance of form-induced stresses have been able to examine the effect of relative submergence (Nikora *et al.*, in press b; Maddux *et al.*, 2003). This is because they have only used a small number of different flow depths.

6.6 Variability in Form-Induced Stress with Bed Slope

The experimental runs performed at the same relative submergence are now analysed in order to discover whether bed slope also has an influence on the contributions of form-induced stress to the total fluid stress (Figure 6.3). For each bed, there are four relative submergences at which experimental runs have the same submergence (Tables 6.3 and 6.4). These runs were created through a combination of flow discharges and bed slopes. It can be seen once again that there are distinct differences in the type of contribution made by the form-induced stresses to the total fluid stress between the two beds. Over the unimodal bed, contributions are both positive and negative, indicating that the form-induced stress is acting in both the downstream and upstream direction. However, over the bimodal bed, apart from one experimental run, all the contributions are positive. The difference in FS_f values between the two beds again infers that the fractional contributions made by the Reynolds stresses over the unimodal bed are higher than over the bimodal bed.

The fractional contributions made by the form-induced stresses are small. Over the unimodal bed, the largest positive contribution is only around 5 %, and the largest

negative contribution is approximately 8 %. The positive contributions are typically larger over the bimodal bed, up to around 9 %, but the negative contribution is negligible at 0.5 %. The range of FS_f values are therefore much larger over the unimodal bed, indicating a greater variability in both the degree and type of contribution made by the form-induced stresses. The magnitude of the fractional contributions are not, however, greatly different given that $\sigma_{\bar{u}}$ was consistently higher over the bimodal bed. Such a difference does not induce such a great variation in absolute FS_f between the two beds, as the differences in the degree of spatial variability in \bar{u} initially suggested.

Over the unimodal bed, there is no consistent relationship between FS_f and bed slope. At relative submergences of both 4.1 and 9.0, a positive relationship is observed, but at a relative submergence of 5.7 an opposing association is observed, whilst for the remaining relative submergence, no consistent relationship is present. Over the bimodal bed, the experimental runs performed at three of the relative submergences display a positive relationship with bed slope, but a negative association is found for a relative submergence of 7.0. Therefore, again no consistent relationship is found between FS_f and bed slope. This is plausible given that $\sigma_{\bar{u}}$ and $\sigma_{\bar{w}}$, which is the major contributor to FS_f , also did not show any consistent relationship with bed slope over the two beds.

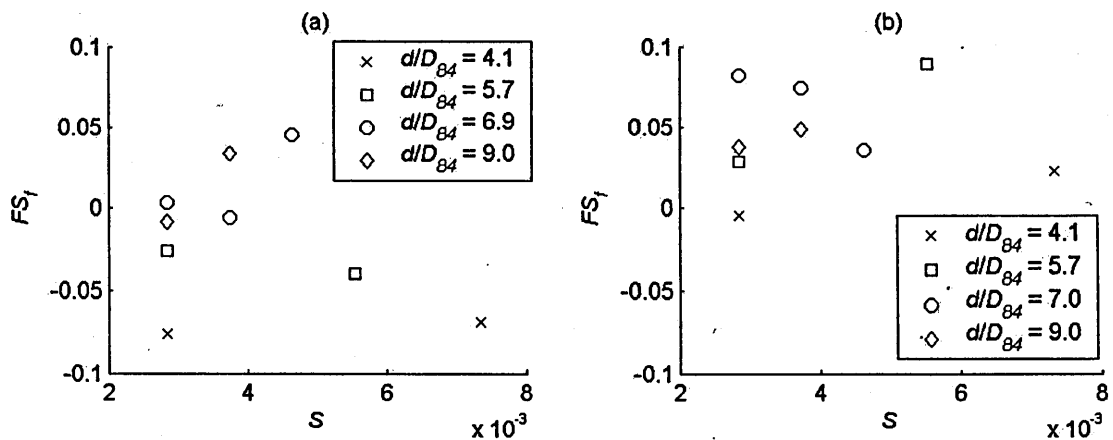


Figure 6.3. Variation in the fractional contributions made by the form-induced stresses to the total fluid stress FS_f with bed slope S for the experimental runs carried out at the same relative submergences over (a) the unimodal bed; and (b) the bimodal bed.

Table 6.3. Summary of the experimental conditions for the experimental runs carried out at the same relative submergences over the unimodal bed, where S is the bed slope, d is the flow depth, D_{84} is the grain size at which 84 per cent of the bed material is finer, \bar{U} is the average flow velocity (calculated from the ratio of flow discharge to the cross-sectional area of the flow), τ_0 is the bed shear stress and Fr is the Froude number (calculated from \bar{U}/\sqrt{gd} , where g is the force due to gravitational attraction).

Run	S	d (mm)	d/D_{84}	\bar{U} (m ² /s)	τ_0 (N/m ²)	Fr
2U	0.00285	28.6	4.1	0.27	0.72	0.51
12U	0.00735	29.5	4.2	0.44	1.90	0.83
3U	0.00285	39.5	5.6	0.32	0.95	0.52
10U	0.00555	39.9	5.7	0.49	1.87	0.78
4U	0.00285	48.4	6.9	0.36	1.13	0.52
8U	0.00375	48.2	6.9	0.47	1.77	0.69
9U	0.00465	49.2	7.0	0.50	1.87	0.72
5U	0.00285	62.8	9.0	0.45	1.40	0.57
7U	0.00375	63.5	9.1	0.51	1.86	0.65

6.7 Variability in Form-Induced Stress Under Conditions of Constant Bed Shear Stress

The experimental runs that were carried out at the same mean bed shear stress (Tables 6.5 and 6.6) are now assessed for each bed. These experimental runs involved a combination of bed slopes and flow depths, and therefore encompass the effects of both relative submergence and bed slope. It means that an assessment can be made of which of these two variables has a greater effect on FS_f , by examining which of the effects of the variables, established from above, is evident. Under these conditions of constant mean bed shear stress, the implication is that the average rate of momentum transfer at the bed is approximately the same for each of the experimental runs. Therefore, for example, if FS_f changes under these conditions, the relative contribution from both the Reynolds stress and form-induced stress must also change. It would then suggest that the momentum transfer mechanisms for each of the experimental runs are different even

when the rate of transfer is the same. The variable that is the primary cause of these changes can then be inferred.

The variation in FS_f under these conditions of constant mean bed shear stress is examined in Figure 6.4 for both beds. The FS_f values have been plotted against relative submergence, but equally could have been plotted against bed slope. Again it can be seen that there are clear differences in FS_f values between the two beds. There are an equal number of experimental runs that have negative and positive contributions over the unimodal bed, but all experimental runs display positive contributions over the bimodal bed. The difference in FS_f values again implies that the contributions made by the Reynolds stress are higher over the unimodal bed.

Table 6.4. Summary of the experimental conditions for the experimental runs carried out at the same relative submergences over the bimodal bed, where S is the bed slope, d is the flow depth, D_{84} is the grain size at which 84 per cent of the bed material is finer, \bar{U} is the average flow velocity (calculated from the ratio of flow discharge to the cross-sectional area of the flow), τ_0 is the bed shear stress and Fr is the Froude number (calculated from \bar{U}/\sqrt{gd} , where g is the force due to gravitational attraction).

Run	S	d (mm)	d/D_{84}	\bar{U} (m ² /s)	τ_0 (N/m ²)	Fr
2B	0.00284	27.2	4.1	0.20	0.68	0.39
12B	0.00734	26.8	4.1	0.27	1.74	0.52
3B	0.00284	37.3	5.7	0.28	0.90	0.47
10B	0.00554	37.1	5.6	0.39	1.75	0.65
4B	0.00284	45.5	6.9	0.36	1.07	0.53
8B	0.00374	46.6	7.1	0.40	1.71	0.60
9B	0.00464	47.2	7.2	0.47	1.80	0.69
5B	0.00284	59.5	9.0	0.43	1.34	0.56
7B	0.00374	59.4	9.0	0.47	1.76	0.62

Table 6.5. Summary of the experimental conditions for the experimental runs carried out at the same mean bed shear stress over the unimodal bed, where S is the bed slope, d is the flow depth, D_{84} is the grain size at which 84 per cent of the bed material is finer, \bar{U} is the average flow velocity (calculated from the ratio of flow discharge to the cross-sectional area of the flow), τ_0 is the bed shear stress and Fr is the Froude number (calculated from \bar{U}/\sqrt{gd} , where g is the force due to gravitational attraction).

Run	S	d (mm)	d/D_{84}	\bar{U} (m ² /s)	τ_0 (N/m ²)	Fr
6U	0.00285	90.0	12.9	0.62	1.85	0.66
8U	0.00375	63.5	9.1	0.51	1.86	0.65
9U	0.00465	49.2	7.0	0.50	1.87	0.72
10U	0.00555	39.9	5.7	0.49	1.87	0.78
11U	0.00645	33.5	4.8	0.413	1.87	0.72
12U	0.00735	29.5	4.2	0.44	1.90	0.83

Table 6.6. Summary of the experimental conditions for the experimental runs carried out at the same mean bed shear stress over the bimodal bed, where S is the bed slope, d is the flow depth, D_{84} is the grain size at which 84 per cent of the bed material is finer, \bar{U} is the average flow velocity (calculated from the ratio of flow discharge to the cross-sectional area of the flow), τ_0 is the bed shear stress and Fr is the Froude number (calculated from \bar{U}/\sqrt{gd} , where g is the force due to gravitational attraction).

Run	S	d (mm)	d/D_{84}	\bar{U} (m ² /s)	τ_0 (N/m ²)	Fr
6B	0.00284	84.5	12.8	0.58	1.76	0.64
8B	0.00374	59.4	9.0	0.47	1.76	0.62
9B	0.00464	47.2	7.2	0.47	1.80	0.69
10B	0.00554	37.1	5.6	0.39	1.75	0.65
11B	0.00644	31.7	4.8	0.35	1.77	0.62
12B	0.00734	26.8	4.1	0.27	1.74	0.52

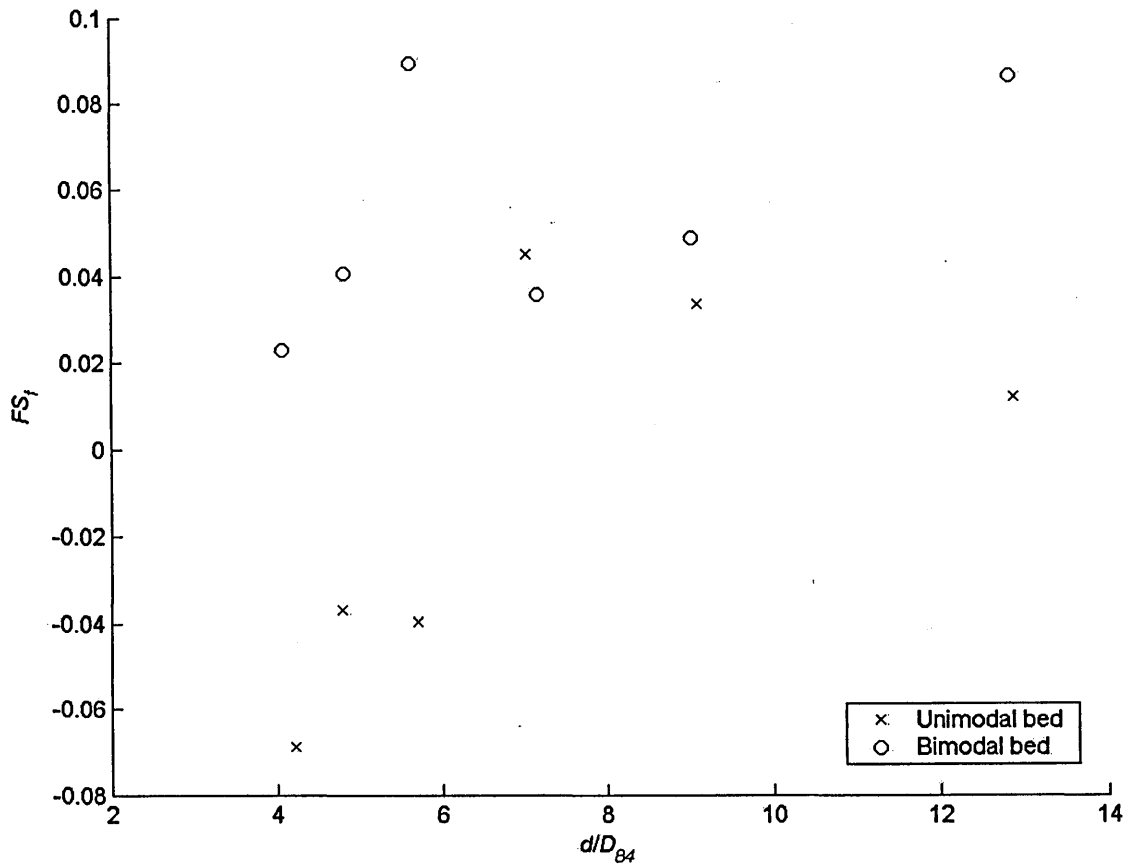


Figure 6.4. Variation in the fractional contributions made by the form-induced stresses to the total fluid stress FS_f with relative submergence d/D_{84} for the experimental runs carried out at the same mean bed shear stress over each of the beds, where d is flow depth and D_{84} is the grain size at which 84 per cent of the bed material is finer.

The contributions made by the form-induced stresses are small over both beds. Over the unimodal bed, the largest positive contribution is just under 5% and the largest negative contribution is slightly higher at around 7%. Over the bimodal bed, the positive contributions are as high as around 9%, but can be as low as just over 2%. The range of FS_f values is clearly higher over the unimodal bed. The experimental runs performed at the lowest relative submergences display the greatest variation between the beds.

Another key feature of the plots is that despite the mean bed shear stress being the same for each experimental run over a given bed, there are significant variations in FS_f . These, in general, increase with relative submergence over each bed, and therefore

decrease with bed slope. Over the bimodal bed, there is almost a fourfold increase in FS_f with relative submergence from the lowest to the highest relative submergence. In other words FS_f increases nearly four times from the highest to the lowest bed slope. This therefore infers that the fractional contributions made by Reynolds stress are reducing with increases in relative submergence, and increasing with a reduction in bed slope. Over the unimodal bed, the changes can be such that at the lowest submergence (or highest bed slope), form-induced stress can make a negative contribution but then a positive contribution at the highest submergences (lowest bed slope). This implies that for the experimental runs at the lowest submergences and highest bed slopes, the Reynolds stress can be greater than the total fluid stress. However, at the higher submergences and shallower bed slopes, the Reynolds stress could be less than the total fluid stress, making less of a contribution. This indicates that the momentum transfer mechanisms change even for experimental runs that have approximately the same average rate of momentum transfer at the bed.

The discrepancy between the variation in FS_f with bed slope to that observed for the experimental runs carried out at the same relative submergences, suggests that bed slope is unlikely to account for these changes in momentum transfer mechanisms. However, the same positive relationship between FS_f and relative submergence was also observed at a single bed slope over both beds. It would therefore appear that a change in relative submergence might be the primary cause for a change in FS_f over a given bed.

6.8 Does Relative Submergence or Bed Slope have the Greater Influence on Form-induced Stress?

Although the experimental runs performed at the same mean bed shear stress provide an indication as to whether relative submergence or bed slope has the primary influence on FS_f , a more rigorous approach is required. This can be achieved by carrying out a multiple linear regression between the predictor variables, relative submergence and bed slope, and the response variable FS_f ,

$$FS_f = \alpha + \beta_1 \frac{d}{D_{84}} + \beta_2 S \quad (6.15)$$

This provides a simple model for estimating FS_f and for calculating the percentage of the variation in FS_f between experimental runs that is explained by differences in relative submergence and bed slope, given by R^2 . A bivariate linear regression was also carried out between FS_f and relative submergence, and between FS_f and bed slope. These values were taken from each of the 11 experimental runs over the two beds. The R^2 values from these regressions are compared to establish the relative strength of the relationships of the two variables with FS_f , and by what degree each variable contributed to the strength of the associations in equation (6.15). It was found that a simple linear regression between FS_f and relative submergence, and between FS_f and bed slope produced higher R^2 values than through any multiplicative transform of the variables (not shown).

In Table 6.7 the R^2 values resulting from these bivariate and multiple regressions for FS_f are shown. It can be seen that over the unimodal bed, there is no strong association between FS_f and relative submergence across all 11 of the experimental runs, unlike that seen at a single bed slope and the same mean bed shear stress. This also applies over the bimodal bed, where the relationship is even weaker. There is an even poorer relationship between FS_f and bed slope both of the beds. The association between FS_f and relative submergence largely influences the R^2 values from the multiple regression over each of the beds. Bed slope has a greater influence over the bimodal bed than the unimodal bed, but this is small. It is clear that relative submergence in addition to bed slope has far more effect on FS_f , than bed slope in addition to relative submergence, over each of the beds. It shows that bed slope does have a small effect on FS_f , but that its effects operate mainly via relative submergence.

The p -values for β_1 and β_2 are also shown in Table 6.7 for each of the beds. Over the unimodal bed it can be seen that the association between relative submergence and FS_f is statistically significant at the 5 % level, but the association between bed slope and FS_f is not. Over the bimodal bed, the significance of the relationships between both relative submergence and bed slope with FS_f are also not statistically significant. Nonetheless it shows that over both of the beds, relative submergence has a greater influence than

bed slope on FS_f . It means that relative submergence mainly caused the change in FS_f under conditions of constant mean bed shear stress. It would therefore appear that a change in relative submergence could be the primary cause for a change in momentum transfer mechanisms over water-worked gravel beds.

Table 6.7. The R^2 values from the bivariate linear regression between relative submergence d/D_{84} and the fractional contributions made by the form-induced stresses to the total fluid stress FS_f , and between bed slope S and FS_f for the two beds. Also shown are the R^2 values, multiplying coefficients β , and p -values from the multiple linear regression between predictor variables, d/D_{84} and S , and response variable FS_f for the two beds.

Bed	Bivariate R^2		Multiple	β		Multiple p -values	
	d/D_{84}	S	R^2	d/D_{84}	S	d/D_{84}	S
Unimodal	0.48	0.13	0.48	0.010	-0.32	0.049	0.97
Bimodal	0.27	0.070	0.32	0.0076	4.60	0.093	0.49

6.9 Lateral Variability in Form-induced Stress over the Bed

The only other study that has used PIV to examine the significance of form-induced stresses over a gravel bed was that made Campbell *et al.* (2005), who used one vertical plane measurement on the centreline of the flume. It is therefore useful to examine the form-induced stresses at each of the nine lateral locations across the bed, in order to understand the reasons for the differences in the FS_f values presented here to those presented by Campbell *et al.* This will allow a more direct comparison of FS_f , so it can be seen how representative the values presented were, and it will also be possible to discover the degree to which fractional contributions vary across the bed.

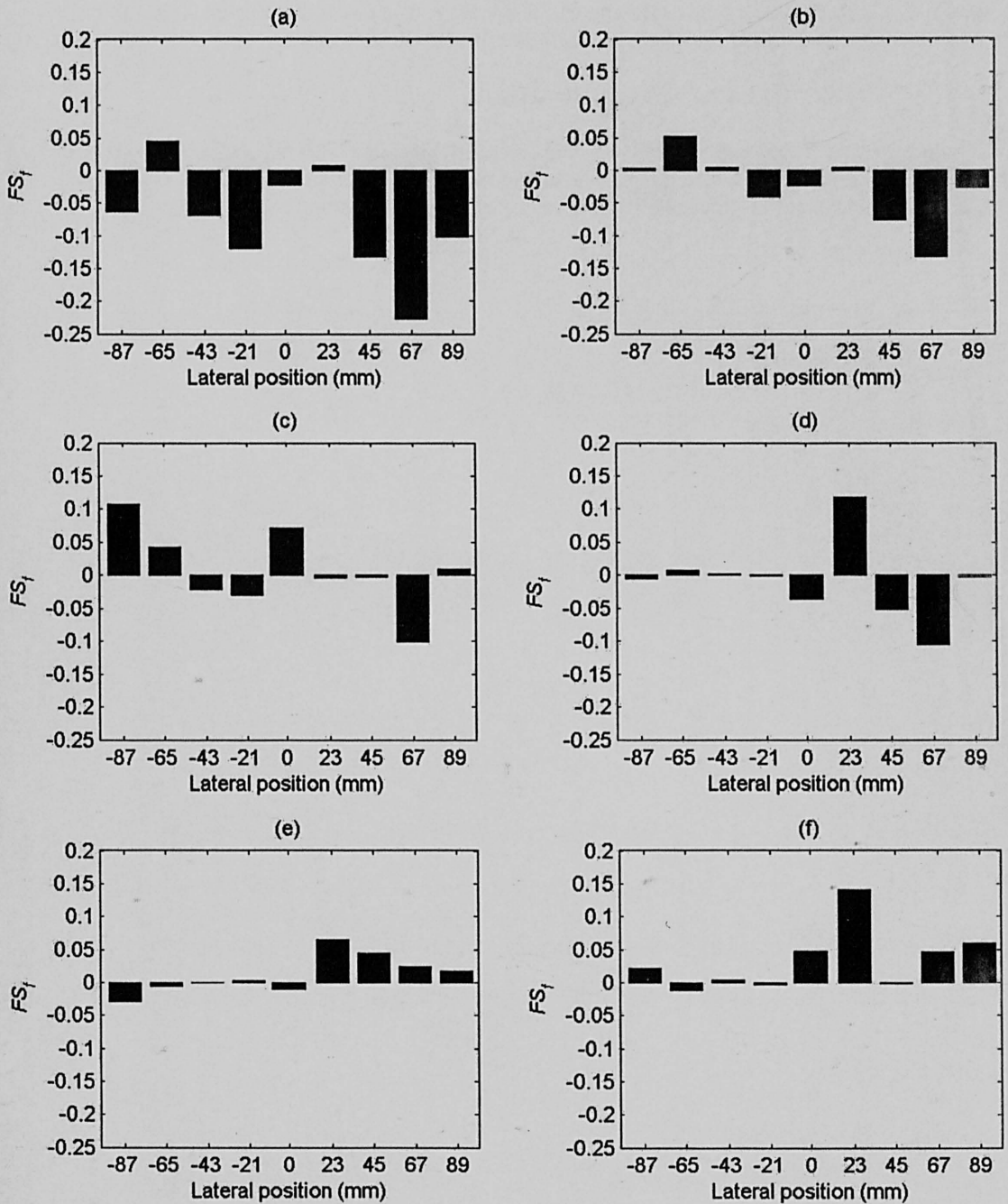
For each lateral location, the $\tilde{u}\tilde{w}$ values were taken and spatially-averaged to produce $\langle\tilde{u}\tilde{w}\rangle$ values for nine lateral locations across the bed. The streamwise length of the measurement areas for each vertical plane measurement was 138.165 mm which means

that the $\tilde{u}\tilde{w}$ values were averaged over an area of 312.9 mm². From this, FS_f was calculated, producing nine FS_f values for each experimental run. These values are presented in Figures 6.5 and 6.6 for the unimodal and bimodal beds, respectively. It is noticeable that there is considerable lateral variability in FS_f between the nine different measurements for each of 11 experimental runs over both of the beds. Over the unimodal bed, the result is that for a given experimental run, one lateral location can indicate that form-induced stress is making a large positive contribution, whilst another can indicate it is making a considerable negative contribution. For example for run 4U (Figure 6.5d), at one lateral location form-induced stress can make a positive contribution of nearly 15 %, but at another it can make a negative contribution of over 10 %. A similar situation is also observed for the bimodal bed. For example for run 6B, one lateral location indicates that form-induced stress is making nearly a 35 % positive contribution to the total fluid stress, but at another it indicates that form-induced stress is making a negligible contribution. This lateral variability over both of the beds suggests that the contributions made by Reynolds stresses could also demonstrate considerable lateral variability across water-worked gravel beds. Lien and Yee (2004) also examined the lateral variability in form-induced stresses. By averaging over long, thin slabs of fluid at different lateral positions within an array of cubes, they found that the form-induced stress for one slab could be up to 6 times larger than for another slab at the same relative height. Although greater differences are observed for some of the experimental runs in Figures 6.5 and 6.6, Lien and Yee's results are within the typical range of lateral variability seen in these figures.

The FS_f values presented in Figures 6.5 and 6.6 are significantly larger than those derived as representative of the whole bed. They indicate that form-induced stresses can locally make very significant contributions to the total fluid stress, both in the upstream and downstream direction. Over the unimodal bed, the maximum positive contribution is nearly 20 % and the maximum negative contribution is over 20 %. Over the bimodal bed, this is nearly 35 % and over 10 %, respectively.

It is clear that a lateral location over a given bed that makes either a positive or negative contribution for one experimental run does not always make the same direction of contribution for another experimental run. In addition, the magnitude of FS_f for a given lateral location can also vary between experimental runs. The results from

Chapter 4 showed how the spatial pattern in $\bar{u}/\langle\bar{u}\rangle$ changed with relative submergence. Relative submergence is likely to have determined whether a vertical plane PIV measurement was located in a streamwise strip of positive or negative \tilde{u} . This, combined with the fact that in Chapter 5 the spatial pattern in \tilde{w}/u_* was found to not be consistent across all runs for a given lateral location, is likely to have caused the disassociation in FS_f for a given lateral location between the runs. Therefore, FS_f for an individual lateral location is likely to be poorly related to the location of individual roughness elements on the beds.



Continued from previous page

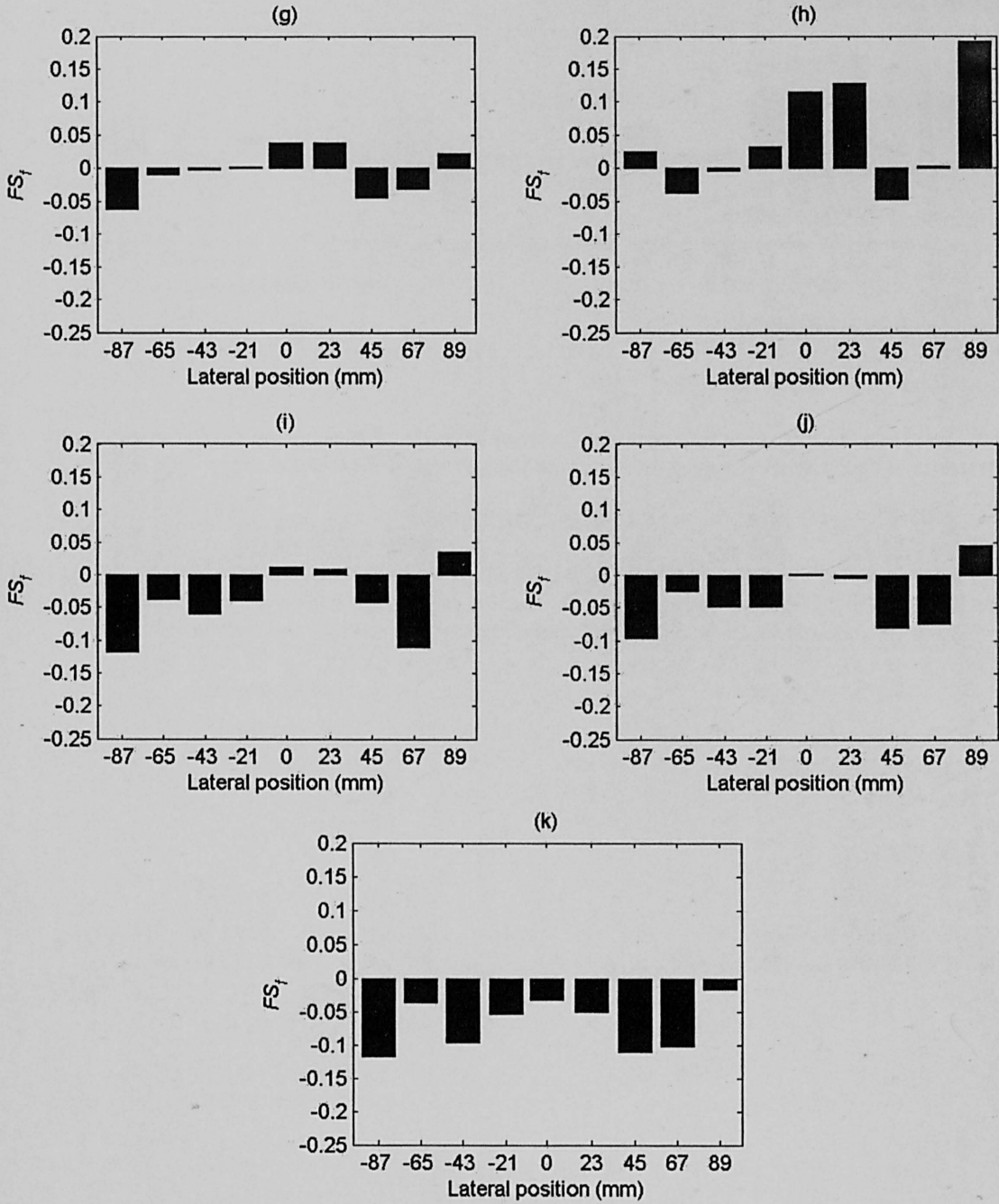
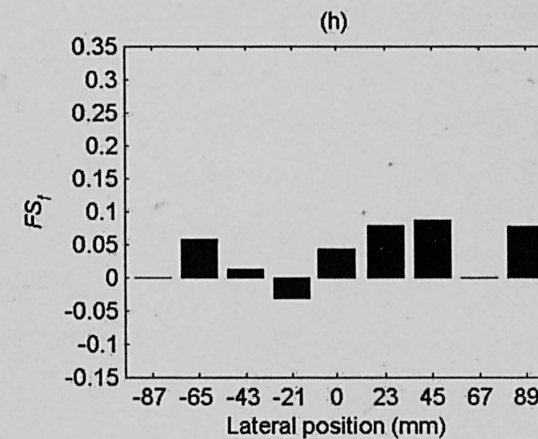
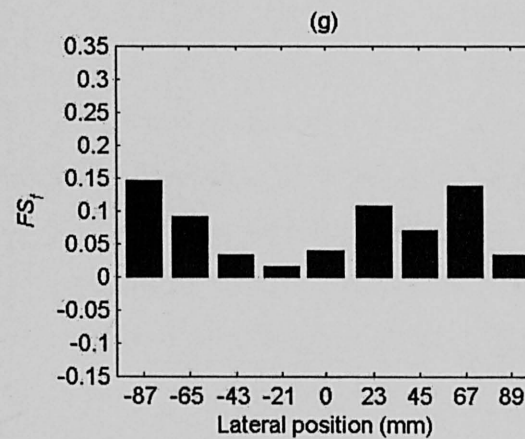
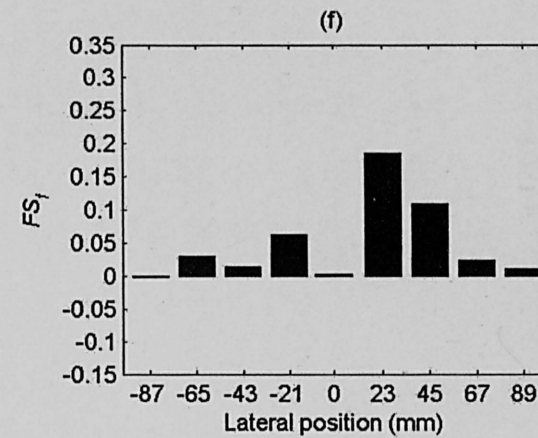
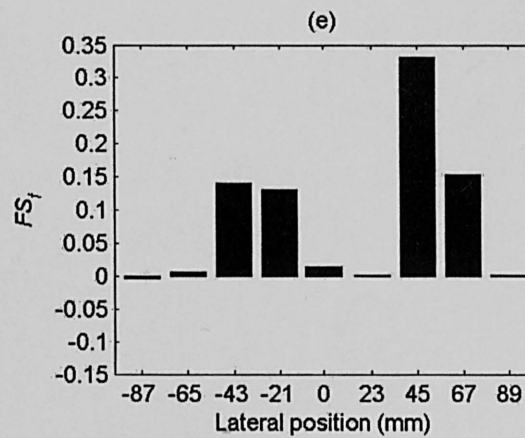
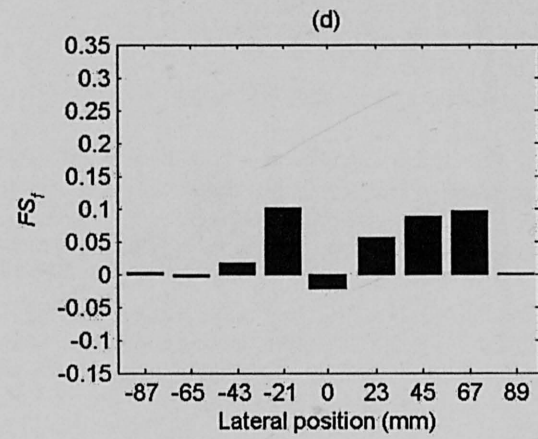
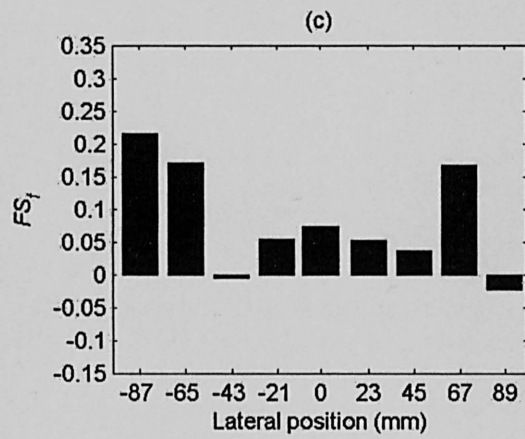
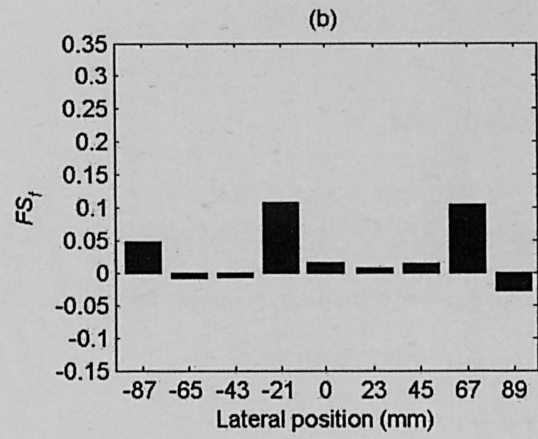
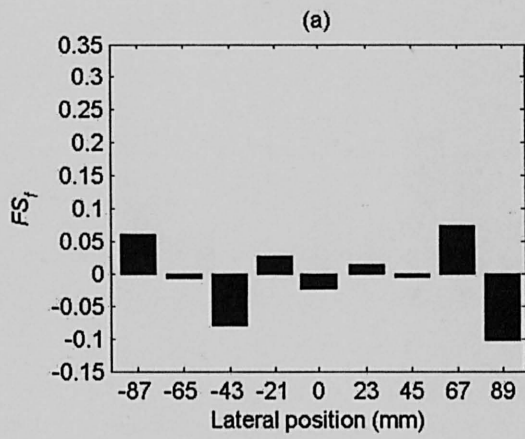


Figure 6.5. Lateral variation in the fractional contributions made by the form-induced stresses to the total fluid stress FS_f over the unimodal bed for (a) run 2U; (b) run 3U; (c) run 4U; (d) run 5U; (e) run 6U; (f) run 7U; (g) run 8U; (h) run 9U; (i) run 10U; (j) run 11U; and (k) run 12U. A lateral position of 0 mm denotes the centreline of the flume.



Continued overleaf

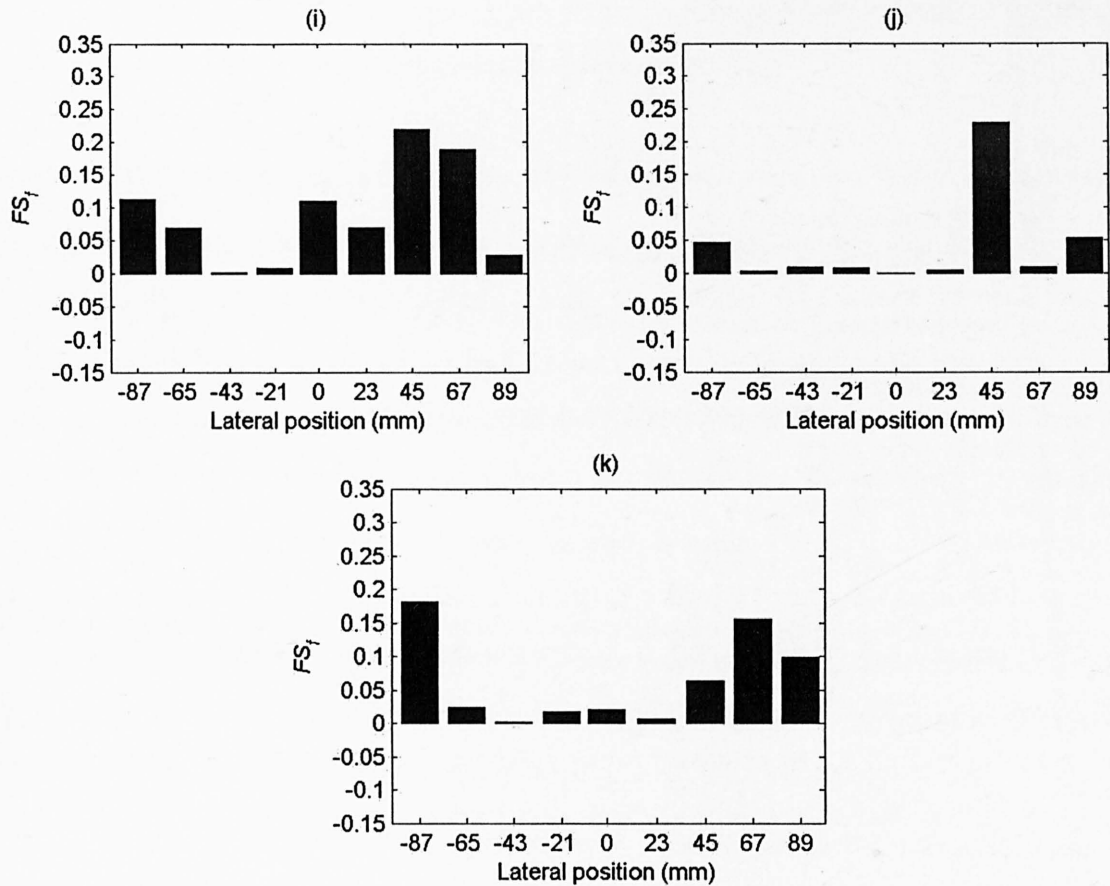


Figure 6.6. Lateral variation in the fractional contributions made by the form-induced stresses to the total fluid stress FS_f over the bimodal bed for (a) run 2B; (b) run 3B; (c) run 4B; (d) run 5B; (e) run 6B; (f) run 7B; (g) run 8B; (h) run 9B; (i) run 10B; (j) run 11B; and (k) run 12B. A lateral position of 0 mm denotes the centreline of the flume.

The majority of the FS_f values in Figures 6.5 and 6.6 are more comparable to other studies that have studied the significance of form-induced stresses above rough boundaries at a similar relative height within the flow, than those derived as representative of the whole bed. It has been found that positive contributions can typically be around 12-16 % for fixed, 2-D (Nikora *et al.*, in press b) and 3-D (Maddux *et al.*, 2003) dune shaped bedforms, 2-D transverse ribs (Pokrajac *et al.*, 2003; Nikora *et al.*, in press b), static armoured beds (Nikora *et al.*, in press b) and fixed gravel bed with moving bedload (Campbell *et al.*, 2005). However, in this later case, during no feed they found much higher positive contributions of 30 %, and these levels were only found for one lateral location over the bimodal bed. Yet it is interesting that the FS_f

values produced by spatially averaging over a smaller area and over a smaller number of measurements, are now more comparable to previous studies.

However, the considerable variability in FS_f values across the nine lateral locations for an experimental run highlights a concern over how representative the form-induced stresses presented by previous studies are likely to be. The FS_f values for each lateral location over the bed in Figures 6.5 and 6.6 was based on averaging 61 measurements, but other studies have typically only used between 10 and 25 point measurements to represent FS_f for the whole boundary. For example, Nikora *et al.* (in press b) took 24 randomly located measurements over a static armoured bed, a bed that has a considerably greater degree of surface complexity than the two beds examined here (see Aberle and Nikora, submitted). This concern does not only apply to the use of point measurements to examine form-induced stresses. Campbell *et al.* (2005) only used one vertical plane PIV measurement, and this was over an area less than half of that used here.

6.10 Form-induced Stresses at the Point Measurement Scale

This reliance on using point velocity measurements to estimate form-induced stress over a rough boundary (Raupach *et al.*, 1986; Böhm *et al.*, 2000; Nikora *et al.*, 2001; Cheng and Castro, 2002; Maddux *et al.*, 2003; Poggi *et al.*, 2004; Nikora *et al.*, in press b) means that it is desirable to examine the form-induced stresses at this point measurement scale in order to understand the reasons for the differences in the FS_f values presented here, to those by other studies. It should also provide an indication of how representative their measurements are likely to have been, and how representative future attempts using point measurements, such as in the field, are likely to be.

The separation distance between measurement positions and the height of the averaging slab was 2.265 mm, so the $\tilde{u}\tilde{w}$ values were spatially-averaged over an area of 5.130 mm². This area is equivalent to the area of fluid (or interrogation area) which the PIV software integrated over in order to detect the most probable velocity within this small area. Spatially averaging in this manner produced 549 $\langle\tilde{u}\tilde{w}\rangle$ values for each experimental run. This is nearly 22 times more measurements than those used by Nikora *et al.* (in press b) over a static, armoured bed. From these values, 549 FS_f values were

produced for each run. The D_{50} of the unimodal and bimodal beds were 4.971 and 4.415 mm, respectively. Assuming that the area of the median grain on the bed can be approximated by the area of a circle, the D_{50} values can be used to calculate areas of 19.41 mm² and 15.31 mm² for the median grain for the unimodal and bimodal bed, respectively. Comparing these areas to the averaging area of 5.130 mm², it means that the form-induced stresses can be examined at the sub-grain scale.

The FS_f values are presented in the form of a probability density function (*pdf*) in Figure 6.7 for each of the experimental runs over the two beds. Displaying the FS_f values in this way enables the range of values over the bed to be easily assessed and for the shape of distribution to be seen. Many of the distributions in Figure 6.7 have a well defined peak and long tails. This has also been found for the distributions of Reynolds stress fluctuations over time (e.g. Antonia and Atkinson, 1973; Nakagawa and Nezu, 1977). Over the unimodal bed, it can be seen that the long tails indicate that form-induced stresses can make both positive and negative contributions of up to 70 % to the total fluid stress at particular locations over the bed. Whilst over the bimodal bed, positive and negative contributions can be as large as nearly 100 %. This indicates that at some positions over the bed, form-induced stress can fully carry the fluid stress. The spread of FS_f values is very large, orders of magnitude greater than the mean. The distributions demonstrate that form-induced stress over some areas of the bed are likely to contribute significantly to the fluid stress but to experience much lower Reynolds stress contributions, and the converse will happen over other areas of the bed. It means that the use of a point velocity measurement to determine the Reynolds stress, for predicting the mean bed shear stress, is likely to give variable results across the bed. Measurements over some areas of the bed are likely to over-predict heavily the mean bed shear stress, whilst others will significantly under-predict the mean bed shear stress. For example, over the bimodal bed, form-induced stress contributions to the total fluid stress, and by inference contributions made by Reynolds stress, at some positions could be as much as double that at other positions over the bed. It indicates that there is significant spatial variability in the manner in which momentum is transferred over the beds.

A comparison of these FS_f values to those presented by previous studies at a similar relative height above the bed, reveals that they are typical of those found by Nikora *et*

al. (2001) from ADV measurements at points within an arrangement of fixed spheres in a laboratory flume. They are also similar to the values reported by Campbell *et al.* (2005) for much of their screeded, fixed gravel bed, but they did find that the isolated particle on the bed caused contributions as high as 650 % of the total fluid stress, which is unlikely to be representative of a water-worked gravel bed.

The distributions suggest that the use of a low number of point velocity measurements over a water-worked gravel bed, or indeed over other spatially complex bed surfaces, is unlikely to sample fully the range of FS_f values, and by inference, also the range of Reynolds stress fractional contributions over the bed. It is likely to lead to a misleading understanding of the processes transferring momentum in the flow, and misrepresentative predictions of mean bed shear stress.

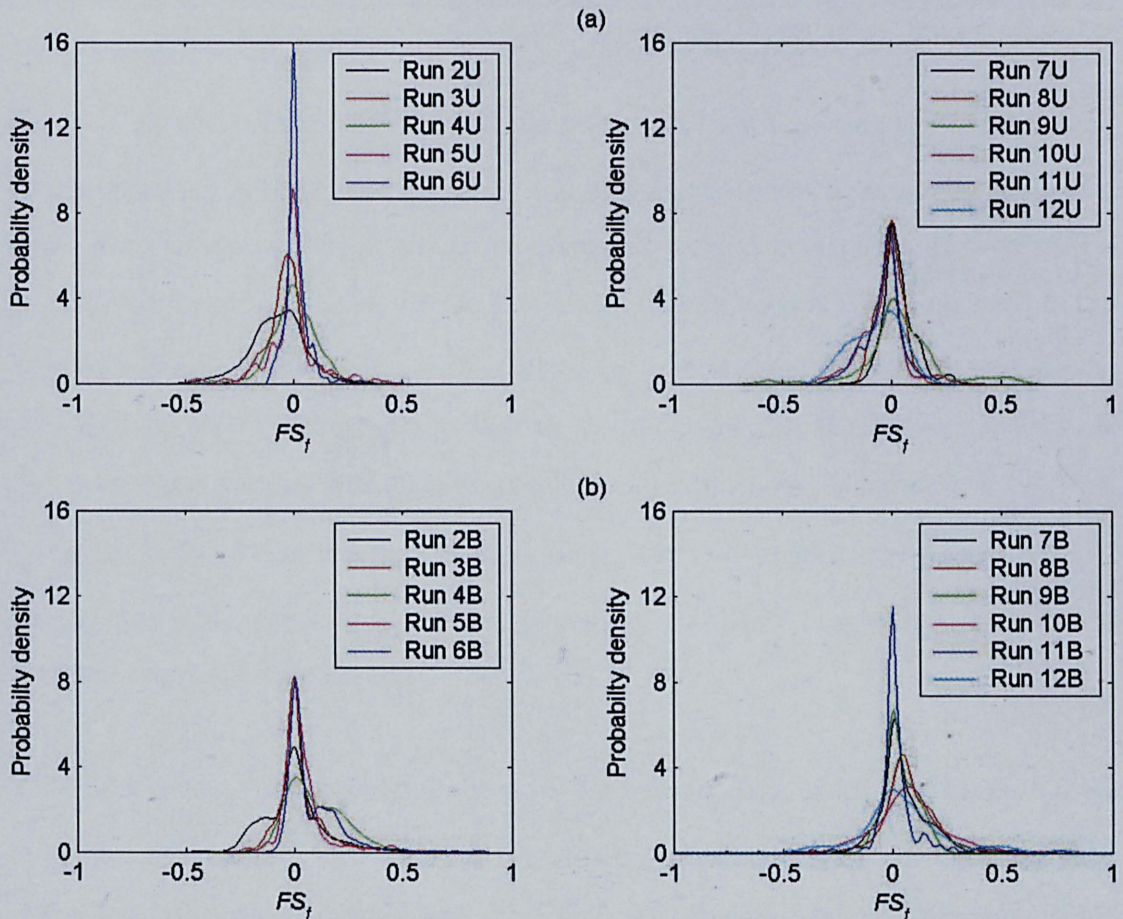


Figure 6.7. Probability density functions of the fractional contributions made by the form-induced stresses at the point measurement scale FS_f for each of the experimental runs over (a) the unimodal bed; and (b) the bimodal bed.

6.11 Spatial Variability in Form-induced Stress over the bed at the Point Measurement Scale

The spread of values in the distributions of FS_f for each of the experimental runs in Figure 6.7 reveals that there is considerable spatial variability in form-induced stress over the two beds. This needs to be quantified in order to understand fully whether estimates of FS_f from point velocity measurements are likely to be representative of the whole bed surface. This variability is given by the second-order moment of the distribution of FS_f at the point measurement scale over the bed σ_{FS_f}

$$\sigma_{FS_f} = \sqrt{\frac{1}{N} \sum_{i=1}^N (FS_{f_i} - \langle FS_f \rangle)^2} \quad (6.16)$$

where N is the total number of measurements within the nine vertical plane measurements (= 549) and $\langle FS_f \rangle$ is FS_f spatially-averaged over these nine planes. The σ_{FS_f} for each of the experimental runs over both beds are displayed in Figure 6.8. This is presented in the form of a direct comparison between the two beds in order to enable the distributions from all 22 experimental runs to be examined, producing a summary of the σ_{FS_f} values for the two beds. This is possible because each of the experimental runs over the bimodal bed were designed so that the relative submergence and bed slope were similar to the runs over the unimodal bed. It can be seen from the σ_{FS_f} values that there is considerable spatial variability in FS_f over each of the beds. For the majority of the runs σ_{FS_f} is larger than $\langle FS_f \rangle$. It suggests once again that it is unlikely that a low number of point measurements can fully sample the variability in form-induced stress over the bed.

The values of σ_{FS_f} are typically higher over the bimodal bed, and there is a good range of values over each bed. These were found to be unrelated to either relative submergence or bed slope under any condition (not shown). This implies that it is not possible to predict what the spatial variability in form-induced stress contributions is likely to be over a water-worked gravel bed. By implication, it also implies that the spatial variability in Reynolds stress contributions cannot be easily predicted.

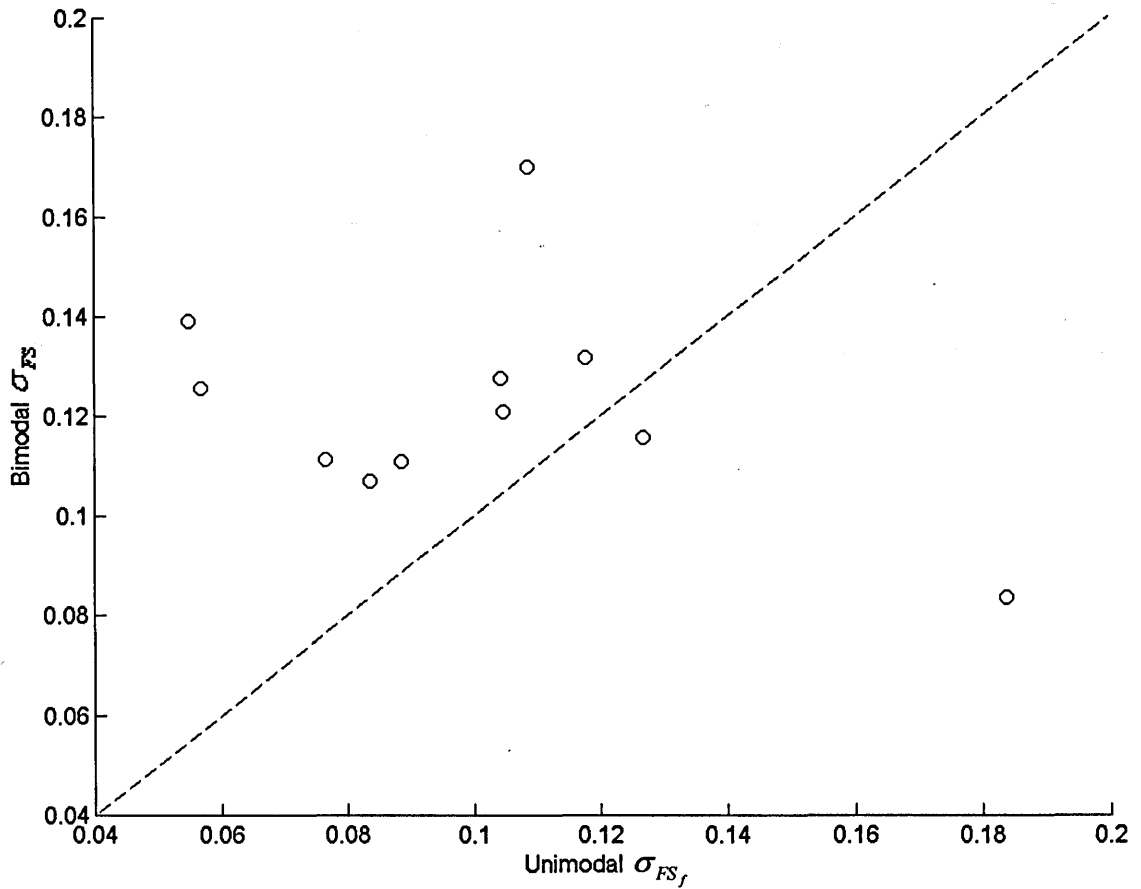


Figure 6.8. A comparison of the standard deviation in the fractional contributions made by the form-induced stresses at the point measurement scale σ_{FS_f} between the two beds. The dashed line is a line of equality.

Kanda *et al.* (2004) examined the degree of spatial variability in total momentum flux over an array of cubes using an equation equivalent to (6.16). They found standard deviation values of around 0.4 to 0.6 at the same relative heights as examined here. Given the results in Figure 6.8, it is likely that similar degrees of spatial variability in total fluid stress are likely to be observed over the unimodal and bimodal beds.

6.12 The Relationship Between the Form-induced Stresses at the Point Measurement Scale and Bed Surface Topography

The *pdf*'s of FS_f showed that there are likely to be regions of the bed where form-induced stress can contribute significantly to the fluid stress and to experience low Reynolds stress contributions, and for other areas of the bed to experience the complete

reverse. This was shown to lead to considerable spatial variability in FS_f over each of the beds. It needs to be understood whether this variability in form-induced stress contributions is associated with the surface topography of the bed. This is achieved by carrying out a simple cross-correlation between FS_f and bed surface elevation z_b . This is only carried out for the measurements of FS_f and z_b that have the same lateral positions over the bed. This clearly does not take into account any lateral correlation in bed surface elevation that could influence FS_f . In other words it does not account for the effect of any spatially coherent bed structure that could influence FS_f . A cross-correlogram was used to quantify the spatial covariance between pairs of FS_f and measurements of z_b . A series of streamwise lags l_x between FS_f and z_b were applied to take into account the streamwise propagation of the flow relative to the bed. Using a cross-correlogram in this way means that the cross-covariance C between FS_f and z_b is given by

$$C(l_x) = \frac{1}{N_C} \sum_{x=2.265}^{N_C} FS_f(x) \cdot z_b(x-l_x) - m_{FS_f} \cdot m_{z_b} \quad (6.17)$$

where

$$m_{FS_f} = \frac{1}{N_C} \sum_{x=2.265}^{N_C} FS_f(x) \quad (6.18)$$

$$m_{z_b} = \frac{1}{N_C} \sum_{x=2.265}^{N_C} z_b(x-l_x) \quad (6.19)$$

and N_C is the number of cross-correlated measurements and x is the streamwise position within the measurement section. From this, a cross-correlogram was used to calculate the correlation coefficient η to provide a measure of spatial cross-correlation:

$$\eta(l_x) = \frac{C(l_x)}{\sqrt{\sigma_{FS_f}^2 \cdot \sigma_{z_b \Delta x}^2}} \in [-1, +1] \quad (6.20)$$

where

$$\sigma_{FS_f}^2 = \frac{1}{N_C(l_x)} \sum_{x=2.265}^{N_C} [FS_f(x) - m_{FS_f}]^2 \quad (6.21)$$

and

$$\sigma_{z_b}^2 = \frac{1}{N_C} \sum_{x=2.265}^{N_C} [z_b(x - l_x) - m_{z_b}]^2 \quad (6.22)$$

A maximum lag of 100 mm was chosen to account fully for the propagation possible for the range of $\langle \bar{u} \rangle$ values. This resulted in less than all the FS_f values being available for the correlation.

The η values are shown in Figure 6.9 for each of the experimental runs over the two beds. It can be seen that over the unimodal bed there is a poor association between FS_f and z_b , with only three runs having reasonably high η values. This association is even poorer over the bimodal bed. The results are not surprising given that the distributions of $\bar{u}/\langle \bar{u} \rangle$ and \tilde{w}/u_* were also found to have a relatively poor linear association with z_b . However, given that a η value of zero does not necessarily mean that there is no correlation at all, the results do not rule out any subtle or more complicated association between FS_f and z_b , such as a high non-linear correlation, or a relationship between FS_f and any spatially coherent bed features.

6.13 The Effect of Averaging Area on the Estimation of Form-induced Stress

It has been seen how the fractional contributions of the form-induced stresses to the total fluid stress change according to the position and size of area over which the $\tilde{u}\tilde{w}$ values are integrated. An examination of how the fractional contributions progressively change with averaging area should provide some indication of the importance of averaging area. This should therefore indicate whether studies using different averaging areas (and hence, in most cases, involving a different number of averaged

measurements) are comparable, and what effect such differences are likely to have on their estimations of form-induced stress over the bed.

For every possible averaging area, the FS_f values were calculated. This was carried out firstly by taking the $\tilde{u}\tilde{w}$ values at each lateral location and averaging them over all possible streamwise lengths within the measurement area. Therefore the averaging was carried out from the point measurement scale, an area of 5.130 mm^2 , until the values were averaged over all nine lateral locations, at an averaging area of 2816.5 mm^2 . This resulted in a decreasing number of FS_f values at each averaging area as averaging area was increased. The $\langle \bar{u} \rangle$ and $\langle \bar{w} \rangle$ values were the same as used earlier and remained the same for all averaging areas.

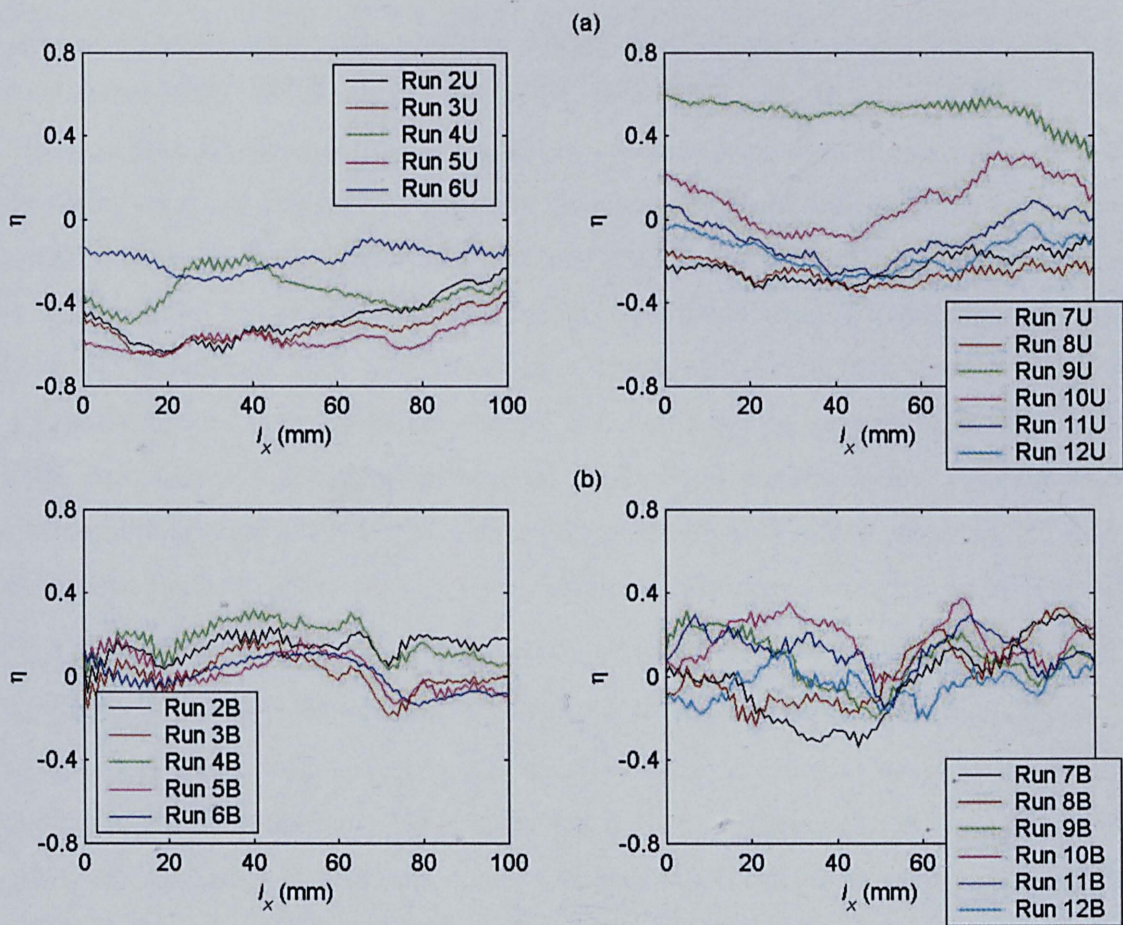
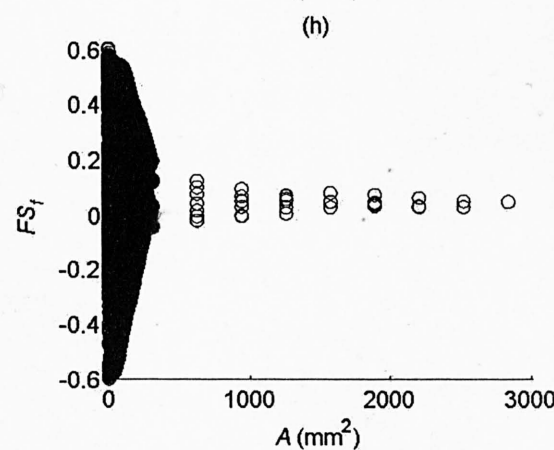
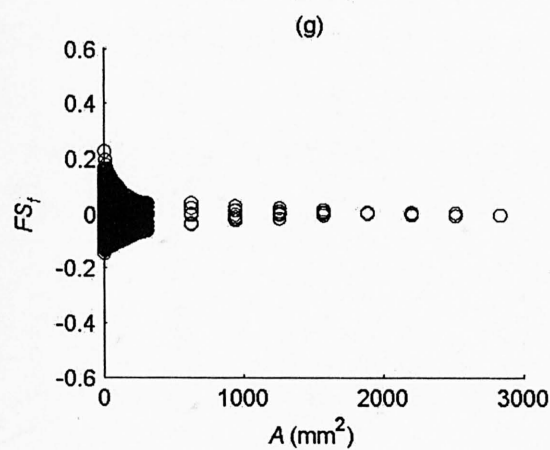
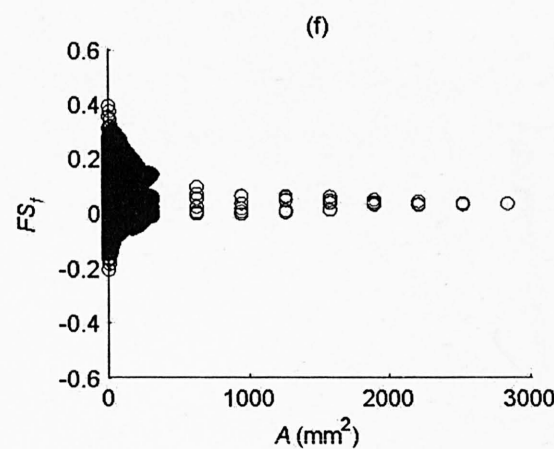
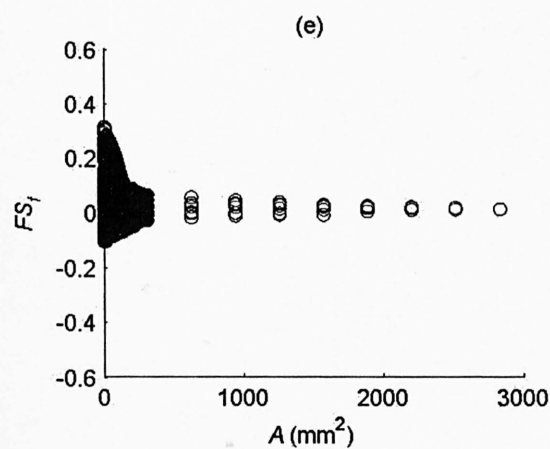
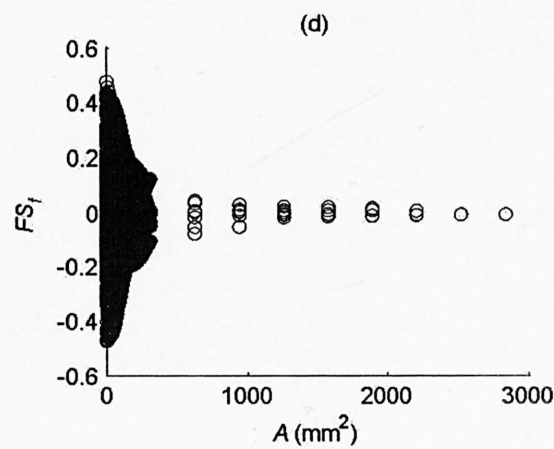
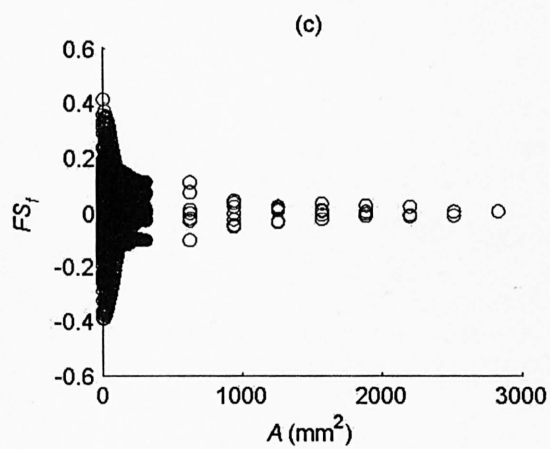
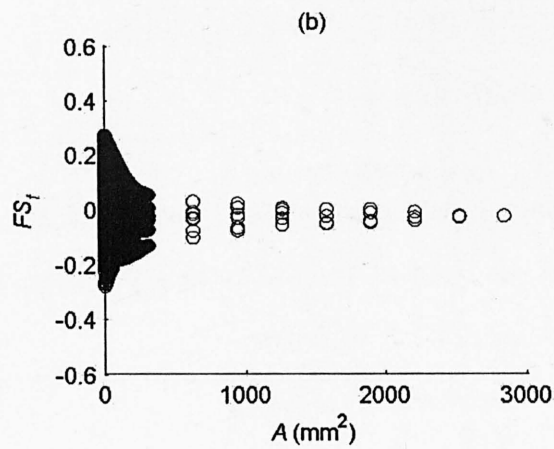
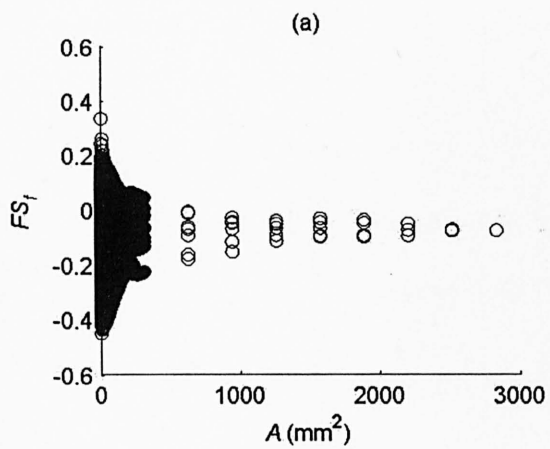


Figure 6.9. The coefficient of cross-correlation η between the fractional contributions made by the form-induced stresses to the total fluid stress FS_f and bed surface elevation for each of the experimental runs over (a) the unimodal bed; and (b) the bimodal bed, where l_x is the streamwise lag between FS_f and bed surface elevation.

The variation in FS_f with averaging area A is shown for the experimental runs over the unimodal and bimodal beds in Figures 6.10 and 6.11, respectively. At an averaging area of 312.9 mm^2 the nine protrusions in the mass of values corresponds to the FS_f value for each of the nine different lateral locations over the bed. Above this averaging area, the spatial averaging involved integrating across these nine values, which explains the larger separation between averaging areas. All the plots show that as averaging area increases FS_f dramatically decreases. Clearly, the averaging area has a significant effect on the interpretation of the significance of form-induced stresses to carrying momentum. Different averaging areas result in different conclusions being drawn at those different spatial scales.

Studies that have examined the flow within arrays of cubes have also observed how averaging area, and the number of measurements within that area, influences the estimate of double-averaged quantities. This kind of examination has been limited to studies that have used numerical modelling, largely because of their ability to gather sufficient data. Kanda *et al.* (2004) found that computational domain size (equivalent to averaging area) has a significant effect on the estimate of total fluid stress. The smallest domain size considerably underestimated total fluid stress, such that it was 25 % lower at the maximum bed elevation than for the largest domain size. This, they thought, was because the coherent flow structures had a streamwise length that was an order of magnitude greater than the canopy height that could not be properly simulated by a small computational domain. Coceal *et al.* (submitted) examined how computational grid resolution (equivalent to the number of measurements within an averaging area) influenced the estimation of $\langle \bar{u} \rangle$. Using different resolutions over the same array of staggered cubes they revealed significant differences in the estimation of $\langle \bar{u} \rangle$, especially for the flow above the cubes, such that there could be a 6 % difference in $\langle \bar{u} \rangle$ between the highest and lowest resolution. This difference would be even greater for total fluid stress estimations. They claim that it is the difference in the computational grids resolution used by different studies that accounts for the difference in the success of studies using LES to reproduce accurately experimental results.



Continued overleaf

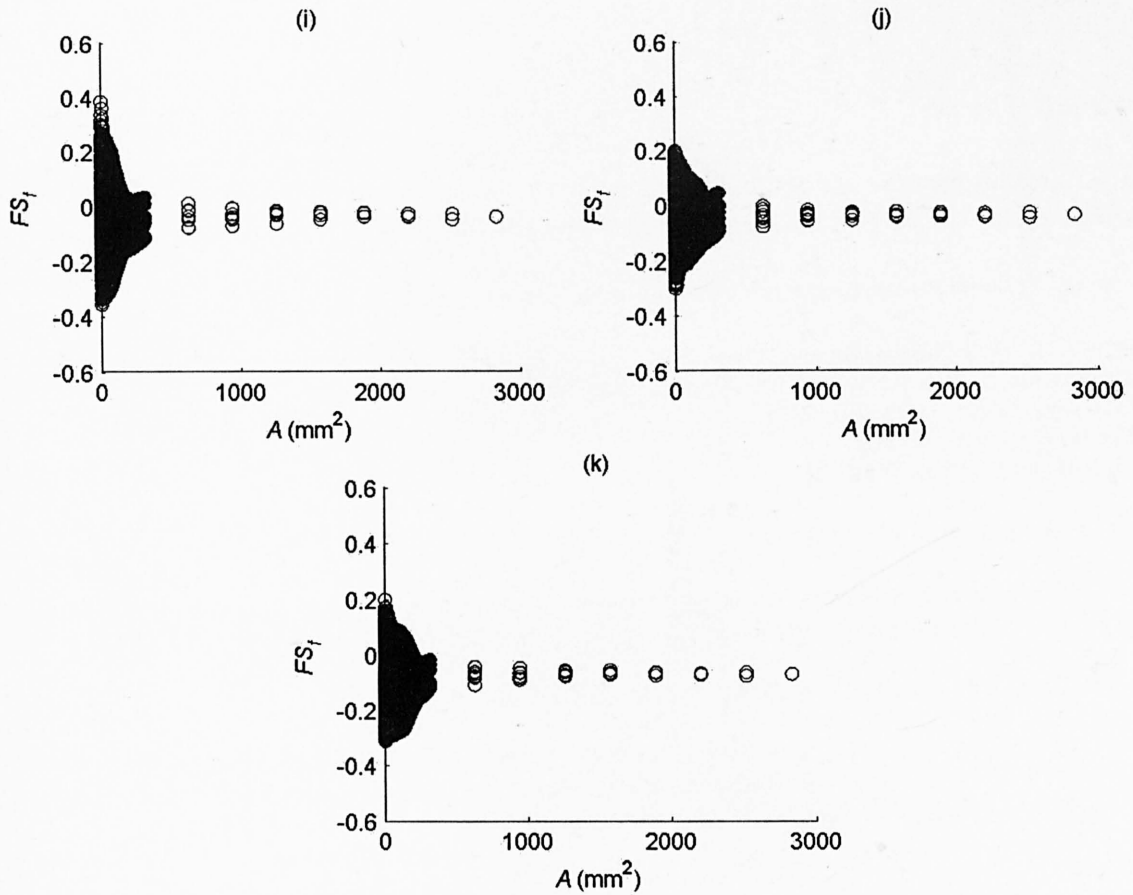
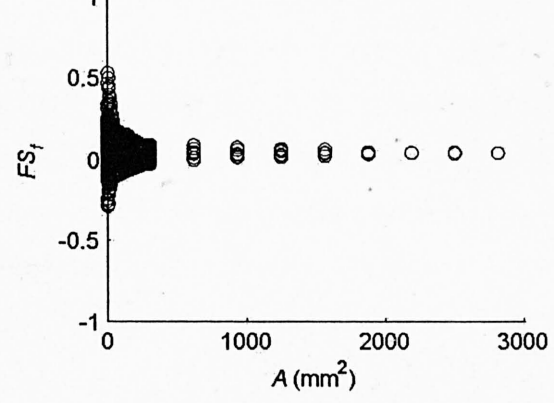
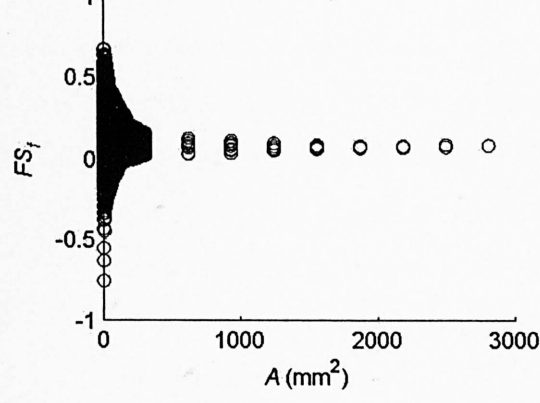
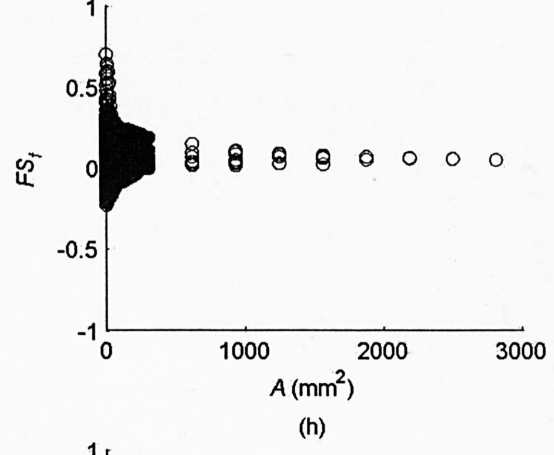
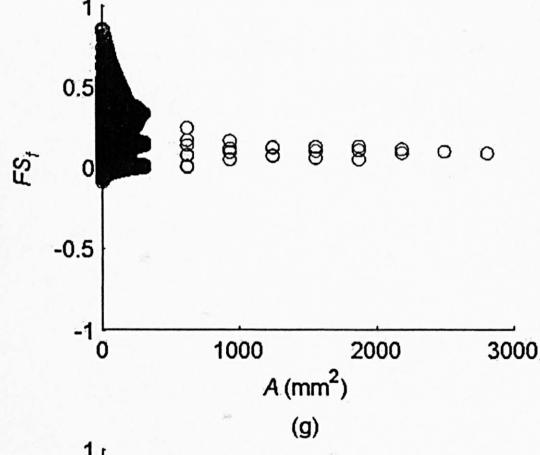
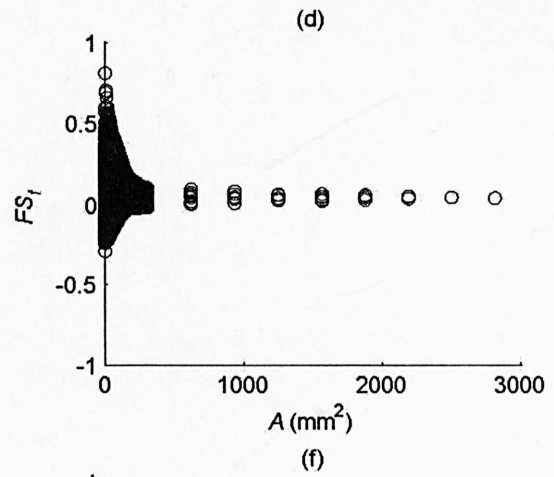
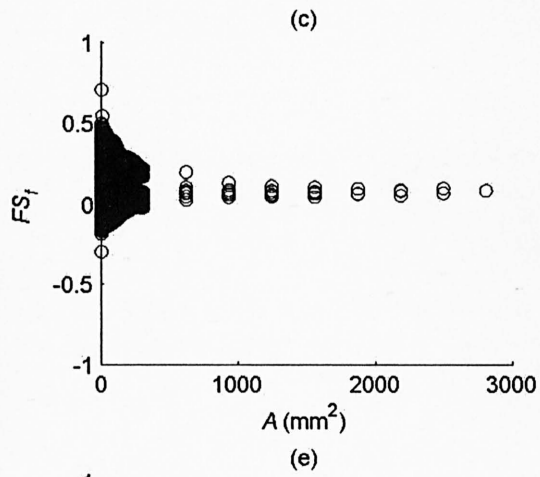
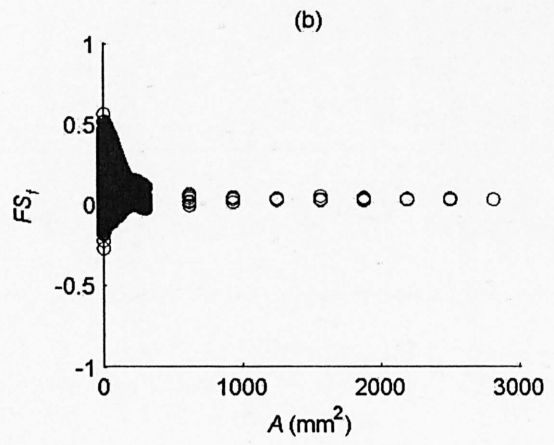
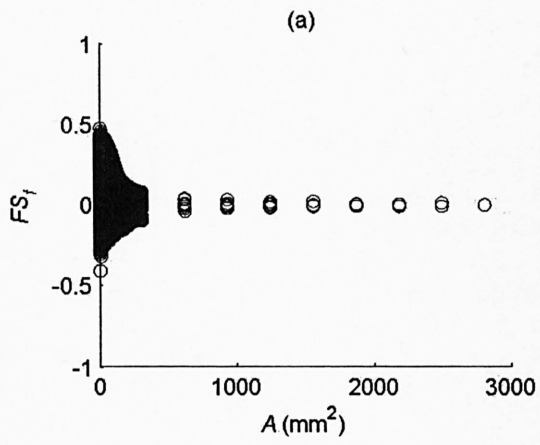


Figure 6.10. Variation in the fractional contributions made by the form-induced stresses to the total fluid stress FS_f with spatial-averaging area A over the unimodal bed (a) run 2U; (b) run 3U; (c) run 4U; (d) run 5U; (e) run 6U; (f) run 7U; (g) run 8U; (h) run 9U; (i) run 10U; (j) run 11U; and (k) run 12U.

The decrease in FS_f with averaging area in Figures 6.10 and 6.11 is especially large at the lower averaging areas, and it these areas which are similar to those used by previous studies. The results indicate that careful consideration is required of the choice of averaging area when assessing the significance of form-induced stresses. These averaging area effects also make it difficult to directly compare the FS_f between studies that have used different averaging areas. This is further complicated because each study will have a different relationship for FS_f with averaging area. This will cause averaging areas in some studies to be less or more representative of FS_f over the bed than other studies.



-Continued overleaf

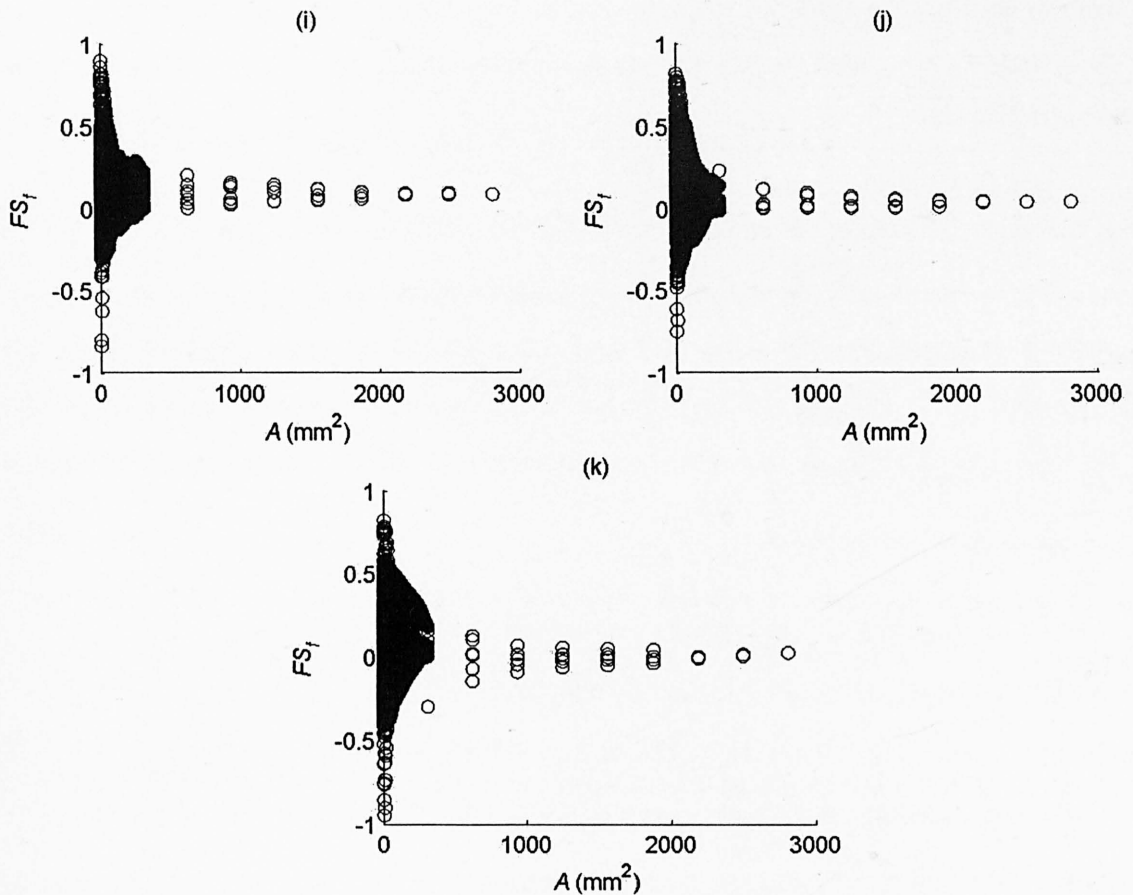


Figure 6.11. Variation in the fractional contributions made by the form-induced stresses to the total fluid stress FS_f with spatial-averaging area A over the bimodal bed for (a) run 2B; (b) run 3B; (c) run 4B; (d) run 5B; (e) run 6B; (f) run 7B; (g) run 8B; (h) run 9B; (i) run 10B; (j) run 11B; and (k) run 12B.

It is unclear how the number of measurements and the areas they were taken over relates to averaging area or averaging volume. For PIV measurements the situation is clearer because it is possible to take many measurements within a thin, continuous streamwise slab of fluid. However, when it involves using point velocity measurements at various positions that are well separated over the bed, the averaging area/volume can be interpreted in different ways. For example, the LDA measurements performed by Nikora *et al.* (in press b) were taken at 24 randomly determined positions over a static, armoured gravel bed. These 24 measurements were contained within an area of 2400 x 360 mm (Aberle, pers. comm.), and were used to calculate the form-induced stresses over this area of bed. Therefore, were the measurements spatially-averaged over an area of 2400 x 360 mm or averaged over 24 individual volumes that were equal to the

measuring volume used by the LDA probes to resolve the velocity? It questions whether studies that have used point measurements can specify the averaging area/volume they measured over.

In Figures 6.10 and 6.11 there appears to be variation in the degree by which FS_f varies with averaging area between the experimental runs. The experimental runs carried at a single bed slope (Tables 6.1 and 6.2) are again examined to discover whether a change in relative submergence can account for this variation. To directly compare the sensitivity of FS_f to averaging area between the experimental runs, the change in

$$\sigma_{\tilde{u}\tilde{w}} = \sqrt{\frac{1}{N_A} \sum_{i=1}^N (\tilde{u}\tilde{w}_i - \langle \tilde{u}\tilde{w} \rangle)^2} \quad (6.23)$$

with averaging area, where $\tilde{u}\tilde{w}_* = \tilde{u}\tilde{w} / \langle \tilde{u}\tilde{w} \rangle_{A_B}$ and A_B is the largest averaging area, is examined. The results are shown in Figure 6.12 and reveal that over both beds there is no association between the degree of change in $\sigma_{\tilde{u}\tilde{w}}$ and relative submergence, with similar degrees of change being observed between the two beds.

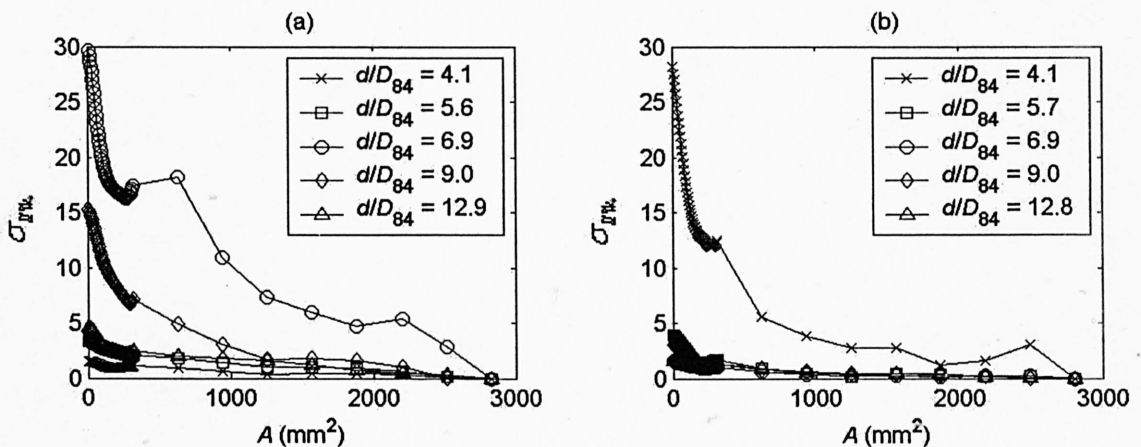


Figure 6.12. Variation in the standard deviation in dimensionless form-induced stress $\sigma_{\tilde{u}\tilde{w}}$ with spatial-averaging area A for the experimental runs carried out at a single slope over (a) the unimodal bed; and (b) the bimodal bed, where $\tilde{u}\tilde{w}_* = \tilde{u}\tilde{w} / \langle \tilde{u}\tilde{w} \rangle_{A_B}$, A_B is the largest averaging area, d/D_{84} is relative submergence, d is flow depth and D_{84} is the grain size at which 84 per cent of the bed material is finer.

To discover whether bed slope has an influence on the sensitivity of FS_f to averaging area, the experimental runs performed at the same relative submergences over the unimodal and bimodal beds (Tables 6.3 and 6.4) were examined in Figures 6.13 and 6.14. Over the unimodal bed, it can be seen that $\sigma_{\tilde{u}\tilde{w}}$ is consistently higher at the shallower slopes, but there is little consistent variation with bed slope over the bimodal bed.

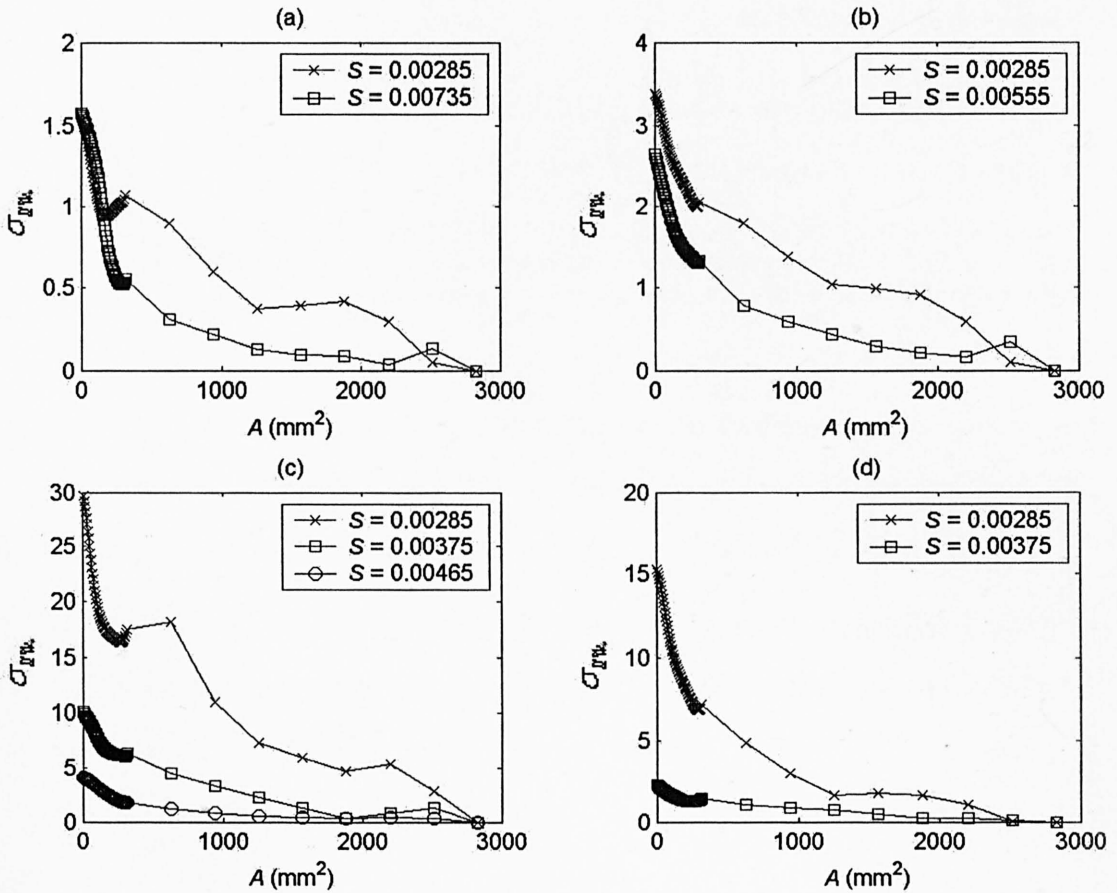


Figure 6.13. Variation in the standard deviation in dimensionless form-induced stress $\sigma_{\tilde{u}\tilde{w}}$ with spatial-averaging area A , for the experimental runs carried out at the same relative submergences over the unimodal bed at (a) $d/D_{84} = 4.1$; (b) $d/D_{84} = 6.6$; (c) $d/D_{84} = 6.9$; (d) $d/D_{84} = 9.0$, where $\tilde{u}\tilde{w}_* = \tilde{u}\tilde{w}/\langle\tilde{u}\tilde{w}\rangle_{A_B}$, A_B is the largest averaging area, d/D_{84} is relative submergence, d is flow depth, D_{84} is the grain size at which 84 per cent of the bed material is finer and S is bed slope.

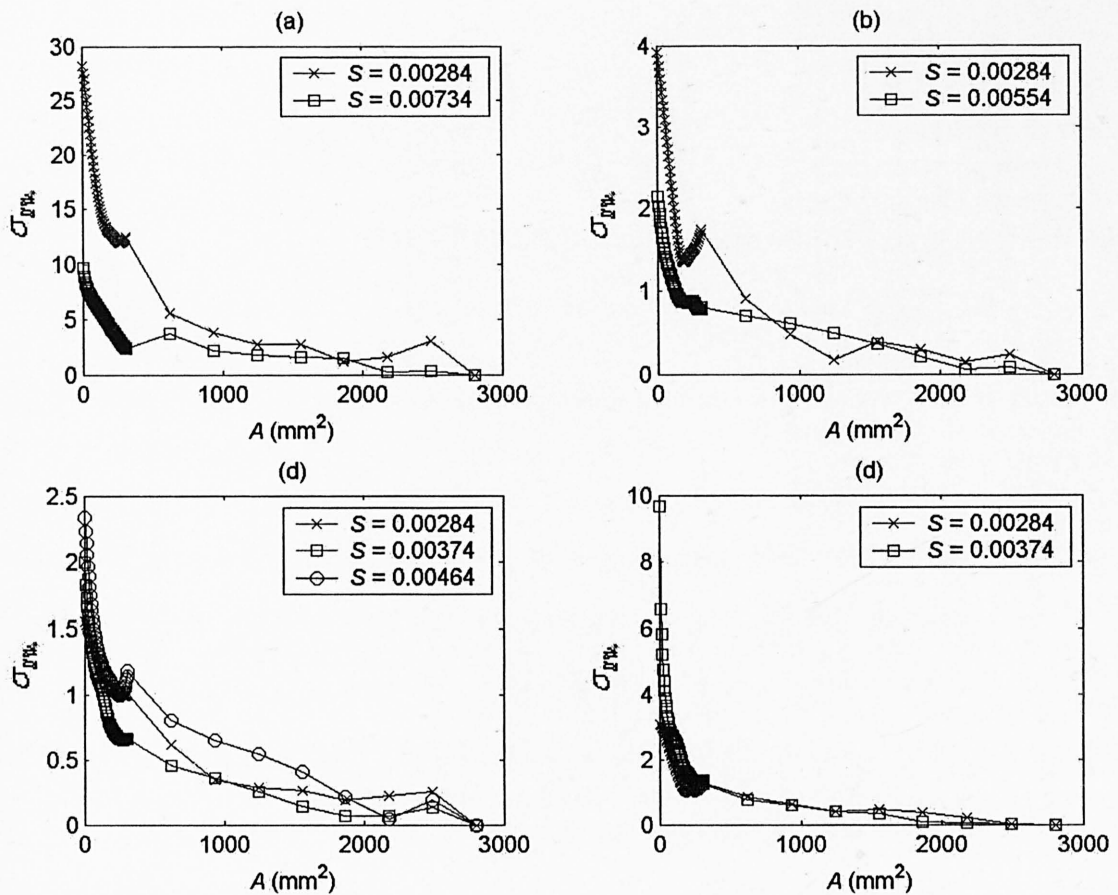


Figure 6.14. Variation in the standard deviation in dimensionless form-induced stress $\sigma_{\tilde{u}\tilde{w}}$, with spatial-averaging area A , for the experimental runs carried out at the same relative submergences over the bimodal bed at (a) $d/D_{84} = 4.1$; (b) $d/D_{84} = 6.7$; (c) $d/D_{84} = 6.9$; (d) $d/D_{84} = 9.0$, where $\tilde{u}\tilde{w}_* = \tilde{u}\tilde{w}/\langle\tilde{u}\tilde{w}\rangle_{A_B}$, A_B is the largest averaging area, d/D_{84} is relative submergence, d is flow depth, D_{84} is the grain size at which 84 per cent of the bed material is finer and S is bed slope.

The combined effect of relative submergence and bed slope for the experimental runs carried out at the same mean bed shear stress can be seen in Figure 6.15. Over the unimodal bed, $\sigma_{\tilde{u}\tilde{w}}$ clearly increases with relative submergence, and therefore reduces with bed slope. This same relationship with bed slope was also observed in Figure 6.13. However, over the bimodal bed, the reverse is seen. The values of $\sigma_{\tilde{u}\tilde{w}}$ are higher at the lower submergences and higher bed slopes.

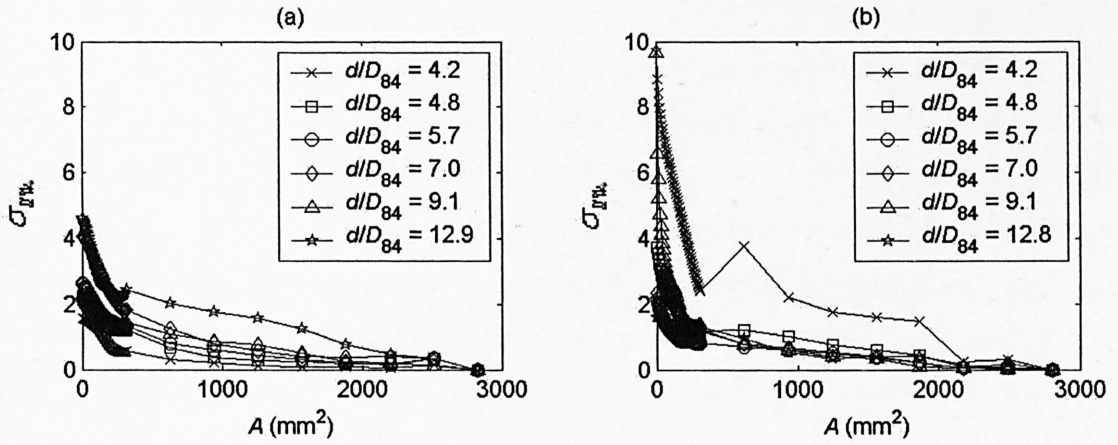


Figure 6.15. Variation in the standard deviation in dimensionless form-induced stress $\sigma_{\tilde{u}\tilde{w}}$ with spatial-averaging area A , for the experimental runs carried out at the same mean bed shear stress over (a) the unimodal bed; and (b) the bimodal bed, where $\tilde{u}\tilde{w}_* = \tilde{u}\tilde{w} / \langle \tilde{u}\tilde{w} \rangle_{A_B}$, A_B is the largest averaging area, d/D_{84} is relative submergence, d is flow depth, D_{84} is the grain size at which 84 per cent of the bed material is finer and S is bed slope.

If $\sigma_{\tilde{u}\tilde{w}}$ is plotted as a function of averaging area A , A/d^2 and A/D_{84}^2 it can be seen what the differences are between the two beds, and whether this variability can be accounted for by differences in flow depth or a property of the bed, here represented by D_{84} , a surrogate approximation for bed roughness (Figure 6.16). The results show that the variability between the beds and each of the experimental runs is significantly less when averaging area is non-dimensionalised by flow depth, suggesting that flow depth has the greater control on the sensitivity of FS_f on averaging area.

6.14 Averaging Area Required for a Representative Estimate of Form-induced Stress

6.14.1 Definition

This data can be used to assess whether the averaging area used to calculate FS_f in Figure 6.1 provided a representative estimate of form-induced stress for the bed. The way in which FS_f changes with averaging area (Figures 6.10 and 6.11) resembles how

Hassanizadeh and Gray (1979) theoretically describe averaging area influences averaged quantities. This study described this relationship by using an example of the change in the double-averaged mass density of a material for the α -phase (Figure 6.17), in which the α -phase occupied only a small proportion of the material, which is analogous to a portion of fluid. They described that at the small averaging areas, fluctuations in the double-averaged mass density are evident because relatively large portions of the α -phase and other phases become included in the averaging area (or region). As the averaging area increases, these fluctuations decrease until, within a range of averaging areas D , the mass density is no longer sensitive to the size of the averaging area. This is the range of areas at which the averaging process is valid, where the scale of the area is larger than the scale of the variations. It is therefore the range of areas at which spatial averaging should be performed. They also mentioned that further increases in the averaging area can cause 'gross inhomogeneities' in the medium, such that the averaged quantity becomes unstable, denoted by the increase in the double-averaged mass density above point L , where L is the scale of the gross inhomogeneities. Such gross inhomogeneities are not evident in Figures 6.10 or 6.11, indicating that the averaging area used to produce the FS_f values for the bed was not too large.

Hassanizadeh and Gray (1979) derived a requirement from these theoretical considerations, that for the averaging process to be valid and for the averaged quantity to be meaningful, the length of the averaging area must satisfy the following relationship

$$l \leq D \leq L \quad (6.24)$$

where l is the characteristic length of the variations in the quantity. They stated that the length of the averaging area should be such that the resulting averaged quantity is insensitive to small changes in the length of the area. In other words, the quantities that are a result of the averaging process should be independent of the averaging area and should be continuous in time and space. If for a particular quantity the characteristic lengths cannot be identified, equation (6.24) does not hold, or if the scale of interest is of the order D , the averaging technique should be considered invalid.

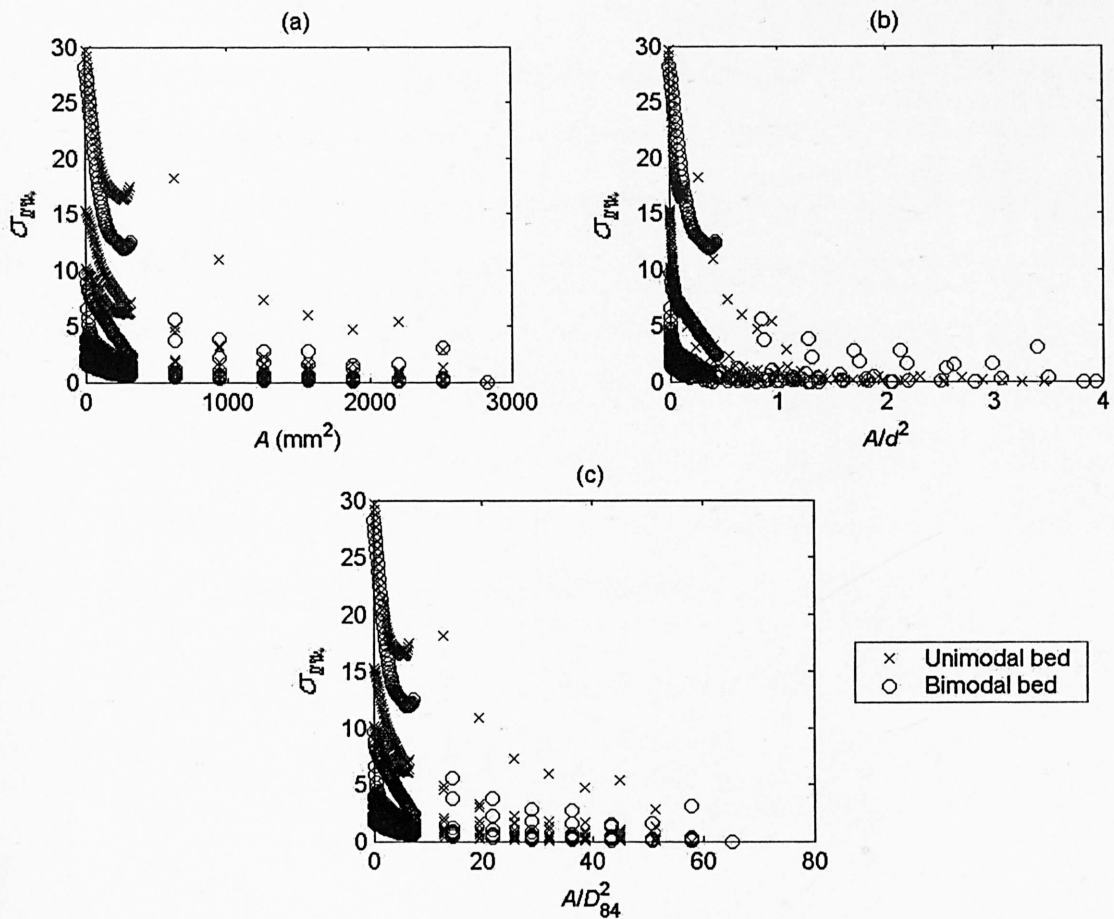


Figure 6.16. Variation in the standard deviation in dimensionless form-induced stress $\sigma_{\tilde{u}\tilde{w}}$ with (a) spatial-averaging area A ; (b) A/d^2 ; and (c) A/D_{84}^2 , where $\tilde{u}\tilde{w} = \tilde{u}\tilde{w}/\langle\tilde{u}\tilde{w}\rangle_{A_B}$, A_B is the largest averaging area, d is flow depth and D_{84} is the grain size at which 84 per cent of the bed material is finer.

If the descriptions of Hassanizadeh and Gray (1979) are applied to the results presented here, it suggests that an identification of the area at which the variations in the form-induced stresses across the bed become insignificant may reveal the minimum averaging area required to obtain a representative value of FS_f over a water-worked gravel bed. No other study has been able to measure continuously over space at such a high spatial resolution and over nine lateral locations across the bed over a wide range of hydraulic conditions. The data, therefore, provides a unique opportunity to determine the minimum averaging area required. A linear regression between the theoretical probability associated with the ordered observation FS_f from a standard normal distribution and the observed probability for FS_f showed that all but two of the

distributions of FS_f over the beds can be considered to follow approximately a normal distribution. Therefore the central-limit theorem can be used for defining this minimum area A_{\min} . If A_B is equal to the averaging area used to calculate FS_f for the whole bed in Figure 6.1, A_{\min} is defined here as the averaging area at which 95 % of the $\tilde{u}\tilde{w}_*$ values are within 5 % of $\tilde{u}\tilde{w}_*$ at A_B , such that if the sample was repeated an infinite number of times and this interval was constructed for every sample, then $\langle \tilde{u}\tilde{w} \rangle_{A_{\min}}$ will fall into 95 % of such intervals. This means that $\tilde{u}\tilde{w}_*$ values have to fall within an interval of [0.975, 1.025], given that $\tilde{u}\tilde{w}_*$ at A_B is equal to unity. The value of $\sigma_{\tilde{u}\tilde{w}_*}$ where this condition is met firstly needs to be determined. Central-limit theorem indicates that the upper limit of a 95 % confidence interval x_2 is defined as

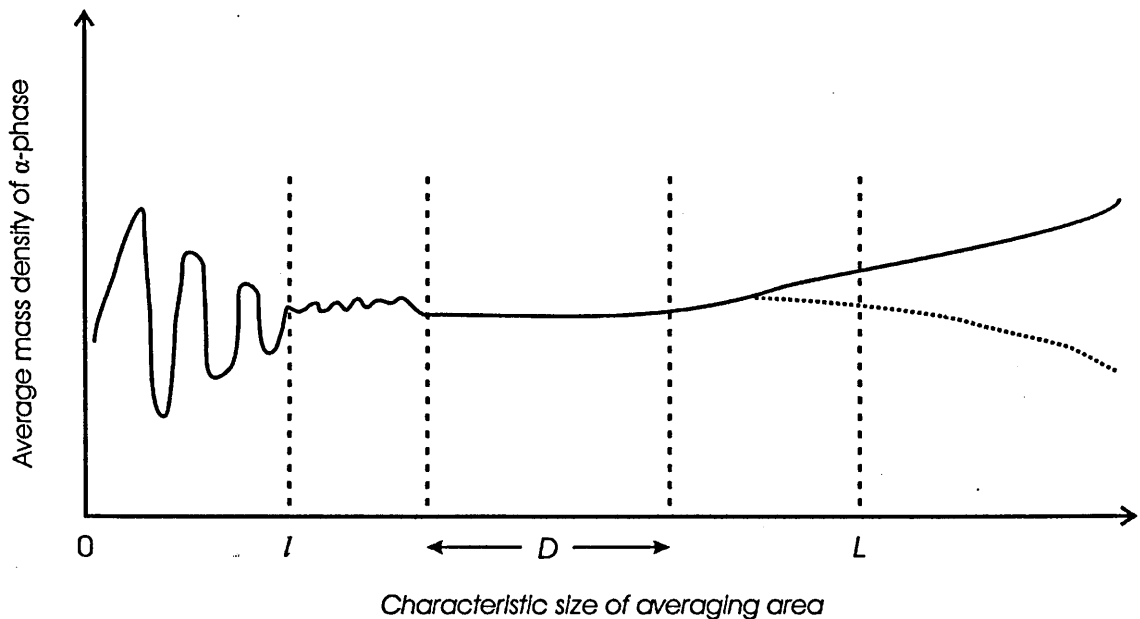


Figure 6.17. The theoretical variation in a double-averaged quantity with spatial-averaging area. This example shows the double-averaged mass density of a material of α -phase as a function of averaging area, where l is the characteristic length of the variations in mass density, D is the range of averaging areas where the mass density is no longer sensitive to the size of the averaging area and L is the scale of the gross inhomogeneities. Redrawn from Hassanizadeh and Gray (1979).

$$x_2 = \bar{x} + 1.96 \frac{\sigma}{\sqrt{N}} \quad (6.25)$$

where \bar{x} is the sample mean, σ is the populations standard deviation and N is the total number of measurements. Equation (6.25) in terms of $\tilde{u}\tilde{w}_*$ becomes

$$\sigma_{\tilde{u}\tilde{w}_*} = \frac{\sqrt{N}}{1.96} (x_2 - 1) \quad (6.26)$$

which means A_{\min} is defined as the area at which $\sigma_{\tilde{u}\tilde{w}_*} = 0.299$. The assumption has to be made that $\langle \tilde{u}\tilde{w} \rangle_{A_B}$ is the actual form-induced stress over the bed. However, it is important to note that a double-averaged quantity will not necessarily be exactly equal to the average of the corresponding point quantities (Hassanizadeh and Gray, 1979), so such an assumption is not extreme as it may appear. It is also noted that the precision of $\sigma_{\tilde{u}\tilde{w}_*}$ decreases as averaging area increases, because it is based on a progressively lower number of $\tilde{u}\tilde{w}_*$ values.

An understanding of how A_{\min} relates to properties of the fluid and the bed will help future studies estimate the averaging area they need to produce representative values of FS_f . It will also be useful for critically assessing whether it is likely that previous studies have produced representative values of FS_f over gravel beds. In addition, given that A_{\min} is defined as the area at which $\sigma_{\tilde{u}\tilde{w}_*} = 0.299$, A_{\min} will reveal the characteristic spatial scale at which the form-induced stresses largely operate over. If A_{\min} is consistently equivalent to a specific bedform scale, it makes it easier to determine A_{\min} for different gravel bed surface topographies. This would not require any information on the characteristic scales of spatial variability in the time-averaged flow field, which is largely unknown and is difficult and time-consuming to measure.

6.14.2 Variability with Relative Submergence

The variation in A_{\min} with relative submergence for the experimental runs carried out a single bed slope is shown for both beds in Figure 6.18. The variation is shown in terms

of A_{\min} , A_{\min}/d^2 , A_{\min}/D_{84}^2 and $A_{\min}/l_{x_0}^2$ to discover whether the variability between the experimental runs and the two beds can be accounted for by flow depth, bed roughness (approximated by D_{84}) or the characteristic streamwise correlation length of the bed elevations l_{x_0} . Flow depth can be considered as a surrogate measure of the degree of spatial variability in the time-averaged flow field, given the results in Chapters 4 and 5. The streamwise correlation length of the bed elevations was estimated from a 2-D structure function of the bed elevations (see Figure 3.14). Studying the variation in A_{\min} in these different non-dimensional forms enables an examination as to whether A_{\min} is a function of a property of the flow or dependent on the properties of the solid boundary.

The results in Figure 6.18a show that over the unimodal bed, A_{\min} displays a general increase with relative submergence, but the changes are slight. It means that A_{\min} is quite uniform across these experimental runs. However, over the bimodal bed, no such relationship is observed, with differences being larger between experimental runs. Yet the variation in A_{\min} between the two beds becomes negligible when A_{\min} is non-dimensionalised by flow depth. Also, in this form both beds now show the same tendency to display an exponential decrease with relative submergence. Flow depth appears to produce a very good collapse of the A_{\min} values. Non-dimensionalising by D_{84} reduces the variation between the experimental runs in comparison to A_{\min} in its dimensional form, but to not such an extent as flow depth. In the case of l_{x_0} , it actually causes the differences between the two beds to be more clearly seen.

6.14.3 Variability with Bed Slope

The variation in A_{\min} with bed slope for the experimental runs carried out at the same relative submergences (Tables 6.3 and 6.4) in its dimensional and its various non-dimensional forms is shown in Figure 6.19 for the unimodal bed. The A_{\min} values are observed to decrease with bed slope for each of the four different relative submergences, such that A_{\min} can decrease by nearly four times from the lowest to the highest bed slope. Neither of the variables used to non-dimensionalise A_{\min} appear to produce a reduction in the differences between the experimental runs. Over the bimodal

bed, a decrease in A_{\min} with bed slope is also seen (Figure 6.20), but for only three of the four different relative submergences, with the changes being relatively insignificant to those seen over the unimodal bed.

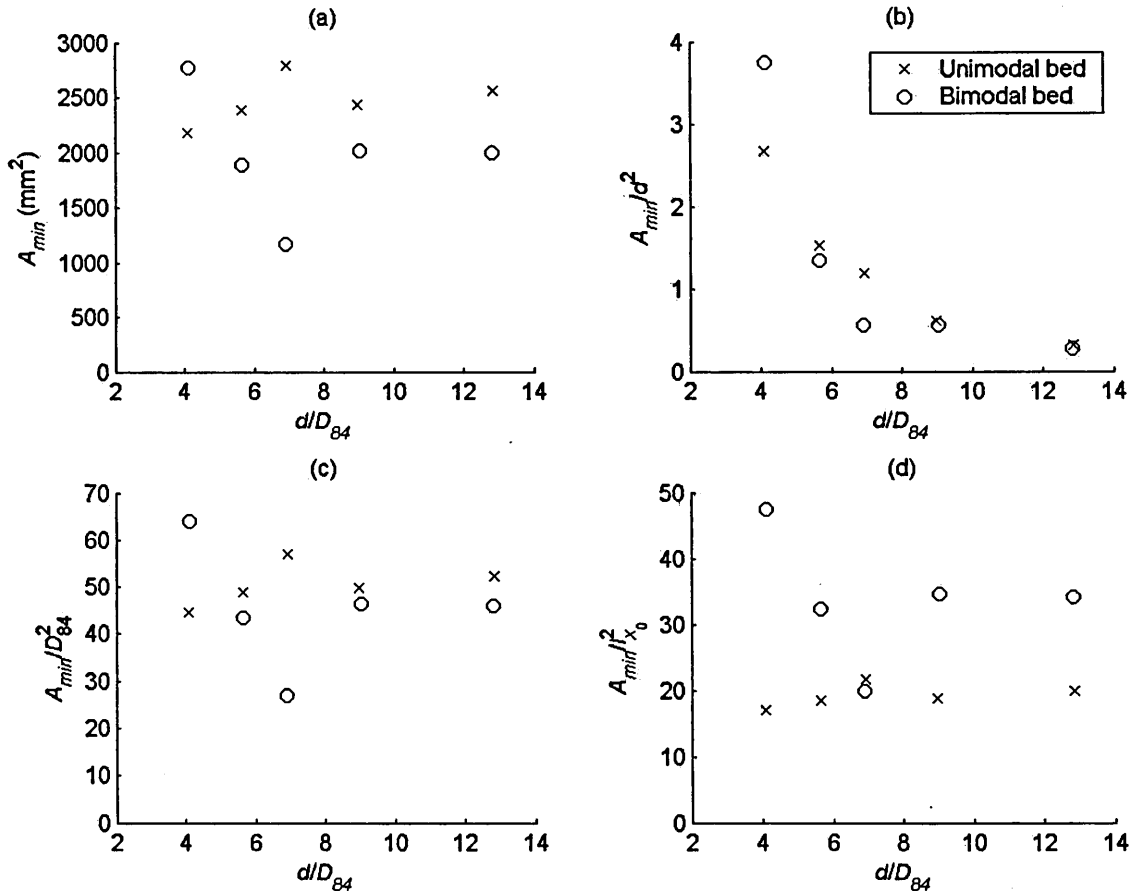


Figure 6.18. Variation in (a) the minimum area required to provide a representative value of form-induced stress over the bed A_{\min} ; (b) A_{\min}/d^2 ; (c) A_{\min}/D_{84}^2 ; and (d) A_{\min}/l_x^2 with relative submergence d/D_{84} for the experimental runs carried out at a single bed slope over each of the beds, where d is flow depth, D_{84} is the grain size at which 84 per cent of the bed material is finer and l_x is the characteristic streamwise correlation length of the bed elevations.

6.14.4 Variability Under Conditions of Constant Bed Shear Stress

The A_{\min} values in its four different forms for the experimental runs carried out at the same mean bed shear stress (Tables 6.5 and 6.6), is shown as a function of relative

submergence for both beds in Figure 6.21. The dimensional A_{\min} values are observed to show a general increase with relative submergence, and therefore a decrease with bed slope, over the unimodal bed. This results in A_{\min} increasing by nearly four times from the lowest to the highest submergence. Therefore, A_{\min} also decreases by four times from the lowest to the highest bed slope. Over the bimodal bed, the A_{\min} values show little variation with relative submergence, and therefore bed slope.

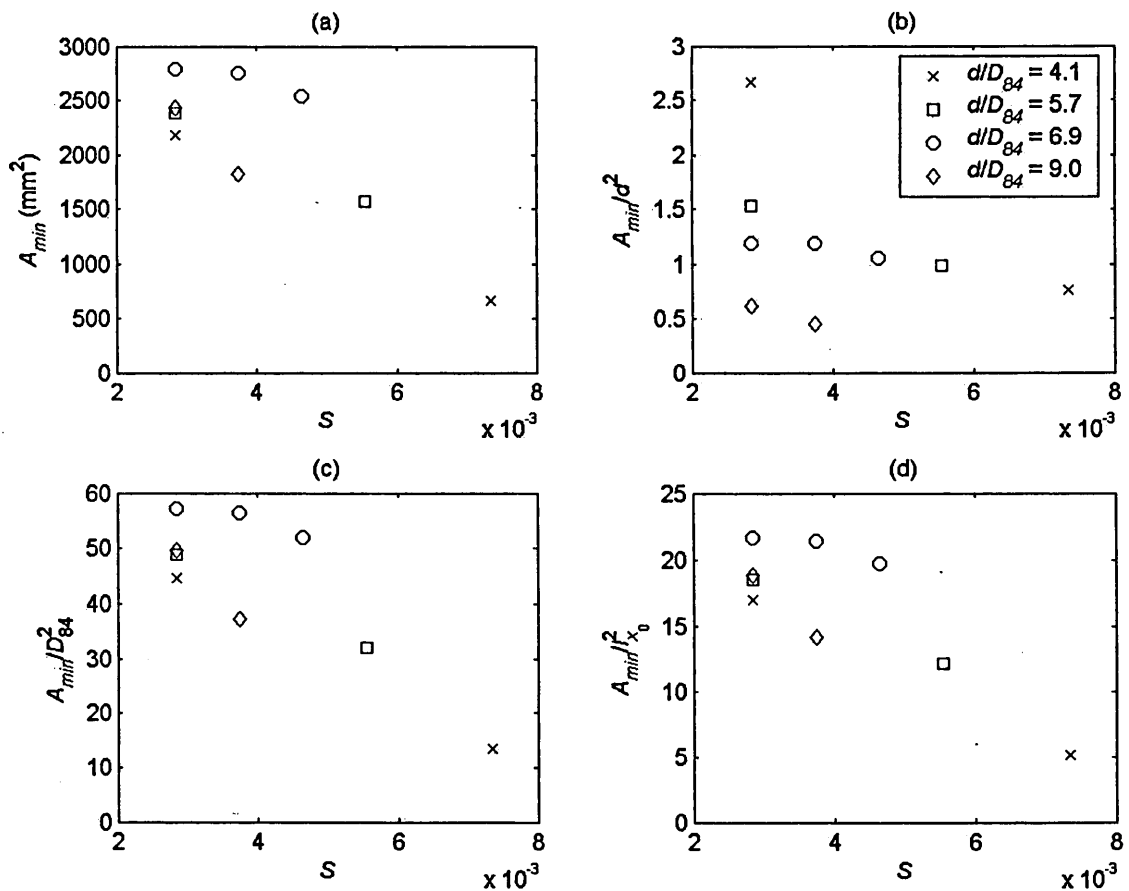


Figure 6.19. Variation in (a) the minimum area required to provide a representative value of form-induced stress over the unimodal bed A_{\min} ; (b) A_{\min}/d^2 ; (c) A_{\min}/D_{84}^2 ; and (d) $A_{\min}/l_{x_0}^2$ with bed slope S for the experimental runs carried out at the same relative submergences, where d is flow depth, D_{84} is the grain size at which 84 per cent of the bed material is finer and l_{x_0} is the characteristic streamwise correlation length of the bed elevations.

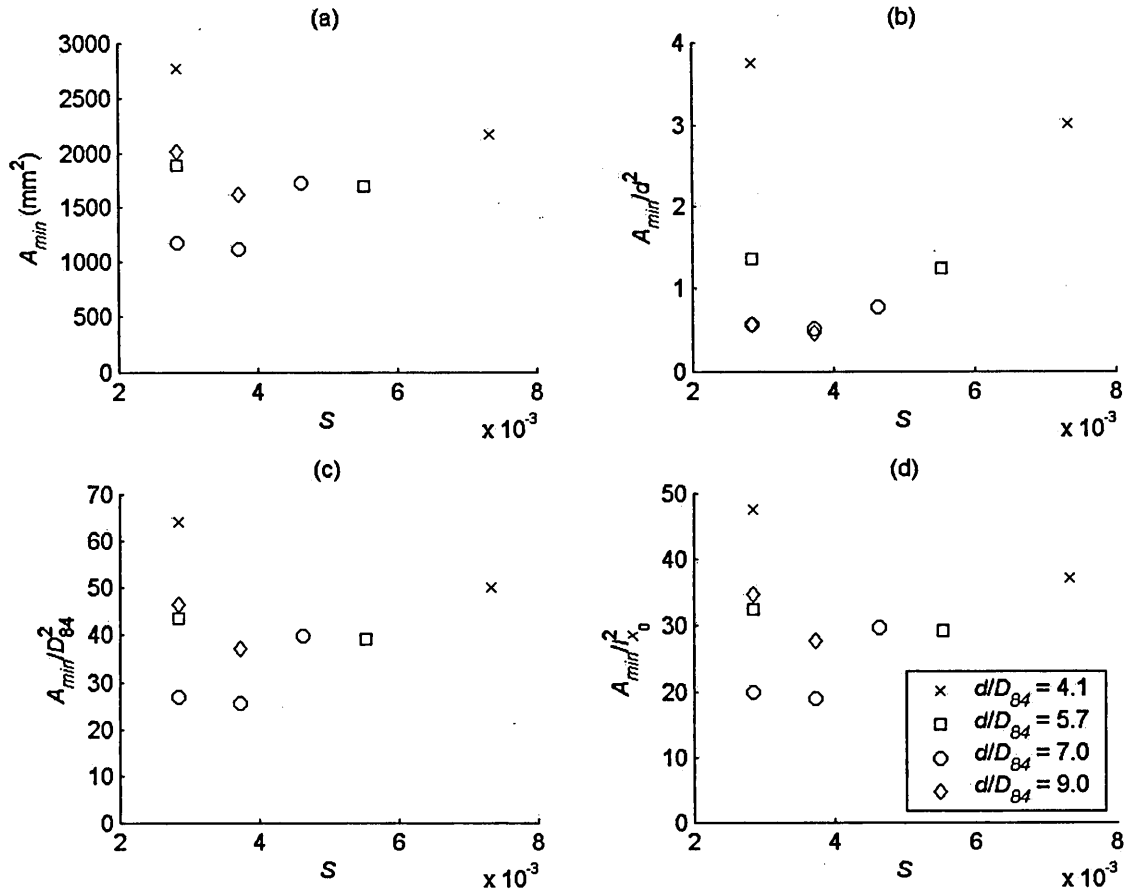


Figure 6.20. Variation in (a) the minimum area required to provide a representative value of form-induced stress over the bimodal bed A_{min} ; (b) A_{min}/d^2 ; (c) A_{min}/D_{84}^2 ; and (d) $A_{min}/l_{x_0}^2$ with bed slope S for the experimental runs carried out at the same relative submergences, where d is flow depth, D_{84} is the grain size at which 84 per cent of the bed material is finer and l_{x_0} is the characteristic streamwise correlation length of the bed elevations.

The differences in A_{min} values between the two beds become negligible at the same relative submergences (or bed slopes) when non-dimensionalised by flow depth. Both beds show the same clear tendency to decrease with relative submergence. Flow depth once again produces a very good collapse of the A_{min} values. But D_{84} only produces a reasonable scaling for A_{min} , and l_{x_0} performs poorly.

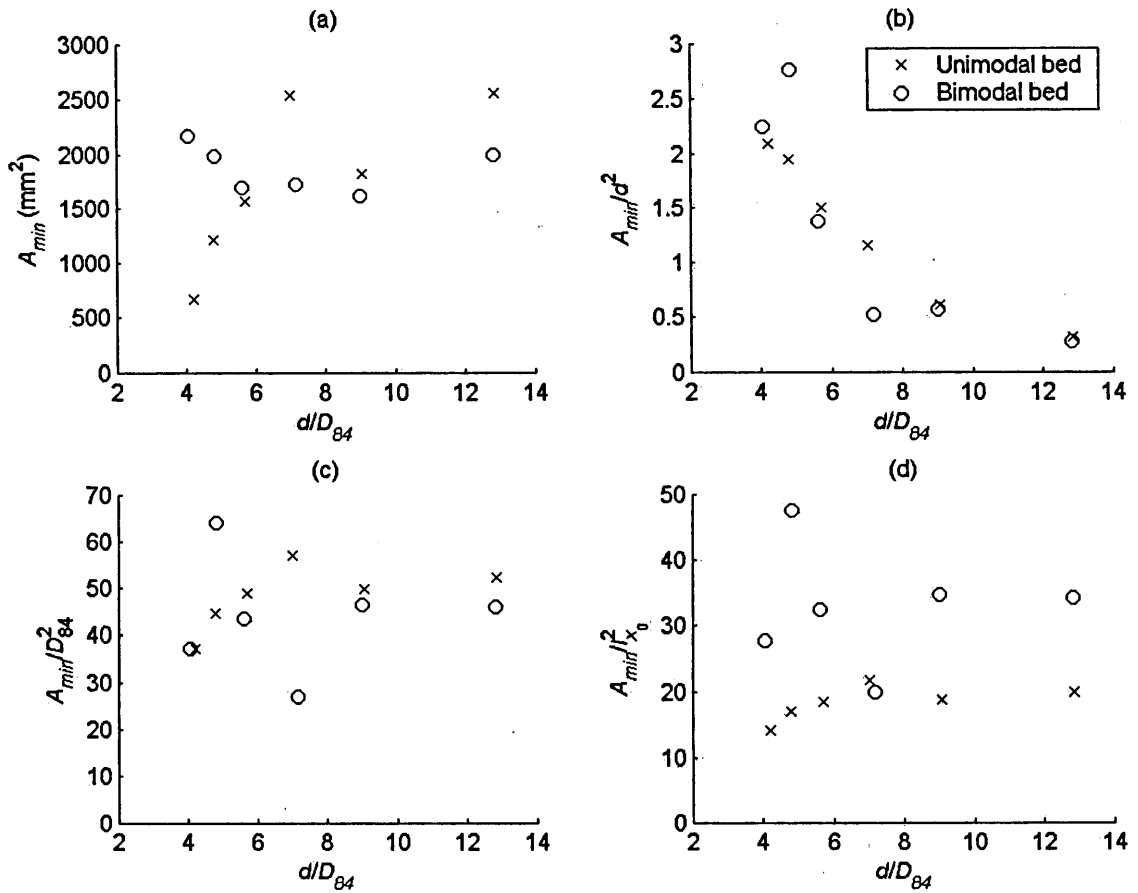


Figure 6.21. Variation in (a) the minimum area required to provide a representative value of form-induced stress over the bed A_{min} ; (b) A_{min}/d^2 ; (c) A_{min}/D_{84}^2 ; and (d) A_{min}/l_x^2 with relative submergence d/D_{84} for the experimental runs carried out at the same mean bed shear stress over each of the beds, where d is flow depth, D_{84} is the grain size at which 84 per cent of the bed material is finer and l_x is the characteristic streamwise correlation length of the bed elevations.

6.14.5 Parameterisation

It has been seen that the differences between the two beds is reduced when A_{min} in its various forms is plotted as a function of relative submergence. The A_{min} values from all the experimental runs over the two beds are displayed in this way in Figure 6.22. The dimensional values are not typically higher over either bed, with the majority of the runs over each bed being contained within a small range of values. However, the variation between the beds is typically greater at the lower relative submergences. The A_{min} values in Figure 6.22a reveal that the largest averaging area used for calculating FS_f in

this study (2816.5 mm^2) was large enough to produce representative values of form-induced stress over the bed.

The A_{\min} values in Figure 6.22a, in terms of the averaging area of one vertical plane measurement, range from 2.1 to 8.9. Typically the A_{\min} ranges from five to eight vertical plane measurements, implying that nine vertical plane measurements did fully sample the variability in form-induced stresses over the bed. However, given that the maximum A_{\min} was close to nine, a greater number of vertical plane measurements across the bed would provide a higher degree of confidence. In fact, given the spatial pattern in $\bar{u}/\langle\bar{u}\rangle$ that was seen in Chapter 4 and how this changed with relative submergence, a recommended approach for flows above the boundary would be to take 3-D PIV measurements in a horizontal plane at a number of different heights above the bed.

The variation between the beds is still large when A_{\min} is scaled by D_{84} (Figure 6.22c), but is smaller than for the A_{\min} values. The A_{\min}/D_{84}^2 values reveal that A_{\min} over the two beds range from $3.7D_{84} \times 3.7D_{84}$ to $8.0D_{84} \times 8.0D_{84}$, and that the majority of the values are contained within the range $6.2D_{84} \times 6.2D_{84}$ to $7.2D_{84} \times 7.2D_{84}$. These areas interestingly correspond to the areas of stone cells that have found to form over water-worked gravel beds in the field (Church *et al.*, 1998) and in the laboratory (Tait and Willetts, 1992; Tait *et al.*, 1992; Tait, 1993; Church *et al.*, 1998; Hassan and Church, 2000; Pender *et al.*, 2001). These structures tend to be elongated, due to their diamond-like shape, but this comparison is made on the assumption that that they are square. It still suggests that the form-induced stresses are likely to operate over the bedform scale, bedforms which involve an assemblage of many grains, rather than those involving a small number of grains like particle clusters. This is similar to the scale at which fluid stress has been suggested to operate over. Stone cells have been found to be a major contributor to flow resistance over armoured beds (Church *et al.*, 1998; Hassan and Church, 2000; Pender *et al.*, 2001), and therefore fluid stress is likely to be scaled to this bedform scale.

The A_{\min}/D_{84}^2 values suggest that the streamwise length (or size) of the averaging area has to be larger than the streamwise length (or area) of bed features involving

assemblages of many grains to produce a representative value of form-induced stress over a water-worked gravel bed. However, given that the differences in A_{\min}/D_{84}^2 values between the two beds are significant, D_{84} only provides a rough approximation to the A_{\min} required.

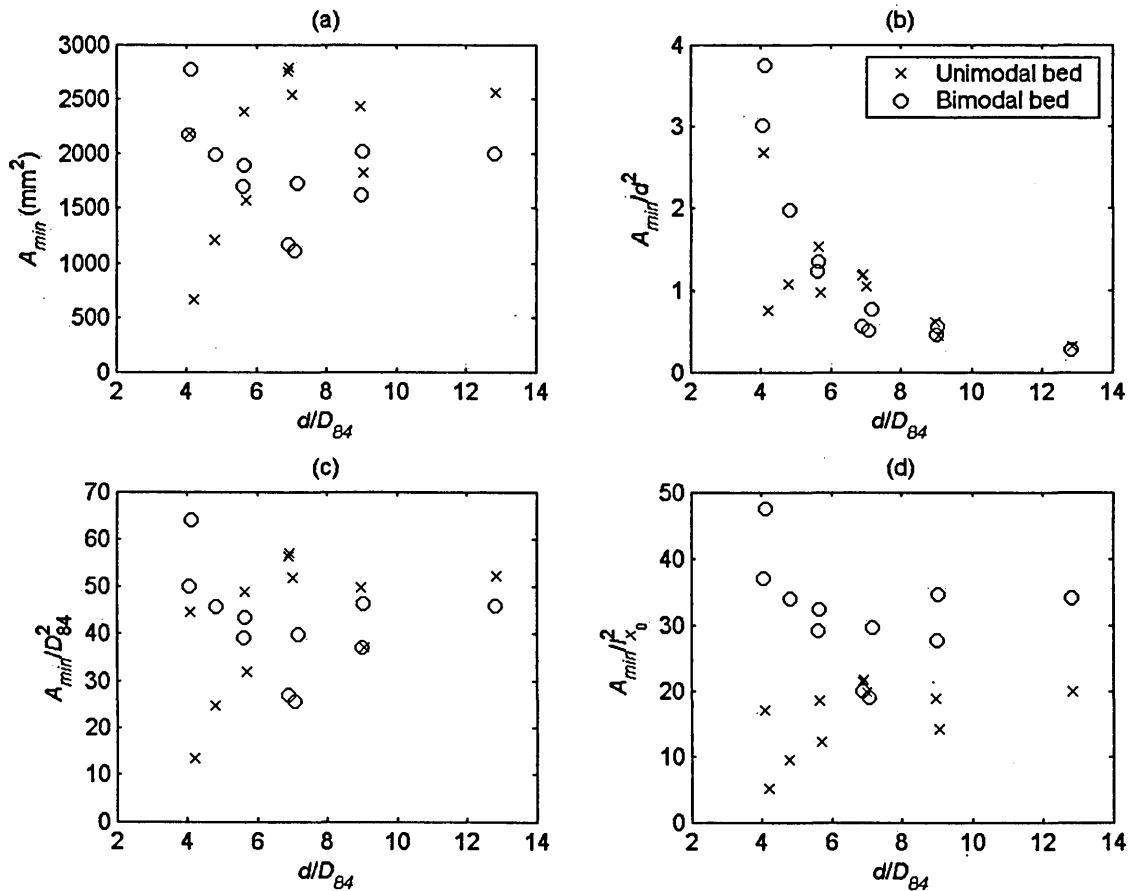


Figure 6.22. Variation in (a) the minimum area required to provide a representative value of form-induced stress over the bed A_{\min} ; (b) A_{\min}/d^2 ; (c) A_{\min}/D_{84}^2 ; and (d) A_{\min}/l_x^2 with relative submergence, d/D_{84} for each of the experimental runs carried out over each of the two beds, where d is flow depth, D_{84} is the grain size at which 84 per cent of the bed material is finer and l_x is the characteristic streamwise correlation length of the bed elevations.

The variation in $A_{\min}/l_{x_0}^2$ with relative submergence is shown in Figure 6.22d. Non-dimensionalising A_{\min} in this way makes the differences between the beds larger than for the A_{\min} values. It suggests that A_{\min} is not a function of l_{x_0} . However, the differences between the two beds are negligible when A_{\min}/d^2 is plotted against relative submergence, producing a good collapse of the data. There is a clear exponential decrease in A_{\min}/d^2 with relative submergence over each of the beds. It appears that A_{\min} is scaled by flow depth, particularly at the mid to high submergences, and implies that the characteristic scale at which form-induced stresses over is also scaled by flow depth. This cannot be entirely associated with the effect of increasing mean velocity with flow depth, which would produce a rise in the downstream elongation in the time-averaged spatial pattern and therefore the need for a larger A_{\min} to sample this pattern. This is because, although mean velocity does increase with flow depth for the experimental runs carried out at a single bed slope, more than half of the remaining runs had similar mean velocities. However, the manner in which A_{\min}/d^2 varies with relative submergence does suggest that A_{\min} can be predicted by flow depth. A least-squares fit to the A_{\min}/d^2 values (Figure 6.23) shows that the following equation

$$\frac{A_{\min}}{d^2} = 26.5 \left[\frac{d}{D_{84}} \right]^{-1.78} \quad (6.27)$$

provides a good fit for the mid to high relative submergences, $d/D_{84} > 5$ but a poor fit at the lower submergences, $d/D_{84} < 5$. For the former, an equation of the form

$$\frac{A_{\min}}{d^2} = 27.7 \left[\frac{d}{D_{84}} \right]^{-1.80} \quad (6.28)$$

provides a better fit, and for $d/D_{84} < 5$ A_{\min}/d^2 shows a poor relationship with relative submergence. The result is that the minimum averaging area can only be approximated for flows with $d/D_{84} > 5$. Campbell *et al.* (2005) studied flows with d/D_{84} that varied from approximately 21.0 to 22.3. Using equation (6.28) to estimate A_{\min}/d^2 required to

produce a representative value of FS_f produces values of 0.062 to 0.070. However, the A/d^2 they used was approximately between 0.10 to 0.12, indicating that it is likely that their estimates of FS_f were not a reliable indication of the significance of form-induced stresses over a gravel bed. It is difficult to assess the averaging area used by Nikora *et al.* (in press b) over their static, armoured bed, because of problems of defining an averaging area in relation to point measurements, but the results in Figure 6.22a suggest that it is doubtful that 24 point measurements were sufficient.

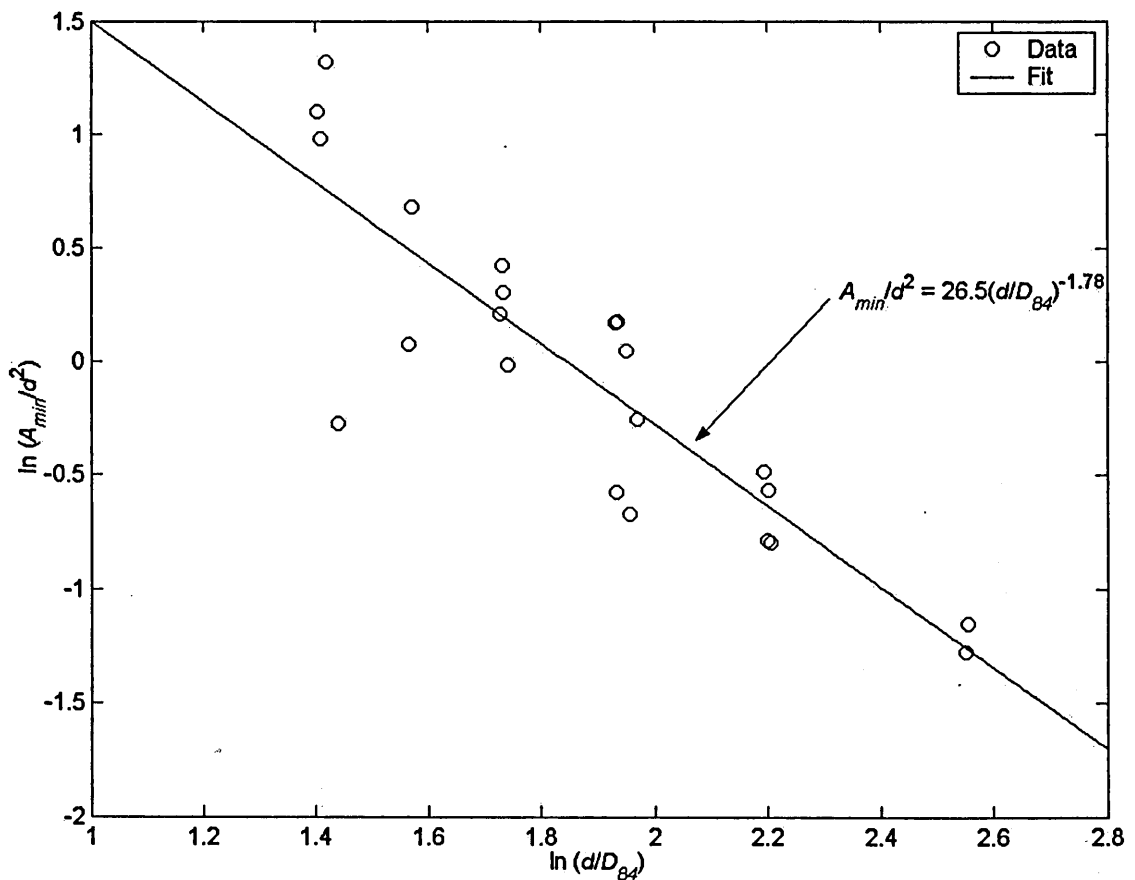


Figure 6.23. Variation in A_{min}/d^2 with relative submergence d/D_{84} for all the experimental runs carried out over the two beds, where A_{min} is the minimum averaging area required to provide a representative value of form-induced stress over the bed, d is flow depth and D_{84} is the grain size at which 84 per cent of the bed material is finer. The fitted equation has been determined through least-squares regression.

6.14.6 Interpretation

Experimental studies have made little explicit consideration of the averaging area that is required when applying the spatial averaging theorem to their data, and the influence of this on their estimates of double-averaged quantities. The only studies that have analysed this, as mentioned earlier, are those that have applied numerical modelling to the study of turbulent flow over and within rough boundaries (Hanna *et al.*, 2002; Stoesser *et al.*, 2003; Kanda *et al.*, 2004; Coceal *et al.*, submitted). This is likely because numerical modelling enables domain sizes and grid resolutions to be changed systematically, whereas experimental studies have never had the density of velocity measurements over a sufficiently large area to tackle this issue. In addition, there are practical problems with trying to achieve this in the laboratory or in the field. For example, measurements would have to be made in many different configurations for the same flow and bed conditions, which may not be possible. However, for all previous experimental studies, according to Hassanizadeh and Gray's (1979) criteria, the averaging technique they used would be invalid because they cannot determine if the resulting averaged quantity is insensitive to small changes in the length of the area.

Several studies have considered theoretically how to relate the averaging area required to produce a representative double-averaged quantity averaging to the physical system. This has been based on two schools of thought: (i) that the averaging area should be a function of the properties of the averaged fluid; and/or (ii) it should be dependent on the properties of the boundary. Yet there is no accepted definition. Considering the latter first, for atmospheric flows within plant canopies it has been stated that the streamwise length of the averaging area (or volume) should be large enough to eliminate the variations in canopy structure in the streamwise direction, but small enough in their vertical direction to preserve the fundamental vertical heterogeneity of the canopy (Raupach and Shaw, 1982; Finnigan, 1983; Brunet *et al.*, 1994; Ayotte *et al.*, 1999; Finnigan, 2000). However, interestingly, Raupach *et al.* (1986) considers averaging area differently. They suggest that the length scale of the area in each coordinate direction should be much less than the length scale of the large-scale, non-random inhomogeneity in the canopy. It suggests that the averaging area should be used to preserve the spatial heterogeneity in the canopy, not only in the vertical direction, but also in the streamwise and lateral directions. Wilson and Shaw (1977) state that spatial averaging should be

carried out over a streamwise length that is large in comparison to the distance between individual plants.

Studies of wind-flows within arrays of cubes, to simulate urban-like roughness, have also considered the averaging area as a function of the roughness array. Cheng and Castro (2002) state that spatial averaging should be taken over at least one repeating-unit of a uniform array, enabling the double-averaged quantities to be regarded as homogeneous in the streamwise direction on scales larger than that unit. But Kanda *et al.* (2004) suggest that the streamwise length of the averaging area should be at least an order of magnitude greater than the height of the array. All of these considerations assume that the canopy, whether it is the vegetation or urban canopy, is homogenous in the streamwise direction. Even for this simple case, there is no consensus of opinion.

For these types of boundary, the averaging area does not depend on the coordinates within the flow field. This assumption is not valid for water-worked gravel beds. Therefore studies over these surfaces have extended the ideas from the canopy studies to include a consideration of this non-uniformity. Nikora *et al.* (2001) interprets the square root of the averaging area A as the scale of a spatial rectangular window, with a linear scale of $< A^{0.5}$ which ‘smoothes’ the irregularities in the bed topography. They state that two linear scales should be considered, longitudinal, L_0 and transverse, W_0 such that $A = L_0 W_0$. They believe that a “convenient scale” (but is this an appropriate scale?) are the streamwise and lateral correlation lengths of rough bed elevations. Nikora *et al.* (1998) state that the standard deviation in bed elevations may also be an appropriate scale for bed surface topography. But given that Nikora *et al.* (2001) states that the double-averaged quantities for the flow region above the maximum bed elevation (equation (6.11)) do not depend on ϕ and therefore on A because in this region $\phi = A$, does this suggest that the form-induced stresses examined in this chapter do not depend on A , and therefore on some scale of bed topography? The results in Figures 6.10 and 6.11 clearly show that it does depend on A , and if Nikora *et al.* (2001) suggestions are correct, it means that it will also be a function on some scale of bed topography. Nikora *et al.* (in press a) more recently have stated that the dimensions of the averaging area should be much smaller than the large-scale features in bed topography. Therefore, in a gravel-bed river it should be much larger than gravel particles, but much smaller than the size of riffles or pools. They also state that the

streamwise length of the averaging area should be determined by the scales of the roughness (Nikora *et al.*, in press b). Campbell *et al.* (2005) also consider the spatial averaging area over a gravel bed to be related to the bed topography, with the area “chosen to be representative of the fixed sediment bed topography throughout the flume”. This has shown that there is no clear understanding of which bed property the averaging area should relate to over gravel beds.

As mentioned earlier, studies have also considered the averaging area to be a function of a property of the fluid being averaged. It follows from the fundamental equation for spatial averaging, equation (6.3), that the double-averaged quantity is related directly to the streamwise and lateral variability in the quantity. As Hassanizadeh and Gray (1979) put it, “in defining an operator for averaging, one should take into account the intrinsic nature of that property”. They also stated that the double-averaged quantity must exactly account for the total amount of the corresponding point quantities. In other words, the total momentum fluxes through a given boundary must be equal to the total point momentum fluxes through that boundary. Therefore, an averaging area must be chosen that enables the double-averaged quantity to adhere to this criterion, and is therefore entirely a function of the point quantities. This kind of approach is therefore more robust because it does not depend on the properties of the solid boundary, but on the properties of the flow, and requires no presumption of the relationship between the boundary and the flow. It is therefore more explicit and transparent, and is more transferable to studies of flows over different topographies. It is not an approach that has been largely used for studying the aerodynamics of vegetation canopies, because they are working with a canopy which is uniform and regular in the streamwise direction, making a definition based on bed surface topography less complicated. However, for examining flows over and within spatially heterogeneous surfaces, it is a more appropriate approach. Crapiste *et al.* (1986) believe that an averaging area can be deemed appropriate if the characteristic length over which point variables undergo significant variation is small compared to the length over which the double-averaged quantity is derived. In terms of flows over rough surfaces, Gimenez-Curto and Corniera Lera (1996) stated that the streamwise length of the area should be large in comparison to the characteristic wave-lengths of the spatial deviations in the time-averaged flow field, in order to guarantee that the resulting averaged values vary over length scales which are large enough to be comparable to those of the disturbances. This is equivalent to Coceal *et al.*'s (submitted) suggestion that the streamwise length of averaging region

should be long enough to eliminate flow variations due to individual roughness elements. Also to that of Lien and Yee's (2004) who stated that the averaging area should be chosen to resolve the characteristic variation of the flow property. Nikora *et al.* (in press b) described that the streamwise length of the averaging domain is determined by the overall geometry of the flow of interest. However, in their accompanying paper (in press a) they are more specific. They state that the averaging region should be much larger than the dominant turbulence scales but much smaller than the scales of the slowly varying mean flow. It is unclear why temporal flow features should influence the size of the averaging area, when averaging is being performed on a time-averaged flow field. It would appear more reasonable that it should be associated with the spatial pattern of the time-averaged flow, not the instantaneous, turbulent pattern. There still remains confusion of how the averaging area should be associated to the properties of the flow being averaged.

The choice of averaging area based on either a property of the bed or the flow is problematic, especially in the field. The problem with stating that the averaging area must be a function of some property of the flow is that *a priori* information is required on the flow before any measurements are taken, and therefore before an informed decision can be made on the number of measurements required and over what size of area. There is a great wealth of data on the temporal characteristics of the flow, allowing this aspect to be predicted with reasonable accuracy, but there is an acute lack of data on the spatial variability in the flow. It becomes even more problematic in the field. In order to gain an understanding of the spatial variability, a dense network of point velocimeters, such as ADV probes, would have to be deployed over a vast area of the bed (perhaps through moving the network over different areas of the bed), in order to be certain that the characteristic scale of variations are sampled. This can be highly unpractical and time-consuming (raising concerns over whether the flow conditions can be considered to be the same throughout all the measurements). An approach based on some property of the boundary or on the flow depth would mean that this would not be required.

However, this approach would also be associated with its own problems. For example, consider a gravel-bed river. If the characteristic scale of the bedforms is required, there is no way of understanding whether it is the scale of grain structures such as particle clusters, or structures involving an assemblage of grains such as longitudinal ridges,

transverse ribs or stone-cells that should be resolved. There is no information on the role of bed surface topography in creating spatial variability in the time-averaged flow field, and in particular on the bedform scale at which the form-induced stresses operate over. It is therefore difficult to specify which characteristic length scale should be used for defining the averaging area required. This is of course assuming that it is possible to obtain bed elevation data at a sufficient spatial resolution.

The results presented here, provide a less complicated way of defining the averaging area that is required to produce representative form-induced stress values over a water-worked gravel bed. They suggest that flow depth is a good scaling for the minimum averaging area. Flow depth is a more easily defined and measured quantity than the ones suggested by previous studies, making it easier to estimate the minimum averaging required before designing a measurement programme. Along with the results in Chapters 4 and 5, it further suggests that the association between the flow and the bed surface topography is not as great as previously assumed. Through the effect of flow depth on the degree of spatial variability in the time-averaged flow and form-induced stress, it implies that Hassanizadeh and Gray's (1979) simple notion that "in defining an operator for averaging, one should take into account the intrinsic nature of that property" is likely to be the most robust way in which representative double-averaged quantities should be derived.

6.14.7 *Relationship with Observational Scale*

The focus has been on producing estimates of the minimum averaging area required to produce a representative value of form-induced stress over the bed. However, the manner in which FS_f varies with averaging area (Figures 6.10 and 6.11) suggests that more information can be derived from this association. This can be achieved by considering averaging area as a function of the scale of interest, and how this influences the interpretation of the significance of form-induced stresses at that scale.

The results in Figures 6.10 and 6.11 showed that the contributions of form-induced stress, and by implication, the contributions of spatially-averaged Reynolds stress to the total fluid stress are a function of averaging area. Nikora *et al.* (in press a) believes that this dependence means spatial averaging is a better basis for bed shear stress partitioning, especially for the case of multi-scale roughnesses (e.g. grain and bedform

roughnesses). However, this idea can be taken forward and extended. If an investigator is interested in the stress components around a individual particle on the bed and the possible role of each component on its susceptibility to entrainment, the use of A_{\min} is unlikely to produce good estimates of the form-induced stress acting on that particular particle. Clearly a smaller averaging area (with a significant number of measurements within) would be more appropriate. Perhaps an averaging length similar to that of the b -axis of the grain would be appropriate, given the particles angle of orientation to the streamwise direction of the flow in water-worked gravel beds, in order for the grain-scale spatial variability in stress components not to be removed through spatial averaging. However, A_{\min} would be better for producing a representative value of form-induced stress over the bed for predicting the mean bed shear stress over the bed. Therefore, the choice of averaging area should depend on the purpose of the investigation, and the scale of interest. This appears logical. In the temporal domain, the flow field would not be averaged over a long time series if you were interested in individual turbulent events, but in contrast, nor would only a very short time frame be examined to estimate Reynolds stress. The length of the temporal averaging window is dependent on the temporal scale of interest. So in the same manner, the size of the averaging area should be dependent on the spatial scale of interest. It therefore means that the examination of how FS_f changes with averaging area is not solely of interest for estimating A_{\min} . The significance of form-induced stresses for a range of scales of interest (and for a range of river processes operating at different scales), can be easily interpreted from these plots.

These thoughts raise the question of whether the spatial resolution (or density) of measurements is also of some importance. Would a number of measurements N contained within a small averaging area (say over an individual grain) produce a representative estimate of form-induced stress for that given scale in the same way as a significantly larger area (say more than an order of magnitude larger) which contained N measurements would for that larger scale? Is the degree of representation r at a given scale, or area A_r , given by $r(A_r) = f(N/A_r)$? Coceal *et al.*'s (submitted) study of the effect of computational grid resolution on $\langle \bar{u} \rangle$ suggests this could be true.

6.15 Summary

The contribution to momentum transfer from correlations between point-to-point spatial variations in the time-averaged flow was examined. Through spatially averaging the Reynolds equations a new stress term, the form-induced stress, was derived to account for this component of momentum transfer. The stresses were found to be significant for flows above two water-worked gravel beds. They attained their maximum values closest to the maximum bed elevation, and could make both positive and negative contributions to the total fluid stress. Form-induced stresses that were representative of the bed made positive contributions of up to 12 % and negative contributions of up to nearly 8 %. They were found to remain significant for up to half of the flow depth, and in some cases up into the upper reaches of the flow, indicating that form-induced stresses do not disappear within the logarithmic and outer layer as previously thought. Therefore measurements of Reynolds stress alone, whether spatially-averaged or not, cannot be used to determine the mean bed shear stress over water-worked gravel beds. Clearly, for flows above the maximum bed elevation, shear stress cannot be predicted accurately by a linear distribution of Reynolds stress.

It was shown that increases in relative submergence can result in a change in how much momentum is being carried by spatial deviations in the flow, and therefore also by turbulent fluctuations. This even occurred when the average rate of momentum transfer at the bed was the same. This relationship between form-induced stress and relative submergence suggested that Reynolds stresses would be typically greater than the resultant total fluid stress at the low submergences but less than the total fluid stress at the higher submergences. Therefore, the relative contribution of momentum transfer mechanisms appears to be a function of relative submergence, particularly for the mid to high relative submergences. It means that the accuracy of using Reynolds stress to estimate mean bed shear stress is also dependent on relative submergence.

Form-induced stress was also shown to be highly dependent on the averaging area over which the time-averaged flow field was averaged. The degree of change in the contributions made by form-induced stress with averaging area was also found to be dependent on relative submergence. Different averaging areas resulted in different conclusions being drawn over the significance of form-induced stresses to momentum transfer. For example, at the point measurement scale, form-induced stresses could

nearly equal the mean bed shear stress, but also make a negative contribution of nearly 100 % to the total fluid stress at other positions, in contrast to that seen over the bed as a whole. However, this distribution was not well associated with the bed surface topography beneath, suggesting that these stresses are unlikely to be fully induced by the form of the boundary, as previously thought. The spread in the contributions made by the form-induced stresses to the total fluid stress were an order of magnitude greater than the contributions over the whole bed. It means that Reynolds stress could make very small contributions to the total fluid stress over some areas of water-worked gravel beds, and yet make very large contributions over others.

The form-induced stresses were also found to show considerable lateral variability, with some locations across the bed indicating that form-induced stresses could make both large positive and negative contributions, and others implying that form-induced stresses are negligible. The maximum positive and negative contributions to the total fluid stress were 35 % and nearly 20 %, respectively, which was similar to previous studies.

Importantly, it was shown that the averaging area used to assess the form-induced stresses over the whole bed produced representative values. It indicated that form-induced stresses are likely to operate at a bedform scale, such as that similar to stone cells or other bedforms that involve an assemblage of many grains. The minimum area required to produce a representative value of form-induced stress must be larger than the scale of these bed features. This area, non-dimensionalised by flow depth, was found to exponentially decrease with relative submergence in a consistent manner over each bed, revealing that the minimum area can be predicted by relative submergence. This information can therefore be used by future studies to determine the minimum measurement area that is required to measure form-induced stress over the bed. The presented values of minimum areas uncovered concerns over previous attempts to measure form-induced stress over gravel beds. It might be that a sufficient degree of confidence in a value of form-induced stress over a water-worked gravel-bed could only be achieved by using 3-D PIV in a horizontal plane at many heights above the bed.

CHAPTER 7
DISCUSSION: THE PHYSICAL
SIGNIFICANCE OF FORM-INDUCED STRESS
AND SPATIAL VARIABILITY
IN THE TIME-AVERAGED FLOW FIELD

7.1 Introduction

The previous chapters have described experimental observations of the time-averaged flow fields over ‘flat’ (at the macroscopic scale) water-worked gravel beds. These results have been compared to previous studies and how they may inform future approaches to measuring and describing form-induced stress and spatial variability in the time-averaged components of turbulent flows. This chapter will draw together the conclusions made from the previous chapters in order to provide a physical insight into the significance of the results. The concept of whether form-induced stress and spatial variability in the time-averaged flow field are entirely induced by bed surface topography will be discussed. It will also be examined whether form-induced stress can be considered to account merely for the departure in Reynolds stress from an assumed linear distribution, or whether it has a physical significance of its own. Further examination will be made of whether point velocity measurements are sufficient for characterising form-induced stress and spatial variability in time-averaged flow fields over water-worked gravel beds. Lastly there will be discussion of the implications of form-induced stress and spatial variability on solute, suspended sediment and bedload transport.

7.2 Is Spatial Variability Form-induced or an Inherent Property of the Flow?

It has been previously assumed that spatial variability in the time-averaged flow field is entirely associated with the effects of the rough boundary on the flow (Gimenez-Curto and Corniero Lera, 1996; Nikora *et al.*, 2001; Nikora *et al.*, in press a, b). The assumption is that they are “disturbances [in the flow] due to boundary irregularities” (Gimenez-Curto and Corniero Lera, 1996) and are “attributed to the effects of local

conditions on the bed” (Nikora *et al.*, 2002). This has led studies into the hydrodynamics of rough boundaries to term the spatial deviations as ‘boundary disturbances’ (Gimenez-Curto and Corniero Lera, 1996), ‘form-induced fluctuations’ or ‘form-induced intensities’, because “boundary irregularities originate perturbations in ensemble averaged flow” (Nikora *et al.*, 2001). The stresses that arise from the point-to-point correlations in spatial deviations in time-averaged streamwise velocity \bar{u} and time-averaged vertical velocity \bar{w} have been termed ‘form-stresses’, and more commonly ‘form-induced stresses’ (Nikora *et al.*, 2001; Nikora *et al.*, 2002; Pokrajac *et al.*, 2003; Maddux *et al.*, 2003; Campbell *et al.*, 2005; Nikora *et al.*, in press a, b). This is because it is assumed that form-induced stress “owes its existence to the presence of forms in the boundary”, and “are induced by the geometrical irregularities of the boundary” and is “the mean momentum flux of boundary disturbances originated by surface irregularities” (Gimenez-Curto and Corniero Lera, 1996).

Taking account of these assumptions, Nikora *et al.* (2001) has subdivided the distribution of fluid stress within open-channel flows above a rough boundary into the following specific regions:

1. The form-induced sublayer, which lies just above the maximum bed elevation, is where the flow is influenced by individual roughness elements. This is therefore where form-induced stresses are thought to be important. This layer is so called because it is where the form-induced stresses and the spatial variability caused by the form of the bed are to be found. According to Raupach *et al.* (1991) for atmospheric flows within vegetation canopies, the roughness elements may influence the local flow structure within the region $0 < z - z_c < (1 - 4)\Delta$, so the thickness of the form-induced sublayer is given by $(1 - 4)\Delta$, where z is the height above the maximum bed elevation z_c and Δ is the roughness height of the bed;
2. The logarithmic layer exists, above the form-induced sublayer, if the flow depth is sufficiently larger than Δ (Raupach *et al.*, 1991). This layer occupies the flow region $(2 - 5)\Delta$ to $0.5H$, where H is the maximum flow depth.
3. The outer layer is where the viscous effects and the form-induced stresses are negligible and the double-averaged Navier-Stokes equations are identical to the Reynolds equations.

From this subdivision, Nikora *et al.* (2001) obtained the following relationships for the total fluid stress distribution τ , assuming steady, uniform flow and neglecting any viscous effects, for the form-induced layer

$$\frac{\tau(z)}{\rho} = gS[z_{ws} - z] = [-\langle \overline{u'w'} \rangle(z) - \langle \tilde{u}\tilde{w} \rangle(z)] \quad (7.1)$$

and for the logarithmic and outer layers

$$\frac{\tau(z)}{\rho} = gS[z_{ws} - z] = -\langle \overline{u'w'} \rangle(z) = -\overline{u'w'}(z) \quad (7.2)$$

where ρ is the fluid density, g is the acceleration due to gravity, S is the bed slope, z_{ws} is the height above the maximum bed elevation at which the averaged water surface occurs, \tilde{u} is the spatial deviation in \bar{u} , and \tilde{w} is the spatial deviation in \bar{w} . It follows that the gravity force $gS[z - z_{ws}]$ is balanced by the spatially-averaged Reynolds stress $-\langle \overline{u'w'} \rangle$ and the form-induced stress $\langle \tilde{u}\tilde{w} \rangle$ in the form-induced layer. The total stress in the logarithmic and outer layers can be characterised by a point measurement of Reynolds stress, $\overline{u'w'}$, as $\langle \tilde{u}\tilde{w} \rangle = 0$ given it is assumed there is no spatial variability in Reynolds stress. This implies that the thickness of the form-induced sublayer should be a function of the height at which the form-induced stresses become negligible.

The implicit statement of these equations made by Nikora *et al.* (2001) is that form-induced stresses are not significant, and spatial averaging of the Reynolds stress is not required above the form-induced sublayer. Thus in the outer and logarithmic layers of the flow the total stress must be comprised of the Reynolds stress. Therefore it has been assumed that a linear fit to the Reynolds stress (from one point measurement, rather than from spatially-averaged measurements) can be used to predict the total fluid shear stress in these regions.

This subdivision of the flow appears to be dependent on accepting that spatial deviations in the time-averaged flow field, and the stress this creates, is form-induced, and therefore produces a form-induced sublayer above the bed surface. This assumption has remained largely because of a lack of detailed spatial information over either a

number of boundaries or for various hydraulic conditions. Yet the outcome is crucially important for determining whether form-induced stress and spatial variability in the time-averaged flow field can be predicted by the form of the bed, or whether considerations are also required of the hydraulic conditions.

The results from the previous chapters indicated that form-induced stress and spatial variability in the time-averaged flow field were not negligible in the regions of the flow above where the form-induced sublayer was shown to exist. They were found to be non-zero in the logarithmic and outer layers of the flow. For example, in some experimental runs the spatial variability in \bar{u} remained significant all the way up to the water surface. Also the spatial variability in \bar{w} was observed to increase from close to the bed towards the water surface, such that for some experimental runs it could be larger at the water surface than the bed surface. Furthermore, the fractional contributions of form-induced stress to the total fluid stress FS_f were found in some instances to be comparable in size to that close to the bed, for up to half of the flow depth. These results suggest that either the bed has a direct influence on the flow higher into the flow than previously thought, or that form-induced stress and the spatial variability in the time-averaged flow field is not entirely 'form-induced'. There is substantial evidence to suggest the latter may be true. This discussion will begin with an examination of the evidence, then look more closely at how the bed affects form-induced stress and spatial variability in the time-averaged flow field.

7.2.1 Evidence Against Spatial Variability Being Form-induced

The spatial patterns of $\bar{u}/\langle\bar{u}\rangle$ and \bar{w}/u_* were found to be similar over the two different water-worked gravel beds, despite the clear differences in bed surface topography. In addition neither of these spatial patterns, and the form-induced stresses over the bed, were found to show any correlation with bed surface elevation. This prompted the conclusion that organised features of the spatial patterns in $\bar{u}/\langle\bar{u}\rangle$ and \bar{w}/u_* were a class of spatially coherent time-averaged flow structures that might be an inherent feature of turbulent flows over water-worked gravel beds.

Instead, form-induced stress and spatial variability in the time-averaged flow field had a close association with relative submergence. The spatial patterns of $\bar{u}/\langle\bar{u}\rangle$ and \bar{w}/u_*

were comparable at similar relative submergences, and displayed considerable change with increases in relative submergence, even at the same z/D_{84} . This implies that the effect of bed surface roughness on the flow cannot fully account for the variability in the spatial flow field pattern.

The spatial pattern of \tilde{w}/u_* was not consistent across different hydraulic conditions at the same lateral location over the bed. Indeed, the spatial pattern appeared just as consistent across the nine different lateral positions for a given experimental run as it could across runs of different relative submergence at a given lateral position. Thus relative submergence may have an equally important influence on the pattern as bed surface topography. In addition, the change in the spatial pattern of \tilde{w}/u_* was found to have greater correspondence with the changes in the water surface with relative submergence, than with bed surface topography.

Increases in relative submergence were found to cause up to a 300 % increase in $\sigma_{\bar{u}}$, the degree of spatial variability in \bar{u} . This was much greater than the difference in $\sigma_{\bar{u}}$ between the two beds. The vertical patterns of $\sigma_{\bar{w}}$, the degree of spatial variability in \bar{w} , were also grouped according to relative submergence. Furthermore, neither the degree of spatial variability in \bar{u} or \bar{w} was found to show a universal relationship with z/d across the range of observed hydraulic conditions. This would have been expected to occur if the bed surface topography was inducing this spatial variability. The vertical profiles showed a greater tendency to be influenced by relative submergence.

Relative submergence was also shown to have a strong influence on the fractional contributions made by the form-induced stresses to the total fluid stress. It resulted in the contributions being negative at the lowest submergences, but positive at the higher submergences, at the same height above the same bed surface. In other words, with an increase in relative submergence, the implication is that the relative contributions from Reynolds stresses would reduce. It was observed that even when the mean bed shear stress was the same, increases in relative submergence could cause up to a fourfold increase in FS_f . Also, FS_f at the same lateral positions over the bed was found to show little correspondence across the different hydraulic conditions, and changes in relative submergence could produce similar degrees of change in FS_f at different

lateral positions. This suggested that a change in relative submergence could result in significant changes in the amount of momentum carried by both the turbulent and spatial fluctuations in the flow. Thus relative submergence could potentially have an equally important influence on momentum transfer mechanisms over water-worked gravel beds as bed surface topography.

The relationship between form-induced stress and relative submergence was further demonstrated by the fact that the vertical profiles of FS_f , and the manner in which FS_f varied with the spatial averaging area, was found to be better scaled by differences in flow depths, rather than by a difference in D_{84} (used as an approximation to the difference in roughness between the two beds). This was also discovered for the minimum averaging area required to produce a representative estimate of FS_f over a water-worked gravel bed. Indeed this minimum area was similar over the two beds and was found to increase with relative submergence, suggesting that the scale over which form-induced stresses operate is a function of relative submergence, not bed surface topography. The minimum averaging area can therefore be predicted for water-worked gravel beds by scaling with the flow depth and not from some property of the bed surface.

7.2.2 Evidence for Spatial Variability Being Form-induced

There is significant evidence that relative submergence can have a strong influence on form-induced stress and spatial variability in the time-averaged flow field. Yet it would be unwise to assume that relative submergence is the sole cause of form-induced stress and spatial variability in the flow. There were also occasions when the effect of the bed surface was evident.

The spatial patterns of both $\bar{u}/\langle\bar{u}\rangle$ and \tilde{w}/u_* were better scaled by bed roughness than flow depth. For example, the disappearance of the high-speed streaks in the spatial pattern of $\bar{u}/\langle\bar{u}\rangle$ was found to occur at nearly the same z/D_{84} for all values of relative submergence. Also, the spatial pattern had a greater similarity between the experimental runs at the same z/D_{84} than at the same z/d , particularly for the low to mid relative submergences. If high-speed streaks were present they tended to occur across all the experimental runs, apart from at the highest relative submergence, and the low-speed

spots tended to show greater spatial persistence than seen at the same z/d . Also, the vertical extent of the zones of upward and downward moving fluid was controlled by z/D_{84} , such that there was more spatial persistence in the regions of upward and downward fluid than at the same z/d . In other words by plotting the spatial pattern of \tilde{w}/u_* against z/D_{84} it revealed that the small areas of upward and downward motions that occurred close to the bed when plotted against z/d at the higher relative submergences largely corresponded with the vertical zones of fluid at the lower submergences. It meant that there was less variability in the spatial patterns of \tilde{w}/u_* at a given lateral position than when \tilde{w}/u_* was plotted against z/d .

The variability in the spatial patterns and FS_f across the bed further indicates that the bed must have some influence. Also, $\sigma_{\bar{u}}$ and FS_f , and in particular whether form-induced stresses predominately make positive or negative contributions to the total fluid stress, were different between the two beds. Furthermore, $\sigma_{\bar{u}}$ and FS_f showed a general decrease with z/D_{84} , suggesting that it decreases as the influence of the bed diminishes.

However, the effect of the bed on the flow could rarely be separated from the effects of relative submergence. For example, although the spatial patterns of $\bar{u}/\langle\bar{u}\rangle$, and \tilde{w}/u_* were better scaled by bed roughness than flow depth, bed roughness could never fully account for the variability in the spatial pattern between the runs. At the same z/D_{84} , the spatial patterns of $\bar{u}/\langle\bar{u}\rangle$ and \tilde{w}/u_* were comparable at similar relative submergences. It is therefore likely that the spatial pattern of $\bar{u}/\langle\bar{u}\rangle$ is influenced by a combination of bed roughness and flow depth. Bed roughness appeared to be the main influence on the spatial patterns at low and mid relative submergences, but there was some smoothing out of the effects of the bed at the higher submergences. Therefore the suggestion is that flow structures which are scaled by both bed roughness and flow depth influence these spatial patterns. This was confirmed by the fact that, although flow depth was found to produce a better scaling for $\sigma_{\bar{u}}$ and $\sigma_{\bar{w}}$ than bed roughness in the upper regions of the flow, they were equally scaled by these two variables close to the bed. A near-proportional relationship between $\sigma_{\bar{u}}$ and relative submergence was observed at any given z/d which also indicated a relationship between $\sigma_{\bar{u}}$ and z/D_{84} ,

which further implies that both the bed and relative submergence has an influence on spatial variability.

There is an apparent interaction between the influence of the bed on spatial variability and that of relative submergence. For example, the effect of relative submergence on $\sigma_{\bar{u}}$ was shown to increase with z/d . From this it was concluded that bed roughness (and the vertical extent of its influence, scaled by z/d) is likely to determine the degree of effect of relative submergence on $\sigma_{\bar{u}}$ and where its effects become apparent.

However, the results from the spatial patterns of $\bar{u}/\langle\bar{u}\rangle$ and \tilde{w}/u_* showed that this notion could equally be reversed, that relative submergence could influence the effects of the bed on the time-averaged flow. For instance, it was mentioned earlier that bed roughness appeared to be the main influence on the spatial patterns of $\bar{u}/\langle\bar{u}\rangle$ and \tilde{w}/u_* at low and mid relative submergences, but there was some smoothing out of the effects of the bed at the higher submergences. This suggests that the effect of bed roughness could equally be some function of relative submergence, as the influence of relative submergence is a function of bed roughness. It appears that spatial variability is controlled by an inter-relationship between the effects of the bed and relative submergence.

It can therefore be deemed unlikely that form-induced stress and spatial variability in the time-averaged flow field is entirely induced by the surface topographies of water-worked gravel beds. The effects of the bed are limited in terms of its vertical extent of influence and the range of relative submergences at which its influence is clearly apparent above that of relative submergence. The effects of relative submergence could potentially have an equal influence to bed surface topography because its effects should be felt, even if they are not apparent, throughout the depth of the flow and for all flows. Since relative submergence is a property of the flow, it indicates that spatial variability in the time-averaged flow field might be an inherent feature of flows over water-worked gravel beds.

This means that the terms 'form-induced fluctuations', 'form-induced intensities' and 'form-induced stresses' are rather misleading, and that it is not appropriate to attribute spatial variability in the time-averaged flow field to flow separation from roughness

elements (Gimenez-Curto and Corniero Lera 1996; Nikora *et al.*, 2001). The intensity of flow separation is related to the flow Reynolds number, and scaled with grain size and the near-bed flow velocity. However, the height of the form-induced sublayer does not scale with the near-bed flow velocity (not shown), which suggests that simple flow separation cannot explain the spatial variability in the time-averaged flow field.

The terminology used by atmospheric studies is preferable. The term ‘dispersive’ rather than ‘form-induced’ was first introduced by Raupach and Shaw (1982). The phrase ‘dispersive stress’ has very recently been used in hydraulic studies as an alternative to form-induced stress (Nikora *et al.*, in press, a, b), but more for cross-referencing back to atmospheric studies, with the term ‘form-induced’ still being used for examining the stresses in a hydraulic environment. Therefore, \tilde{u} should be termed the dispersive streamwise deviation, $\sigma_{\tilde{u}}/\langle\bar{u}\rangle$ the dispersive streamwise intensity, and so on.

The results question whether the fluid stress distributions within the flow can be subdivided in such a simple manner by considering where the effects of the bed would not be apparent and basing it on the characteristics of the bed, as carried out by Nikora *et al.* (2001). This subdivision may be appropriate for the vertical profile of $\langle\bar{u}\rangle$, but for fluid stress it would appear that further investigation is required of how the thickness of the three regions changes for a range of relative submergences over water-worked gravel beds. The clear indication is that the form of the boundary cannot predict the level of form-induced stress, as consideration is also required of the depth of the flow.

7.3 Physical Interpretation of Form-Induced Stress

The majority of studies that have examined form-induced stress have made no physical interpretation of form-induced stress. They have either mentioned that it arises from point-to-point correlations of spatial deviations in the time-averaged flow field, or from the irregularities in the boundary. Others have considered form-induced stress to be a numerical value that accounts for, or is responsible for, the departure in Reynolds stress close to a rough surface from the assumed linear distribution of fluid stress with height above a rough boundary (Finnigan, *pers. comm.*). It is considered as a balance to the changes in Reynolds stress (Nikora *et al.*, in press b), and therefore has no physical meaning or significance. This has prompted some well-known proponents of the double-averaging technique to question why there is such a great interest in form-

induced stress (Finnigan, *pers. comm.*). Indeed the choice of the term ‘dispersive stress’ by atmospheric studies implies that they consider form-induced stresses to purely account for the dispersion in Reynolds stress close to a rough boundary.

A study that has attempted to provide a physical interpretation of form-induced stress is that by Lien and Yee (2004). They examined the significance of form-induced stresses for atmospheric flows over staggered arrays of cubes using CFD. Lien and Yee interpreted form-induced stresses to be the forces acting on the double-averaged flow field. Furthermore, their study suggests that form-induced stress can be either diffusive (dissipative) or reactive (dispersive) in nature. They state that the form-induced stress tensor $\langle \tilde{u}\tilde{w} \rangle$ explicitly depends on the characteristic filter width $\gamma \equiv \phi^{1/3}$, where ϕ is the spatial averaging area, and that it is associated with its own kinetic energy term, the dispersive kinetic energy $k_f = 0.5\langle \tilde{u} \rangle^2$. Based on this, they claim that a diffusive form-induced stress implies there is an energy drain from the resolved scale (scales greater than γ and up to ϕ) to the sub-resolved scale (scales smaller than γ). A reactive form-induced stress implies there is a backward scatter of energy from the sub-resolved scale to the resolved scale. Therefore, if $FS_f < 0$, the form-induced stress is reactive and if $FS_f > 0$, the form-induced stress is diffusive. For example if $FS_f < 0$ it has the opposite sign to the fractional contributions made by Reynolds stress to the total fluid stress, and given that

$$\frac{\partial \langle \bar{u} \rangle \langle \bar{w} \rangle}{\partial z} = \frac{\partial \langle \bar{p} \rangle}{\partial x} - \frac{\partial \langle \overline{u'w'} \rangle}{\partial z} - \frac{\partial \langle \tilde{u}\tilde{w} \rangle}{\partial z} + \nu \frac{\partial^2 \langle \bar{u} \rangle}{\partial z^2} \quad (7.3)$$

it means that $\langle \tilde{u}\tilde{w} \rangle \partial \langle \bar{u} \rangle / \partial z > 0$, where p is fluid pressure and u' and w' are the temporal fluctuations in streamwise and vertical velocity, respectively. In other words, the shear production term that converts resolved-scale kinetic energy $0.5\langle \bar{u} \rangle^2$ to $0.5\langle \tilde{u} \rangle^2$ corresponds to a backscatter of energy from the sub-filter scales to the resolved scales.

They also interpreted the sign of FS_f , and therefore the direction in which the form-induced stress is acting (upstream or downstream), in terms of its interaction with Reynolds stress and its significance for total momentum transfer. They note that when

$FS_f < 0$, form-induced stress can be considered as ‘destructive’ relative to Reynolds stress because the momentum flux arising from the turbulent stress is reduced by the form-induced stress. But when $FS_f > 0$, the form-induced stress has the same sign as the Reynolds stress so is ‘constructive’ in nature because the momentum flux arising from the turbulent and form-induced stresses reinforce each other.

It is also considered here that form-induced stress has some physical meaning. The form-induced stress influences the force felt by the flow, on average, over a long period of time, in contrast to Reynolds stress which influences the force felt by the flow at a particular point in time. Regardless of turbulence and the temporal fluctuation this creates in fluid drag and lift, over a long interval of time, different regions of the flow alone will experience different levels of forces due to the spatial deviations in the time-averaged flow field. Therefore for example, some grains will experience, on average, a different level of force than other grains on the bed.

7.4 Implications for Point Measurements

7.4.1 Quantifying Variables Derived from Spatial Averaging

In Chapter 6 it was shown that FS_f displayed considerable spatial variability over the bed. This indicated that a relatively small number of point measurements may not fully sample the variability in form-induced stress over the bed, and could therefore lead to a misrepresentative value of FS_f for the bed. This variability will now be examined and extended to looking at $\langle \bar{u} \rangle$, $\sigma_{\bar{u}}$ and $\sigma_{\bar{w}}$. This was achieved using the velocity measurements obtained using the vertical plane PIV measurements. The time-averaged flow field data from each of the nine planes over the bed, for a given experimental run, was assimilated. Each of the vertical planes at a given level above the bed contained 61 vectors, so the assimilation produced a matrix of 549 vectors at each measurement level above the bed. Twenty four locations within the matrix were randomly chosen from which $\langle \bar{u} \rangle$, $\sigma_{\bar{u}}$, $\sigma_{\bar{w}}$ and FS_f were calculated to give $\langle \bar{u} \rangle_p$, $\sigma_{p\bar{u}}$, $\sigma_{p\bar{w}}$ and FS_{pf} , respectively. This number of locations was chosen because it is the number of LDA point measurements used by Nikora *et al.* (in press b) to examine the significance of form-induced stresses over an armoured gravel bed. It is also a greater number of point measurements than generally used in the field, so it should not underestimate how

representative attempts in the field are likely to be. The random selection was repeated 100 times for each experimental run at every vertical height above the maximum bed elevation. It was designed so that for each repetition the same velocity vector was not randomly chosen more than once.

To discover how $\langle \bar{u} \rangle_p$, $\sigma_{p\bar{u}}$, $\sigma_{p\bar{w}}$ and FS_{pf} compare to the values derived from the whole matrix, $\langle \bar{u} \rangle_{bed}$, $\sigma_{bed\bar{u}}$, $\sigma_{bed\bar{w}}$ and $\langle FS_f \rangle$, and therefore how representative they are likely to be of the bed, the departure in values was calculated between those averaged over the 24 locations and those averaged over the whole bed. This was given by

$$\sigma_{\langle \bar{u} \rangle} = \sqrt{\frac{1}{N} \sum_{i=1}^{N_R} (\langle \bar{u} \rangle_{p_i} - \langle \bar{u} \rangle_{bed})^2} \quad (7.4)$$

$$\sigma_{\sigma_{\bar{u}}} = \sqrt{\frac{1}{N} \sum_{i=1}^{N_R} (\sigma_{p\bar{u}_i} - \sigma_{bed\bar{u}})^2} \quad (7.5)$$

$$\sigma_{\sigma_{\bar{w}}} = \sqrt{\frac{1}{N} \sum_{i=1}^{N_R} (\sigma_{p\bar{w}_i} - \sigma_{bed\bar{w}})^2} \quad (7.6)$$

and

$$\sigma_{FS} = \sqrt{\frac{1}{N} \sum_{i=1}^{N_R} (FS_{pf_i} - \langle FS_f \rangle)^2} \quad (7.7)$$

where N_R is the total number of repetitions (= 100). The four sets of values for each of the experimental runs, over both of the beds, are displayed in Figure 7.1. This is presented in the form of a direct comparison between the two beds in order to enable the distributions from all 22 experimental runs to be examined, producing a summary of the values for the two beds. It is possible because each of the experimental runs over the bimodal bed were designed so that the relative submergence and bed slope were similar to the runs over the unimodal bed. The comparison shows that $\sigma_{\langle \bar{u} \rangle}$ is more than an order of magnitude lower than $\langle \bar{u} \rangle_{bed}$, which suggests that 24 point measurements

produce accurate estimates of $\langle \bar{u} \rangle_{bed}$ (Figure 7.1a). Also the range of $\sigma_{\langle \bar{u} \rangle}$ values is similar over the two beds, which indicates that the estimates produced by 24 measurements are equally representative over both of the beds. The range of $\langle \bar{u} \rangle_p / \langle \bar{u} \rangle_{bed}$ values is also similar, being only 0.94 to 1.03 over the unimodal bed and 0.91 to 1.07 over the bimodal bed. Virtually all (99.9 %) of the $\langle \bar{u} \rangle_p$ values over the unimodal bed fall within 5 % of their respective $\langle \bar{u} \rangle_{bed}$ values, and over the bimodal bed this figure is 99.7 %. This further indicates that the $\langle \bar{u} \rangle_{bed}$ values are well approximated by 24 point measurements. Coceal *et al.* (submitted) examined how computational grid resolution (equivalent to the number of measurements within an averaging area) for the simulation of flows over staggered arrays of cubes influenced the estimation of $\langle \bar{u} \rangle$. Using different resolutions, they revealed that there could be a 6 % difference in $\langle \bar{u} \rangle$ between the highest and lowest resolution. The range of $\langle \bar{u} \rangle_p / \langle \bar{u} \rangle_{bed}$ indicates that the majority of the $\langle \bar{u} \rangle_p$ values displayed a similar degree of departure to $\langle \bar{u} \rangle_{bed}$ as that found by Coceal *et al.* (submitted).

However, the values of $\sigma_{\sigma_{\bar{u}}}$ (Figure 7.1b) are of a very similar magnitude to those for $\sigma_{bed\bar{u}}$ (see Figure 4.3a). It results in the range of $\sigma_{p\bar{u}} / \sigma_{bed\bar{u}}$ values being very large, and again similar over both beds. They range from just 0.4 to as high as 1.7 over the unimodal bed, and from 0.2 to 1.4 over the bimodal bed. Also only 26.0 % and 31.3 % of the $\sigma_{p\bar{u}}$ values fall within 5 % of their respective values of $\sigma_{p\bar{u}}$.

The values of $\sigma_{\sigma_{\bar{w}}}$ in Figure 7.1c also have similar values to $\sigma_{bed\bar{w}}$ (see Figure 5.1a), and in some cases, they can be an order of magnitude greater than $\sigma_{bed\bar{w}}$. It gives rise to a range of $\sigma_{p\bar{w}} / \sigma_{bed\bar{w}}$ values over the unimodal bed that are almost exactly the same as observed for $\sigma_{p\bar{u}} / \sigma_{bed\bar{u}}$, ranging from 0.3 to 1.8. Over the bimodal bed, this range is higher from 0.4 to 2.4. Only 26.4 % and 27.5 % of the $\sigma_{p\bar{w}}$ values fall within 5 % of $\sigma_{bed\bar{w}}$ over the unimodal and bimodal beds, respectively.

The results for the fractional contributions of the form-induced stresses show that, typically, σ_{FS} is also an order of magnitude greater than $\langle FS_f \rangle$ (see Figure 6.1). The very high values of σ_{FS} correspond to when $\langle FS_f \rangle \approx 0$, and give rise to very high and

low values of $FS_{pf} / \langle FS_f \rangle$ which indicate that FS_{pf} can be up to two orders of magnitude higher or lower than $\langle FS_f \rangle$. Only 4.5 % and 8.1 % of the FS_{pf} values are within 5 % of $\langle FS_f \rangle$ for the unimodal and bimodal beds, respectively. The results from Figures 7.1 therefore indicate that, on most occasions, a random selection of 24 point measurements over the bed are likely to give rise to large errors in the estimation of the degree of spatial variability in \bar{u} and \bar{w} , and in the form-induced stress over the bed.

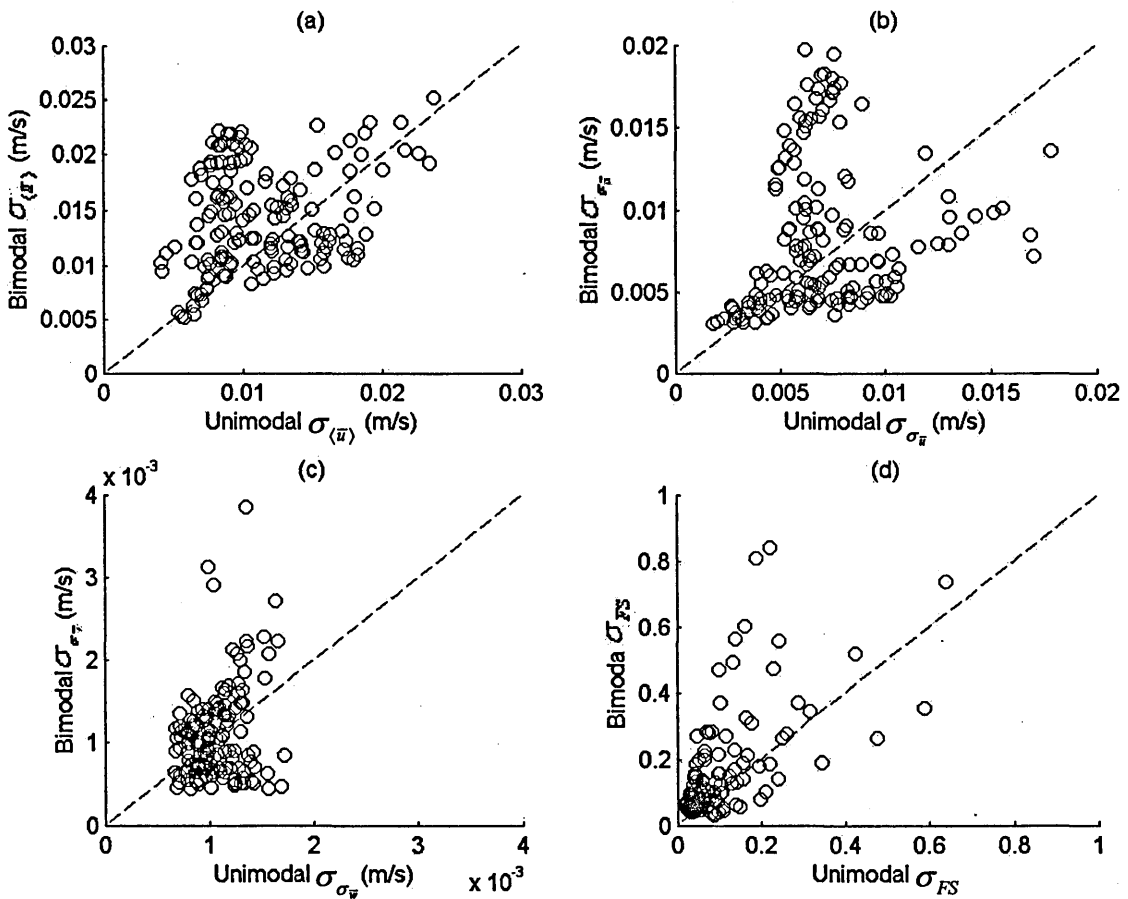


Figure 7.1. A comparison between the two beds of (a) the standard deviation in the double-averaged streamwise velocity $\sigma_{\langle \bar{u} \rangle}$; (b) the standard deviation in the degree of spatial variability in time-averaged streamwise velocities σ_{σ_u} ; (c) the standard deviation in the degree of spatial variability in time-averaged vertical velocities σ_{σ_w} ; and (d) the standard deviation in the fractional contributions made by the form-induced stresses at σ_{FS} , derived from 24 locations over the bed from that averaged over the whole bed.

7.4.2 Number of Point Measurements Required to Quantify Accurately Variables Derived from Spatial Averaging

To investigate further whether 24 point measurements are sufficient for producing representative values of $\langle \bar{u} \rangle$, $\sigma_{\bar{u}}$, $\sigma_{\bar{w}}$ and FS_f , the number of point measurements n required to produce these values was estimated. A representative value was defined as occurring when 95 % of the estimates from the 100 repetitions were within 5 % of the value calculated for the whole bed. For example, it was considered to occur when 95 % of the 100 values of $\langle \bar{u} \rangle_p$ were within 5 % of $\langle \bar{u} \rangle_{bed}$. The values of $\langle \bar{u} \rangle_p$, $\sigma_{p\bar{u}}$, $\sigma_{p\bar{w}}$ and FS_{pf} were calculated using an increasing number of randomly selected measurements within the matrix of 549 vectors until this condition was satisfied, at which n was given.

These n values for the estimation of $\langle \bar{u} \rangle_{bed}$ are shown in Figure 7.2 in the form of a direct comparison between the two beds at $z/d = 0.074$ and $z/d = 0.060$ for the unimodal and bimodal beds, respectively. The results for other heights above the bed show very similar results. Figure 7.2a demonstrates that only up to 19 randomly selected point measurements are required to produce representative estimates of $\langle \bar{u} \rangle$. The n values are quite consistent across the two beds and the different experimental runs, demonstrating that the estimation of $\langle \bar{u} \rangle$ is not very sensitive to the number of point measurements taken over the bed. The results indicate that the use of a low number of point measurements is valid for calculating $\langle \bar{u} \rangle$ over the two beds, which has important implications for the validity of estimating flow resistance using point measurements.

However, contrasting results were discovered for the estimation of $\sigma_{bed\bar{u}}$, $\sigma_{bed\bar{w}}$ and $\langle FS_f \rangle$. Only for three of the experiential runs could representative estimates of $\sigma_{bed\bar{u}}$ be produced without having to sample fully all the measurements over the bed. The n values in such cases were 280 over the unimodal bed, and 376 and 400 over the bimodal bed. This is still significantly higher than the number of point measurements commonly used by studies over water-worked gravel beds, including those that have used PIV. For the estimation of $\sigma_{bed\bar{w}}$ there was only one such occasion, but again this was still high at 401. But for the estimation of $\langle FS_f \rangle$, representative values could only be derived when

all the measurements over the bed were sampled. It would appear likely therefore, that the 24 point measurements that Nikora *et al.* (in press b) used over an armoured gravel bed to examine the significance of form-induced stresses were insufficient. More emphatically, it shows that spatial variability in the time-averaged flow field and form-induced stress over water-worked gravel beds is difficult to measure, and that errors will arise when using point measurements for these purposes. It further suggests, as pointed out in Chapter 6, that a sufficient degree of confidence in a value of form-induced stress over a water-worked gravel bed, and also in the degree of spatial variability in the time-averaged flow, might only be achieved by using 3-D PIV in a horizontal plane at many heights above the bed.

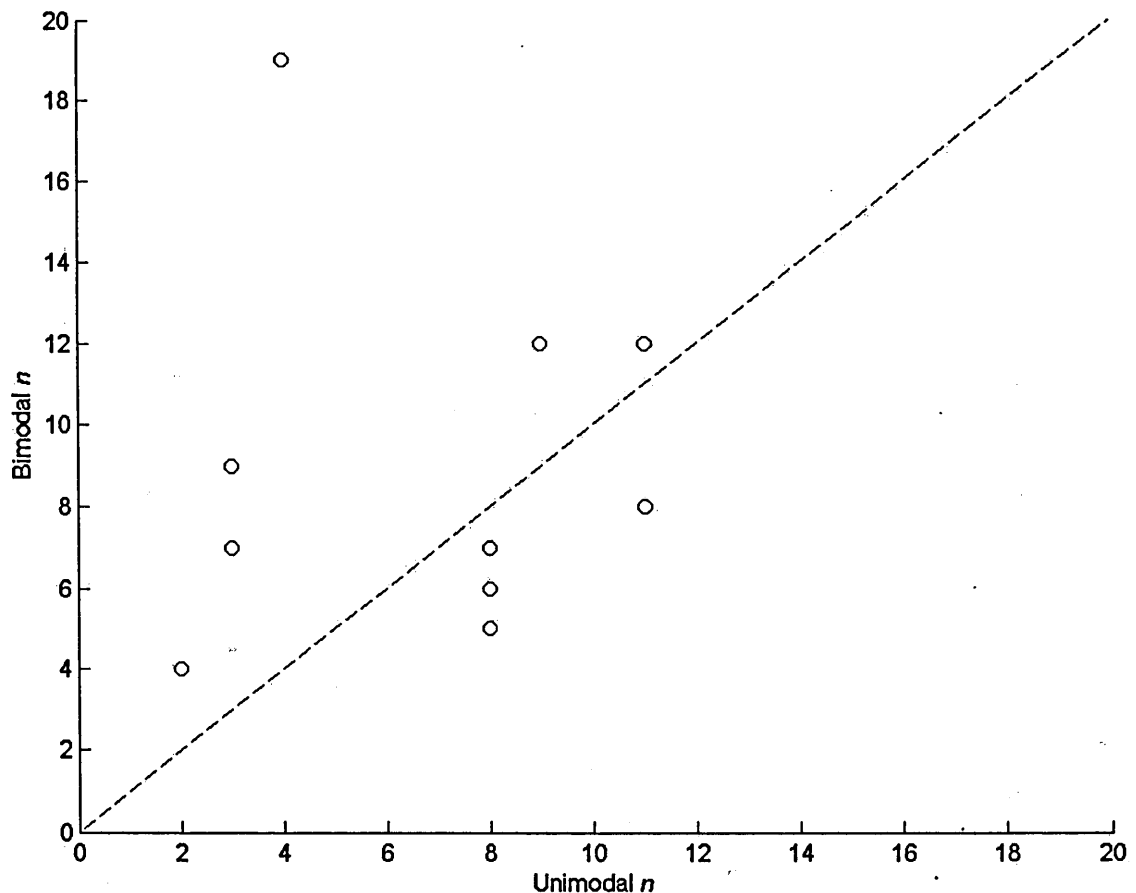


Figure 7.2. A comparison between the two beds of the number of point measurements n required to provide representative estimates of double-averaged streamwise velocity. The dashed line is a line of equality.

7.5 Potential Implications for Solute and Suspended Sediment Transport

The three mixing processes that are at work in rivers are molecular diffusion, shear dispersion and turbulent diffusion, and it is these processes which influence the mixing of pollutants. Mixing can occur in both the transverse (lateral) and longitudinal (streamwise) domain, and are both inversely related (Fischer, 1969). Transverse mixing has been found to determine the rate of longitudinal mixing because it governs the rate of exchange between regions of different streamwise velocity.

The spatial patterns in $\bar{u}/\langle\bar{u}\rangle$ showed that \bar{u} can be variable in both the lateral and streamwise directions. It is more variable in the lateral direction, because of the occurrence of streamwise streaks of high-speed fluid that followed a fairly straight course down the channel. This pattern could cause considerable spatial variability in mixing rates over water-worked gravel beds. The effect is likely to diminish with increasing distance from the bed surface, as the distribution of $\bar{u}/\langle\bar{u}\rangle$ becomes more homogeneous. Thus it could be the greater lateral variation in \bar{u} that will cause longitudinal mixing rate to be inversely related to transverse mixing rate close to water-worked gravel beds, with transverse mixing controlling longitudinal mixing rate. Since the spatial patterns in $\bar{u}/\langle\bar{u}\rangle$ were found to be similar over the two water-worked gravel beds, this understanding could potentially be included in pollutant mixing models.

These effects are not limited to solute transport. The high-speed streaks could result in regions of the bed either transporting suspended sediment of larger particle sizes than elsewhere over the bed, or a greater concentration of a given size on average over the bed. Amongst this large-scale pattern there could be small areas of the bed, on average, that transport either lower concentrations or smaller particle sizes, due to the occurrence of low-speed spots occurring over the bed. Given that the distribution of $\bar{u}/\langle\bar{u}\rangle$ over the bed was fairly homogeneous in the upper regions of the flow and that $\sigma_{\bar{u}}$ diminished with height, the effects of spatial variability in \bar{u} on solute and suspended sediment transport are likely to be limited to close to the bed.

However, because $\sigma_{\bar{w}}$ decreased quickly to a minimum value close to the bed but then increased into the upper regions of the flow, and the upward and downward moving regions of fluid persisted for much of the flow depth, the effects of spatial variability in

\bar{w} are, conversely, likely to be greater away from the bed surface. This could influence the vertical dispersion of solutes and movement of suspended sediment. For example, it is known that vertical turbulent diffusion leads to an upward migration to regions of lower concentration (Chanson, 1999). It appears reasonable, therefore, that the vertical gradient created by the nature of the vertical profiles of $\sigma_{\bar{w}}$ could result in, on average, a similar upward migration. The implication is that it might result in more uniform concentration profiles, and therefore higher transport rates, as more solute and suspended sediment will be in regions of higher streamwise flow velocities.

The alternating vertical zones of upward and downward moving fluid are also likely to cause vertical movements in solutes and suspended sediment. This could result in preferential infiltration of fine sediment into the interstices of an open gravel framework in the areas of the bed that experience downward zones of motion. Furthermore, this could cause a greater exchange of solutes between the bed and the flow, and subsequently greater releases from contaminated sediments. The stream–subsurface exchange of solutes can occur due to either bedform-induced advection (Thibodeaux and Boyle, 1987; Elliott and Brooks, 1997a; 1997b) or due to the turbulent coupling of stream and pore water flows (Shimizu *et al.*, 1990; Nagaoka and Ohgaki, 1990; Zhou and Mendoza, 1993). It is likely that spatial variability in the time-averaged flow field could influence the advection process. It is known that periodic variations in the hydraulic head at the bed surface caused by variations in the form of the bed, and the pressure variation this creates induces advective subsurface flow paths that carry water into and out of the subsurface (Zhou and Mendoza, 1993). The induced advective pore water flow carries stream-borne solutes into, through, and then out of the bed. This so-called bedform-induced advection is thought to be caused by flow separation and recirculation by the bed elements (Packman *et al.*, 2004). Given it has been shown that spatial variability in the time-averaged flow field is not entirely form-induced, it might be possible for subsurface advection to occur without the presence of significant bedforms. It could be influenced by the periodic change in the spatial patterns of $\bar{u}/\langle\bar{u}\rangle$ and \tilde{w}/u_* over flat (at the macroscopic scale) water-worked gravel beds. The streaky nature of the pattern of $\bar{u}/\langle\bar{u}\rangle$ means there is likely to be lateral pressure variations, on average, over the bed which could induce subsurface advection in the streamwise direction, and the alternating zones of upward and downward moving fluid could induce subsurface advection in the streamwise direction. This is possible because gravel beds

have a high permeability (Packman *et al.*, 2004). The regions of upward and downward moving fluid could also act more directly by, on average, assisting in the pumping process of inward and outward movement of solutes from the subsurface that is created by subsurface advection. Recently, Packman *et al.* (2004) has showed that subsurface advection can occur over flat gravel beds, further demonstrating that the effect of the spatial patterns on subsurface advection could be possible. However, they attributed this to small topographical features on the bed surface of the order of the one grain diameter, which produced flow separations that provided sufficient head differences to drive advective pumping flows. Yet the results presented here suggest it is unlikely that the topography of the bed entirely induced this process. The spatial variability in the flow, which appears to be an inherent feature of time-averaged flows over water-worked gravel beds, may cause subsurface advection to occur over all such beds.

Differential advection, as well as subsurface advection could be influenced by spatial variation in the time-averaged flow. Differential advection in a soluble or suspended material occurs when parcels of the material within the flow experience different velocities at different spatial locations (Guymer *et al.*, 2005). This advection produces a spreading, commonly called 'shear dispersion'. The degree of spatial variability in the time-averaged flow will therefore influence the rate of this shear dispersion. This should occur throughout the depth of the flow because spatial variability was apparent for the whole flow depth.

Given that the majority of mixing models treat the time-averaged velocity to be constant over the bed (a 1-D treatment), the spatial variability in time-averaged velocities will give errors in the estimate of dispersion rates and therefore solute and suspended sediment concentrations. The calculated dispersion rate and concentration would be dependent on the position over the bed at which the time-averaged velocities are measured. Due to the influence of relative submergence on the spatial variability in the time-averaged flow field, the effects of this spatial variability on solute and suspended sediment transport that have been described above will be a function of relative submergence.

7.6 Implications for Bedload Transport

7.6.1 *The Effect of Spatial Variability in the Time-averaged Flow Field*

It has long been established that bedload transport is spatially heterogeneous over water-worked gravel beds, with certain areas of the bed experiencing a greater number of entrainments and others providing preferential sites for deposition (e.g. Drake *et al.*, 1988). This can cause bedload transport rates to be highly spatially variable (e.g. Gomez, 1991; Konrad *et al.*, 2002). Since bedload transport laws are non-linear, this spatial variability can potentially cause large errors in the prediction of bedload transport over a water-worked gravel bed when using conventional bedload transport models.

To consider the influence of spatial variability in the time-averaged flow field on bedload transport means discussing how it influences time-averaged entrainment rates and bedload transport rates. It is recognised that turbulent, bursting motions will account for the spatial variability in entrainment at a given point in time, but it cannot fully account for the spatial variability in time-averaged entrainment. Given that bedload transport rate is an integral of mass collected over space *and* time, it is also unlikely to account fully for the spatial variability in bedload transport rate. Therefore a discussion of the influence of spatial variability in time-averaged velocities on bedload transport is required.

It is likely that bedload transport is most affected by absolute, rather than relative, spatial changes in time-averaged velocity over the bed. It is therefore unlikely that the spatial variations in \bar{w} can, alone, affect bedload transport, especially given that these tended to be lower closer to the bed, and higher towards the water surface. Whereas it was discovered that particular areas of the bed can experience \bar{u} values as low as 60 %, but also as high as 140 % of the double-averaged streamwise velocity. Thus some areas of the bed can have velocities that are more than two times higher than those over other parts of the bed. Remarkably, this also applied to neighbouring locations over the bed. The result was a similarity in magnitude between the range of time-averaged streamwise velocities over the beds and the double-averaged streamwise velocity. It is therefore likely that spatial variations in \bar{u} can have an influence on bedload transport. This could result in spatial variability in time-averaged entrainment rates and bedload

transport rates over the bed. The spatial variability in \bar{u} results in areas of the bed having higher \bar{u} and therefore on average these areas will be preferential sites for entrainment, if a single sized, flat bed is assumed.

It means that there is likely to be preferential entrainment within the high-speed streaks. As such bedload transport rates will be higher over streamwise strips of the bed. A number of studies have mentioned that armoured gravel beds can often exhibit an alternating lateral pattern of streamwise strips of ridges and troughs in the bed surface topography (Nezu and Nakagawa, 1993; Tait, 1993; McLelland *et al.*, 1999; Schvidchenko and Pender, 2001). Visual observations have shown that the most active sediment movement takes place along the troughs. Therefore, the high-speed streaks may account for some of this bed pattern, especially given that it has been shown that \bar{u} is higher in the troughs (Nezu and Nakagawa, 1993).

Most calculations of bedload transport in rivers are 1-D, by averaging hydraulic and transport-rate calculations over the channel width. However, because of the non-linear nature of bedload transport, this means that any spatial variability in shear stress τ will cause underestimation in the true bedload flux. With this in mind, Ferguson (2003) carried out a theoretical study to quantify the effect of lateral variability in shear stress on bedload transport capacity. The Meyer-Peter and Müller (1948) bedload transport equation was used to model width-averaged bedload transport rate q_b

$$q_b = k(\tau - \tau_c)^{1.5} \quad (7.8)$$

where τ_c is the critical shear stress for entrainment and k is an empirical coefficient. In a 1-D estimate of bedload flux the assumption is that $q_b = q_b(\tau_{av})$, in which τ_{av} is the mean shear stress averaged across the channel width w_c . From this a width-averaged estimate of bedload flux Q_b can be obtained from $Q_b = w_c q_b$. Ferguson compared the estimates of Q_b made by a 1-D estimate to those made when a lateral variability in τ was induced over the channel width. This lateral variability was simulated by using a statistical model that described the probability distribution for the spatial distribution of τ . This allowed both the mean and variance of the distributions to be changed, allowing

different degrees of lateral variability in τ to be applied. From this distribution, a width-averaged estimate of bedload transport rate q_{av} was given by

$$q_{av} = k \int_0^{y_{max}} y^{1.5} p(y) dy \quad (7.9)$$

where $y = \tau - \tau_c$ and $p(y)$ is the probability density function of y . The bedload flux was calculated as $Q_{av} = w_c q_{av}$ and compared to that based on a 1-D treatment, Q_b . This was carried out for different $p(y)$ and τ_c , based on the assumption that the bed was covered with a single-sized sediment, so that τ_c was the same everywhere in the channel. Ferguson (2003) found that the bedload flux was considerably greater under non-uniform flow, such that bedload flux increased with the variance of τ .

It would appear that Ferguson's approach might be useful for examining the effect of spatial variability in \bar{u} on bedload flux. This requires the assumption that $\tau \propto \bar{u}^2$ and, therefore that $\tau = \bar{u}^2$ and $\tau_c = m\langle\bar{u}\rangle^2$, where m is some multiplying coefficient. In order to compare the effects across different experimental runs, τ is replaced with $\tau^* = (\bar{u}/\langle\bar{u}\rangle)^2$ and τ_c becomes $\tau_c^* = m(\langle\bar{u}\rangle/\langle\bar{u}\rangle)^2 = m$. Therefore transport occurs when $\tau^* > \tau_c^*$ or $(\bar{u}/\langle\bar{u}\rangle)^2 > m\langle\bar{u}\rangle^2$. This makes the assumption, like Ferguson, that τ_c^* is the same all over the bed. Instead of having to model the lateral distribution, the horizontal plane PIV measurements can be used to provide a distribution of $\bar{u}/\langle\bar{u}\rangle$ from measurements of \bar{u} at different lateral and streamwise positions within the flow, rather than at one lateral position as modelled by Ferguson. By modifying equation (7.9) used by Ferguson, the width-averaged bedload transport rate for the measurement section is given by

$$q_{sp}(m) = k \int_0^{h_{max}} h^{1.5} p(h) dy \quad (0 < m < 1) \quad (7.10)$$

where $h = \tau^* - \tau_c^*$ and $p(h)$ is the probability density function (*pdf*) of h . From this the width-averaged bedload flux can be calculated as $Q_{sp}(m) = w_c q_{sp}(m)$. This can be compared to the flux based on the assumption of no spatial variability in \bar{u} , which

assumes that $\langle \bar{u} \rangle$ holds everywhere in the measurement section (1-D treatment). The width-averaged bedload transport rate q_0 for this condition is given by setting $\tau^* = 1$, since $(\langle \bar{u} \rangle / \langle \bar{u} \rangle)^2 = 1$, and the width-averaged bedload flux can be calculated from $Q_0(m) = w_c q_0(m)$. The relative bedload flux $Q^*(m) = Q_{sp}(m) / Q_0(m)$ can be used as a measure of the effect of spatial variability in \bar{u} on bedload flux, which means that k and s can be set to any arbitrary value. The flux has arbitrary units such that $Q^* = 1$ when there is no spatial variability in \bar{u} . The key limitation with this approach is that sub-threshold flow conditions cannot be investigated, although from the understanding of the shape of the distributions of $\bar{u} / \langle \bar{u} \rangle$ developed from Chapter 4, it would be possible to predict qualitatively how this would influence Q^* .

This analysis was undertaken for all 12 experimental runs over both of the beds for various values of m . It was performed for the PIV planes taken closest to the bed surface, at $z/D_{84} = 0.43$ for the unimodal bed and $z/D_{84} = 0.42$ for the bimodal bed. The variation in Q^* with m is shown for each of the beds in Figure 7.3. Over the unimodal bed it can be seen that up to $m \approx 0.7 - 0.8$ the bedload conveyance under spatially variable flow is greater than under the condition of uniform flow. This m value varies between the experimental runs. This condition occurs up to a lower value for some of the runs over the bimodal bed, ranging from $m \approx 0.4 - 0.8$. There is also much greater variability in these values between the runs than over the unimodal bed. The spatial variability in \bar{u} generally does not appear to have such an influence on bedload flux over the bimodal bed, because the values of Q^* are typically lower than over the unimodal bed. The bedload conveyance is higher when the flow is spatially variable because the increase in specific flux q_{sp} in areas of the bed with $\bar{u} > \langle \bar{u} \rangle$ is bigger than the decrease in q_{sp} in areas with $\bar{u} < \langle \bar{u} \rangle$. Thus at low values of m , and therefore low values of critical shear stress, bedload flux can be as much as four times higher than under the assumption of uniform flow over each of the beds. This is a similar degree of increase to that found by Ferguson (2003). Paola (1996) and Nicholas (2000) used a similar general model to Ferguson using flow depth as a surrogate for shear stress. They applied their model to specific flume experiments and field sites, respectively. The levels of difference between Q_{sp} and Q_0 are also similar to that reported by these two studies.

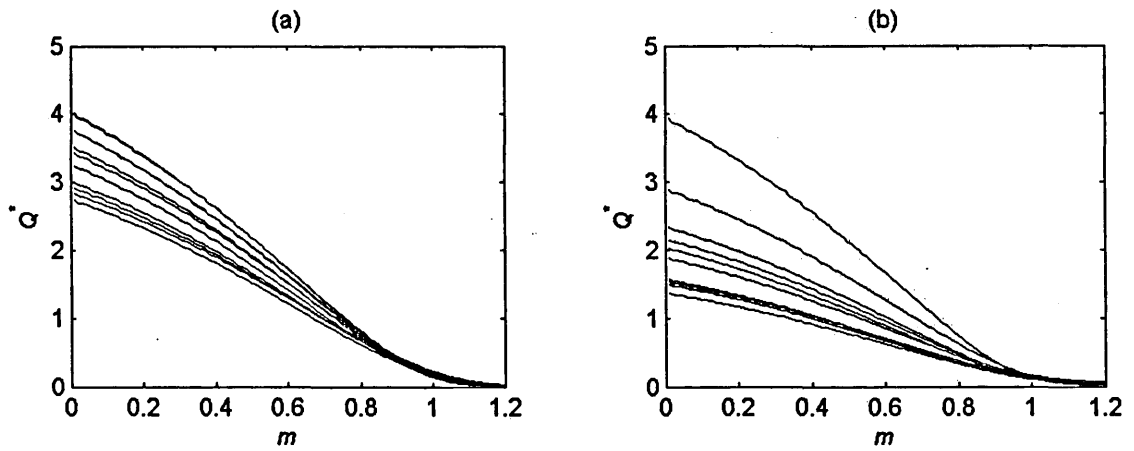


Figure 7.3. The change in relative width-averaged bedload flux Q^* with critical shear stress, indexed by $1/m$, to show the effect of spatial variability in \bar{u} on bedload flux relative to an estimate of bedload flux based on an assumption of uniform \bar{u} , where m is some multiple of $\langle \bar{u} \rangle$, \bar{u} is the time-averaged streamwise velocity and $\langle \bar{u} \rangle$ is the double-averaged streamwise velocity. Flux is in arbitrary units such that $Q^* = 1$ for uniform \bar{u} .

The difference between Q_{sp} and Q_0 in Figure 7.3 diminishes with m , such that above a value of 0.4-0.8 (dependent on the run), Q_{sp} becomes lower than Q_0 . This suggests that the effect of spatial variability in \bar{u} on bedload flux decreases with increasing values of critical shear stress. Also that it is more important at high transport intensities, where τ is much larger than τ_c , than at low transport intensities. This is the reverse of the findings by Ferguson (2003). He found that the effect of lateral variability in τ is greatest when $\tau \approx \tau_c$, given the nonlinearity of the Meyer-Peter Müller bedload transport equation. But the results that are found in Figure 7.3 are likely to be due to the negative skewness in the distributions of \bar{u} . As m increases, τ_c^* is located further to the right of the distribution, so the negative skewness of the distributions of $\bar{u}/\langle \bar{u} \rangle$ has less and less of an influence on Q^* , causing a reduction in the effect of spatial variability in \bar{u} on Q^* . This type of distribution was not used as a model for the lateral distribution of τ by Ferguson and explains the difference in results.

The results show that 1-D calculations of bedload transport can greatly underestimate bedload transport at high transport intensities, but as τ approaches τ_c , it can then overestimate transport. This was not found by Nicholas (2000) and Ferguson (2003). This again appears to be related to the negative skewness in the distributions of \bar{u} . At high m values, τ_c^* is located further to the right of the distribution, so the proportion of the bed that has high \bar{u} is less than the proportion of the bed that has low \bar{u} . Therefore the decrease in specific flux q_{sp} in areas of the bed with $\bar{u} < \langle \bar{u} \rangle$ is bigger than the increase in q_{sp} in areas with $\bar{u} > \langle \bar{u} \rangle$. But at low values of m , more of the areas of the distribution that have $\bar{u} > \langle \bar{u} \rangle$ are taken into account, so Q_{sp} is higher than Q_0 .

The results imply that for a given value of τ/τ_c , a channel with spatially variable \bar{u} can convey a given bedload flux by a lower flow at mid to high transport intensities than a channel with uniform flow. This is similar to the conclusions made by Nicholas (2000). But at low transport intensities, a higher flow is required to convey a given flux in a channel with spatially variable \bar{u} . Put simply an increase in transport intensity means the same total bedload flux is conveyed in less and less width. As pointed out by Ferguson (2003) this corresponds with the observation that in irregular natural channels that have non-uniform flow, bedload continues to move at discharges well below bankfull. The variability in the change in Q^* with m between runs over a given bed, and between the two beds, suggests that the accuracy of a 1-D treatment will depend on both hydraulic and bed conditions.

7.6.2 *The Effect of Relative Submergence*

It has been shown that the spatial variability in \bar{u} and the contributions made by form-induced stress to the total fluid stress are dependent on relative submergence. This was also observed for the experimental runs carried out at the same mean bed shear stress. It is therefore likely that the effects of form-induced stress and spatial variability on bedload transport are likely to be a function of relative submergence, even when the average momentum transfer rate is the same. This means that through the effect that form-induced stress has on entrainment, the probability of entrainment is likely to be a function of relative submergence.

The effect of relative submergence on bedload transport can be demonstrated by re-examining the influence of the spatial variability in \bar{u} on bedload flux for the experimental runs performed at a single bed slope, and those performed at the same mean bed shear stress. This is shown in Figures 7.4 and 7.5. Over the unimodal bed it can be seen that at a single bed slope, with the exception of the experimental run carried out at a relative submergence of 12.9, there is a clear decrease in Q^* with relative submergence, with the plots grouped into mid and low submergences (Figure 7.4a). Over the bimodal bed, with the exception of the experimental run carried out at a relative submergence of 2.6, there is also a general decrease in Q^* with relative submergence (Figure 7.4b). This decrease reduces with m over both beds, showing that relative submergence has less of an influence on Q^* with an increase in m . Thus relative submergence has little effect above $m \approx 0.8$, and therefore little influence on how much a 1-D treatment of bedload flux overestimates total flux at low transport intensities. However at higher intensities the underestimation made by a 1-D treatment is clearly a function of relative submergence.

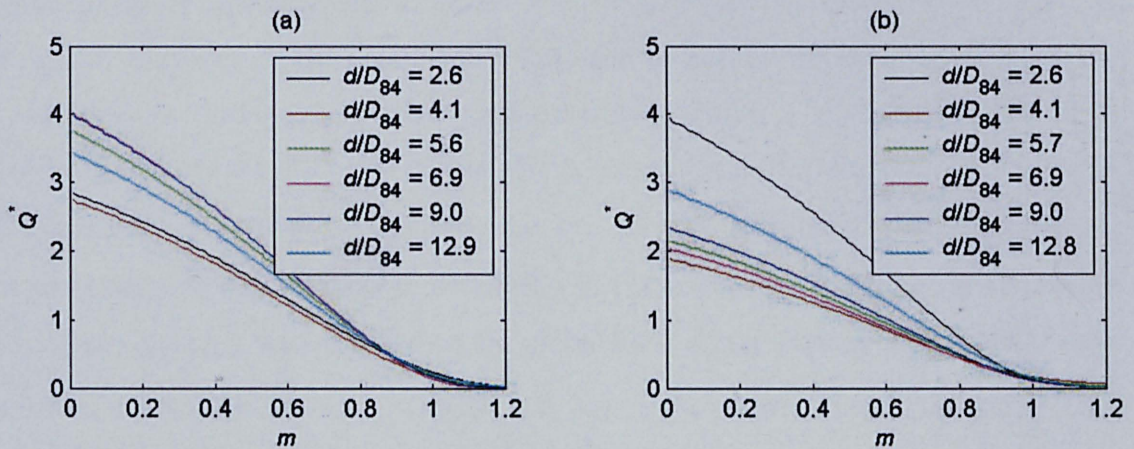


Figure 7.4. The change in relative width-averaged bedload flux Q^* with critical shear stress, indexed by $1/m$, for the experimental runs carried out at a single bed slope over (a) the unimodal bed; and (b) the bimodal bed. This shows the effect of spatial variability in \bar{u} on bedload flux relative to an estimate of bedload flux based on an assumption of uniform \bar{u} , where m is some multiple of $\langle \bar{u} \rangle$, \bar{u} is the time-averaged streamwise velocity and $\langle \bar{u} \rangle$ is the double-averaged streamwise velocity. Flux is in arbitrary units such that $Q^* = 1$ for uniform \bar{u} .

For the experimental runs performed at the same mean bed shear stress, it is apparent that over the unimodal bed the difference in Q^* between the runs is now reduced (Figure 7.5). Again with the exception of the run carried out a relative submergence of 12.9, Q^* now increases with relative submergence, the reverse to that seen at a single bed slope. It again appears that this degree of underestimation made in bedload flux by a 1-D model is a function of relative submergence. However, over the bimodal bed this is largely not the case, with Q^* being similar for all but one of the experimental runs. The degree of underestimation over both the beds under these conditions is of a similar magnitude to that seen at a single bed slope, even though the mean bed shear stress is the same. Clearly, spatial variability in \bar{u} has a persistent effect on bedload transport.

Chapter 6 showed that increases in relative submergence can result in a change in how much momentum is being carried by spatial deviations in the flow, and therefore also by turbulent fluctuations. It is thus reasonable to assume that relative submergence could also influence the spatial distribution of instantaneous streamwise velocities. Although the focus so far has been on time-averaged velocities, it is worth considering instantaneous velocities because it is these that may cause grain entrainment. Entrainment is often treated to occur if a single-valued threshold shear stress is exceeded. However, if the destabilising fluid forces and the threshold shear stress are considered as distributions rather than as single values, a probabilistic model of sediment entrainment can be developed. With knowledge of the temporal distribution of instantaneous streamwise velocities V_F and of the distribution of instantaneous streamwise velocities required to destabilise the grains on the bed from their positions V_G (grain resisting velocities), then the probability of entrainment occurring within a velocity interval dV around V_F (Figure 7.6) is given by (McEwan *et al.*, 2004)

$$pr[V_G < V_F] = \int_0^{V_F} f_G(V_G) dV = G(V_F) \quad (7.11)$$

where f_G is the *pdf* of the distribution of V_G . Given that the probability of V_F lying within the interval dV centred at V is given by

$$pr\left[V - \frac{1}{2}dV \leq V_F \leq V + \frac{1}{2}dV\right] = f_F(V_F) \quad (7.12)$$

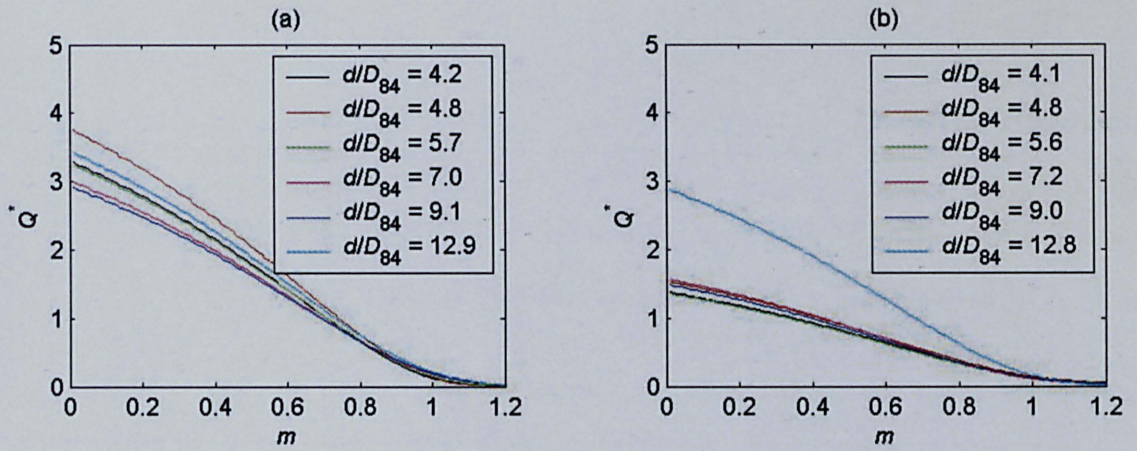


Figure 7.5. The change in relative width-averaged bedload flux Q^* with critical shear stress, indexed by $1/m$, for the experimental runs carried out at the same mean bed shear stress over (a) the unimodal bed; and (b) the bimodal bed. This shows the effect of spatial variability in \bar{u} on bedload flux relative to an estimate of bedload flux based on an assumption of uniform \bar{u} , where m is some multiple of $\langle \bar{u} \rangle$, \bar{u} is the time-averaged streamwise velocity and $\langle \bar{u} \rangle$ is the double-averaged streamwise velocity. Flux is in arbitrary units such that $Q^* = 1$ for uniform \bar{u} .

the elemental risk of entrainment dE within this same interval can be estimated through

$$dE(V_F) = f_F(V_F) dVG(V_F) \quad (7.13)$$

where f_F is the *pdf* of the distribution of V_F . This generates a *pdf* of the distribution of V_F at which the grains on the bed are susceptible to entrainment. The number of grains within a measurement area susceptible to entrainment N_E can then be given by

$$N_E = N_G \int_0^{\infty} dE(V_F) dV \quad (7.14)$$

where N_G is the number of grains on the bed surface.

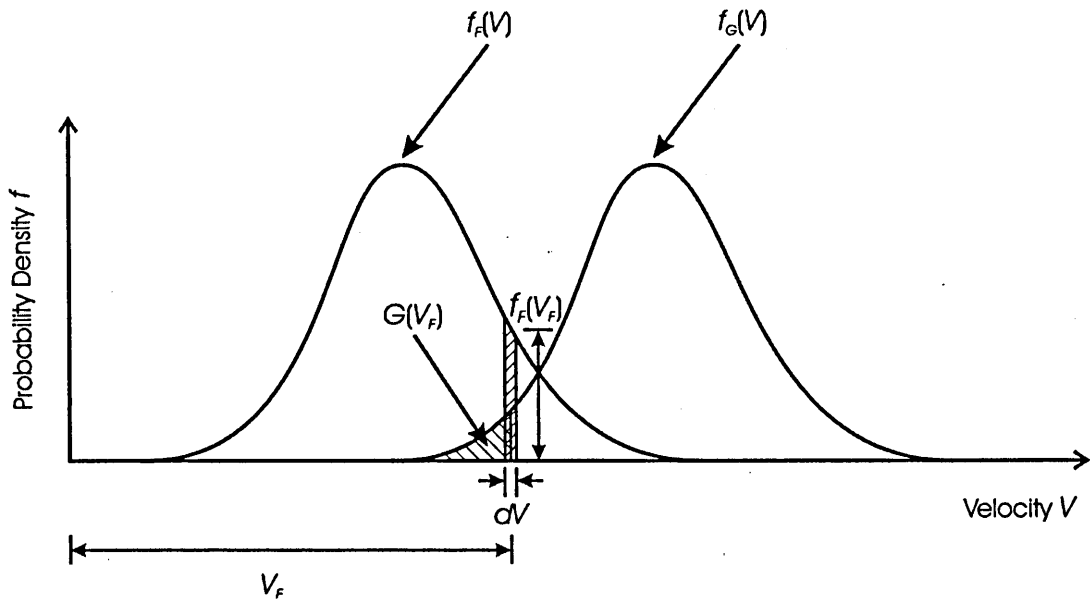


Figure 7.6. Schematic illustration of the existence of a probability density function of instantaneous streamwise velocities f_F and a probability density function of the instantaneous streamwise velocities required to destabilise the grains on the bed from their positions f_G over a mixed grain-size bed. The threshold of entrainment is achieved when the two probability distributions overlap, with the degree of overlap controlling the entrainment rate. The probability of entrainment occurring within a within a small velocity interval dV around an instantaneous streamwise velocity V_F is therefore given by $G(V_F)$. Adapted from McEwan *et al.* (2004).

The measurements carried out here only provide information on V_F . However, simultaneous measurements of instantaneous flow velocities and the movement of the bed surface were made previously by Chegini *et al.* (2002) (also see Barison *et al.*, 2003). This involved using one camera to take horizontal plane PIV measurements of V_F at 5 mm above the maximum bed elevation and a second camera to track the movement of the bed (see Chegini *et al.* (2002) for further details). This provides measurements of V_F and dE , and N_G can be estimated for the original bed surface. By using equation (7.14) a value of N_E can therefore be calculated for the bed. A Discrete Particle Model was used to generate f_G over this bed surface (details of this model can be found in Heald *et al.* (2004)). This model represents individual grains as spheres and forms a macroscopically flat sediment bed of a known grain-size distribution under

conditions of ballistic deposition. A sphere is released in sequence into a still fluid, each from a random position in a horizontal plane located well above the surface. The particle falls under the influence of gravitational and fluid drag forces before it undergoes a series of collisions with previously deposited particles, and then eventually rests a stable position. The geometry of the numerically deposited beds is then analysed to reveal the resisting velocity of individual particles exposed on the surface. These velocities were found to follow approximately a normal distribution. By making this assumption, f_G could be calibrated by adjusting its mean and variance until it produced a distribution of dE that was the same as that measured by Chegini *et al.* (2002).

For the experimental runs that were studied in the preceding chapters, only f_F is known. However, the measurements made by Chegini *et al.* (2002) were carried out at a flow depth of 90 mm and over a water-worked bed that was formed from a 100 % gravel mixture. This study has measurements of V_F at the same height above the bed surface, at the same depth (experimental run 6U) and over a similar bed. The gravel mixture used by Chegini and the unimodal bed used here do not differ greatly in their grain size distribution, with D_{50} being 4.82 and 4.97 mm, respectively. Both have unimodal, log-normal distributions, with the main difference being in the tails of the distributions, with the unimodal bed having a higher proportion of its mixture contained in both the coarser and finer ends of the distribution (Figure 7.7). It therefore appears reasonable to use the data from Chegini's experiments to examine the influence of relative submergence on the susceptibility of grains on the bed to be entrained. Given that all of the runs studied in the preceding chapters were performed at sub-threshold depths, the mean of the distribution of V_G was decreased until N_E for experimental run 6U was the same as that measured by Chegini.

The change in N_E with relative submergence is shown in Figure 7.8 for the experimental runs performed at a single bed slope (Figure 7.8a), and those carried out at the same mean bed shear stress (Figure 7.8b). This uses the horizontal plane PIV measurements that were taken at 5 mm above the bed surface elevation, a height of $z/D_{84} = 0.71$. These provide information on f_F over the bed, which were overlapped onto f_G to provide estimates of N_E . Since all the experimental runs were carried out over the same bed surface, it represents a way in which to isolate the effect of relative submergence on entrainment. This is not possible in experimental studies when

measuring the change in entrainment rate with increasing discharge, or comparing entrainment rates for different relative submergences at the same mean bed shear stress, because the bed surface will always be different as entrainment occurs. It is important to note that f_F is not taken from one point over the bed but is from all the measurements collected over the bed surface and over the whole measurement period. It therefore inherently includes the spatial variability that was seen in \bar{u} .

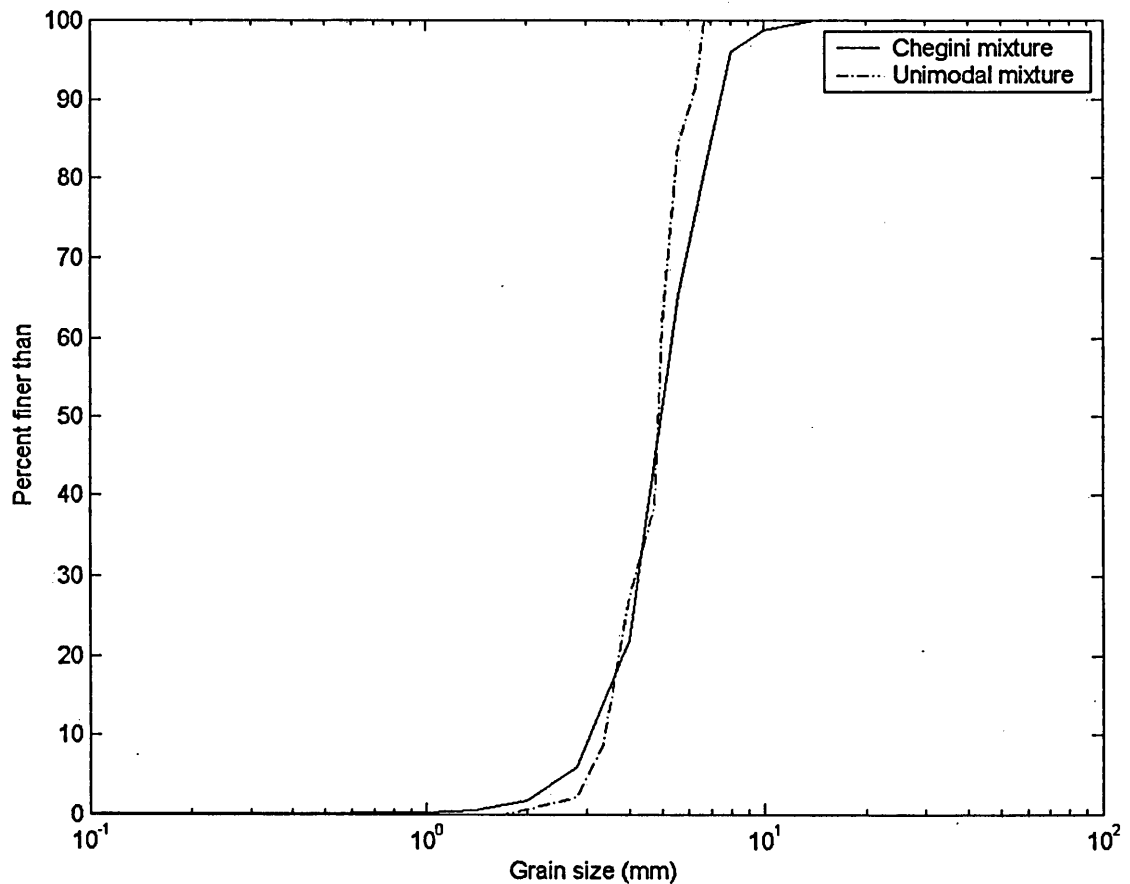


Figure 7.7. A comparison between the bed mixture used by Chegini *et al.* (2002) and the one used to produce the unimodal bed.

The results at a single bed slope show that, as to be expected, N_E increases with discharge, and therefore relative submergence (Figure 7.8a). More interestingly this also occurs for the experimental runs at the same mean bed shear stress (Figure 7.8b). Furthermore the increase is a similar magnitude to that observed at a single bed slope. Given that N_E is proportional to entrainment rate, the implication is that the shallower

the depth, and therefore the steeper the bed slope, the higher the shear stress must be to produce a given entrainment rate. Assuming bedload transport rate is the product of entrainment rate and hop length, and that hop lengths are sensibly stable with grain size, these results further suggest that transport rate has a strong dependence on relative submergence. This potentially demonstrates that transport rate is not a direct function of mean bed shear stress. The results describe a mechanism that will cause river channels with contrasting morphologies (and therefore different relative submergence), but similar levels of average bed shear stress, to experience different levels of sediment mobility. This could help to explain why studies have shown that the threshold shear stress (time-averaged) for entrainment appears to increase in very shallow flows (Bathurst *et al.*, 1983; 1987; Shvidchenko and Pender, 2000), and as such explain to some degree why there is data scatter in the Shields diagram (Buffington and Montgomery, 1997).

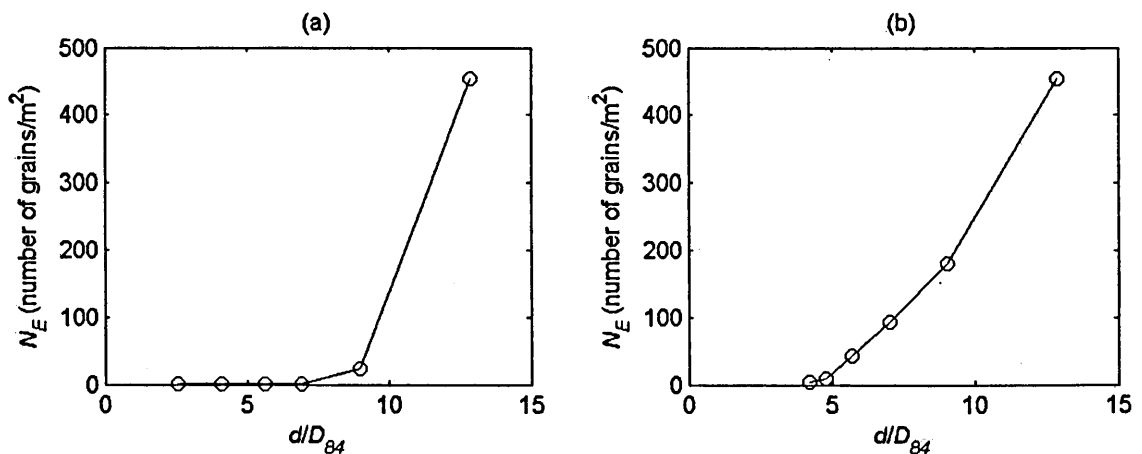


Figure 7.8. The change in the number of grains within a unit area susceptible to entrainment N_E with relative submergence d/D_{84} over the unimodal bed for the experimental runs carried out (a) at a single bed slope; and (b) at the same mean bed shear stress.

7.7 Summary

Discussion has been made of the physical interpretation and significance of form-induced stress and spatial variability in the time-averaged flows over water-worked gravel beds. Neither appears to be induced entirely by bed surface topography, as so

often assumed by previous studies. Relative submergence can potentially have an equally important influence on form-induced stress and spatial variability as bed surface topography. The effects of bed surface topography and relative submergence are interrelated, with bed roughness having a greater influence at low to mid submergences, but the effects smoothed out at the higher submergences. There is a strong argument to suggest that the term 'form-induced' should be replaced by that used in atmospheric studies, 'dispersive'.

The number of point measurements that are required for characterising time-averaged flow variables and form-induced stress was estimated. The results indicated that the use of a low number of point measurements is valid for calculating the double-averaged streamwise velocity. However, it demonstrated emphatically that errors will arise when using point measurements for examining form-induced stress and the degree of spatial variability in time-averaged flows over water-worked gravel beds. It suggested that a sufficient degree of confidence in the estimation of these quantities might only be achieved by using 3-D PIV in a horizontal plane at many heights above the bed.

The implications of spatial variability in the time-averaged flow on solute and suspended sediment transport were also discussed. It is likely to influence the rate of shear dispersion by promoting differential advection in a soluble or suspended material within the flow. It could also result in the subsurface advection of solutes taking place in flat (at the macroscopic scale) water-worked gravel beds without the presence of any significant bedforms. Given that spatial variability in the flow appears to be an inherent feature of time-averaged flows over water-worked gravel beds, it means that subsurface advection may not be bedform-induced as previously thought. The majority of dispersion models treat the time-averaged velocity to be constant over the bed (a 1-D treatment), therefore the spatial variability in time-averaged velocities will produce errors in the estimation of dispersion rates and therefore solute and suspended sediment concentrations. The calculated dispersion rate and concentration will be dependent on the position over the bed at which the time-averaged velocities are measured.

It was demonstrated theoretically that spatial variability in time-averaged streamwise velocities could cause 1-D calculations of bedload transport to underestimate greatly bedload transport at high transport intensities, but to overestimate transport as the shear stress approaches the threshold for entrainment. At very high intensities, total bedload

flux in spatially variable flow could be as much as four times higher than under the assumption of uniform flow. This effect was shown to be a function of relative submergence and to decrease with increases in shear stress, and therefore decreases in bedload intensity. The results implied that for a given ratio of shear stress to threshold stress, a channel with spatially variable time-averaged streamwise velocities can convey a given bedload flux by a lower flow at mid to high transport intensities than a channel with uniform flow. However, at lower intensities, a higher flow is required to convey a given flux in a channel with spatially variable flow.

The results from the preceding three chapters were supplemented with data from a previous study, in which the near-bed velocity field in the vicinity of a grain at the point of entrainment was measured using a combined PIV/image analysis system. This was combined with information on the shape of the probability density function of flow velocities capable of causing individual grain movement, derived from a discrete-particle model. By examining how the distribution of instantaneous streamwise velocities changed over the bed with relative submergence at the same mean bed shear stress, it was shown that an increase in relative submergence can cause a considerable rise in the number of grains that are susceptible to entrainment. The shallower the depth and the steeper the bed slope, the higher the shear stress must be to produce a given entrainment rate. The overriding implication is that transport rate is not a direct function of mean bed shear stress and will cause river channels with contrasting morphologies (and therefore different relative submergences), but similar levels of mean bed shear stress, to experience different levels of sediment mobility.

CHAPTER 8

CONCLUSIONS

High spatial resolution measurements of velocity were made to assess quantitatively the degree of spatial variability in the time-averaged flow and its potential for transferring momentum over water-worked gravel beds. These were made for a range of hydraulic conditions and over two beds of different surface topographies to understand how this can change the degree of spatial variability and the spatial structure in the time-averaged flow field over water-worked gravel beds, and its potential for transferring momentum.

These results were successfully used to demonstrate that time-averaged streamwise velocities display considerable spatial variability over water-worked gravel beds. It was discovered that particular areas of the bed can experience values as low as 60 %, but also as high as 140 %, of the double-averaged streamwise velocity. It means that some areas of the bed can have velocities that are over two times higher than those over other parts of the bed. Remarkably, this also applied to neighbouring locations over the bed. It resulted in the range of time-averaged streamwise velocities over the beds being similar in magnitude to the double-averaged streamwise velocity. The spatial variability was, however, less significant than the temporal variations in instantaneous streamwise velocities. The degree of spatial variability in time-averaged streamwise velocities was scaled by the double-averaged streamwise velocity, rather than bed shear velocity, and its vertical variability was scaled with flow depth rather than bed roughness. Spatial variability did not disappear in the logarithmic and outer regions of the flow, which was in direct contrast to previous thinking that spatial variability is only evident in the form-induced sublayer. The degree of spatial variability at given height within the flow was shown to clearly increase with relative submergence, such that it could be three times higher at the higher relative submergences than at the lower submergences.

It was discovered that the degree of spatial variability in time-averaged vertical velocities was a magnitude lower than that observed for the time-averaged streamwise velocities. Furthermore, the degree of spatial variability in time-averaged vertical velocities was a magnitude lower than the temporal variations in instantaneous vertical velocities. Surprisingly, it was found to increase in the logarithmic and outer regions of

the flow, and in some cases was higher closer to the water surface than the bed surface, which again indicated that spatial variability does not disappear within the logarithmic and outer layer as previously thought. Bed shear velocity, rather than the double-averaged streamwise velocity, scaled the degree of spatial variability. This indicated that it was not related to the vertical velocity profile of the flow. The vertical variation in the degree of spatial variability was scaled by flow depth rather than bed roughness, as was found for the streamwise velocities. Furthermore, it was shown that the degree of spatial variability was typically greater at the higher submergences than the lower submergences, up to as much as three times larger. This increase with relative submergence was equally large for the experimental runs carried out at the same mean bed shear stress.

The time-averaged flow velocities showed a considerable degree of organisation over the two beds. Close to the bed, the streamwise velocities were organised into streamwise streaks of high-speed fluid which were overlain by spots of low-speed fluid. The time-averaged vertical velocities were structured in such a way that indicated there were alternating vertical zones of upward and downward moving fluid over the bed, which could extend from the bed surface up into the outer region of the flow. This organisation in the time-averaged flow field was consistent across the two beds and revealed the existence of a class of flow structure that is different from the one for turbulent flow structures; these were spatially coherent time-averaged flow structures. Bed roughness appeared to scale these spatial patterns, but this influence was a function of relative submergence. Bed roughness had a greater influence at low to mid submergences, but the effects were smoothed out at the higher submergences. This demonstrated that flow features that scale with both bed roughness and flow depth must control the spatial patterns. It remains unclear whether turbulent flow features are likely to have caused the appearance of these time-averaged flow structures, but for this to be the case, it would require the turbulent structures to be both spatially and temporally persistent such that their presence appeared within the flow after time-averaging.

The contribution to momentum transfer from the spatial heterogeneity in the flow was examined by estimating the form-induced stress within the flow. The form-induced stresses were found to be significant for flows over both of the water-worked gravel beds. They attained their maximum values closest to the maximum bed elevation, and made both positive and negative contributions to the total fluid stress. Form-induced

stresses that were representative of the bed made positive contributions of up to 12 % and negative contributions of up to nearly 8 %. They were found to remain significant for up to half of the flow depth, and in some cases up into the upper reaches of the flow, indicating that form-induced stresses do not disappear within the logarithmic and outer layer as previously thought. Therefore measurements of Reynolds stress alone, whether spatially-averaged or not, cannot be used to determine the mean bed shear stress over water-worked gravel beds. Clearly, for flows above the maximum bed elevation, shear stress cannot be predicted accurately by a linear distribution of Reynolds stress.

It was shown that increases in relative submergence can result in a change in the level of momentum carried by spatial deviations in the flow, and by inference how much is carried by turbulent fluctuations. This even occurred when the average rate of momentum transfer at the bed was the same. This relationship between form-induced stress and relative submergence suggested that Reynolds stresses would be typically greater than the resultant total fluid stress at the low submergences but less than the total fluid stress at the higher submergences. Therefore, the relative contributions of momentum transfer mechanisms appear to be a function of relative submergence. It means that the accuracy of using Reynolds stress to estimate mean bed shear stress is also dependent on relative submergence.

Estimation of the magnitude of form-induced stress was also shown to be highly dependent on the averaging area over which the time-averaged flow field was averaged. The degree of change in the contributions made by form-induced stress with averaging area was also found to be dependent on relative submergence. Different averaging areas resulted in different conclusions being drawn over the significance of form-induced stresses to momentum transfer. For example, at the point measurement scale, form-induced stresses nearly equalled the mean bed shear stress at some positions over the bed, and at other locations they made a negative contribution of nearly 100 % to the total fluid stress. This indicated that form-induced stresses are highly significant at this spatial scale. However, for the bed as a whole, form-induced stresses only made positive contributions of up to 12 % and negative contributions of up to nearly 8 %. Clearly the averaging area has a significant effect on the interpretation of the significance of form-induced stresses to carrying momentum. Different averaging areas result in different conclusions being drawn at those different spatial scales.

The form-induced stresses at the point measurement scale were highly variable over the bed. It implied that Reynolds stress could make very small contributions to the total fluid stress over some areas of water-worked gravel beds, and yet make very large contributions over others. This variability means that a large averaging area is required to produce a representative value of form-induced stress for the bed. The minimum area required to produce a representative value can be predicted by relative submergence, and its size revealed that form-induced stresses are likely to operate at a bedform scale, such as that similar to stone cells or other bedforms that involve an assemblage of many grains. This information can be used by future studies to determine the minimum measurement area required to measure form-induced stress over the bed. It was shown emphatically that errors are likely to arise when using a low number of point measurements for examining form-induced stress and the degree of spatial variability in time-averaged flows over water-worked gravel beds. It was suggested that a sufficient degree of confidence in the estimation of these quantities might only be achieved by using 3-D PIV in a horizontal plane at many heights above the bed.

The spatial patterns in the time-averaged flow field were found to be poorly associated with bed surface topography, but to be dependent on relative submergence. It suggested that the time-averaged flow structures might be an inherent feature of turbulent flows over water-worked gravel beds. Furthermore the distributions of form-induced stresses over the bed had a weak correlation with bed surface topography. Given that form-induced stress and spatial variability in the time-averaged flow field were also significant above the form-induced sublayer, it suggested that spatial variability is not entirely induced by bed surface topography. It was concluded that relative submergence might have equally as important an influence on spatial variability as bed surface topography over water-worked gravel beds.

It was demonstrated theoretically that spatial variability in time-averaged streamwise velocities could cause 1-D calculations of bedload transport to underestimate greatly bedload transport at high transport intensities, but to overestimate transport as the shear stress approaches the threshold for entrainment. This effect was shown to be a function of relative submergence and to decrease with increases in shear stress, and therefore decreases in bedload intensity. The results implied that for a given ratio of shear stress to threshold stress, a channel with spatially variable time-averaged streamwise velocities can convey a given bedload flux by a lower flow at mid to high transport

intensities, than a channel with uniform flow. However, at lower intensities a higher flow is required to convey a given flux in a channel with spatially variable flow. It was also shown that an increase in relative submergence can cause a considerable rise in the number of grains that are susceptible to entrainment when the mean bed shear stress is the same. The shallower the depth and the steeper the bed slope, the higher the shear stress must be to produce a given entrainment rate. The overriding implication is that transport rate is not a direct function of mean bed shear stress, and this will cause river channels with contrasting morphologies (and therefore different relative submergences) but similar levels of mean bed shear stress to experience different levels of sediment mobility. This could help to explain why studies have shown that the threshold shear stress (time-averaged) for entrainment appears to increase in very shallow flows.

CHAPTER 9

FURTHER WORK

9.1 Introduction

The results have demonstrated that further study is required into spatial variability in the flow and the influence of this on momentum transfer over water-worked gravel beds. This can be split into work achievable with the data already available from this study, and work requiring the collection of additional data. There are numerous avenues of further investigation beyond those discussed here, however this chapter will concentrate on those most closely associated with the results of the thesis.

9.2 Approaches Using Existing Data

The changes in the fractional contributions made by form-induced stresses to the total fluid stress were investigated for one height just above the maximum bed elevation, and it is important to discover whether relative submergence is likely to cause a change in momentum transfer mechanisms throughout the rest of the flow. The relationship between relative submergence and the degree of spatial variability in the time-averaged flow was discovered to occur throughout the flow depth, but to be more consistent higher into the flow where the influence of bed roughness was not apparent. It could therefore result in relative submergence potentially having a greater influence on momentum transfer mechanisms above the form-induced sublayer.

It is known that Reynolds stress is predominately produced by a spatial coherency in the joint distributions of the turbulent fluctuations in instantaneous streamwise and vertical velocities in the form of ejections and sweeps, with other quadrant events making little contribution. Form-induced stresses arise from the correlations between point-to-point spatial variations in time-averaged streamwise and vertical velocities, so it will be interesting to discover whether there is any such coherency in the spatial variations in these velocities. This can be performed using the quadrant technique in the same way it is used for examining the turbulent structure of the flow, by examining the joint distributions in the spatial variations in time-averaged streamwise and vertical

velocities. It is unlikely that any coherency would be observed because form-induced stress makes both negative and positive contributions to the total fluid stress and it is therefore likely that all quadrants will be important in the production of form-induced stress.

It would also be desirable to investigate the flow within the interfacial layer, the region of flow between the maximum and minimum bed elevations. It may be that spatial variability and form-induced stresses will be much greater in this flow region and there will be greater coupling between the time-averaged flow and bed surface topography. It is likely that the flow will also be influenced by the porosity of the bed, which can be estimated from the bed surface scans. The porosity and permeability of the unimodal and bimodal beds are different due to the varying degrees of sand within the bed mixtures. Therefore the flow characteristics are likely to be different between the two beds. The porosity of the bed, and the effect of this on the spatial variability in the flow in the interfacial layer, should influence the infiltration of fines and solutes into the bed.

It is speculated that form-induced stress is the additional momentum flux term that can correct the imbalance in the momentum equations that arises because of the departure of Reynolds stress from a linear vertical distribution. It would be desirable to examine each of the stress components in the double-averaged Navier-Stokes equations, and to discover the relative significance of all the components and whether the change in Reynolds stress is balanced by a change in form-induced stress. Parameterisation of all the stress components, especially form drag, is important for successfully using the double-averaged Navier-Stokes equations for numerical modelling of gravel bed flows. Given that a cube of fluid was measured using PIV in two configurations it will also be possible to characterise the forces felt on each face of the cube. This information would be important for producing parametric equations of form-induced stress and validating numerical models of turbulent flows.

Form-induced stress demonstrated considerable spatial variability over the bed. This indicated that there might also be spatial variability in Reynolds stress over the bed, which would have important implications for solute and sediment transport processes. The PIV data and bed surface topography data can be used to discover if this does occur over water-worked gravel beds and will allow its spatial distribution to be explicitly linked to bed surface topography. It could also be examined how the distribution

changes with relative submergence and bed slope. Several studies have shown that bed shear stress is not uniform over the bed and, using the information on the spatial variability in form-induced stress and Reynolds stress, it would be possible to quantify this variability. Furthermore it could be understood how this changes with hydraulic conditions and bed surface topography so that relationships could be derived and included, for instance, in bedload transport models for water-worked gravel beds. This appears especially desirable, given that spatial variability in bed shear stress has been shown numerically by previous studies, and in surrogate terms in Chapter 7, to cause 1-D bedload transport calculations to potentially misrepresent the true bedload flux. A probabilistic approach to predicting entrainment rates, which examines the overlap in the probability distributions of fluid velocities and the velocities required to entrain the grains over the bed, was shown in Chapter 7 to be a possible way in which a more rigorous model could be developed. This probabilistic treatment explicitly takes into account the spatial variability in fluid velocities and the velocities required to move grains over the bed. The potential of such an approach needs to be explored using measurements of bed shear stress and predicted critical shear stress. Information on the spatial variability in bed shear stress could also be used for developing a relationship between mean flow velocity and the bed surface topography to produce a physically based flow resistance equation.

It remains unclear whether turbulent flow features are likely to have caused the appearance of time-averaged flow structures over the two water-worked gravel beds. For this to be the case, it would require the turbulent structures to be both spatially and temporally persistent such that their presence appeared within the flow after time-averaging. The PIV data could be used to test whether this is possible. By examining the instantaneous flow fields and noting the frequency of occurrence and spatial locations of turbulent flow features that resemble the time-averaged flow structures, it would be possible to understand whether turbulent flow structures caused these time-averaged flow structures to appear. For example, it could be discovered whether the high-speed streaks appearing in the time-averaged flow are also present in the instantaneous flow field and whether they appear in the same spatial locations, and occur frequently enough at this location, to appear within the time-averaged flow field. In addition, it would be possible to discover whether the alternating vertical zones of upward and downward moving fluid were caused by turbulent large-scale flow structures. These structures have recently received much attention within the literature, but most previous studies have

relied on a correlation between point velocity measurements in order to identify these spatial features within the flow and to attain their scaling. Also, they have only examined a small number of different depths in order to investigate their scaling with depth, and have not been able to investigate numerically the relationship between the structures and the bed surface. Thus, as well as allowing an examination of their association with the time-averaged flow structures, the available data would enable the first high spatial resolution study of the interaction between large-scale flow structures and the bed, and their scaling over a range of depths. This is important because they are thought to initiate sediment entrainment.

9.3 Approaches Using Additional Data

Further investigation of form-induced stresses and spatial variability in the time-averaged flow field is required over rough sediment beds in order to incorporate their effects into numerical models of turbulent flows. This would elucidate whether the time-averaged flow structures observed in this study are also present over other water-worked gravel beds of different topographies, and therefore truly whether they are inherent features of flows over these types of bed. It would also be useful to examine the time-averaged flow over smooth beds in order to gain an insight into the degree of spatial variability and level of form-induced stress that can be achieved without the presence of a rough boundary. If spatial variability and form-induced stress are also significant over a smooth bed it would further indicate that it is unlikely to be (entirely) form-induced. It would also be possible to isolate the effects of relative submergence on the flow, because the influence made by bed roughness would be small. This would provide a very clear indication of the role of relative submergence in influencing spatial variability and momentum transfer mechanisms within the flow, and whether it does have a greater influence than bed surface topography. It would be possible to compare directly the results to those of this study by carrying out the smooth beds tests at the same flow depth to bed roughness ratio and at the same bed slopes. This would further allow the effects of relative submergence, bed slope and bed roughness on the flow to be elucidated. A number of similarities exist between smooth-wall flows and rough-wall flows in the coherent turbulent flow structures that exist within the flow, with many studies suggesting that these structures are inherent features of turbulent flows. It would be interesting to discover whether the time-averaged flow structures that were observed over the two water-worked gravel beds are also present over a smooth bed. A number of

studies have documented that time-averaged flow structures exist over smooth beds, but they provide little information on their morphology. Therefore the smooth-wall tests would enable the discovery of whether smooth- and rough-wall flows also have a similar organisation in their time-averaged flow fields. Tests could also be carried out over a bed of uniform grain sizes, to discover further whether the time-averaged flow structures are inherent features of turbulent flows. This would also allow the flow variables derived from double-averaging to be compared to those estimated by the law of the wall, because the law of the wall holds over uniform beds.

There is a need to understand the influence that spatial patterns within the flow have on solute and sediment transport. This can only be achieved by high spatial resolution and simultaneous measurements of the flow and the sediment or solute being transported. Much effort should be concentrated on carrying out these measurements so that the effects of spatial variability in the flow can be explicitly linked to the changes this causes in their transport. Of particular interest is the influence that spatial variability has on the transport of solutes within the bulk of the flow and on the exchange of solutes between the bed and the flow. This information could be provided by simultaneous PIV and Laser Induced Fluorescence (LIF) measurements. The double-averaging of the Navier-Stokes equations also provides the theoretical means by which to examine such processes, enabling spatial information from the flow to be explicitly linked to the spatial variability in concentration, and for the flow within the interfacial and subsurface layers of the bed to be investigated. It would be possible to test the suggestion made in Chapter 7 that subsurface advection may occur over flat (at the macroscopic scale) water-worked gravel beds due to spatial variability in the time-averaged flow. It would also enable the examination of the relative roles of subsurface advection and the turbulent coupling between surface and subsurface flows on the exchange of solutes between the bed and the flow.

It would be expected that certain areas of the bed will be preferential sites for the penetration of solutes into the bed and others will be preferential sites for their release back into the flow. This will be a function of, amongst other things, the spatial distribution in velocity and the porosity and permeability of the bed. The double-averaging methodology provides the means by which to link explicitly the spatial variability in concentrations within the interfacial and subsurface layers to the statistical properties of the bed. The porosity and permeability of manually, screeded beds is likely

to be much higher than for fed beds, and this will influence interfacial and subsurface flow, and increase the probability of interchange between surface and subsurface flow. Therefore the relative roles of advection and the coupling between the surface and subsurface flow for manually screeded beds are likely to be different from those for fed beds. Screeded beds may experience a greater degree of coupling than fed beds. On similar lines, the bimodal bed is likely to have a lower porosity and permeability than the unimodal bed. This means that the two beds are likely to experience different levels of exchange of solutes between the bed and the flow. Also, the relative importance of coupling between surface and subsurface flow on the exchange of solutes between the bed and the flow might be different.

It was concluded in Chapter 7 that point measurements of velocity over the bed may misrepresent the degree of spatial variability in the time-averaged flow and the level of form-induced stress over water-worked gravel beds, and that significant levels of confidence in these estimates might only be achieved by using 3-D PIV in a horizontal plane at many heights above the bed. Effort should now be made to attempt such an approach because it offers the potential to produce an even greater understanding of the spatial variability in stress components over the bed and their relationship with bed surface topography.

REFERENCES

- Aberle J. and Nikora V. Statistical properties of armoured gravel-bed surfaces, *Water Resources Research*, submitted.
- Aberle J. and Smart G.M. 2003 The influence of roughness structure on flow resistance on steep slopes, *Journal of Hydraulic Research*, **41**, 3, 259-269.
- Antohe B.V. and Lage J.L. 1997 A general two-equation macroscopic turbulence model for incompressible flow in porous media, *International Journal of Heat and Mass Transfer*, **40**, 13, 3013-3024.
- Antonia R.A. and Atkinson J.D. 1973 High-order moments of Reynolds shear-stress fluctuations in a turbulent boundary-layer, *Journal of Fluid Mechanics*, **58**, 8, 581-593.
- Ashworth P.J., Bennett S.J., Best J.L. and McLelland S.J. 1996 *Coherent Flow Structures in Open Channels*, John Wiley & Sons, Chichester.
- Ayotte K.W., Finnigan J.J. and Raupach M.R. 1999 A second-order closure for neutrally stratified vegetative canopy flows, *Boundary-Layer Meteorology*, **90**, 2, 189-216.
- Babakaiff C.S. and Hickin E.J. 1996 Coherent flow structures in Squamish River Estuary. In Ashworth, P.J., Bennett, S.J., Best, J.L., McLelland, S.J. (eds), *Coherent Flow Structures in Open Channels*, John Wiley & Sons, Chichester, 321-342.
- Barison S., Chegini A., Marion A. and Tait S.J. 2003 Modifications in near bed flow over sediment beds and the implications for grain entrainment, *Proceedings of XXX IAHR Congress, Thessalonki, Greece, Theme C: Turbulence-2*, 509-516.
- Batchelor G.K. 1969 Computation of the energy spectrum in homogeneous two-dimensional turbulence, *Physics of Fluids Supplement*, **II**, 233.
- Bates P.D., Horritt M.S., Hunter N.M., Mason D. and Cobby D. 2005 Numerical modelling of floodplain flow. In Bates, P.D., Lane, S.N., Ferguson, R., I. (eds), *Computational Fluid Dynamics: Applications to Environmental Hydraulics*, John Wiley & Sons, Chichester, 271-304.
- Bathurst J.C., Graf W.H. and Cao H.H. 1983 Initiation of sediment transport in steep channels with coarse bed material. In Sumer, B.M., Muller, A. (eds), *Mechanics of Sediment Transport*, A. A. Balkema, Brookfield, 207-213.

- Bathurst J.C., Graf W.H. and Cao H.H. 1987 Bed load discharge equations for steep mountain rivers. In Thorne, C.R., Bathurst, J.C., Hey, R.D. (eds), *Sediment Transport in Gravel-Bed Rivers*, John Wiley & Sons, New York, 453–477.
- Bennett S.J. and Best J., L. 1996 Mean flow and turbulence structure over fixed ripples and the ripple-dune transition. In Ashworth, P.J., Bennett, S.J., Best, J.L., McLelland, S.J. (eds), *Coherent Flow Structures in Open Channels*, John Wiley & Sons, Chichester, 281-304.
- Bergeron N.E. 1996 Scale-space analysis of stream-bed roughness in coarse gravel-bed streams, *Mathematical Geology*, **28**, 5, 537-561.
- Best J. and Kostaschuk R. 2002 An experimental study of turbulent flow over a low-angle dune, *Journal of Geophysical Research - Oceans*, **107**, C9, 3135, doi: 3110.1029/2000JC000294.
- Biron P.M., Robson C., Lapointe M.F. and Gaskin S.J. 2004 Comparing different methods of bed shear stress estimates in simple and complex flow fields, *Earth Surface Processes and Landforms*, **29**, 11, 1403-1415.
- Blackwelder R.F. and Kovaszny L.S. 1972 Timescales and correlations in a turbulent boundary layer, *Physics of Fluids*, **15**, 1545-1554.
- Böhm M., Finnigan J.J. and Raupach M.R. 2000 Dispersive fluxes and canopy flows: just how important are they?, *Proceedings of American Meteorology Society 24th Conference on Agricultural and Forest Meteorology, Davis*, 106-107.
- Booker D.J., Sear D.A. and Payne A.J. 2001 Modelling three-dimensional flow structures and patterns of boundary shear stress in a natural pool-riffle sequence, *Earth Surface Processes and Landforms*, **26**, 5, 553-576.
- Boxall J.B. and Guymer I. 2003 Analysis and prediction of transverse mixing coefficients in natural channels, *Journal of Hydraulic Engineering, ASCE*, **129**, 2, 129-139.
- Brown G.L. and Thomas A.S.W. 1977 Large structure in a turbulent boundary-layer, *Physics of Fluids*, **20**, 10, S243-S251.
- Brumley B.H. and Jirka G.H. 1987 Near-surface turbulence in a grid-stirred tank, *Journal of Fluid Mechanics*, **183**, 235-263.
- Brunet Y., Finnigan J.J. and Raupach M.R. 1994 A wind-tunnel study of air-flow in waving wheat - single-point velocity statistics, *Boundary-Layer Meteorology*, **70**, 1-2, 95-132.

- Buffin-Bélanger T. and Roy A.G. 1998 Effects of a pebble cluster on the turbulent structure of a depth-limited flow in a gravel-bed river, *Geomorphology*, **25**, 3-4, 249-267.
- Buffin-Bélanger T., Roy A.G. and Kirkbride A.D. 2000 On large-scale flow structures in a gravel-bed river, *Geomorphology*, **32**, 3-4, 417-435.
- Buffin-Bélanger T., Reid I., Rice S., Chandler J.H. and Lancaster J. 2003 A casting procedure for reproducing coarse-grained sedimentary surfaces, *Earth Surface Processes and Landforms*, **28**, 7, 787-796.
- Buffington J.M. and Montgomery D.R. 1997 A systematic analysis of eight decades of incipient motion studies, with special reference to gravel-bedded rivers, *Water Resources Research*, **33**, 8, 1993-2029.
- Butler J.B., Lane S.N. and Chandler J.H. 1998 Assessment of DEM quality for characterizing surface roughness using close range digital photogrammetry, *Photogrammetric Record*, **16**, 92, 271-291.
- Butler J.B., Lane S.N. and Chandler J.H. 2001 Characterization of the structure of river-bed gravels using two-dimensional fractal analysis, *Mathematical Geology*, **33**, 3, 301-330.
- Butler J.B., Lane S.N., Chandler J.H. and Porfiri E. 2002 Through-water close range digital photogrammetry in flume and field environments, *Photogrammetric Record*, **17**, 99, 419-439.
- Byrd T.C., Furbish D.J. and Warburton J. 2000 Estimating depth-averaged velocities in rough channels, *Earth Surface Processes and Landforms*, **25**, 2, 167-173.
- Ca V.T., Ashie Y. and Asaeda T. 2002 A k-epsilon turbulence closure model for the atmospheric boundary layer including urban canopy, *Boundary-Layer Meteorology*, **102**, 3, 459-490.
- Campbell L., McEwan I., Nikora V., Pokrajac D., Gallagher M. and Manes C. 2005 Bed-load effects on hydrodynamics of rough-bed open-channel flows, *Journal of Hydraulic Engineering, ASCE*, **131**, 7, 576-585.
- Carling P.A., Cao Z.X., Holland M.J., Ervine D.A. and Babaeyan-Koopaei K. 2002 Turbulent flow across a natural compound channel, *Water Resources Research*, **38**, 12, 6-11.
- Chanson H. 1999 *The Hydraulics of Open Channel Flow: An Introduction*, Arnold, London.
- Chegini A., Tait S.J., Heald J. and McEwan I. 2002 The development of an automated system for the measurement of near bed turbulence and grain motion, *Proceedings*

of ASCE Conference on Hydraulic Measurements and Experimental Methods, Colorado, USA, CD-ROM, ISBN 0-7844-0407-7840.

- Cheng H. and Castro I.P. 2002 Near wall flow over urban-like roughness, *Boundary-Layer Meteorology*, **104**, 2, 229-259.
- Church M., Hassan M.A. and Wolcott J.F. 1998 Stabilizing self-organized structures in gravel-bed stream channels: field and experimental observations, *Water Resources Research*, **34**, 11, 3169-3179.
- Clifford N.J. 1996 Morphology and stage-dependent flow structure in a gravel-bed river. In Ashworth, P.J., Bennett, S.J., Best, J.L., McLelland, S.J. (eds), *Coherent Flow Structures in Open Channels*, John Wiley & Sons, Chichester, 545-566.
- Clifford N.J. and French J.R. 1993 Monitoring and modelling turbulent flow: historical and contemporary perspectives. In Clifford, N.J., French, J.R., Hardisty, J. (eds), *Turbulence: Perspectives on Flow and Sediment Transport*, John Wiley & Sons, Chichester, 1-34.
- Clifford N.J., Robert A. and Richards K.S. 1992 Estimation of flow resistance in gravel-bedded rivers - a physical explanation of the multiplier of roughness length, *Earth Surface Processes and Landforms*, **17**, 2, 111-126.
- Coceal O., Thomas T.G., Castro I.P. and Belcher S.E. Numerical simulation of turbulent flow over cubic roughness arrays, *Journal of Fluid Mechanics*, submitted.
- Coleman J.M. 1969 Brahmaputra River: channel processes and sedimentation, *Sedimentary Geology*, **3**, 129-239.
- Crapiste G.H., Rotstein E. and Whitaker S. 1986 A general closure scheme for the method of volume averaging, *Chemical Engineering Science*, **41**, 2, 227-235.
- Dantec. 2000 *FlowMap Particle Image Velocimetry Instrumentation: Installation and Users Guide*, Dantec Measurement Technology, Skovlunde.
- Defina A. 1996 Transverse spacing of low-speed streaks in a channel flow over a rough bed. In Ashworth, P.J., Bennett, S.J., Best, J.L., McLelland, S.J. (eds), *Coherent Flow Structures in Open Channels*, John Wiley & Sons, Chichester, 87-99.
- Dittrich A., Nestmann F. and Ergenzinger P. 1996 Ratio of lift and shear forces over rough surfaces. In Ashworth, P.J., Bennett, S.J., Best, J.L., McLelland, S.J. (eds), *Coherent Flow Structures in Open Channels*, John Wiley & Sons, Chichester, 125-146.
- Drake T.G., Shreve R.L., Dietrich W.E., Whiting P.J. and Leopold L.B. 1988 Bedload transport of fine gravel observed by motion-picture photography, *Journal of Fluid Mechanics*, **192**, 193-217.

- Drobinski P. and Foster R.C. 2003 On the origin of near-surface streaks in the neutrally-stratified planetary boundary layer, *Boundary-Layer Meteorology*, **108**, 2, 247-256.
- Durst F., Jovanovic J. and Kanevce L. 1987 Probability density distribution in turbulent wall boundary-layer flows, *Turbulent Shear Flows 5*, Springer, Berlin, 197-220.
- Dyer K.R. 1986 *Coastal and Estuarine Sediment Dynamics*, John Wiley & Sons, Chichester.
- Elliott A.H. and Brooks N.H. 1997a Transfer of nonsorbing solutes to a streambed with bed forms: laboratory experiments, *Water Resources Research*, **33**, 1, 137-151.
- Elliott A.H. and Brooks N.H. 1997b Transfer of nonsorbing solutes to a streambed with bed forms: theory, *Water Resources Research*, **33**, 1, 123-136.
- Falco R.E. 1977 Coherent motions in outer region of turbulent boundary-layers, *Physics of Fluids*, **20**, 10, S124-S132.
- Favre A., Gaviglio J. and Dumas R. 1957 Space-time double correlations and spectra in a turbulent boundary layer, *Journal of Fluid Mechanics*, **2**, 313-342.
- Ferguson R.I. 2003 The missing dimension: effects of lateral variation on 1-D calculations of fluvial bedload transport, *Geomorphology*, **56**, 1-2, 1-14.
- Ferguson R.I., Kirkbride A.D. and Roy A.G. 1996 Markov analysis of velocity fluctuations in gravel-bed rivers. In Ashworth, P.J., Bennett, S.J., Best, J.L., McLelland, S.J. (eds), *Coherent Flow Structures in Open Channels*, John Wiley & Sons, Chichester, 165-183.
- Ferguson R.I., Parsons D.R., Lane S.N. and Hardy R.J. 2003 Flow in meander bends with recirculation at the inner bank, *Water Resources Research*, **39**, 11, doi: 10.1029/2003WR001965.
- Finnigan J. 2000 Turbulence in plant canopies, *Annual Review of Fluid Mechanics*, **32**, 519-571.
- Finnigan J.J. 1983 Turbulent heat and mass transport in flexible plant canopies, *Proceedings of Eighth Australasian Fluid Mechanics Conference, New South Wales, Australia*, 1A.9-1A.13.
- Finnigan J.J. 1985 Turbulent transport in flexible plant canopies. In Hutchinson, B.A., Hicks, B.B. (eds), *The Forest-Atmosphere Interaction*, D. Reidel Publishing Company, Dordrecht, 443-480.
- Fischer H.B. 1969 The effects of bends on dispersion in streams, *Water Resources Research*, **5**, 2, 496-506.
- Furbish D.J. 1987 Conditions for geometric similarity of coarse stream-bed roughness, *Mathematical Geology*, **19**, 4, 291-307.

- Gessler D., Hall B., Spasojevic M., Holly F., Pourtaheri H. and Raphelt N. 1999 Application of 3D mobile bed, hydrodynamic model, *Journal of Hydraulic Engineering, ASCE*, **125**, 7, 737-749.
- Gimenez-Curto L.A. and Corniero M.A. 1996 Oscillating turbulent flow over very rough surfaces, *Journal of Geophysical Research - Oceans*, **C9**, 20745-20758.
- Gimenez-Curto L.A. and Corniero M.A. 2003 Highest natural bed forms, *Journal of Geophysical Research - Oceans*, **108**, C2, doi: 10.1029/2002JC001474.
- Gomez B. 1991 Bedload transport, *Earth-Science Reviews*, **31**, 2, 89-132.
- Goring D.G., Nikora V.I. and McEwan I.K. 1999 Analysis of the texture of gravel beds using 2-D structure functions, *Proceedings of IAHR Symposium on River, Coastal and Estuarine Morphodynamics, Genova, Italy*, 111-120.
- Grass A.J. and Mansour-Tehrani M. 1996 Generalized scaling of coherent bursting structures in the near-wall region of turbulent flow over smooth and rough boundaries. In Ashworth, P.J., Bennett, S.J., Best, J.L., McLelland, S.J. (eds), *Coherent Flow Structures in Open Channels*, John Wiley & Sons, Chichester, 40-61.
- Grass A.J., Stuart R.J. and Mansour-Tehrani M. 1991 Vortical structures and coherent motion in turbulent-flow over smooth and rough boundaries, *Philosophical Transactions of the Royal Society of London Series A - Mathematical Physical and Engineering Sciences*, **336**, 1640, 35-65.
- Gray W.G. 1975 A derivation of the equation for multi-phase transport, *Chemical Engineering Science*, **30**, 229-233.
- Guymer I., Wilson C.A.M.E. and Boxall J.B. 2005 Modelling solute transport processes in free surface flow CFD schemes. In Bates, P.D., Lane, S.N., Ferguson, R., I. (eds), *Computational Fluid Dynamics: Applications to Environmental Hydraulics*, John Wiley & Sons, Chichester, 50-69.
- Gyr A. and Schmid A. 1997 Turbulent flows over smooth erodible sand beds in flumes, *Journal of Hydraulic Research*, **35**, 4, 525-544.
- Hanna S.R., Tehranian S., Carissimo B., Macdonald R.W. and Lohner R. 2002 Comparisons of model simulations with observations of mean flow and turbulence within simple obstacle arrays, *Atmospheric Environment*, **36**, 32, 5067-5079.
- Hassan M.A. and Church M. 2000 Experiments on surface structure and partial sediment transport on a gravel bed, *Water Resources Research*, **36**, 7, 1885-1895.
- Hassanizadeh M. and Gray W.G. 1979 General conservation equations for multi-phase systems: 1. averaging procedure, *Advances in Water Resources*, **2**, 131-144.

- Heald J., McEwan I. and Tait S. 2004 Sediment transport over a flat bed in a unidirectional flow: simulations and validation, *Philosophical Transactions of the Royal Society of London Series A - Mathematical Physical and Engineering Sciences*, **362**, 1822, 1973-1986.
- Hey R.D. and Thorne C.R. 1986 Stable channels with mobile gravel beds, *Journal of Hydraulic Engineering, ASCE*, **112**, 8, 671-689.
- Hodkinson A. and Ferguson R.I. 1998 Numerical modelling of separated flow in river bends: model testing and experimental investigation of geometric controls on the extent of flow separation at the concave bank, *Hydrological Processes*, **12**, 8, 1323-1338.
- Hoffmann M.R. 2004 Application of a simple space-time averaged porous media model to flow in densely vegetated channels, *Journal of Porous Media*, **7**, 3, 183-191.
- Hsu T.J., Sakakiyama T. and Liu P.L.F. 2002 A numerical model for wave motions and turbulence flows in front of a composite breakwater, *Coastal Engineering*, **46**, 1, 25-50.
- Jackson R.G. 1976 Sedimentological and fluid-dynamic implications of turbulent bursting phenomenon in geophysical flows, *Journal of Fluid Mechanics*, **77**, 531-560.
- Kaimal J.C. and Finnigan J.J. 1994 *Atmospheric Boundary Layer Flows: Their Structure and Measurement*, Oxford University Press, Oxford.
- Kanda M., Moriwaki R. and Kasamatsu F. 2004 Large-eddy simulation of turbulent organized structures within and above explicitly resolved cube arrays, *Boundary-Layer Meteorology*, **112**, 2, 343-368.
- Katul G.G., Mahrt L., Poggi D. and Sanz C. 2004 One- and two-equation models for canopy turbulence, *Boundary-Layer Meteorology*, **113**, 1, 81-109.
- Kim S.C., Friedrichs C.T., Maa J.P.Y. and Wright L.D. 2000 Estimating bottom stress in tidal boundary layer from Acoustic Doppler Velocimeter data, *Journal of Hydraulic Engineering, ASCE*, **126**, 6, 399-406.
- Kirkbride A. 1993 Observations of the influence of bed roughness on turbulence structure in depth limited flows over gravel beds. In Clifford, N.J., French, J.R., Hardisty, J. (eds), *Turbulence: Perspectives on Flow and Sediment Transport*, John Wiley & Sons, Chichester, 185-196.
- Kirkbride A.D. and Ferguson R. 1995 Turbulent flow structure in a gravel-bed river: Markov chain analysis of the fluctuating velocity profile, *Earth Surface Processes and Landforms*, **20**, 8, 721-733.

- Kırkgöz M.S. and Ardiçlioğlu M. 1997 Velocity profiles of developing and developed open channel flow, *Journal of Hydraulic Engineering, ASCE*, **123**, 12, 1099-1105.
- Kironoto B.A. and Graf W.H. 1994 Turbulence characteristics in rough uniform open-channel flow, *Proceedings of the Institution of Civil Engineers - Water Maritime and Energy*, **106**, 4, 333-344.
- Klewicki J.C., Metzger M.M., Kelner E. and Thurlow E.M. 1995 Viscous sublayer flow visualizations at $R_\theta \approx 1\,500\,000$, *Physics of Fluids*, **7**, 4, 857-863.
- Kline S.J., Reynolds W.C., Schraub F.A. and Runstadler P.W. 1967 The structure of turbulent boundary layers, *Journal of Fluid Mechanics*, **30**, 741-773.
- Komar P.D. and Li Z. 1986 Pivoting analyses of the selective entrainment of sediments by shape and size with application to gravel threshold, *Sedimentology*, **33**, 3, 425-436.
- Komori S., Murakami Y. and Ueda H. 1989 The relationship between surface-renewal and bursting motions in an open-channel flow, *Journal of Fluid Mechanics*, **203**, 103-123.
- Komori S., Ueda H., Ogino F. and Mizushima T. 1982 Turbulence structure and transport mechanism at the free-surface in an open channel flow, *International Journal of Heat and Mass Transfer*, **25**, 4, 513-521.
- Konrad C.P., Booth D.B., Burges S.J. and Montgomery D.R. 2002 Partial entrainment of gravel bars during floods, *Water Resources Research*, **38**, 7, doi: 10.1029/2001WR000828.
- Kostaschuk R.A. and Church M.A. 1993 Macroturbulence generated by dunes - Fraser-River, Canada, *Sedimentary Geology*, **85**, 1-4, 25-37.
- Kovaszny L.S., Kibens V. and Blackwelder R.F. 1970 Large-scale motion in intermittent region of a turbulent boundary layer, *Journal of Fluid Mechanics*, **41**, 283-325.
- Kraichnan R.H. 1967 Inertial subranges in two-dimensional turbulence, *Physics of Fluids*, **10**, 1417-1423.
- Kumar S., Gupta R. and Banerjee S. 1998 An experimental investigation of the characteristics of free-surface turbulence in channel flow, *Physics of Fluids*, **10**, 2, 437-456.
- Lancaster J. 1999 Small-scale movements of lotic macroinvertebrates with variations in flow, *Freshwater Biology*, **41**, 3, 605-619.

- Lancaster J. and Belyea L.R. 1997 Nested hierarchies and scale-dependence of mechanisms of flow refugium use, *Journal of the North American Benthological Society*, **16**, 1, 221-238.
- Lane S.N., Hardy R.J., Elliott L. and Ingham D.B. 2002 High-resolution numerical modelling of three-dimensional flows over complex river bed topography, *Hydrological Processes*, **16**, 11, 2261-2272.
- Lane S.N., Hardy R.J., Elliott L. and Ingham D.B. 2004 Numerical modeling of flow processes over gravelly surfaces using structured grids and a numerical porosity treatment, *Water Resources Research*, **40**, 1, doi: 40:W01302JAN82004.
- Lawless M. and Robert A. 2001 Scales of boundary resistance in coarse-grained channels: turbulent velocity profiles and implications, *Geomorphology*, **39**, 3-4, 221-238.
- Legg B.J., Raupach M.R. and Coppin P.A. 1986 Experiments on scalar dispersion within a model-plant canopy: 3. an elevated line source, *Boundary-Layer Meteorology*, **35**, 3, 277-302.
- Legleiter C.J., Phelps T.L. and Wohl E.E. Geostatistical analysis of the effects of stage and roughness on reach-scale spatial patterns in velocity and turbulence intensity, *Geomorphology*, in press.
- Lien F.S. and Yee E. 2004 Numerical modelling of the turbulent flow developing within and over a 3-D building array, part I: a high-resolution Reynolds-averaged Navier-Stokes approach, *Boundary-Layer Meteorology*, **112**, 3, 427-466.
- Lien F.S., Yee E. and Wilson J.D. 2005 Numerical modelling of the turbulent flow developing within and over a 3-D building array, part II: a mathematical foundation for a distributed drag force approach, *Boundary-Layer Meteorology*, **114**, 2, 245-285.
- Liu Z., Adrian R.J. and Hanratty T.J. 2001 Large-scale modes of turbulent channel flow: transport and structure, *Journal of Fluid Mechanics*, **448**, 53-80.
- López F. and Garcia M. 1998 Open-channel flow through simulated vegetation: suspended sediment transport modeling, *Water Resources Research*, **34**, 9, 2341-2352.
- López F. and Garcia M.H. 2001 Mean flow and turbulence structure of open-channel flow through non-emergent vegetation, *Journal of Hydraulic Engineering, ASCE*, **127**, 5, 392-402.

- Maddux T.B., McLean S.R. and Nelson J.M. 2003 Turbulent flow over three-dimensional dunes: 2. fluid and bed stresses, *Journal of Geophysical Research - Earth Surface*, **108**, F1, doi: 10.1029/2003JF000018.
- Marion A., Tait S.J. and McEwan I.K. 2003 Analysis of small-scale gravel bed topography during armoring, *Water Resources Research*, **39**, 12, doi: 10.1029/2003WR002367.
- McEwan I., Sorensen M., Heald J., Tait S., Cunningham G., Goring D. and Willetts B. 2004 Probabilistic modeling of bed-load composition, *Journal of Hydraulic Engineering, ASCE*, **130**, 2, 129-139.
- McLean S.R., Nelson J.M. and Wolfe S.R. 1994 Turbulence structure over 2-dimensional bed forms - implications for sediment transport, *Journal of Geophysical Research - Oceans*, **99**, C6, 12729-12747.
- McLean S.R., Nelson J.M. and Shreve R.L. 1996 Flow-sediment interactions in separating flows over bedforms. In Ashworth, P.J., Bennett, S.J., Best, J.L., McLelland, S.J. (eds), *Coherent Flow Structures in Open Channels*, John Wiley & Sons, Chichester, 202-226.
- McLean S.R., Wolfe S.R. and Nelson J.M. 1999 Spatially averaged flow over a wavy boundary revisited, *Journal of Geophysical Research - Oceans*, **104**, C7, 15743-15753.
- McLelland S.J., Ashworth P.J., Best J.L. and Livesey J.R. 1999 Turbulence and secondary flow over sediment stripes in weakly bimodal bed material, *Journal of Hydraulic Engineering, ASCE*, **125**, 5, 463-473.
- McQuivey R.S. and Richardson E. 1969 Some turbulence measurements in open channel flows, *Journal of Hydraulics Division, ASCE*, **95**, 209-223.
- Meyer-Peter E. and Muller R. 1948 Formulas for bed-load transport, *Proceedings of 2nd Congress of IAHR, Stockholm, Sweden*, 39-64.
- Mulhearn P.J. 1978 Turbulent flow over a periodic rough surface, *Physics of Fluids*, **21**, 1113-1115.
- Muller A. and Gyr A. 1986 On the vortex formation in the mixing layer behind dunes, *Journal of Hydraulic Research*, **24**, 359-375.
- Murota A., Fukuhara T. and Sato M. 1984 Turbulence structure in vegetated open channel flows, *Journal of Hydroscience and Hydraulic Engineering, JSCE*, **2**, 1, 47-61.
- Nagaoka H. and Ohgaki S. 1990 Mass-transfer mechanism in a porous riverbed, *Water Research*, **24**, 4, 417-425.

- Nakagawa H. and Nezu I. 1977 Prediction of contributions to Reynolds stress from bursting events in open-channel flows, *Journal of Fluid Mechanics*, **80**, 4, 99-128.
- Nakagawa H. and Nezu I. 1981 Structure of space-time correlations of bursting phenomena in an open-channel flow, *Journal of Fluid Mechanics*, **104**, 1-43.
- Nakagawa H., Nezu I. and Ueda H. 1975 Turbulence of open channel flow over smooth and rough beds, *Proceedings of the Japan Society of Civil Engineers*, **241**, 155-168.
- Naot D., Nezu I. and Nakagawa H. 1996 Hydrodynamic behavior of partly vegetated open channels, *Journal of Hydraulic Engineering, ASCE*, **122**, 11, 625-633.
- Neary V.S. 2003 Numerical solution of fully developed flow with vegetative resistance, *Journal of Engineering Mechanics, ASCE*, **129**, 5, 558-563.
- Nezu I. and Rodi W. 1986 Open-channel flow measurements with a laser doppler anemometer, *Journal of Hydraulic Engineering, ASCE*, **112**, 5, 335-355.
- Nezu I. and Nakagawa H. 1993 *Turbulence in open channel flows*, A. A. Balkema, Rotterdam.
- Nicholas A.P. 2000 Modelling bedload yield in braided gravel bed rivers, *Geomorphology*, **36**, 1-2, 89-106.
- Nicholas A.P. and Smith G.H.S. 1999 Numerical simulation of three-dimensional flow hydraulics in a braided channel, *Hydrological Processes*, **13**, 6, 913-929.
- Nield D.A. 2001 Alternative models of turbulence in a porous medium, and related matters, *Journal of Fluids Engineering, Transactions of the ASME*, **123**, 4, 928-931.
- Nikora V. and Goring D. 2000 Flow turbulence over fixed and weakly mobile gravel beds, *Journal of Hydraulic Engineering, ASCE*, **126**, 9, 679-690.
- Nikora V. and Walsh J. 2004 Water-worked gravel surfaces: high-order structure functions at the particle scale, *Water Resources Research*, **40**, 12, doi: 10.1029/2004WR003346.
- Nikora V., Goring D., McEwan I. and Griffiths G. 2001 Spatially averaged open-channel flow over rough bed, *Journal of Hydraulic Engineering, ASCE*, **127**, 2, 123-133.
- Nikora V., McEwan I., McLean S., Coleman S., Pokrajac D. and Walters R. Double-averaging concept for rough-bed open-channel and overland flows: theoretical background, *Journal of Hydraulic Engineering, ASCE*, in press a.
- Nikora V., McLean S., Coleman S., Pokrajac D., McEwan I., Campbell L., Aberle J., Clunie D. and Koll K. Double-averaging concept for rough-bed open-channel and overland flows: applications, *Journal of Hydraulic Engineering, ASCE*, in press b.

- Nikora V.I. and Smart G.M. 1997 Turbulence characteristics of New Zealand gravel-bed rivers, *Journal of Hydraulic Engineering, ASCE*, **123**, 9, 764-773.
- Nikora V.I., Goring D.G. and Biggs B.J.F. 1998 On gravel-bed roughness characterization, *Water Resources Research*, **34**, 3, 517-527.
- Nikora V.I., Goring D.G. and Biggs B.J.F. 2002 Some observations of the effects of micro-organisms growing on the bed of an open channel on the turbulence properties, *Journal of Fluid Mechanics*, **450**, 317-341.
- Nychas S.G., Hershey H.C. and Brodkey R.S. 1973 Visual study of turbulent shear-flow, *Journal of Fluid Mechanics*, **61**, 20, 513-540.
- Packman A., Salehin M. and Zaramella M. 2004 Hyporheic exchange with gravel beds: basic hydrodynamic interactions and bedform-induced advective flows, *Journal of Hydraulic Engineering, ASCE*, **130**, 7, 647-656.
- Paola C. 1996 Incoherent structure: turbulence as a metaphor for stream braiding. In Ashworth, P.J., Bennett, S.J., Best, J.L., McLelland, S.J. (eds), *Coherent Flow Structures in Open Channels*, John Wiley & Sons, Chichester, 705-723.
- Paola C., Parker G., Seal R., Sinha S.K., Southard J.B. and Wilcock P.R. 1992 Downstream fining by selective deposition in a laboratory flume, *Science*, **258**, 1757-1760.
- Papanicolaou A.N. and Hildale R. 2002 Turbulence characteristics in gradual channel transition, *Journal of Engineering Mechanics, ASCE*, **128**, 9, 948-960.
- Papanicolaou A.N., Diplas P., Dancey C.L. and Balakrishnan M. 2001 Surface roughness effects in near-bed turbulence: implications to sediment entrainment, *Journal of Engineering Mechanics, ASCE*, **127**, 3, 211-218.
- Pedras M.H.J. and de Lemos M.J.S. 2000 On the definition of turbulent kinetic energy for flow in porous media, *International Communications in Heat and Mass Transfer*, **27**, 2, 211-220.
- Pedras M.H.J. and de Lemos M.J.S. 2001 Macroscopic turbulence modeling for incompressible flow through undeformable porous media, *International Journal of Heat and Mass Transfer*, **44**, 6, 1081-1093.
- Pender G., Hoey T.B., Fuller C. and McEwan I.K. 2001 Selective bedload transport during the degradation of a well sorted graded sediment bed, *Journal of Hydraulic Research*, **39**, 3, 269-277.
- Perry A.E., Lim K.L. and Henbest S.M. 1987 An experimental study of the turbulence structure in smooth-wall and rough-wall boundary-layers, *Journal of Fluid Mechanics*, **177**, 437-466.

- Poggi D., Katul G.G. and Albertson J.D. 2004 A note on the contribution of dispersive fluxes to momentum transfer within canopies - research note, *Boundary-Layer Meteorology*, **111**, 3, 615-621.
- Pokrajac D., Campbell L.J., Manes C., Nikora V.I. and McEwan I.K. 2003 Spatially-averaged flow over ribbed roughness: a new application of quadrant analysis, *Proceedings of XXX IAHR Congress, Thessalonki, Greece, Theme C: Turbulence-1*, 103-110.
- Pratury A.K. and Brodkey R.S. 1978 A stereoscopic visual study of coherent structures in turbulent shear flow, *Journal of Fluid Mechanics*, **89**, 251-272.
- Rashidi M. and Banerjee S. 1988 Turbulence structure in free-surface channel flows, *Physics of Fluids*, **31**, 9, 2491-2503.
- Rashidi M., Hetsroni G. and Banerjee S. 1991 Mechanisms of heat and mass-transport at gas-liquid interfaces, *International Journal of Heat and Mass Transfer*, **34**, 7, 1799-1810.
- Raupach M.R. 1981 Conditional statistics of Reynolds stress in rough-wall and smooth-wall turbulent boundary-layers, *Journal of Fluid Mechanics*, **108**, 363-382.
- Raupach M.R. 1994 Simplified expressions for vegetation roughness length and zero-plane displacement as functions of canopy height and area index, *Boundary-Layer Meteorology*, **71**, 1-2, 211-216.
- Raupach M.R. and Shaw R.H. 1982 Averaging procedures for flow within vegetation canopies, *Boundary-Layer Meteorology*, **22**, 1, 79-90.
- Raupach M.R., Thom A.S. and Edwards I. 1980 A wind-tunnel study of turbulent-flow close to regularly arrayed rough surfaces, *Boundary-Layer Meteorology*, **18**, 4, 373-397.
- Raupach M.R., Coppin P.A. and Legg B.J. 1986 Experiments on scalar dispersion within a model-plant canopy: 1. the turbulence structure, *Boundary-Layer Meteorology*, **35**, 1-2, 21-52.
- Raupach M.R., Antonia R.A. and Rajagopalan S. 1991 Rough-wall turbulent boundary layers, *Applied Mechanics Reviews*, **44**, 1, 1-25.
- Reynolds O. 1895 On the dynamical theory of incompressible viscous fluids and the determination of the criterion, *Philosophical Transactions of the Royal Society of London*, **186A**, 123-164.
- Robert A. 1988 Statistical properties of sediment bed profiles in alluvial channels, *Mathematical Geology*, **20**, 3, 205-225.

- Robert A. 1990 Boundary roughness in coarse-grained channels, *Progress in Physical Geography*, **14**, 1, 42-70.
- Robert A. 1991 Fractal properties of simulated bed profiles in coarse-grained channels, *Mathematical Geology*, **23**, 3, 367-382.
- Rowinski P.M. and Kubrak J. 2002 A mixing-length model for predicting vertical velocity distribution in flows through emergent vegetation, *Hydrological Sciences Journal - Journal Des Sciences Hydrologiques*, **47**, 6, 893-904.
- Roy A.G., Buffin-Belanger T. and Deland S. 1996 Scales of turbulent coherent flow structures in a gravel-bed river. In Ashworth, P.J., Bennett, S.J., Best, J.L., McLelland, S.J. (eds), *Coherent Flow Structures in Open Channels*, John Wiley & Sons, Chichester, 147-164.
- Roy A.G., Biron P.M., Buffin-Belanger T. and Levasseur M. 1999 Combined visual and quantitative techniques in the study of natural turbulent flows, *Water Resources Research*, **35**, 3, 871-877.
- Roy A.G., Buffin-Belanger T., Lamarre H. and Kirkbride A.D. 2004 Size, shape and dynamics of large-scale turbulent flow structures in a gravel-bed river, *Journal of Fluid Mechanics*, **500**, 1-27.
- Schoppa W. and Hussain F. 2002 Coherent structure generation in near-wall turbulence, *Journal of Fluid Mechanics*, **453**, 57-108.
- Seal R., Paola C., Parker G., Southard J.B. and Wilcock P.R. 1997 Experiments on downstream fining of gravel: 1. narrow-channel runs, *Journal of Hydraulic Engineering, ASCE*, **123**, 10, 874-884.
- Shimizu Y. and Tsujimoto T. 1994 Numerical analysis of turbulent open-channel flow over vegetation using a k-epsilon turbulence model, *Journal of Hydroscience and Hydraulic Engineering, JSCE*, **11**, 2, 57-67.
- Shimizu Y., Tsujimoto T. and Nakagawa H. 1990 Experiment and macroscopic modelling of flow in highly permeable porous medium under free-surface flow, *Journal of Hydroscience and Hydraulic Engineering, JSCE*, **8**, 1, 69-78.
- Shvidchenko A.B. and Pender G. 2001 Macroturbulent structure of open-channel flow over gravel beds, *Water Resources Research*, **37**, 3, 709-719.
- Sinha S.K., Sotiropoulos F. and Odgaard A.J. 1998 Three-dimensional numerical model for flow through natural rivers, *Journal of Hydraulic Engineering, ASCE*, **124**, 1, 13-24.

- Siqueira M. and Katul G. 2002 Estimating heat sources and fluxes in thermally stratified canopy flows using higher-order closure models, *Boundary-Layer Meteorology*, **103**, 1, 125-142.
- Smart G., Aberle J., Duncan M. and Walsh J. 2004 Measurement and analysis of alluvial bed roughness, *Journal of Hydraulic Research*, **42**, 3, 227-237.
- Smart G.M. 1999 Turbulent velocity profiles and boundary shear in gravel bed rivers, *Journal of Hydraulic Engineering, ASCE*, **125**, 2, 106-116.
- Smith C.R. 1996 Coherent flow structures in smooth-wall turbulent boundary layers: facts, mechanisms and speculation. In Ashworth, P.J., Bennett, S.J., Best, J.L., McLelland, S.J. (eds), *Coherent Flow Structures in Open Channels*, John Wiley & Sons, Chichester, 1-39.
- Smith C.R. and Metzler S.P. 1983 The characteristics of low-speed streaks in the near-wall region of a turbulent boundary-layer, *Journal of Fluid Mechanics*, **129**, 27-54.
- Smith C.R. and Schwartz S.P. 1983 Observation of streamwise rotation in the near-wall region of a turbulent boundary-layer, *Physics of Fluids*, **26**, 3, 641-652.
- Smith C.R., Walker J.D.A., Haidari A.H. and Soburn U. 1991 On the dynamics of near-wall turbulence, *Philosophical Transactions of the Royal Society of London, Series A*, **336**, 131-175.
- Smith J.D. and Mclean S.R. 1977 Spatially averaged flow over a wavy surface, *Journal of Geophysical Research - Oceans and Atmospheres*, **82**, 12, 1735-1746.
- Smutek R. 1969 Discussion on 'Measurement of turbulence in water' by Richardson and McQuivey, *Journal of Hydraulics Division, ASCE*, **95**, HY-1, 519-523.
- Song T. and Chiew Y.M. 2001 Turbulence measurement in nonuniform open-channel flow using Acoustic Doppler Velocimeter (ADV), *Journal of Engineering Mechanics, ASCE*, **127**, 3, 219-232.
- Song T., Lemmin U. and Graf W.H. 1994 Uniform-flow in open channels with movable gravel-bed, *Journal of Hydraulic Research*, **32**, 6, 861-876.
- Statzner B. and Higler B. 1986 Stream hydraulics as a major determinant of benthic invertebrate zonation patterns, *Freshwater Biology*, **16**, 1, 127-139.
- Stoesser T., Matthey F., Frohlich J. and Rodi W. 2003 LES of flow over multiple cubes, *ERCRAFT Bulletin No. 56: Complex Flow Problems*.
- Tait S.J. 1993 The physical processes of bed armouring in mixed grain sediment transport, PhD Thesis, University of Aberdeen, Aberdeen, UK.
- Tait S.J. and Willetts B.B. 1992 Characterisation of armoured bed surfaces, *Proceedings of International Grain Sorting Seminar, Zurich*, **117**, E.T.H. Zurich.

- Tait S.J., Willetts B.B. and Maizels J.K. 1992 Laboratory observations of bed armouring and changes in bedload composition. In Billi, P., Hey, R.D., Thorne, C.R., Tacconi, P. (eds), *Dynamics of Gravel-Bed Rivers*, John Wiley & Sons, Chichester, 205-225.
- Tait S.J., Willetts B.B. and Gallagher M.W. 1996 The application of Particle Image Velocimetry to the study of coherent flow structures over a stabilizing sediment bed. In Ashworth, P.J., Bennett, S.J., Best, J.L., McLelland, S.J. (eds), *Coherent Flow Structures in Open Channels*, John Wiley & Sons, Chichester, 184-201.
- Tamburrino A. and Gulliver J.S. 1999 Large flow structures in a turbulent open channel flow, *Journal of Hydraulic Research*, **37**, 3, 363-380.
- Thibodeaux L.J. and Boyle J.D. 1987 Bedform-generated convective-transport in bottom sediment, *Nature*, **325**, 6102, 341-343.
- Tinkler K.J. 1997 Critical flow in rockbed streams with estimated values for Manning's n , *Geomorphology*, **20**, 1-2, 147-164.
- Toro-Escobar C.M., Paola C., Parker G., Wilcock P.R. and Southard J.B. 2000 Experiments on downstream fining of gravel: II. wide and sandy runs, *Journal of Hydraulic Engineering, ASCE*, **126**, 3, 198-208.
- Tritico H.M. and Hotchkiss R.H. 2005 Unobstructed and obstructed turbulent flow in gravel bed rivers, *Journal of Hydraulic Engineering, ASCE*, **131**, 8, 635-645.
- Walters R.A. 2002 From river to ocean: a unified modelling approach. In Spaulding M.L. (ed), *Estuarine and Coastal Modelling*, ASCE, Reston, 683-694.
- Westerweel J. 1994 Efficient detection of spurious vectors in Particle Image Velocimetry data, *Experiments in Fluids*, **16**, 3-4, 236-247.
- Wiberg P.L. and Smith J.D. 1991 Velocity distribution and bed roughness in high-gradient streams, *Water Resources Research*, **27**, 5, 825-838.
- Wilson C.A.M.E., Boxall J.B., Guymer I. and Olsen N.R.B. 2003 Validation of a three-dimensional numerical code in the simulation of pseudo-natural meandering flows, *Journal of Hydraulic Engineering, ASCE*, **129**, 10, 758-768.
- Wilson N.R. and Shaw R.H. 1977 A higher-order closure model for canopy flow, *Journal of Applied Meteorology*, **16**, 11, 1197-1205.
- Yaglom A.M. 1979 Similarity laws for constant-pressure and pressure-gradient turbulent wall flows, *Annual Review of Fluid Mechanics*, **11**, 505-540.
- Yalin M.S. 1992 *River Mechanics*, Pergamon, Oxford.
- Zhou D.H. and Mendoza C. 1993 Flow through porous bed of turbulent stream, *Journal of Engineering Mechanics, ASCE*, **119**, 2, 365-383.

NOTATION

a	gradient of the linear least-squares fit of a spectral range within the power spectrum of water surface elevations
A	averaging area
A_c	cross-sectional area of the flow
A_f	fluid domain within averaging area
A_{\min}	minimum averaging area required to obtain a representative value of the fractional contribution of form-induced stress to the total fluid stress
A_B	largest averaging area used to calculate the fractional contribution of form-induced stress to the total fluid stress
A_0	total averaging area
C	cross-covariance between two variables
d	flow depth
d_{\max}	upper limit of the particle displacements that can be measured by the Particle Image Velocimetry system
dE	elemental risk of grain entrainment
dV	velocity range
D_b	structure function
D	scale of interest
D_u	empirical constant in equation for vertical variability in turbulence intensity
$D_{\bar{u}}$	empirical constant in equation (4.5)
D_x	empirical constant in equation (5.5)
D_y	empirical constant in equation (5.6)
D_{50}	grain size at which 50 per cent of the bed material is finer
D_{84}	grain size at which 84 per cent of the bed material is finer
f	frequency
f_G	probability density function of the instantaneous streamwise velocities required to destabilise grains on a bed from their positions

f_F	probability density function of instantaneous streamwise velocities
f_s	sampling frequency
F	flow variable defined in the fluid to be spatially averaged
\bar{F}	time-averaged flow variable
$\langle \bar{F} \rangle$	double-averaged flow variable
F'	temporal fluctuation in flow variable
\tilde{F}	spatial deviation in flow variable
Fr	Froude number of the flow
FS_f	fractional contribution of form-induced stress to the total fluid stress
FS_{pf}	FS_f derived from 24 randomly selected points within the matrix of velocity vectors
$\langle FS_f \rangle$	FS_f derived from the whole matrix of velocity vectors
g	force due to gravitational attraction
G	probability of grain entrainment
H	maximum flow depth
H_x	Hurst exponent for the streamwise variation in bed surface elevations
H_y	Hurst exponent for the streamwise variation in bed surface elevations
k_F	dispersive kinetic energy
k_s	equivalent sand roughness height
K_b	kurtosis of the distribution of bed surface elevations
$K_{\bar{u}}$	kurtosis of the distribution of time-averaged streamwise velocities over the bed
$K_{\bar{w}}$	Kurtosis of the distribution of time-averaged vertical velocities over the bed
K_D	kurtosis of the grain-size distribution
l	characteristic length of the variations in a quantity
l_t	time lag
l_x	spatial lag in the streamwise direction
l_{x_0}	correlation length of bed surface elevations in the streamwise direction
l_y	spatial lag in the lateral direction
l_{y_0}	correlation length of bed surface elevations in the lateral direction

L	upper length scale of a spectral range within the power spectrum of water surface elevations
L_{int}	length of the interrogation area used for cross-correlation of the Particle Image Velocimetry images
L_0	streamwise length scale
L_R	range of length scales of a spectral range within the power spectrum of water surface elevations
m	multiple of the double-averaged streamwise velocity
m_b	multiplying coefficient of the sampling interval in the lateral direction of the bed surface elevation measurements
m_{FS_f}	mean FS_f involved in a cross-correlation
$m_{\bar{u}/\langle\bar{u}\rangle}$	mean ratio of time-averaged streamwise velocity to the double-averaged streamwise velocity involved in a cross-correlation
$m_{\bar{w}/u_*}$	mean ratio of time-averaged vertical velocity to the bed shear velocity involved in a cross-correlation
m_{z_b}	mean bed surface elevation involved in a cross-correlation
M_b	total number of bed surface elevation measurements in the lateral direction
n	number of point measurements required to provide representative estimates of double-averaged streamwise velocity over the bed
n_b	multiplying coefficient of the sampling interval in the streamwise direction
N	total number of measurements within the flow field
N_b	total number of bed surface elevation measurements in the lateral direction
N_C	number of cross-correlated measurements
N_E	number of grains within a measurement area susceptible to entrainment
N_G	number of grains on the bed surface
N_R	total number of repetitions
P	fluid pressure
P	wetted perimeter of the flume
P_{z_w}	power spectral density of the water surface elevations
\bar{P}_s	average power spectral density of the water surface elevations

q_b	width-averaged bedload transport rate
q_s	bedload transport discharge
q_{sp}	width-averaged bedload transport rate for the measurement section
q_0	width-averaged bedload transport rate for the assumption that the double-averaged streamwise velocity holds everywhere in the measurement section
Q	flow discharge
Q_b	width-averaged estimate of bedload flux
Q_{sp}	width-averaged estimate of bedload flux for the measurement section
Q_0	width-averaged bedload flux for the assumption that the double-averaged streamwise velocity holds everywhere in the measurement section
Q^*	relative width-averaged bedload flux
R	hydraulic radius
R^2	proportion of variability in a variable explained by the regression model
R_b	correlation function of the variation in bed surface elevations
R_{z_w}	correlation function of the temporal variation in water surface elevations
Re	Reynolds number of the flow
S	bed slope
Sk_b	skewness of the distribution of bed surface elevations
$Sk_{\bar{u}}$	skewness of the distribution of time-averaged streamwise velocities over the bed
$Sk_{\bar{w}}$	skewness of the distribution of time-averaged vertical velocities over the bed
Sk_D	skewness of the grain-size distribution
t	time
t_s	time separation between two light sheet pluses
u	instantaneous streamwise velocity
u'	temporal fluctuation in streamwise velocity
\bar{u}	time-averaged streamwise velocity
$\langle \bar{u} \rangle$	double-averaged streamwise velocity
$\langle \bar{u} \rangle_s$	$\langle \bar{u} \rangle$ at the height closest to the water surface

$\langle \bar{u} \rangle_p$	$\langle \bar{u} \rangle$ derived from 24 randomly selected points within the matrix of velocity vectors
$\langle \bar{u} \rangle_{bed}$	$\langle \bar{u} \rangle$ derived from the whole matrix of velocity vectors
\tilde{u}	spatial deviation in \bar{u}
u_*	bed shear velocity
$\tilde{u}\tilde{w}$	normalised product of the spatial deviations in the time-averaged flow
\bar{U}	average flow velocity (calculated from the ratio of flow discharge to the cross-sectional area of the flow)
v	instantaneous lateral velocity
V_F	temporal distribution of u
V_G	distribution of u required to destabilise grains on a bed from their positions
$\langle \bar{v} \rangle$	double-averaged lateral velocity
V_{max}	possible velocity range that can be measured by the Particle Image Velocimetry system
w	instantaneous vertical velocity
w_c	width of the channel
\bar{w}	time-averaged vertical velocity
$\langle \bar{w} \rangle$	double-averaged vertical velocity
\tilde{w}	spatial deviation in time-averaged vertical velocity
W_0	lateral length scale
x	streamwise distance
\bar{x}	sample mean
x_2	upper limit of a 95 % confidence interval
y	lateral distance
z	height above the maximum bed elevation
z_b	bed surface elevation
z_c	maximum bed elevation
z_f	height of the channel floor
z_t	height of the troughs of the roughness elements
z_{ws}	height of the water surface
z_R	maximum height at which the form-induced sublayer is present

z_L	maximum height at which the logarithmic regions is present
$(z/d)_{\min}$	height above the maximum bed elevation, relative to the depth of the flow, at which $\sigma_{\bar{w}}/u_*$ attains its minimum value
$(z/D_{84})_{\min}$	height above the maximum bed elevation, relative to D_{84} , at which $\sigma_{\bar{w}}/u_*$ attains its minimum value
Z	normal distribution
β_1	multiplying coefficient for relative submergence in a multiple regression model
β_2	multiplying coefficient for bed slope in a multiple regression model
δ_F	height of the boundary between the form-induced sublayer and the logarithmic layer above the maximum bed elevation
δ_L	height of the boundary between the logarithmic layer and the outer layer above the maximum bed elevation
δx	sampling interval in z_b measurements in the streamwise direction
δy	sampling interval in z_b measurements in the lateral direction
ϕ	normalised value of A_f
γ	characteristic filter width
η	correlation coefficient
κ	von Kármán constant
λ_u	empirical constant in equation for vertical variability in turbulence intensity
$\lambda_{\bar{u}}$	empirical constant in equation (4.5)
λ_x	empirical constant in equation (5.5)
λ_y	empirical constant in equation (5.6)
ν	kinematic viscosity
ρ	fluid density
ρ_s	sediment density
σ	standard deviation in a population
σ_D	sorting coefficient of grain-size distribution
σ_{FS_f}	degree of spatial variability in FS_f over the bed
σ_{FS}	standard deviation in FS_{pf} from $\langle FS_f \rangle$

$\sigma_{\bar{u}}$	degree of spatial variability in \bar{u}
$\sigma_{p\bar{u}}$	$\sigma_{\bar{u}}$ derived from 24 randomly selected points within the matrix of velocity vectors
$\sigma_{bed\bar{u}}$	$\sigma_{\bar{u}}$ derived from the whole matrix of velocity vectors
$\sigma_{\langle\bar{u}\rangle}$	standard deviation in $\langle\bar{u}\rangle_p$ from $\langle\bar{u}\rangle_{bed}$
$\sigma_{\sigma_{\bar{u}}}$	standard deviation in $\sigma_{p\bar{u}}$ from $\sigma_{bed\bar{u}}$
$\sigma_{\tilde{u}\tilde{w}}$	standard deviation in $\tilde{u}\tilde{w}$.
σ_w	standard deviation in w
$\sigma_{\bar{w}}$	degree of spatial variability in \bar{w}
$\sigma_{p\bar{w}}$	$\sigma_{\bar{w}}$ derived from 24 randomly selected points within the matrix of velocity vectors
$\sigma_{bed\bar{w}}$	$\sigma_{\bar{w}}$ derived from the whole matrix of velocity vectors
$\sigma_{\sigma_{\bar{w}}}$	standard deviation in $\sigma_{p\bar{w}}$ from $\sigma_{bed\bar{w}}$
σ_{z_b}	standard deviation in z_b
$\sigma_{z_{bx}}$	standard deviation in spatially lagged z_b
τ	total fluid stress
τ^*	normalised fluid stress
τ_{av}	mean shear stress averaged across the channel width
τ_c	critical shear stress for grain entrainment
τ_c^*	normalised critical shear stress for grain entrainment
τ_0	bed shear stress
ξ_L	thickness of the logarithmic layer relative to the flow depth
ξ_O	thickness of the outer layer relative to the flow depth
Δ	bed roughness height